2013-06-27

Investigation of Water-Molecule Complexes and Their Catalytic Effect on Important Atmospheric Reactions

Taylor Scott Cline
Brigham Young University - Provo

BYU ScholarsArchive Citation
Cline, Taylor Scott, "Investigation of Water-Molecule Complexes and Their Catalytic Effect on Important Atmospheric Reactions" (2013). *All Theses and Dissertations*. 3990.
https://scholarsarchive.byu.edu/etd/3990

Investigation of Water-Molecule Complexes and Their Catalytic Effect on Important Atmospheric Reactions

Taylor S. Cline

A dissertation submitted to the faculty of
Brigham Young University
in partial fulfillment of the requirements for the degree of

Doctor of Philosophy

Jaron C. Hansen, Chair
Steven R. Goates
Paul B. Farnsworth
Milton L. Lee
James E. Patterson

Department of Chemistry and Biochemistry

Brigham Young University

June 2013

ABSTRACT

Investigation of Water-Molecule Complexes and Their Catalytic Effect on Important Atmospheric Reactions

Taylor S. Cline
Department of Chemistry and Biochemistry, BYU
Doctor of Philosophy

This dissertation is a collection of works that investigates issues related to environmental chemistry. The first portion of this research explores the role of water vapor on the kinetics of important atmospheric reactions. Work is presented on the self-reaction of β-hydroxyethyl peroxy radical (β-HEP) and the catalytic increase in reaction rate by water vapor. β-HEP serves as a model system for investigating the possible role of water vapor in perturbing the kinetics and product branching ratio of atmospheric reactions of other alkyl peroxy radicals. The self-reaction rate coefficient of β-HEP was investigated between 274–296 K with 1.0×10^{15} to 2.5×10^{17} molecules cm^{-3} of water vapor at 200 Torr total pressure by slow-flow laser flash photolysis coupled with UV time-resolved spectroscopy and long-path, wavelength-modulated, diode-laser spectroscopy. The overall disproportionation rate constant is expressed as the product of temperature-dependent and water vapor-dependent terms giving $k(\mathrm{T},\mathrm{H_2O}) = 7.8 \times 10^{-14}(\mathrm{e}^{8.2\ (\pm 2.5)\ kJ/RT})(1 + 1.4 \times 10^{-34} \times \mathrm{e}^{92\ (\pm 11)\ kJ/RT}[\mathrm{H_2O}])$. The results suggest that formation of a β-HEP-H_2O complex is responsible for the observed water vapor enhancement of the self-reaction rate coefficient. Complex formation is supported with computational results identifying three local energy minima for the β-HEP-H_2O complex. Both the temperature range and water vapor concentrations used were chosen because of their significance to conditions in the troposphere. As the troposphere continues to get warmer and wetter, more complexes with water will form, which in turn may perturb the kinetics and product branching ratios of atmospheric reactions. Future studies are proposed for the reaction of β-HEP + NO leading to NO_2 formation. A laser-induced fluorescence cell was design, built, and tested in preparation for studies of NO_2 formation. Additionally Harriott-cell optics were manufactured and tested to detect HO_2 using two-tone frequency-modulated diode-laser spectroscopy.

In a related work, the breakdown of the environmental contaminants polychlorinated biphenyls (PCB's) was investigated using a new method. A new method for analyzing anaerobic digestion is also presented. The degradation rate and efficiency of digestion processes are typically measured by introducing a substrate or pollutant into a digester and then monitoring the effluents for the pollutant or substrate, a costly and slow process. A new method for rapid measurement of the rates and efficiencies of anaerobic degradation of pollutants and lignocellulose substrates from various pretreatments is described. The method uses micro-reactors (10–30 mL) containing a mixed culture of anaerobic bacteria obtained from a working anaerobic digester. The rates of degradation and metabolism of pollutants are measured in parallel sets of micro-reactors. Measurements of metabolic rate and pollutant degradation simultaneously is an effective means of rapidly examining pollutant degradation on a micro-scale. Calorimetric measurements alone allow rapid, relative evaluation of various substrate pretreatment methods.

Finally calorimetric and electrophoretic methods were used to further knowledge in analytical techniques applied to important problems. In the last section of this dissertation the thermal and photolytic breakdown of promethazine hydrochloride is reported. Promethazine hydrochloride is a medication that is commonly used as an antihistamine, a sedative, and an antiemetic, and to treat motion sickness. Perivascular extravasation, unintentional intra-arterial injection and intraneuronal or perineuronal infiltration may lead to irreversible tissue damage if the drug is not properly diluted or is administered too quickly. Data on the stability of promethazine hydrochloride diluted in sodium chloride 0.9% are lacking. This study evaluates the thermal and photolytic degradation of promethazine hydrochloride concentrations of 250 μg/mL and 125 μg/mL diluted in sodium chloride 0.9% over a period of 9 days. Degradation rates of promethazine hydrochloride were determined under UV-light, fluorescent light, and no light at various temperatures and concentrations to determine medication stability. The shelf-life (<10% degradation) at 25°C under normal fluorescent lights is 4.9 days, at 25°C protected from light, 6.6 days, and at 7°C in the dark, 8.1 days. These results may increase patient safety by improving current protocols for intravenous promethazine administration.

Keywords: Peroxy Radicals, Radicals, Water Enhancement, Atmospheric Chemistry, Spectroscopy, UV-Vis, Frequency Modulated Spectroscopy, Gas-Phase Kinetics

ACKNOWLEDGMENTS

I would like to thank my advisers, especially Jaron Hansen, Lee Hansen, and Steven Goates for their constant support and high expectations for my development. I would also like to thank my research group, especially Marie Killian, Makena Hinrichs, Joseph Moesley, William Keeton, Robert Baker, Andrew Orton, Nate Killpack, and Nicole Taylor for the great learning atmosphere we developed together. Dr. David Robichaud at NREL deserves special credit for being a mentor to me in spectroscopy and LabVIEW even though he has no affiliation with BYU and had little to gain with my career. The BYU Chemistry department faculty and support staff especially The Instrument shop, Sue Mortensen, Peggy Erickson, and Teresa Harper. Finally, I would like to thank my parents for encouraging me to always learn all that I can since birth and my beloved wife Christina who sacrificed much in our first eight years of marriage having a career of her own while raising our three children Alvin, Chloe, and Porter.

Table of Contents

List of Figures

List of Tables

Chapter 1

Introduction

1.1 Organic peroxy radicals in the troposphere

> ”One of the most striking developments of the past decade, both in the field of air pollution and in that of atmospheric chemistry, has been the recognition that photochemical reactions, produced by sunlight, may convert relatively innocuous pollutants into substances which constitute a nuisance, create a possible health hazard, and cause economic loss to man.”
>
> -Phillip A. Leighton (1961)[1]

The chemistry of the atmosphere is complex and varies with altitude, latitude, season, geology, and human activity. The efficacy of pollution control measures depends on the level of understanding of local chemistry accompanied with measurements of pollution from sources. One example contrasts London, England air dominated by sulfur pollution (from high-sulfur coal leading to particulate matter formation) with Los Angeles, Ca, USA air and its high ozone concentrations (from photolysis of organics and NO_x).[2] Solutions to the pollution problems in London applied to the air in Los Angeles may exacerbate the air quality issues in these areas.

In 1963 the United States Congress passed the Clean Air Act, which commissioned research into tropospheric pollution. In 1970 the act was amended to give federal regulatory powers to the newly created Environmental Protection Agency (EPA). The EPA was legislated to maintain and enforce the National Ambient Air Quality Standards (NAAQS). These standards have been amended numerous times in the past 40 years. The NAAQS list current standards for six principle health related pollutants. (Table 1.1). This dissertation focuses on the balance of the production and destruction of ozone in the troposphere. NO_2 plays a pivotal role in the regulation of ozone and therefore is discussed as well. Ozone is unique in its ability to be a pollutant in the lower troposphere, but provide a shield to protect living organisms from deep UV-light ($\lambda < 300$ nm) while in the stratosphere. The mechanisms that regulate ozone in the troposphere are dominated by radical reactions. Numerous radical reactions in the atmosphere lead to complex chemistry, but the complexity becomes manageable by identifying chemical cycles to monitor important pollutants that are produced from common functional groups. Two important cycles discussed below are the HO_x and NO_x cycles. The reactions and interconnectivity of the HO_x and NO_x cycles play a pivotal role in determining the sinks and sources of ozone.[3]

The history from the discovery of ozone to the implementation of pollution controls spans nearly 150 years. Ozone was discovered in 1840 when Schonbein[4] noticed a distinct smell during his experiments on the electrolysis of water, and he named the substance ozone after the Greek word ”ozein” for smell. It was similar to the smell of lightning and the smell produced by an arc between two electrodes previously noted in 1785 by Van Marum[5], but at the time was attributed to electricity and not a chemical reaction. Schonbein later proposed that ozone may be detectable in air. Andrews[6] in 1868 was able to identify ozone in an air mass through reaction with starch iodide. This was more of a qualitative than quantitative test at the time, but led to the general acceptance that ozone was a constituent of air. Schoenbein even attempted to correlate increased detection of ozone after snowfalls to increased frequency of catarrhal (respiratory and oral inflammation).[7] Cornu[8] in 1879, discovered (while studying the electromagnetic spectrum of the sun) that intensity dropped off rapidly below 300 nm. He correctly postulated that the cutoff was due to an absorbing species, because the intensity decreased further as the sun set throughout the day. The following year, Hartley[9] suggested that the absorber was ozone. Fabry and Buissen[10] measured the cutoff region in the electromagnetic spectrum and deduced that the ozone layer at normal

Table 1.1: National Ambient Air Quality Standards. (Amended 2010)

Pollutant	Primary or Secondary	Averaging time	Level
Ozone	Both	8-h	0.075 ppm
Nitrogen Dioxide	Primary	1-h	100 ppb
	Both	Annual	53 ppb
Carbon Monoxide	Primary	8-h	9 ppm
		1-h	35 ppm
Lead	Both	3 mon	0.15 μg/m^3
Sulfur Dioxide	Primary	1-h	75 ppb
	Secondary	3-h	0.5 ppm
$PM_{2.5}$	Primary	Annual	12 μg/m^3
	Secondary	Annual	15 μg/m^3
	Both	24-h	35 μg/m^3
PM_{10}	Both	24-h	150 μg/m^3

temperature and pressure would have to be 5 mm thick to cause such an intensity loss. Strutt[11] in 1918 attempted to test Fabry's calculation by measuring the absorption of ozone over a 4 mi pathlength, but found no absorption and concluded that the concentration of ozone must be much greater at higher altitudes for the sharp intensity cutoff to be explained by absorption due to ozone. After these initial discoveries, ozone became an important reagent in the discovery of molecular composition of organic products through ozonolysis in the late 1800s, but a greater understanding of the ozone layer and ozone pollution in the troposphere came much later in the twentieth century as described by Leighton[1].

The importance of peroxy radical (RO_2) chemistry was established in the late 1970s and throughout the 1980s, and forms the basis of the HO_x and NO_x cycles.[12] Prior to the understanding of peroxy radicals and the HO_x and NO_x cycles, ozone was known to be produced in air masses containing both organics and the industrial and automotive pollutant NO_x.[13,14] Ozone episodes were first noticed in the 1940s in Los Angeles. The pollution of Los Angeles was strongly oxidizing, eye-watering, and plant killing. As opposed to pollution episodes in London that were characterized as reducing visibility due to high concentrations of particulate matter, these occurred mostly at mid-day with warm temperatures and bright sunshine. The 1950s produced significant achievements in understanding the role of radical chemistry on ozone production. Peroxy radicals were first postulated as intermediates in combustion processes and later applied to atmospheric chemistry. HO_2 was first postulated to exist as an intermediate in the reaction whereby H_2O_2 was created in the photolysis of mixtures of H_2 and O_2.[15] It was not until 1953 that the first evidence of a peroxy radical was discovered by Foner and Hudson.[16] They used mass spectrometry to detect HO_2 in a sample of atomic hydrogen flowed through molecular oxygen in a molecular beam expansion.[17] The most prominent mechanisms for the formation of peroxy radicals in the atmosphere is the addition of either OH or ozone to unsaturated hydrocarbons. The formation of peroxy radicals by either of these pathways sets in motion the HO_x and NO_x cycles.

1.2 HO_X and NO_X cycles

Although N_2, O_2, and Ar make up 99.96% of the Earth's atmosphere, the concentrations of trace species drives the pollution mechanisms of the atmosphere. The lower atmosphere can be thought of as a low temperature combustion system[18], except this system is not driven by heat processes but is initiated through photochemistry. Photolysis of trace species initiates radical propagation, terminating in closed-shell species that pollute the atmosphere. Free radicals have extremely high reactivity and accordingly have short lifetimes and, therefore, are found in the troposphere at concentrations typically less than 100 parts per trillion. Their high reactivity causes the chemistry of the troposphere to be complex, but can be simplified by discovering common reactions for the removal of organics found in the atmosphere. Two prominent cycles that are commonly used to model the troposphere are the HO_x cycle (the reactions governing the radicals OH, HO_2, and hydrogen atoms) and the NO_x cycle (the reactions describing the interconversion of NO and NO_2). These cycles are interconnected but discussed separately here.

The HO_x cycle is depicted schematically in Figure 1.1. The initiator of this cycle is the hydroxyl radical (OH) initially formed by photolysis of ozone in the presence of water.[2]

$$\mathrm{O_3} + h\nu(\lambda < 320nm) \rightarrow \mathrm{O}(^1D) + \mathrm{O_2}(^1\Delta_g) \tag{1.1}$$

$$\mathrm{O}(^1D) + \mathrm{H_2O} \rightarrow \mathrm{OH} + \mathrm{OH} \tag{1.2}$$

OH concentrations typically range from less than 1×10^4 molecules cm^{-3} at night to $\sim 3 \times 10^6$ molecules cm^{-3} at midday.[19,20] OH predominately reacts with CO to form hydrogen atoms that add to O_2 to form HO_2.

$$\mathrm{OH} + \mathrm{CO} \rightarrow \mathrm{CO_2} + \mathrm{H} \tag{1.3}$$

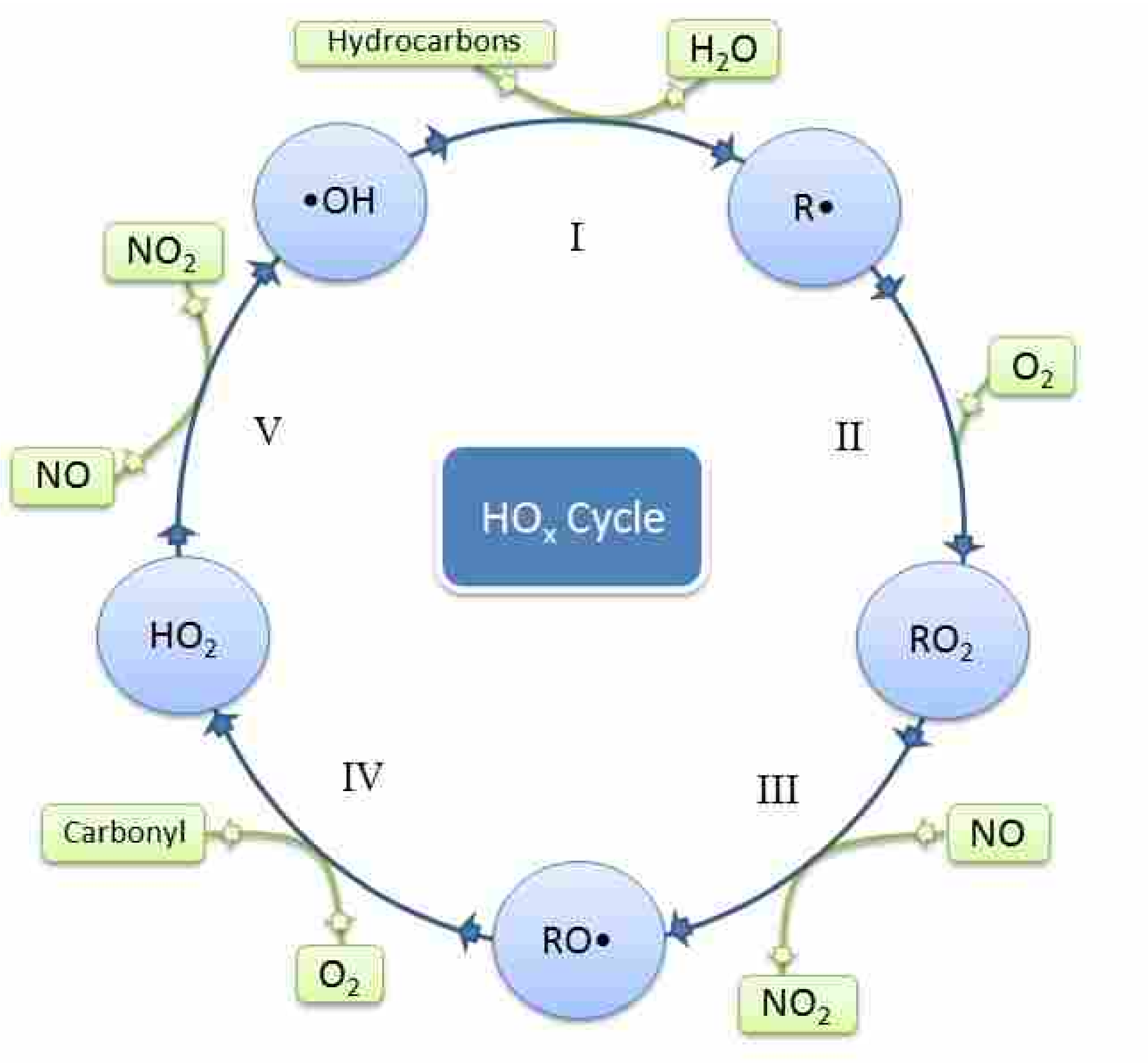

Figure 1.1: The HOx cycle. (Author's Original)

$$H + O_2 \rightarrow HO_2 \tag{1.4}$$

Organic species, whether from biogenic or anthropogenic sources, are removed from the troposphere by way of reaction with OH, creating an alkyl radical (R).

$$OH + RH(Organics) \rightarrow H_2O + R \tag{1.5}$$

With 21% of the atmosphere being O_2, the only significant reaction of alkyl radicals is the addition of O_2 to form peroxy radicals.

$$R + O_2 \rightarrow RO_2 \tag{1.6}$$

RO_2 and the simple and dominant peroxy radical, HO_2 are found in concentrations from 0.2–2.5 × 10^8 molecules cm^3.[2,20] These molecules react with themselves and with each other, especially in pristine environments (low NO_x). The self-reaction of one of the most prominent peroxy radicals, $HOCH_2CH_2O_2$, is the focus of the research in Chapter 2. In more polluted conditions (high NO_x) the self-reactions of peroxy radicals compete with the reaction with NO to oxidize NO to NO_2 and produce an alkoxy radical (RO).

$$RO_2 + NO \rightarrow RO + NO_2 \tag{1.7}$$

Reaction 1.7 has a second minor pathway that produces an organic nitrate ($RONO_2$) and is the focus of the research decribed in chapter 3. Alkoxy radicals react with O_2 to form HO_2 and a carbonyl containing compound.

$$RO + O_2 \rightarrow HO_2 + Carbonyl\ Compound \tag{1.8}$$

The carbonyl compound formed will depend on the R group of the original organic molecule, but often form aldehydes. Many aldehydes are known to photolyze in the day time to produce many other radical-chain pathways. Other carbonyl compounds are oxidized by OH as the HO_x cycle continues. The cycle completes back to where it started when HO_2 is reduced by oxidizing NO to NO_2, just as the peroxy radical did in reaction 1.7.

$$\mathrm{HO_2} + \mathrm{NO} \rightarrow \mathrm{OH} + \mathrm{NO_2} \tag{1.9}$$

Chain termination occurs with peroxide formation from the self-reaction of HO_2 and in many cross reactions of RO_2.

The NO_x cycle is depicted as a schematic in Figure 1.2. This chain is initiated by the emission of NO into the troposphere. NO and NO_2 are formed when N_2 and O_2 are present together at elevated temperature ($T > 2800°F$), which commonly occurs in internal combustion engines and power plant boilers. As previously mentioned, Reactions 1.7 and 1.9 oxidize NO to NO_2. Additionally, ozone may oxidize NO to NO_2, but at slower rates. NO_2 is readily photolyzed to form a radical oxygen that subsequently forms ozone.[21]

$$\mathrm{NO_2} + h\nu(\lambda < 410nm) \rightarrow \mathrm{NO} + \mathrm{O}(^3P) \tag{1.10}$$

$$\mathrm{O}(^3P) + \mathrm{O_2} + M \rightarrow \mathrm{O_3} + M \tag{1.11}$$

This reaction is the predominant mechanism for tropospheric ozone formation.[2] For every carbon in a hydrocarbon that passes through the HO_x cycle, two molecules of ozone are formed. As the sun sets and the supply of OH is depleted, these cycles do not terminate because of night-time chemistry. NO_2 is no longer photolyzed at night but can react with ozone to form the nitrate radical (NO_3).

$$\mathrm{NO_2} + \mathrm{O_3} \rightarrow \mathrm{NO_3} + \mathrm{O_2} \tag{1.12}$$

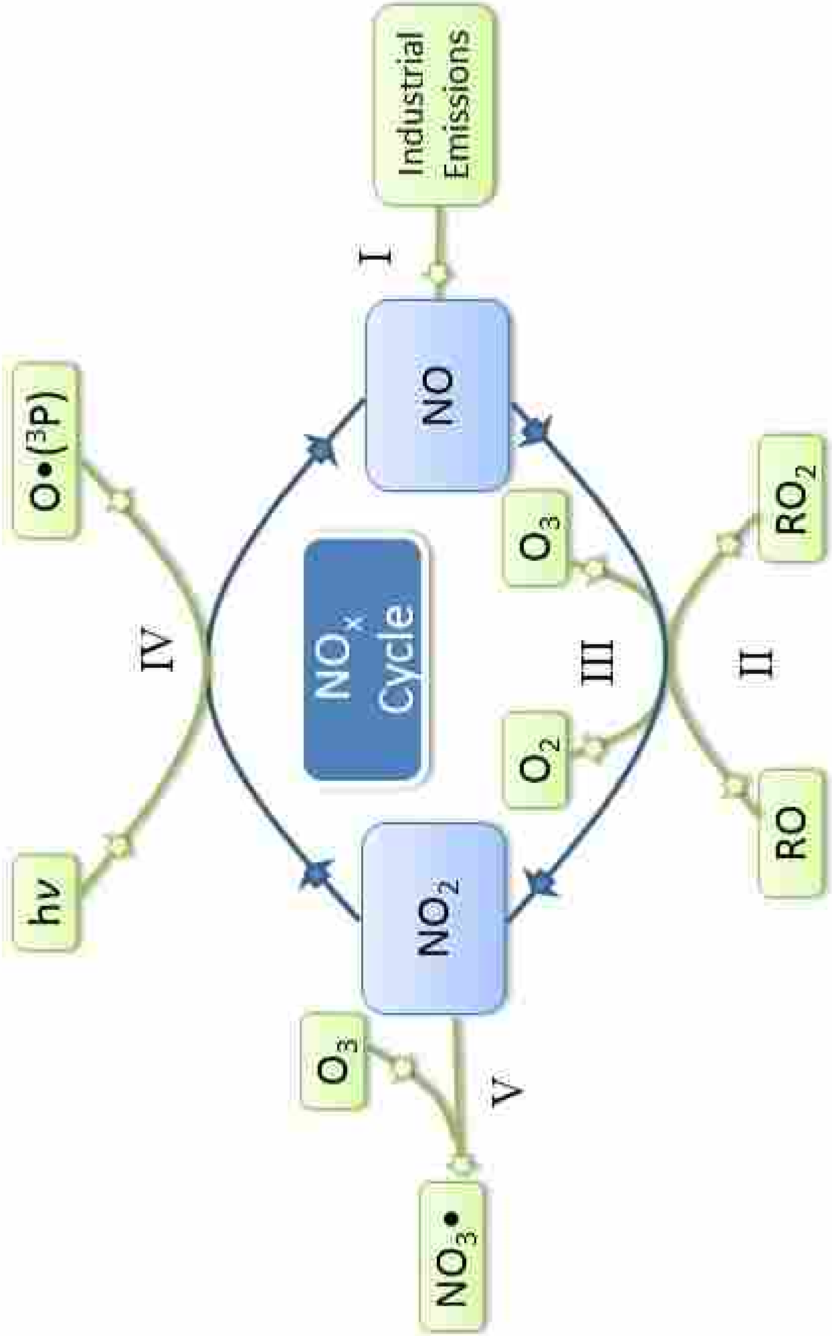

Figure 1.2: The NOx cycle. (Author's Original)

Nitrate subsequently takes the role of OH in the the HO_x cycle in oxidizing hydrocarbons through hydrogen abstraction to alkyl radicals. Nitrate chemistry ceases at dawn because of its large absorption cross section of visible light and high photolysis yield.[22]

1.3 Recent developments in peroxy radical detection for kinetic experiments

The detection of peroxy radicals is divided into two fields in the discipline of atmospheric chemistry, atmospheric monitoring and atmospheric kinetics. Monitoring peroxy radicals in the atmosphere requires selectivity so that different peroxy radicals can be identified, whereas this is of less importance in kinetic experiments because these experiments typically control gas flow to limit production of other peroxy radicals with the exception of peroxy radical cross-reactions. Improvements in kinetic experiments in the past decade have focused on time-resolution as well as detection limits. UV-vis absorption spectroscopy for detection of peroxy radicals has dominated past experiments of peroxy radicals. Peroxy radicals have a large absorption cross section at 245 nm. Detection of RO_2 radicals is plagued with poor selectivity due to the fundamentally broad absorption in the UV. One exception is HO_2 radical. Its $^2B \leftarrow {}^2X$ transition is blue-shifted relative to other RO_2 radicals and absorbs at 220 nm, which allows it to be deconvolved from a mixture of peroxy radicals. The infrared portion of the electromagnetic spectrum has the desired selectivity to distinguish between peroxy radicals. The mid-IR region offers several disadvantages, namely non-radical species absorbing in the region and the high cost, low-tunability of mid-IR lasers.

Near-IR spectroscopy has the advantage of high selectivity and low cost lasers. Tunable lasers have made diode-laser spectroscopy commonplace for trace detection of gas species.[23] Diode lasers provide emission in the near-IR up to 2 microns with 500 to 1000 nm tunability. Additionally, these lasers have no consumables, unlike lead-salt diode lasers that require cryogenic cooling. In 2003, Taatjes[24] identified the HO_2 overtone transitions near the 1.5 micron portion of the infrared spectrum. Nearly 1000 discernible lines of the HO_2 molecule were recorded; nearly 600 of these transitions are attributed to the first overtone of the fundamental O-H stretch, while the majority of the remainder are thought to be Fermi-resonance transitions due to the combination band of $\nu_2 + 5\nu_3$.[24] These transitions have now been used in kinetic and monitoring experiments.[25–29]

The sensitivity of diode laser spectroscopy is improved by employing wavelength modulation with 2f-heterodyne detection. This technique has improved noise-rejection but requires signal calibration, whereas direct absorption does not. Two types of modulation spectroscopy are commonly used: frequency modulation (FMS) and wavelength modulation (WMS). They differ by the chosen modulation frequency. FMS is modulated at frequencies greater than the half-width of the absorption feature (typically ν = 100 MHz to 1 GHz), while WMS is modulated at less than the half-width (typically ν < 10 MHz).[30] WMS is also termed derivative spectroscopy because the small linewidth of the laser over a much larger absorption feature produces the derivative of the gaussian line absorption shape with the maximum intensity at the inflection point. WMS is cheaper to perform because of the extremely fast detection electronics necessary for FMS. The signal-to-noise improvement of WMS-2f over direct absorption has been reported to be 2–100 times.[30–32] The calibration requirement of WMS has been overcome in some instances by using dual lock-in amplifiers to collect simultaneously the 1f and 2f signals. The 1f-signal can then be used as a direct absorption to calibrate the 2f-signal.

If the desired modulation frequency is 1 GHz but the detection electronics to perform FMS are too expensive, then two-tone frequency modulation (TTFMS) can be implemented to achieve fast modulation. TTFMS uses two closely spaced modulation frequencies, but detection occurs at the difference between the two modulation frequencies, termed the beat frequency. The much slower beat frequency is then detected using slower response electronics. A typical experiment mixes a 6 MHz signal with a 16 GHz signal to produce the sum and difference frequencies at 16.006 GHz and 15.994 GHz followed by detection at 12 MHz. TTFMS maintains the simplicity of WMS requiring an unstabilized laser and slow detection while also providing the advantage of an absorption experiment with signal that rises from an essentially zero background. The past decade has seen numerous publications demonstrating the use of WMS and TTFMS for the detection of HO_2 for fast kinetic experiments in atmospheric conditions.[26–29,33] The reader seeking additional information about this technique is directed to Friedrich's[30] review on modulation spectroscopy or Janik's original work[34] on TTFMS.

An additional spectroscopic method for detection of atmospheric constituents is cavity ringdown spectroscopy (CRDS). CRDS has detection limits up to 4 orders of magnitude better than frequency modulation techniques.[35,36] These detection limits are obtained with optical pathlengths reaching into the tens of km's. These pathlengths are achieved with high reflectivity mirrors placed parallel to each other across a distance defining a reaction cell. On each reflection of the laser a small percentage of the light passes through to a detector. As the light continues to reflect through the cavity the light reaching the detector diminishes and creates the ringdown decay. CRDS is insensitive to light fluctuations in the probe laser through measurements of decays rather then direct absorption. This technique is inherently pulsed but recent developments have led to the implementation of continuous-wave lasers, most notably tunable diode lasers. Reviews on CRDS may be found in references[37–40] as well as further discussion on the pulsed technique in Chapter 3 of this work. CW-CRDS uses an acusto optic modulator and piezo-electric transducers to adjust laser alignment to maximize signal build-up in the cell to a set threshold before terminating light input and allowing the ringdown to occur. This is especially beneficial to atmospheric kinetics because of the CW nature of tunable-diode lasers. Recent work[41] has used CW-CRDS to detect near-IR transitions of methyl and ethyl peroxy radicals followed by the work of Atkinson and Spillman[42] to measure the self-reaction kinetics of the ethyl and methyl peroxy radical self-reactions. These are electronic transitions from to $^2A \leftarrow {}^2X$ with structure unique to an individual peroxy radical. Pulsed CRDS and CW-CRDS are more complicated experiments than modulation techniques but provide greater sensitivity while maintaining the selectivity of near-IR transitions.

1.4 Layout of Dissertation

Chapters 2, 4, and 5 are published works, while Chapter 3 is supplemental work that lays the foundation for future research. Chapter 2 details work on the perturbation of the self-reaction kinetics of β-hydroxylethyl peroxy radicals by water vapor and constitutes the principle focus of this dissertation. The other two accompanying publications detail projects related to topics involving pollution remediation. Specifically, Chapter 4 describes a new method for evaluating the performance of an anaerobic digester. Anaerobic digestion is commonly used to detoxify waste. In this chapter, the new method is evaluated based on its ability to break down polychlorinated biphenyls (PCB's). Chapter 5 describes the results of a study designed to measure the effects of photolysis on promethazine, a commonly used anti-nausea drug. The appendix contains the LabVIEW code written with Dr. David Robichaud to control flash-photolysis experiments in the Hansen Lab. The code is presented to aid future students in using the system while also providing sufficient detail to allow alterations for future needs.

Chapter 2

Water Vapor Enhancement of β-HOCH$_2$CH$_2$O$_2$ Self-Reaction Rate

2.1 Disclaimer

The work presented in this chapter has been submitted for publication in The Journal of Physical Chemistry A. It is presented in its entirety with minor changes.

2.2 Abstract

The effect of water vapor on the HOCH$_2$CH$_2$O$_2$ (β-HEP) self-reaction rate coefficient was investigated between 274–296 K with 1.0×10^{15} to 2.5×10^{17} molecules cm^{-3} of water vapor at 200 Torr total pressure by slow-flow laser flash photolysis coupled with UV time-resolved spectroscopy and long-path, wavelength modulated, diode-laser spectroscopy. The overall disproportionation rate constant is expressed as the product of both a temperature dependent and water vapor dependent term giving $k = 7.8 \times 10^{-14}(\mathrm{e}^{8.2\ (\pm 2.5)\ kJ/RT}) \times (1 + 1.4 \times 10^{-34} \times \mathrm{e}^{92\ (\pm 11)\ kJ/RT}[\mathrm{H_2O}])$. The results suggest that formation of a β-HEP-H$_2$O complex is responsible for the observed water vapor enhancement of the self-reaction rate coefficient. Complex formation is supported with computational results identifying three local energy minima for the β-HEP-H$_2$O complex. β-HEP serves as a model system for investigating the possible role of water vapor in perturbing the kinetics and product branching ratio of atmospheric reactions of other alkyl peroxy radicals. Both the temperature range and water vapor concentrations used were chosen because of their significance to conditions in the troposphere. As the troposphere continues to get warmer and wetter, more complexes

with water will form, which in turn may perturb the kinetics and product branching ratios of atmospheric reactions.

2.3 Introduction

Water mediated chemistry contributes significantly to many processes in the atmosphere. A direct relationship has been established between surface temperature and tropospheric water vapor. As the Earth continues to warm and tropospheric water vapor increases, this increase has the potential to perturb the chemistry of the troposphere.[43,44] This work provides experimental evidence for an increased rate of reaction of the organic peroxy radical β-hydroxyethyl peroxy (β-HEP) in the presence of water vapor.

Organic peroxy radicals (RO_2) are intermediates in the oxidation of hydrocarbons and are precursors for tropospheric ozone formation.[2] The first step in the oxidation of saturated hydrocarbons, RH, involves abstraction of a hydrogen atom by hydroxyl radical (OH), nitrate radical (NO_3), or atomic chlorine (Cl), resulting in formation of H_2O, HNO_3 or HCl and an alkyl radical, R. The predominant reaction for unsaturated hydrocarbons is addition of OH radical across the double bond to produce an hydroxyalkyl radical. Addition of O_2 to an alkyl radical forms an alkyl peroxy radical, RO_2. In an urban impacted air mass, the predominant removal mechanism for RO_2 radicals is reaction with NO_x. However, at low NO_x concentrations, the self-reaction, reaction with HO_2, or other RO_2 radicals, become important. All of these reactions promote tropospheric ozone (O_3) production.[2]

In 1975, Hamilton[45] discovered that water vapor enhances the self-reaction rate of HO_2. Since then, numerous studies have verified and refined the findings of this first study.[46–51] The complete rate expression, including the temperature and pressure dependence of this reaction, was published in 1985.[49] More recent studies have evaluated the equilibrium constant for formation of the HO_2-H_2O complex as well as the rate enhancement by NH_3 and CH_3OH.[52–54] Hamilton's original work stated that enhancement of the HO_2 self-reaction rate occurs only with polar gases and hypothesized that the increased reaction rate was caused by formation of a complex between HO_2 and H_2O as one step in the reaction mechanism. Existence of an HO_2-H_2O complex has since been experimentally verified by direct observations by Suma et al.[55] Stockwell[56] modeled the water vapor enhancement of the HO_2 self-reaction as it affects the atmospheric HO_x and O_3 budgets. He predicted decreased concentrations of HO_2 and H_2O_2 under saturated water conditions. The concentration of O_3 was previously overestimated by as much as 75% at the surface and 30% at 10 km. Butkovskaya et al.[57] recently showed that reaction of HO_2 + NO at 50% relative humidity (4×10^{17} molecules cm^{-3} at 298 K) perturbed the branching ratio away from NO_2 production and increased the production of HNO_3 by 800%. They hypothesized that a water complex with hydroperoxy radicals serves as an energy sink and consequently drives formation of HNO_3 at the expense of OH and NO_2. Recent computational work[58] indicates that alkyl peroxy radicals can also complex with water vapor. However, the catalytic effect of water has been discussed at length without agreement on a general theory for predicting a change in the rate of specific reactions in response to changes in water vapor concentration.[59–63]

Although the HO_2 self-reaction rate is increased by water, water has little to no effect on the self-reaction rate of methyl peroxy radical (CH_3O_2) or the reaction of CH_3O_2 + HO_2.[64] The absence of catalysis by water is explained by the small fraction of CH_3O_2 complexed with water owing to the small binding energy between H_2O and CH_3O_2, calculated to be 2.1 kcal mol^{-1}.[46] At 100% relative humidity and 298 K, the percentage of CH_3O_2-H_2O complex is ∼0.02 %, substantially less than the 7.8–15% calculated for the HO_2-H_2O complex.[55] By comparison, the β-HEP-H_2O complex is calculated to be bound by 6.5 kcal mol^{-1}, comparable to the binding energy for the HO_2-H_2O complex (6.9 kcal mol^{-1}).[65] The optimized structure predicted for the β-HEP-H_2O complex (Figure 2.1) is stabilized by the formation of two intermolecular hydrogen bonds, as is the HO_2-H_2O complex.

β-HEP is a derivative of ethylene and plays a significant role in tropospheric chemistry. Ethylene is released both naturally from vegetation and from combustion of wood and fossil fuels with an estimated total emission of 18–25 terragrams yr^{-1}.[66] A typical urban

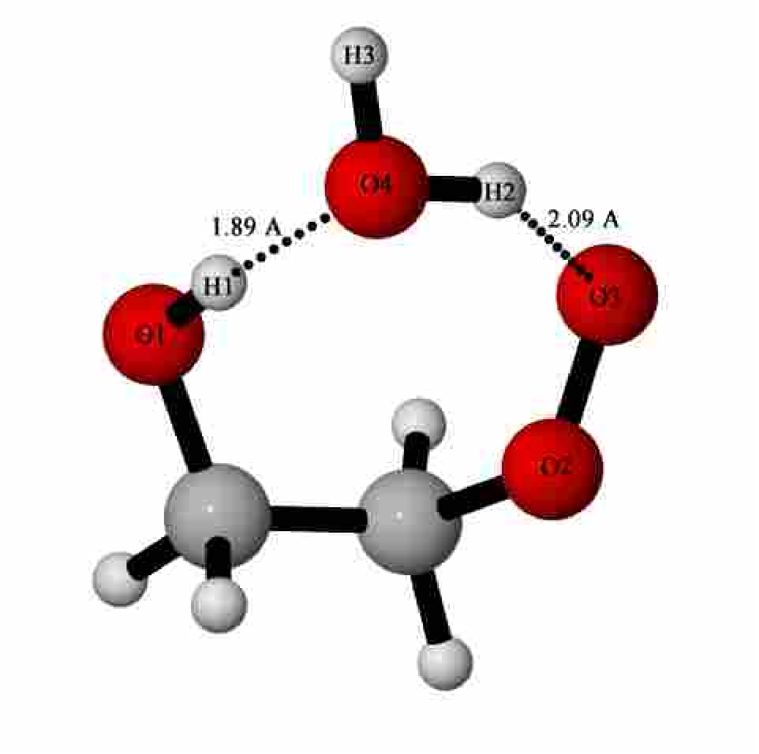

Figure 2.1: MP2(full)/6-311++G(2d,2p) optimized structure of β-HEP-H_2O.

environment contains 50 μg m^{-3} of ethylene with peak concentrations up to 1000 μg m^{-3} during high traffic hours, whereas rural environments range from 1–5 μg m^{-3}.[67]

The self-reaction rate constant of β-HEP over a range of temperatures has previously been established in several studies.[67–73] However, Anastasi et al.[72] reported a reaction rate coefficient of 7.69 $\times$ 10^{-12} cm^3 molecule^{-1} s^{-1} at 298 K, triple the recommended rate by Lightfoot[73] (2.31 $\pm$ 0.3 $\times$ 10^{-12} cm^3 molecule^{-1} s^{-1}). The difference was attributed to the use of different absorption cross sections for β-HEP[67]; however, Anastasi et al.[72] used a water vapor concentration of approximately 1 $\times$ 10^{18} molecules cm^{-3} with initial β-HEP at 8 $\times$ 10^{14} molecules cm^{-3}. The high water concentration was needed to generate OH radicals from pulse radiolysis of SF_6 to form β-HEP whereas the other studies produced β-HEP through photolysis of H_2O_2 and subsequent reaction with ethane. One possible reason for the discrepancy in the β-HEP self-reaction rate coefficient may be formation of a reactive β-HEP-H_2O complex. β-HEP has a large binding energy with water and therefore is susceptible to formation of a complex that may perturb its reactivity in a manner analogous to the $HO_2{-}H_2O$ complex. In this study, we derive an empirical formula to predict the β-HEP self-reaction rate constant as a function of temperature and water vapor, and use high level ab initio calculations to calculate the equilibrium constant for the formation of the β-HEP-H_2O complex.

β-HEP serves as a model system for investigating the possible role of water vapor in perturbing the kinetics and product branching ratio of other alkly peroxy radicals. For water vapor enhancement to be observed, a significant portion of reactants must form a radical-molecule complex.[74,75]. β-HEP is chosen as a model radical to test the theory that strongly hydrogen-bonded complexes increase the rate of self-reaction. Clark et al.[58] demonstrated that β-hydroxy peroxy radicals in general will form complexes with two hydrogen bonds. These molecules are atmospherically relevant because all unsaturated hydrocarbons will add OH across the double bond, and with the addition of O_2 produce β-hydroxy peroxy radicals. Isoprenes and terpenes are two major examples of biogenic sources that will produce

β-hydroxy peroxy radicals. If β-HEP demonstrates a self-reaction rate enhancement, we theorize that peroxy radicals formed from other unsaturated hydrocarbons will also show enhancement with water vapor.

This study presents experimental evidence for the catalytic effect of water vapor on the β-HEP self-reaction rate coefficient. The temperature range and water vapor concentrations were chosen because of their significance to conditions in the troposphere. As the troposphere continues to get warmer and wetter, more complexes with water will form, which in turn may perturb the kinetics and product branching ratios of atmospheric reactions.

2.4 Methods

2.4.1 Apparatus

Figure 2.2 shows the principal components and layout of the experimental apparatus. The photolysis cell is 244 cm long including the end boxes (20 cm × 18 cm) used to house long-pass Harriot cell optics. The end boxes support the glass photolysis cell and are purged with nitrogen to protect optical surfaces from corrosive gases. The Pyrex cylindrical reaction tube (187 cm in length, 5.1 cm in diameter) between the end boxes constitutes the effective path length for photolysis and absorption experiments. The reaction tube is surrounded by a Pyrex jacket through which methanol, or a glycol/water mixture is circulated for temperature regulation.

All gases are precooled or heated before entering the reaction cell by a jacketed long-path manifold that is either cooled with methanol or heated with a glycol/water mixture. K-type thermocouples placed at both ends of the cell monitor the temperature of the system. Typically, less than 1°C difference occurs between the gases entering and exiting the cell. MgF_2 windows are used at both ends of the cell to transmit both UV and IR light over the range of interest. Kinematically mounted mirrors in the optical path of the system make it possible to switch between UV and IR detection methods without changing the position and alignment of the flow cell, light sources and detectors. A purge box placed over the IR

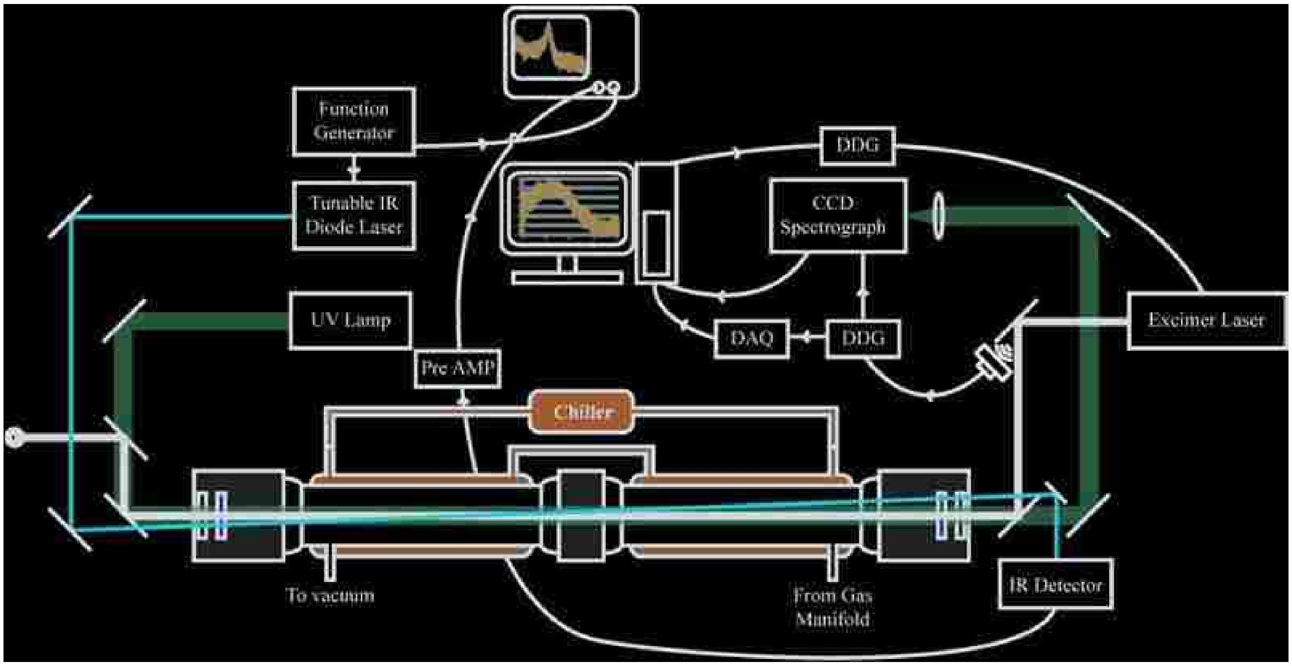

Figure 2.2: Schematic of UV/flash-photolysis system for kinetic measurements.

and UV optics in the path where the excimer-light and D_2-light intersect is purged with a steady flow of nitrogen to reduce production of ozone formed by photolysis of O_2 outside the cell by the excimer laser. Gas mixtures of N_2/O_2/2-chloroethanol/H_2O flow continuously through calibrated Teledyne-Hastings (HFC series) flow controllers at a total flow rate of 14,000 standard cm^3 min^{-1} (sccm). 2-Chloroethanol (99% pure) was purchased from Aldrich and used without further purification. Compressed N_2 and O_2 cylinders (99%) were obtained from Airgas. Pressure was maintained at 200 Torr total pressure and measured with an MKS-Baratron 690A pressure transducer.

2.4.2 Radical Concentration Measurements

Flash photolysis/UV absorption spectroscopy is used to create and monitor β-HEP and ozone, and wavelength-modulated, infrared diode-laser spectroscopy is used to quantify the water vapor concentration. Time-resolved detection of the β-HEP radical is done by directing the output from a 30-Watt D_2 lamp (Oriel model 60010) through the center of the reaction cell. The excimer laser photolysis beam is aligned coaxially with the UV probe beam by use of dielectric mirrors that reflect a 30-nm wide band centered on the 193 nm photolysis beam while passing all other UV wavelengths. UV light absorption is detected by a monochromator (Andor model SR-303i-B with an 1800 l/mm or 600 l/mm grating, depending on the light intensity, which decreases with decreasing wavelength in the D_2 lamp), and either an intensified and gated CCD camera (Andor model CCD30-11) or a photomultiplier tube (PMT Sens-Tech P30A-14).

The CCD setup was used in an exploratory experiment to determine contaminant species, but rate data for the β-HEP self reaction is exclusively from PMT experiments. Detection by the CCD camera was used initially to measure absorption over a wide range of wavelengths, from 220 to 350 nm, enabling identification of products of secondary chemistry. Absorption data at many wavelengths permits a least squares fit to determine multiple species present in the reaction cell. Time resolved data are collected with the CCD by varying the delay from 1 to 10 ms after the excimer laser is fired. The CCD integrates a 5 μs window each time the laser is fired and 500 shots of the laser are averaged to achieve a sufficient signal-to-noise ratio. These experiments are time-consuming because measurement of a decay of β-HEP requires a minimum of 30 delay times to achieve a reproducible fit. At 0.33 Hz, 12 h are needed to obtain a single fit to the self-reaction decay.

Because of the fast response, the PMT together with a monochromator and filters with selected wavelengths of 220, 230, and 254 nm (Figure 2.3 adapted from previously published data[73,76,77]) were used to collect kinetic data after the experiments with the CCD camera identified the major species present. Deconvolution of species concentrations from the total absorption data collected by the PMT requires a decay to be collected at each of the three wavelengths. The PMT collected data at 30 MHz over the first 10 ms after the excimer laser is fired. Sufficient signal to noise is obtained by averaging 300-400 shots of the excimer laser at a repetition rate of 0.33 Hz. Dark counts are recorded before each shot and I_0 is taken as the signal prior to the laser pulse. Collection of dark counts, blank (I_0) and response (I) was controlled through a LabVIEW routine written in-house.

After collecting a decay profile at each of the three wavelengths, we used recommended cross sections from the MPI-Mainz UV-VIS spectral atlas of gaseous molecules[78] to determine concentrations by a least-squares fit. The β-HEP self-reaction rate constants are obtained by fitting time-dependent concentrations to a system of differential equations defined by the reactions listed in Table 2.1. An example of typical concentrations and fit of the β-HEP decay to the model is shown in Figure 2.4, which contains ~800 data points.

2.4.3 Water Concentration Measurements

Water vapor was introduced into the reaction cell by passing N_2 carrier gas through a bubbler immersed in a constant temperature bath. The amount of water vapor in the reaction cell is controlled by both the temperature of the water and the percentage of total flow of the carrier gas passing through the bubbler. The water vapor concentration is varied between

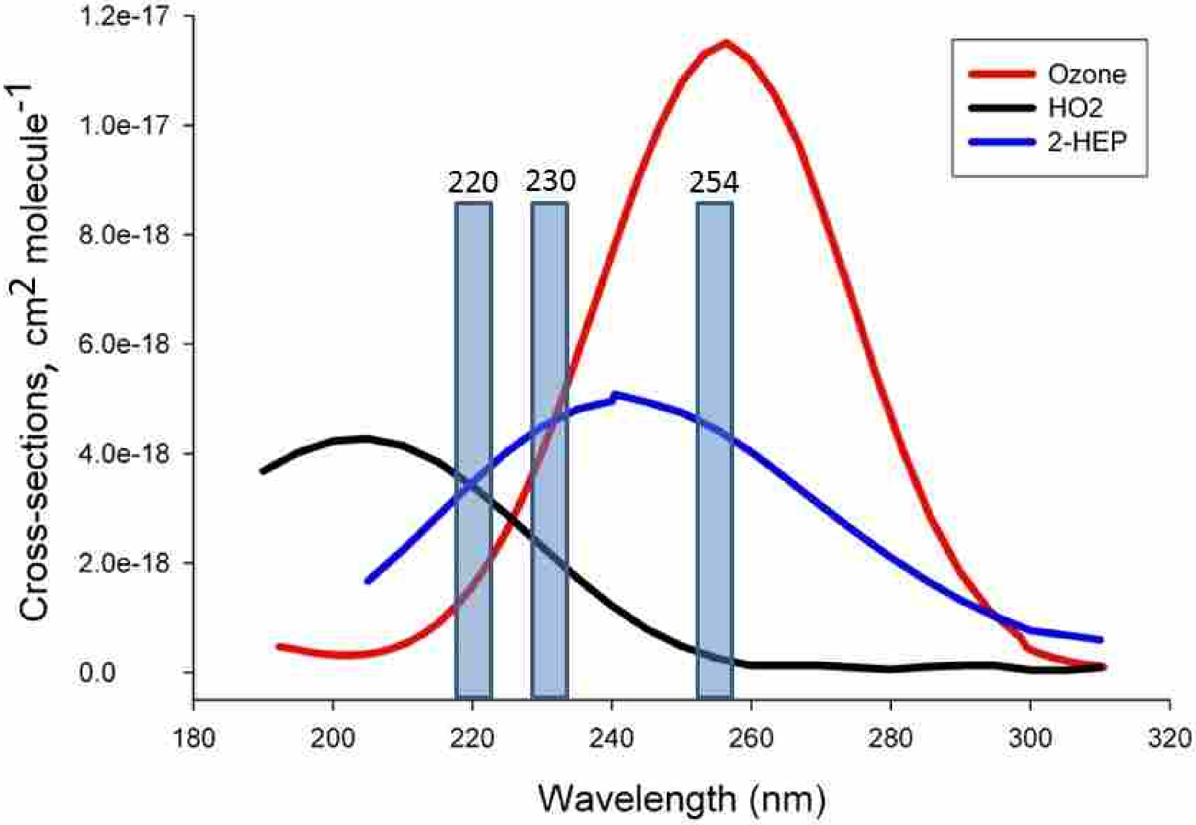

Figure 2.3: Plot of absorption cross sections of β-HEP, O_3, and HO_2 used to fit absorption data to obtain the concentration of each species. The bars superimposed over the plot are the bandpass filters used to select out the specific wavelengths used for data analysis.

Table 2.1: Reactions used to fit β-HEP decays to obtain the self-reaction rate constant.

#	Reaction	k (cm^3 molecule^{-1} s^{-1})	Ref #
(2.1)	$HOCH_2CH_2O_2 + HOCH_2CH_2O_2 \rightarrow$ $\rightarrow 2\ HOCH_2CH_2O + O_2$	1.1×10^{-12}	79
(2.2)	$HOCH_2CH_2O_2 + HOCH_2CH_2O_2 \rightarrow$ $\rightarrow HOCH_2CH_2OH + HOCH_2CHO + O_2$	1.1×10^{-12}	79
(2.3)	$HOCH_2CH_2O_2 + HO_2 \rightarrow HOCH_2CH_2OOH + O_2$	1.0×10^{-11}	80
(2.4)	$HOCH_2CH_2O + O_2 \rightarrow HOCH_2CHO + HO_2$	$5.0 \times 10^{-26}\ e^{(34.92/RT)}$	81
(2.5)	$HOCH_2CH_2O + M \rightarrow CH_2O + HOCH_2 + M$	5.5×10^{5}	79
(2.6)	$HO_2 + HO_2 \rightarrow H_2O_2 + O_2$	$2.2 \times 10^{-13}\ e^{(4.99kJ/RT)}$	47
(2.7)	$HOCH_2 + O_2 \rightarrow CH_2O + HO_2$	9.6×10^{-12}	82
(2.8)	$HO_2 + O_3 \rightarrow OH + 2\ O_2$	$1.1 \times 10^{-14}\ e^{(-4.16kJ/RT)}$	47
(2.9)	$HO_2 + Cl \rightarrow O_2 + HCl$	$1.8 \times 10^{-11}\ e^{(-1.41kJ/RT)}$	79
(2.10)	$Cl + O_3 \rightarrow ClO + O_2$	$2.8 \times 10^{-11}\ e^{(-2.80kJ/RT)}$	79

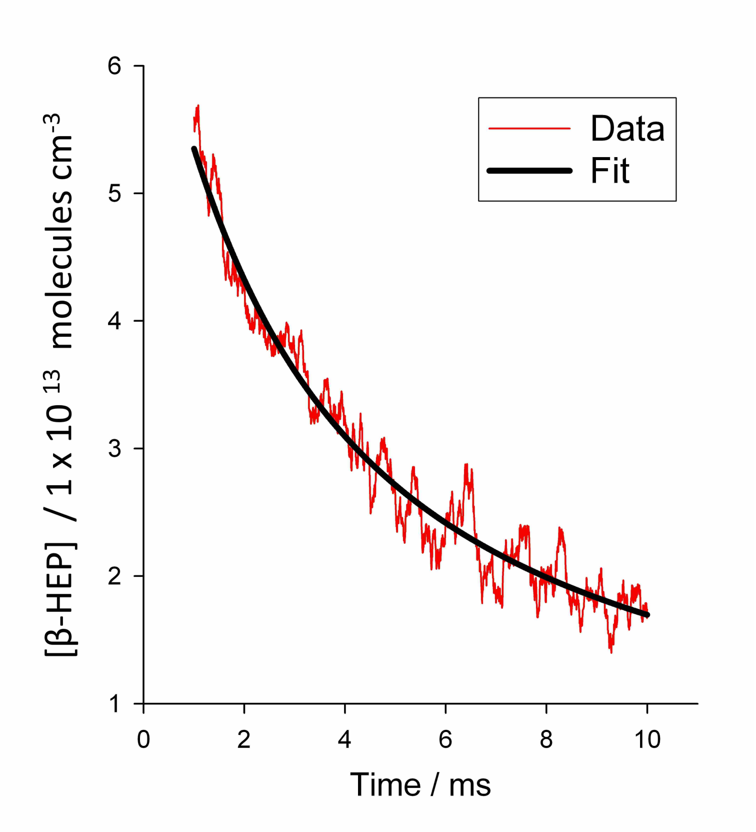

Figure 2.4: Representative fit of the reaction model described in Table 2.1.

1.0×10^{15} and 2.5×10^{17} molecules cm^{-3}. Water vapor concentration is maintained at a constant value (± 2–8 %) over the 8 h duration of an individual trial.

Wavelength modulated IR diode laser spectroscopy is used to quantify the water in the cell. Figure 2.2 shows the IR system components. IR light is scanned over a narrow frequency band (100 Hz) centered at the 6790.65 cm^{-1} line such that the entire peak of the selected rovibrational transition of water vapor is observed. The IR beam is produced by a New Focus TLB-6326 tunable diode laser with a line width of <300 kHz. With the use of Herriott cell optics, the IR beam is passed five times through the reaction cell, and finally directed towards an IR 1-GHz low-noise photoreceiver (New Focus 1611). The signal from the detector is synchronized with the 100 Hz modulation frequency and visualized and recorded by a digital oscilloscope (Textronix model TDS 3024B). Data are processed and converted from absorption measurements to concentrations with a LabVIEW routine. Absorption line strengths are obtained from the HITRAN(34) database and converted to cross sections.

2.4.4 β-$HOCH_2CH_2O_2$ Self-Reaction Kinetics Measurements

β-HEP was formed in the reaction cell by introducing a gas mixture containing typically 6.1×10^{18} molecules cm^{-3} of N_2, 4.7×10^{17} molecules cm^{-3} of O_2, and $\sim 2 \times 10^{16}$ molecules cm^{-3} of 2-chloroethanol ($HOCH_2CH_2Cl$). $HOCH_2CH_2Cl$ was introduced into the gas mixture via dual 100-mL bubblers in series with N_2 at 2000 standard cm^3 min^{-1} (sccm) as the carrier gas. The amount of 2-chloroethanol is an approximation while other gases were metered. Two bubblers in series provide time for carrier N_2 to be saturated with $HOCH_2CH_2Cl$. The temperature of the bubblers was maintained by immersion in a constant temperature bath maintained at 303 K through use of resistive heaters and a PID controller. Pressure in the reaction cell was adjusted to maintain total pressure at 200 Torr. Total flow rate was maintained at 14,000 sccm, resulting in a residence time of ~3 s in the reaction cell. A 15 ns pulse from the ArF excimer laser (LamdaPhysik, model EMG201MSC) at 193 nm and energy of 200 to 400 mJ pulse^{-1} photolyzes an area 2.5 cm wide by 1 cm high. The excimer was fired at 0.33 Hz, allowing for a fresh mixture of gas to be probed with every laser shot. The pulse photolyzed a small fraction ($< 1\%$) of the $HOCH_2CH_2Cl$ molecules to produce $HOCH_2CH_2$ and Cl radicals.[67,83] Subsequent reaction of the $HOCH_2CH_2$ radical with O_2 produced the β-HEP radical. The initial concentration of β-HEP radical is between 3×10^{13} and 6×10^{13} molecules cm^{-3} depending on the concentration of 2-chloroethanol and the strength of the excimer laser pulse.

The self-reaction of β-HEP follows two product branches, reactions 2.1 and 2.2[84]

$$2\,\mathrm{HOCH_2CH_2O_2} \rightarrow 2\,\mathrm{HOCH_2CH_2O} + \mathrm{O_2} \tag{2.1}$$

$$2\,\mathrm{HOCH_2CH_2O_2} \rightarrow \mathrm{HOCH_2CH_2OH} + \mathrm{HOCH_2CHO} + \mathrm{O_2} \tag{2.2}$$

The loss of β-HEP from both reactions was measured in these experiments. The observed rate constant, k_{obs}, is the overall rate constant representing the following four elementary reactions:

$$\mathrm{HOCH_2CH_2O_2} + \mathrm{HOCH_2CH_2O_2} \longrightarrow \mathrm{Products} \tag{2.11}$$

$$\mathrm{HOCH_2CH_2O_2} + \mathrm{H_2O} \rightleftharpoons \mathrm{HOCH_2CH_2O_2{-}H_2O} \tag{2.12}$$

$$\mathrm{HOCH_2CH_2O_2{-}H_2O} + \mathrm{HOCH_2CH_2O_2} \longrightarrow \mathrm{Products} \tag{2.13}$$

$$\mathrm{HOCH_2CH_2O_2{-}H_2O} + \mathrm{HOCH_2CH_2O_2{-}H_2O} \longrightarrow \mathrm{Products} \tag{2.14}$$

Figure 2.4 shows a representative fit to a measured decay using the reactions outlined in Table 2.1. Reactions 2.1 and 2.2 were used in the model to fit decays, but the decays are measurements of the combined loss of β-HEP and β-HEP-H_2O.

193 nm light is used to initiate production of β-HEP, but O_2 is also photolyzed to form singlet oxygen atoms that combined with O_2 to form ozone. The absorption cross sections of ozone overlap strongly with the cross sections of β-HEP and HO_2 (postulated to be formed due to undesirable secondary chemistry), causing an interference with direct absorption measurements. O_2 is essential for the production of β-HEP and is used to convert $HOCH_2CH_2$ to β-HEP, so O_2 could not be excluded from the reaction gas mixture. Small flow rates of O_2 into the reaction mixture lengthened the conversion time of $HOCH_2CH_2$ into β-HEP so the peak concentration occurred at 700–1000 μs after the laser pulse, but unwanted secondary chemistry of $HOCH_2CH_2$ increased. Higher concentrations of O_2 in the reaction cell led to increased production of O_3 that complicated the analysis due to the overlapping absorption spectrum of O_3 with β-HEP. Therefore, the O_2 concentration introduced into the cell was optimized to reduce ozone and diminish unknown chemistry between $O(^1D)$ radicals and other species while still producing β-HEP in less than 1 ms.

A second source of ozone came from outside of the cell from the overlapping regions between the photolysis pulse and the UV detection optics. The absorption due to O_3 was decreased 90% by purging the probe space external to the cell with dry N_2. The three collection wavelengths at 220, 230, and 254 nm provide sufficient data for a least-squares fit to obtain the concentrations of ozone, HO_2, and β-HEP. Photolysis of 2-chloroethanol supposedly forms significant amounts of HO_2[81,85–87], therefore absorption of HO_2 was also considered. However, no significant steady-state concentration of HO_2 was found in our experiments and the least squares fit reduced to a two-parameter least-squares fit (equation 2.15),

$$A_{tot} = Pathlength \quad \times \quad (\sigma_{\beta\text{-}HEP} \times [\beta\text{-}HEP] \quad + \quad \sigma_{O_3} \times [O_3]) \tag{2.15}$$

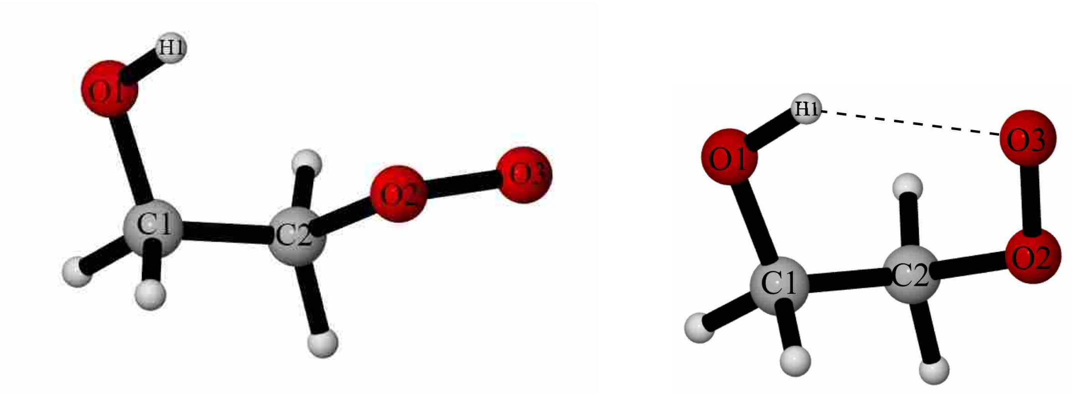

1 2

Figure 2.5: Optimized geometries of β-HEP.

The absence of HO_2 detection in the cell with similar conditions to those used by Murells et al.[67] merits further discussion.

2.4.5 Computational Methods

Conclusions from experimental results are supported with theoretical calculations performed with Gaussian 03[88]. From these results, the equilibrium constant for complexation of β-HEP with H_2O was computed. Both harmonic and anharmonic vibrational frequencies and rotational constants of both the β-HEP molecule and the β-HEP-H_2O complex were optimized with the B3LYP/aug-cc-pVDZ method and basis set. The energies were refined by performing single-point energy calculations with the MP2 and CCSD(T) methods. All local minima with energies within kT of the global minimum geometry at room temperature are populated at room temperature and therefore were used in the equilibrium constant calculation. One global minimum and one local minimum structure were identified for the β-HEP molecule. These structures are shown in Figure 2.5. The global and two local minima energy structures for β-HEP-H_2O complex were identified by Gaussian optimizations through Random Constrained Sampling (RCS) methodology[89] (see Figure 2.6). Seven hundred initial randomly generated geometries were generated by randomly orienting a previously optimized water molecule within a constrained sphere of radius 3.0 $\mathring{A}$ encompassing the optimized β-HEP structure. The energies of each structure were zero-point energy corrected and basis set superposition error corrected from energies calculated with the B3LYP/aug-cc-pVDZ method and basis set in Gaussian 03.

Partition function calculations

From the Gaussian 03 calculations, the partition function of each confirmation of each molecule was calculated according to the theory by McQuarrie et al.[90] The overall partition function for a molecule is the product of its translational, rotational, electronic, and vibrational partition

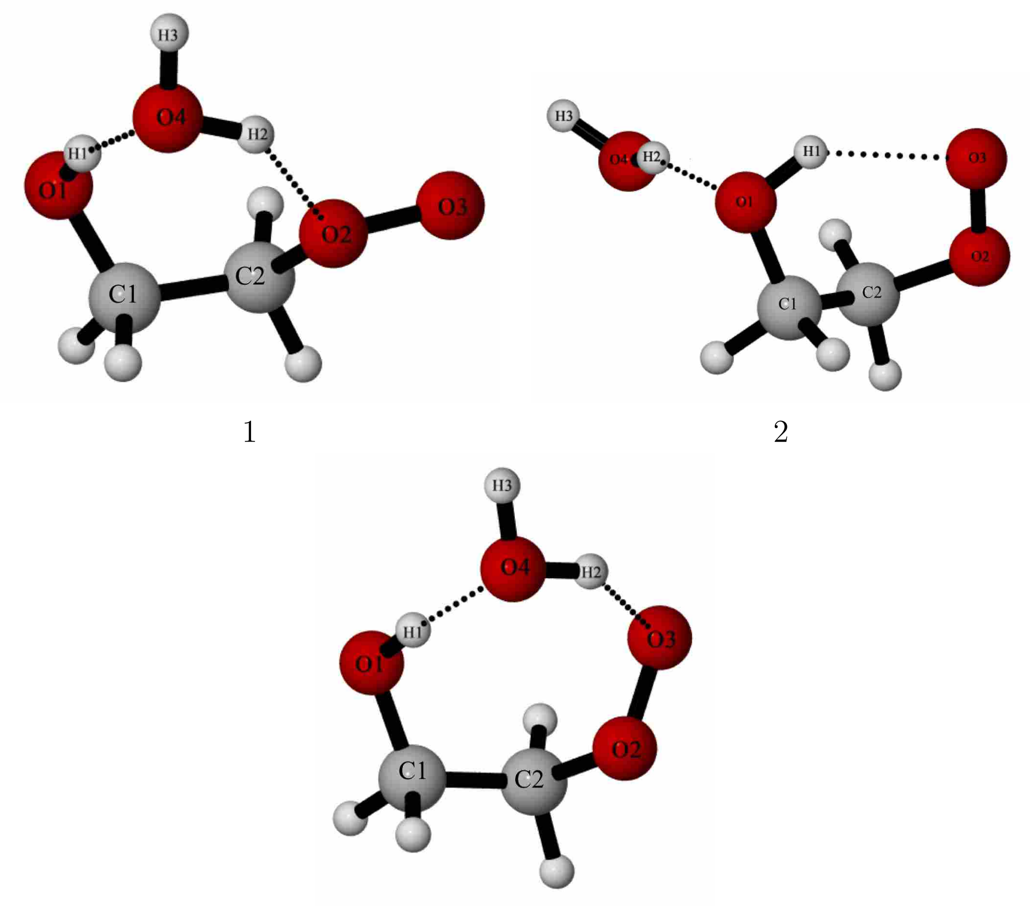

1

2

3

Figure 2.6: Optimized geometries of the β-HEP-H_2O complex.

functions. The expressions for the translational, rotational, and electronic partition functions are:

$$q^T = \frac{V\left(2\pi mkT\right)^{3/2}}{h^3} \tag{2.16}$$

where V is the volume of the reaction cell, m is the mass of the molecule, k is Boltzmann's constant, h is Planck's constant, and T is temperature;

$$q^R = \left(\frac{kT}{hc}\right)^{3/2}\left(\frac{\pi}{ABC}\right)^{1/2} \tag{2.17}$$

where c is the speed of light and A, B, and C are the rotational constants of the molecule;

$$q^E = ge^{-E/(RT)} \tag{2.18}$$

where g is the degeneracy of the electronic ground state and E is the zero-point energy of the ground vibrational state. Note that the energy in the partition function for all molecules and geometries must be in reference to the same reference energy.

Vibrational partition function

The vibrational partition function for a molecule is the product of the partition functions for each of its vibrational modes, assuming that the normal vibrational modes of the molecule are independent. The partition function of a vibrational mode can be calculated as the sum of the contributions from each vibrational state,

$$q^V = \sum_v e^{-\beta E_v} \tag{2.19}$$

where $\beta = 1/(kT)$. The energies of the vibrational states can be calculated according to several models for the vibrational motions. In this calculation, the harmonic oscillator, Morse oscillator, and hindered rotor models were used for each mode according to the model that best approximated the vibrational motion of the mode.

Harmonic oscillator

A harmonic approximation assumes that the energy levels of a vibrational mode are equally spaced. This approximation is accurate for the lowest vibrational modes and therefore can be made when only the ground and first excited states are occupied. For a harmonic oscillator, equation 2.19 becomes

$$q^V = \sum_v e^{-\beta v h c \tilde{\nu}} = \frac{1}{1 - e^{-\beta h c \tilde{\nu}}} \tag{2.20}$$

where $\tilde{\nu}$ is the fundamental frequency of the vibrational mode. In this calculation, the fundamental anharmonic frequency calculated in Gaussian was used for $\tilde{\nu}$.

Morse oscillator

A Morse oscillator can be used to model vibrational modes that are dissociative. A harmonic oscillator model assumes that all vibrational states are equally spaced and does not account for the possibility that a bond can dissociate with sufficient energy. Therefore, the partition function based on the harmonic oscillator tends to underestimate the true partition function of the mode. The Morse oscillator accounts for the decreasing spacing between the vibrationally excited states and eventually the dissociation of the bond.

The energy levels for the Morse oscillator potential are defined by,

$$G(v) = \nu_e \left(v + \frac{1}{2}\right) + x_e \left(v + \frac{1}{2}\right)^2 \tag{2.21}$$

where ν_e is the fundamental harmonic vibrational frequency, v is the vibrational quantum number, and x_e is the diagonal element of the X-matrix corresponding to the vibrational mode. If x_e is negative, the bond will eventually dissociate, whereas if x_e is positive there are infinitely many bound states. The bond will dissociate when $G(v)$ achieves a maximum, or at $v^* = -\frac{\nu_e}{2x_e} - \frac{1}{2}$. Therefore, at the highest energy bound state, $v_{max} = \lfloor v^* \rfloor$ and there are $N = v_{max} + 1$ bound states. For some states, if the vibration primarily involved the stretching of a hydrogen bond, $\tilde{x_e}$ was calculated from the dissociation energy for the breaking of the hydrogen bond, D,

$$\tilde{x_e} = -\frac{\nu_e^2}{4D} \tag{2.22}$$

N was then calculated as $-\frac{\nu_e}{2\tilde{x_e}}$ and rounded to the nearest integer. The partition function was then calculated,

$$q^V = \sum_{v=0}^{v_{max}} e^{-hc(G(v)-G(0)/(kT)} \tag{2.23}$$

from $\tilde{x_e}$ to calculate $G(v)$ and $G(0)$.

Hindered rotor

A hindered rotor model was used to model vibrations that involve the rotation of a functional group on the molecule. The calculation of the partition function for a hindered rotor vibration was based on McClurg et al.[91]

$$q^V = q_{HO} \left(\frac{r\pi}{\theta}\right)^{1/2} e^{-r/(2\theta)} I_0 \left(\frac{r}{2\theta}\right) \tag{2.24}$$

where q_{HO} is the partition function calculated as a harmonic oscillator using the fundamental harmonic frequency , and r and θ are defined as

$$r = \frac{\sqrt{2Iw}}{\hbar} \tag{2.25}$$

$$\theta = \frac{kT}{\hbar}\sqrt{\frac{2I}{w}} \tag{2.26}$$

where w is the barrier height for the hindered rotor (for this complex, the strength of one or two hydrogen bonds) and I is the moment of inertia for the rotation.

Local minima weighting

Three local minimum geometries for the complex and two local minimum geometries for β-HEP are all accessible at room temperature. Therefore the partition function for each of these geometries contributes to the overall equilibrium constant for complex formation. The partition function for a molecule is

$$q = \sum_i e^{-\beta E_i/(kT)} \tag{2.27}$$

where i denotes all of the states for the molecule. Therefore the partition functions for β-HEP-H_2O and β-HEP are equal to the sums of the partition functions for each of the local minimum geometries if they have a common reference energy. Therefore, the equilibrium constant for the complex formation is equal to

$$K_e = \frac{\frac{\mathrm{q}_{[\mathrm{HEP-H2O}]_1}+\mathrm{q}_{[\mathrm{HEP-H2O}]_2}+\mathrm{q}_{[\mathrm{HEP-H2O}]_2}}{V}}{\left(\frac{\mathrm{q}_{[\mathrm{HEP}]_1}+\mathrm{q}_{[\mathrm{HEP}]_2}}{V}\right) \times \left(\frac{\mathrm{q}_{[\mathrm{H2O}]}}{V}\right)} \tag{2.28}$$

2.5 Results

2.5.1 β-$HOCH_2CH_2O_2$ Self-Reaction Kinetics

Typically, 7 to 15 β-HEP decay curves were collected at each water vapor and temperature condition. Each curve was fit to a model composed of coupled differential equations describing the reactions given in Table 2.1. Measured time dependent concentrations of β-HEP and ozone are inputs to the model. The concentration of β-HEP at time 0 and the observed self-reaction rate of β-HEP are the outputs. Decay curves were measured at each condition until the 95% confidence interval of the average self-reaction rate was less than 10% of the

Table 2.2: β-HEP rate constants as a function of H_2O vapor concentration.

274 K						
$[H_2O]^a$	σ^b	$^c k_2$(Fit)	σ^b	$^d[\beta\text{-HEP}]_0$	σ^b	# of Trials
0.18	0.08	3.02	0.13	3.3	0.1	18
1.57	0.14	5.47	0.42	4.3	0.2	12
2.60	0.13	6.46	0.51	3.1	0.3	9
3.32	0.33	7.76	0.83	2.8	0.2	10

280K						
$[H_2O]^a$	σ^b	$^c k_2$(Fit)	σ^b	$^d[\beta\text{-HEP}]_0$	σ^b	# of Trials
0.29	0.13	3.17	0.32	3.1	0.2	13
2.10	0.08	4.50	0.45	3.8	0.3	9
4.70	0.25	5.34	0.26	2.9	0.4	7
5.86	0.16	6.35	0.69	3.9	0.3	11
6.76	0.23	7.32	0.66	3.4	0.4	16

288 K						
$[H_2O]^a$	σ^b	$^c k_2$(Fit)	σ^b	$^d[\beta\text{-HEP}]_0$	σ^b	# of Trials
0.20	0.05	2.46	0.13	3.8	0.1	15
3.80	0.1	3.45	0.34	4	0.1	10
8.21	0.29	4.22	0.14	4.5	0.2	10
12.20	0.07	5.54	0.57	4.1	0.2	14

296 K						
$[H_2O]^a$	σ^b	$^c k_2$(Fit)	σ^b	$^d[\beta\text{-HEP}]_0$	σ^b	# of Trials
0.18	0.05	2.26	0.39	3	0.1	31
6.26	0.2	2.64	0.26	5.4	0.4	10
11.80	0.03	2.8	0.24	5.2	0.2	10
22.50	0.07	3.58	0.18	5.9	0.3	10

[a] molecule cm^{-3} / 1 × 10^{16}
[b] 95% confidence interval
[c] cm^3 $molecule^{-1}$ s^{-1} / 1 × 10^{-12}
[d] extrapolated initial concentration in molecule cm^{-3} / 1 × 10^{13}

mean value of the set. Table 2.2 presents the results of all experiments with 95% confidence intervals for $[H_2O]$, $[\beta\text{-HEP}]_0$, and k_{obs} at 274 K, 280 K, 288 K, and 296 K.

The robustness of the model was tested by changing each rate constant to the extreme of the reported error in the published value. The rate constants were changed one at a time and fit to obtain a new value for k_{obs}. This k_{obs} was compared against the k_{obs} obtained from the fit of the experimental data to the original model. These results are listed in Table 2.3 and reported as the percent difference between the original model and the adjusted model. The total uncertainty in k_{obs} due to fitting of the measured decays is estimated to be 12%, including the uncertainty in each reaction coefficient in the model.

This exercise reveals the weak points in the model and also aids in identifying which reactions have the most weight in the model. The self-reaction of β-HEP has two product branches. Reaction 2.1 creates two alkoxy radicals, whereas Reaction 2.2 creates two stable organic molecules. Since the alkoxy radicals subsequently react with O_2 to form HO_2, Reaction 2.1 makes a more significant contribution to secondary chemistry than Reaction 2.2. Reaction 2.1 causes a 6% change in k_{obs} when adjusted to its maximum uncertainty, whereas Reaction 2.2 causes no significant change. On the basis of model predictions, unwanted secondary chemistry is dominated by reactions involving HO_2. The uncertainty in the rate of the HO_2 + Cl reaction is ~56% and leads to a large (~8%) change in the fit for k_{obs}. More precise measurement of the reaction rate coefficient for the HO_2 + Cl reaction would aid in reducing this uncertainty. The experimental error ranges from 4 to 10% depending on experimental temperature and water vapor concentration. The overall error is dominated by the uncertainty in the rate constants used in the model. This error could be minimized by improving the uncertainty in the rate constants used to model secondary chemistry. Adding the HO_2 concentration as a function of time into our model would reduce the error in our model due to the large uncertainty of HO_2. This would require at least 10 times greater path length than our current path length.

Table 2.3: Model resilience and dependency on previously measured rate constants.

Rxn	low bound	% change in k	high bound	% change in k	Ref
2.1	7.7×10^{-13}	6.1	1.4×10^{-12}	6.3	79[b]
2.2	7.7×10^{-13}	0.0	1.4×10^{-12}	0.0	79[b]
2.3	7.8×10^{-12}	1.3	1.2×10^{-11}	8.6	80
2.4	9.2×10^{-21}	4.0	4.8×10^{-19}	3.7	81
2.5	3.9×10^{5}	0.6	7.2×10^{5}	1.2	79[b]
2.6	8.9×10^{-13}	0.8	3.4×10^{-12}	4.1	47
2.7	7.1×10^{-12}	1.0	1.2×10^{-11}	1.1	82
2.8	3.9×10^{-16}	0.0	1.1×10^{-14}	0.0	47
2.9	4.4×10^{-12}	8.5	2.4×10^{-11}	7.5	79
2.10	8.7×10^{-12}	0.4	1.7×10^{-11}	0.2	79

[a] cm^3 molecule^{-1} s^{-1} [b] error given as 30% because no error was published

Figure 2.7 is a plot of the observed reaction rate as a function of increasing water vapor concentration. As observed previously with the HO_2 self-reaction, little enhancement is observed above 300 K. An expression that describes both the temperature and water vapor dependence of the β-HEP self-reaction must include the reaction of β-HEP with both β-HEP and β-HEP-H_2O. Reactions 2.11–2.14 and the equation derived therefrom describe the water vapor enhancement of the rate coefficient. The observed rate is the combined loss of β-HEP and β-HEP-H_2O (designated as Comp for complex) because the UV absorption cross sections of the two species are assumed not to differ significantly.[46,49,50]

$$\frac{d[\beta\text{-}HEP]}{dt} + \frac{d[Comp]}{dt} = -2k_{obs}([\beta\text{-}HEP] + [\mathrm{Comp}])^2 \tag{2.29}$$

Expanding the right side of Equation 2.29,

$$\begin{aligned} -2k_{obs}([\beta\text{-}HEP] + [Comp])^2 = \\ - 2k_{2.11}[\beta\text{-}HEP]^2 - 2k_{2.13}[\beta\text{-}HEP][Comp] - 2k_{2.14}[Comp]^2 \end{aligned} \tag{2.30}$$

$$K = \frac{[Comp]}{[\beta\text{-}HEP][H_2O]} \tag{2.31}$$

And substitution of [Comp] from Equation 2.31 into Equation 2.30 and canceling the –2 from each side yields equation 2.32.

$$\begin{aligned} k_{obs}([\beta\text{-}HEP] + K[\beta\text{-}HEP][\mathrm{H_2O}])^2 = \\ k_{2.11}[\beta\text{-}HEP]^2 + k_{2.13}K[\beta\text{-}HEP]^2[\mathrm{H_2O}] + k_{2.14}(K[\mathrm{H_2O}][\beta\text{-}HEP])^2 \end{aligned} \tag{2.32}$$

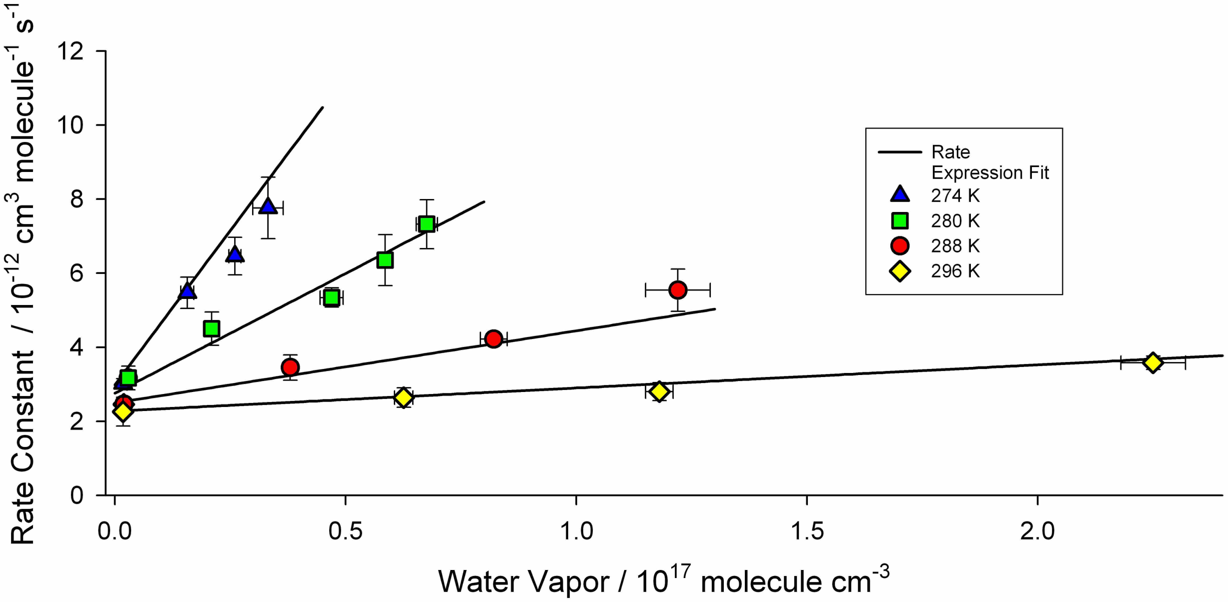

Figure 2.7: Water vapor enhancement of self-reaction of β-HEP rate vs. water vapor concentration. The lines represent the weighted fit to the rate expression (Equation 2.37). The expression describes the rate as a function of both water vapor concentration and temperature.

[β-HEP] is canceled from each side of the equation to isolate k_{obs}.

$$k_{obs}[\beta\text{-}HEP]^2(1+K[H_2O])^2 = [\beta\text{-}HEP]^2(k_{2.11}+k_{2.13}K[H_2O]+k_{2.14}K^2[H_2O]^2) \tag{2.33}$$

$$k_{obs} = \frac{k_{2.11}+k_{2.13}K[H_2O]+k_{2.14}K^2[H_2O]^2}{(1+K[H_2O])^2} \tag{2.34}$$

Equation 2.34 predicts a quadratic dependence on water vapor concentration, but the data in Figure 2.7 show a linear dependence over the temperatures and water concentrations studied. This linearity can only exist if K[H_2O] <<1, thus removing the quadratic terms from equation 2.34. This approximation reduces equation 2.34 to equation 2.35

$$k_{obs} = k_{2.11} + k_{2.13}K[H_2O] \tag{2.35}$$

The data are fit with Equation 2.36, which includes the contribution from the dry rate and the water vapor dependence on the reaction.

$$k_{obs} = k_{2.11}(1 + A[H_2O]exp^{(-\frac{E_a}{RT})}) \tag{2.36}$$

For modeling the HO_2 self-reaction, Kircher[49] included a pressure dependent term, but currently no data for the pressure dependence of the β-HEP self-reaction is found in the literature. Fits to the data with Equation 2.35 are superimposed onto Figure 2.7. The best fit to the data yields the following rate expression:

$$k_{obs}(T,[H_2O]) = 7.8\times10^{-14}e^{(8.3(\pm2.5)kJ/RT)}(1+1.4^{-34}e^{(92(\pm11)kJ/RT)}[H_2O]) \tag{2.37}$$

The contribution of enhancement from water vapor in Equation 2.37 is taken from the data in this work, but the dry rate constant, $k_{2.11}$, contribution has substantial error because only 4 data points (4 different temperatures) are used for the Arrhenius equation. Hence we have used the dry rate constant recommended from Atkinson's evaluation.[85]

The product of K and $k_{2.13}$ defines the slope in Equation 2.36. These two terms are inseparable in these experiments. Kanno et al.[52] in their investigation of the kinetics of the $HO_2 + HO_2{-}H_2O$ reaction measured K_{eq} and the rate constant independently. This work measures β-HEP and β-HEP-H_2O in the UV where their cross sections are indistinguishable. Therefore, the equilibrium constant for the formation of the β-HEP-H_2O complex was estimated using results from *ab initio* calculations, as described in the computation methods section. The equilibrium constant as a function of temperature is given in Figure 2.8 along with uncertainty limits established by changing the binding energies by ± 1 kcal mol^{-1}. The binding energies from *ab initio* calculations have accuracy of ± 1 kcal mol^{-1} although individual complexes have much larger uncertainty.[92] The slopes of the linear regressions from Figure 2.7 divided by K for complex formation yields $k_{2.13}$ as a function of temperature. Large uncertainty in the calculation of K results in large uncertainty in $k_{2.13}$ (Figure 2.8). $k_{2.13}$ is estimated to be 6×10^{-10} cm^3 molecule^{-1} s^{-1} with an uncertainty range of 1.2×10^{-10} – 3.5×10^{-9} cm^3 molecule^{-1} s^{-1} at 296 K. This rate constant approaches the collision rate limit (5×10^{-10} cm^3 molecule^{-1} s^{-1}) within experimental uncertainty. By comparison, the $HO_2 + HO_2{-}H_2O$ reaction rate constant is also near the collision rate limit[93] as calculated by *ab initio* calculations for K, but Kanno[52] experimentally determined the equilibrium constant to be an order of magnitude larger than *ab initio* calculations, which consequently resulted in an order of magnitude slower rate constant for the $HO_2{-}H_2O + HO_2$ reaction. Therefore, the rate constant for β-HEP + β-HEP-H_2O is 2 to 3 orders of magnitude larger than β-HEP + β-HEP, but may be revised downward when a more accurate determination of the equilibrium constant is determined experimentally.

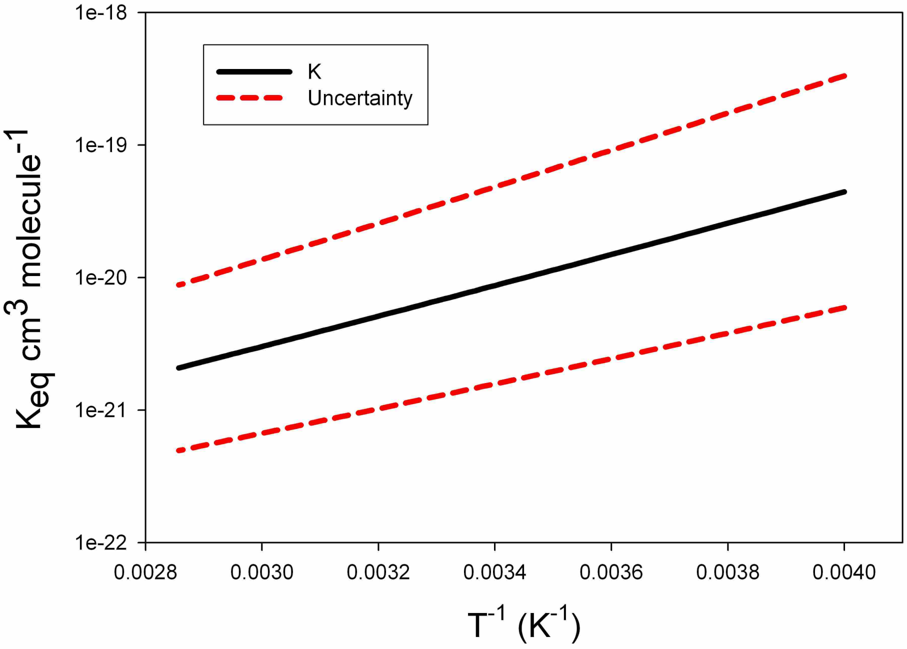

Figure 2.8: Equilibrium constant, K, for the formation of β-HEP-H_2O complex. Uncertainty is calculated at ± 1 kcal mol^{-1} of the binding energy.

2.6 Discussion

The loss of β-HEP with time is measured through UV-absorption spectroscopy at 220 nm, 230 nm, and 254 nm. Measurement at three wavelengths enables the deconvolution of the overlapping absorption features of β-HEP and ozone by a least squares regression. In their investigation of the β-HEP self-reaction kinetics, Murrells et al.[67] reported measuring significant concentrations of HO_2 using source chemistry similar to this study. However, the current study showed no evidence for significant HO_2 production. The lower limit of detection for HO_2 with a PMT and three filters in this study is 2×10^{12} molecules cm^{-3}. With CCD detection, absorption data collected between 220 nm to 350 nm and between 50–30,000 μs after the laser fired was applied to a least-squares regression using the absorption cross sections of HO_2, β-HEP, and O_3. In spectra collected before implementation of the N_2 purge boxes around the optics, ozone dominated the overall absorption. After inclusion of the purge boxes into the experimental set-up, ozone formation was suppressed by $\sim$ 90%. In every spectrum analyzed from CCD detection, HO_2 never exceeded 1×10^{10} molecules cm^{-3} in concentration. This observation is in direct contrast with the findings of Murrells et al.[67] who reported measured HO_2 at twice the concentration of $HOCH_2CH_2O_2$.

One possible explanation for the discrepancy between Murrells and this work is the absence of treatment of ozone by Murrells et al. in their data analysis. No concentrations of precursor gas species were reported, but the published decays of β-HEP have no discernible time delay between the formation of $HOCH_2CH_2$ and β-HEP, suggesting a high concentration of O_2 was used to drive β-HEP formation. The high concentration of O_2 used will produce significant amounts of ozone from photolysis at 193 nm. This ozone was not accounted for by Murrells et al. In addition, their wavelength selection of 225 nm and 260 nm complicates the data analysis. The absorption cross-sections of HO_2, β-HEP, and O_3 are listed in Table 2.4. At 225 nm each are within 20% of one another, but at 260 nm, O_3 is two orders of magnitude larger than HO_2, and β-HEP is halfway between the two. The use of 225 nm and 260 nm as probe wavelengths only provides enough information to deconvolve HO_2 and β-HEP from one

Table 2.4: Absorption cross sections of HO_2, β-HEP, and O_3.

Wavelength	HO_2	β-HEP	O_3
225 nm	3.16×10^{-18}	4.04×10^{-18}	3.17×10^{-18}
260 nm	3.60×10^{-19}	4.03×10^{-18}	1.06×10^{-17}

Cross section units: cm^2 $molecule^{-1}$

another. This presents an issue in data analysis owing to the contribution of O_3 absorption that would overwhelm the signal attributed to HO_2. The absence of the treatment of ozone in their data analysis may explain another discrepancy between the measurements of Murrells et al. and this work. They reported initial concentrations of HO_2 that were twice that of β-HEP and explained that this must be due to an unknown source of HO_2 production. It is likely that the signal attributed to HO_2 is O_3. Our model predicts HO_2 formation to peak at 100 μs and decay significantly by 1000 μs where we begin collecting self-reaction decays (see Figure 2.9). At 1000 μs the HO_2 concentration is predicted to be 7% of the β-HEP concentration (8×10^{11} molecules cm^{-3}) and below our detection limit. Future work will need to implement a more sensitive detection technique to determine the concentration of HO_2. In our experiments, HO_2 is not produced with significant concentrations to contribute to absorption spectra because of a lack of primary chemistry leading to HO_2 production. However, HO_2 is produced from secondary chemistry from the reactions of β-HEP and its precursors. Even though the concentration of HO_2 is below the detection limit of absorption experiments, it still contributes to the decay of β-HEP and is included in our model fits.

Anastasi et al.[72] reported a β-HEP self-reaction rate constant of $7.69\ (\pm 1.2) \times 10^{-12}$ cm^3 molecule^{-1} s^{-1}, much larger than the 2.24×10^{-12} cm^3 molecule^{-1} s^{-1} others reported.[67–71,73] We found that a major difference between Anastasi et al. and other investigations was that a large concentration of water vapor was used in Anastasi's study($\sim 1 \times 10^{18}$ molecules cm^{-3}). The rate expression reported in this work for the β-HEP self-reaction predicts a rate constant of $6.1(\pm 1.2) \times 10^{-12}$ cm^3 molecule^{-1} s^{-1} at 298 K with 1×10^{18} molecules cm^{-3} water vapor. This rate constant falls within experimental uncertainty of the water vapor enhancement expression from our experiments (Equation 2.37). Improper analysis of peroxy radical reactions will continue without a general understanding of water catalysis. As atmospheric water vapor continues to increase under the effects of climate change, modelers need rate constants that accurately predict the perturbation of peroxy radical reactions in the presence of water. Self-reaction rates of HO_2 and β-HEP are water

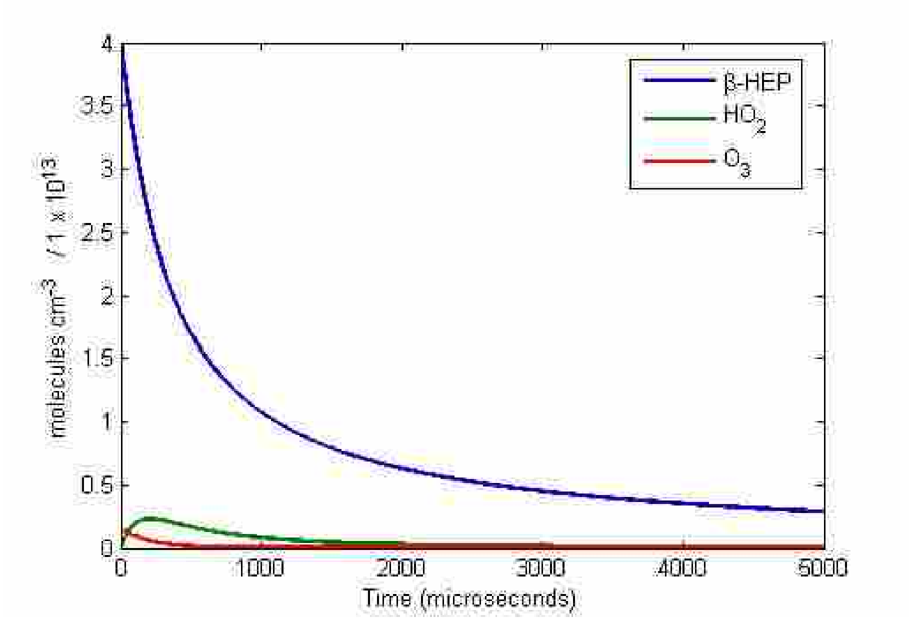

Figure 2.9: Self-reaction of β-HEP model demonstrating the predicted concentrations of HO_2 and O_3 assuming 4×10^{13} molecules cm^{-3} initial β-HEP and 1.5×10^{12} molecules cm^{-3} initial oxygen radicals.

vapor dependent and further investigation is needed to determine if other prominent peroxy radicals in the troposphere manifest the same trend.

The theory presented in this work describes the relationship between increasing rates of reaction of peroxy radicals and increasing water vapor. We postulate that radicals that form strong complexes with water result in a significant percentage of that radical existing as a complex. The complexed molecule acts as an energy bath to remove excess energy from the association reaction of the two radicals. *Ab initio* calculations estimated the equilibrium constant to determine both the percentage of β-HEP complexed with water and the rate constant for β-HEP + Comp (Reaction 2.13). The percent of complex formed has large uncertainty due to the uncertainty in the measurements of water and inital β-HEP as well as the uncertainty in the estimation of K, which is difficult to calculate. The most significant value from the *ab initio* calculation of K is the binding energy, which is only determined within ±1 kcal. Therefore our uncertainty in K, and subsequently, the uncertainty in $k_{2.13}$ is mostly dependent on the uncertainty in the binding energy. To overcome the uncertainty, experimental measurements of K are required. The theory is supported by past evidence with the self-reaction enhancement of HO_2 and the reaction of HO_2 + NO. General enhancement of peroxy radical self-reactions by water will be correlated to the percent of radical complexed with water and also on the nature of the peroxy radical. For example HO_2 and β-HEP have equilibrium constants of formation with water within an order of magnitude, but at 50% relative humidity and 280 K, β-HEP has an enhancement factor of 4.1 while HO_2 has an enhancement factor of 1.5. The correlation between the enhancement of the rate constant and increasing water vapor does not sufficiently explain the data in Figure 2.7. It is also observed that β-HEP + Comp has a stronger temperature dependence than β-HEP + β-HEP giving rise to larger enhancement at lower temperatures even with lower water vapor concentration.

Further investigation is needed to fully establish the theory and accurately predict enhancements of other peroxy radical reactions. Future studies should focus on β-hydroxy peroxy radicals and similiar compounds that form two hydrogen bonds with water that have significant overlap in the O–H–O interaction to produce binding energies greater than 4 kcal mol^{-1}. β-Hydroxy peroxy radicals are atmospherically important because they are products in the reaction of ozone with unsaturated VOCs which have diverse emission sources. Isoprenes and terpenes are two major examples of biogenic sources that likely will produce β-hydroxy peroxy radicals and should demonstrate a water vapor enhancement. Additional studies are required to investigate the absence of water vapor enhancement in the cross reaction of HO_2 and CH_3O_2.[64] HO_2 forms a strong complex with water, leading to self-reaction rate enhancement but without enhancement in reaction with CH_3O_2. We postulate that enhancement is absent due to poor vibrational coupling between HO_2-H_2O and CH_3O_2. β-HEP may have stronger vibrational coupling with HO_2 and consequently demonstrate water vapor enhancement.

2.7 Atmospheric Importance

The loss of β-HEP in the troposphere is dependent on temperature and water vapor concentration. The fractional contribution of water vapor to the loss of β-HEP can be determined by a ratio of rate constants. ($k_{2.13} \times K_{eq} \times [H_2O] / k_{2.11}$). This equation allows a direct comparison of the contribution of water vapor to the loss of β-HEP at differing temperatures but at constant relative humidity. Additionally a comparison is made by the same calculation for HO_2 self-reaction to test the theory from this present work. These data are compared in Table 2.5. These data show the contribution of water vapor to the losses of HO_2 and β-HEP in the atmosphere are equal within experimental uncertainty.

The absence of a self-reaction enhancement by water in current atmospheric models should lead to prediction of more β-HEP in the troposphere than is measured; as is the case with the self-reaction of HO_2[56], overprediction of β-HEP causes models to overestimate ozone formation rates. The β-HEP self-reaction has two product branches with a branching ratio of unity. Observing that the wet rate is 5–15 times faster than the dry rate and the temperature dependence of the wet rate is also significantly greater, we predict that water will perturb the

Table 2.5: Fractional apportionment of the self-reactions of HO_2 and β-HEP attributed to water vapor enhancement at 50% relative humidity.

Temp (K)	$^{a}HO_2$	$^{a}\beta$-HEP
296	1.0 ± 0.7	1.9 ± 0.7
288	0.7 ± 0.5	1.4 ± 0.6
280	0.5 ± 0.4	1.2 ± 0.4
274	0.3 ± 0.3	0.5 ± 0.2

a = $k_{Comp} \times K_{Eq} \times [H_2O] \ / \ k_{dry})$

branching ratio. Unfortunately, the present study did not measure these pathways. Without an understanding of the potential energy surface of β-HEP-H_2O + β-HEP, we cannot fully predict the effect water complexation has on β-HEP in the troposphere. Experimental data on perturbation of the product branching ratio would provide information about the effect on ozone production.

2.8 Conclusions

The increasing rate for β-HEP radical with water vapor concentration combined with the work from Butkovskaya[57], should merit investigations into the effect of water on many other reactions and molecules. Investigation should focus on reactions important in atmospheric chemistry and include radicals that form strong complexes with water, e.g., peroxy radical derivatives of terpenes and isoprene.[58] As evidenced from the work of Stockwell[56], small changes in the reaction rates of HO_2 lead to dramatic differences in predicted and measured HO_2 concentrations. To correctly predict pollution levels, atmospheric models need to be adjusted to include the rate enhancements demonstrated in this work. The implication of this work promotes the path of further discovery of peroxy radical self-reaction and cross reaction enhancements through the formation of pre-reactive complexes between the radicals and polar molecules such as water, methanol, and ammonia. Furthermore, water vapor catalysis will become increasingly more significant in light of global warming that induces increased water vapor concentrations.

Chapter 3

LIF Detection of Nitrogen Dioxide

3.1 Summary

Future work in the Hansen group will investigate the effects of water vapor on the kinetics and product branching ratio of the reaction of organic peroxy radicals with nitric oxide. This was originally my proposed work but the β-hydroxyethyl peroxy radical (β-HEP) self-reaction kinetics and the perturbation of the rate constant in the presence of water is to isolate the effects of water on the β-HEP + NO reaction.

3.2 Introduction

3.2.1 Peroxy Radicals in the Troposphere

Organic peroxy radicals (RO_2) in the atmosphere are intermediates in the combustion of hydrocarbons and serve as precursors for tropospheric ozone formation.[2,12,73,94,95] RO_2 radicals are produced through hydrogen extraction by other radicals, followed by the addition of O_2 to the radical site on the hydrocarbon. The reaction mechanism is summarized by reactions 3.1 and 3.2:

$$\mathrm{RH} + (\mathrm{OH},\ \mathrm{Cl},\ \mathrm{NO_3}) \rightarrow + (\mathrm{H_2O},\ \mathrm{HCl},\ \mathrm{HNO_3}) \tag{3.1}$$

$$\mathrm{R} + \mathrm{O_2} \rightarrow \mathrm{RO_2} \tag{3.2}$$

The reaction of RO_2 with NO produces two different products, as shown in reactions 3.3 and 3.4.

$$RO_2 + NO \rightarrow RO + NO_2 \tag{3.3}$$

$$RO_2 + NO \rightarrow RONO_2 \tag{3.4}$$

The product branching ratio is defined as the ratio of reaction 3.3 to 3.4 ($k_{3.3}/k_{3.4}$). The products of these reactions (NO_2, RO, and $RONO_2$) are intermediates to tropospheric pollution. The photolysis of NO_2 is the primary source of tropospheric ozone. Alkoxy radicals (RO) react with oxygen to produce aldehydes and HO_2. HO_2 is the simplest and most abundant peroxy radical and contributes to pollution by the same mechanism as other peroxy radicals (reactions 3.3 and 3.4). Organic nitrates ($RONO_2$) are the most stable products from reactions 3.3 and 3.4. This stability provides a mechanism for transport of pollution-producing precursors to otherwise pristine environments. Organic nitrates are carried by the wind to adjacent regions. The stability of organic nitrates allows for sufficient time for transport before they breakdown into NO_2 and RO radicals, which consequently leads to ozone production.

3.3 Scientific Background

Previous experimental work shows that the presence of water vapor perturbs reactions 3.5 and 3.6.

$$HO_2 + NO \rightarrow OH + NO_2 \tag{3.5}$$

$$HO_2 + NO \rightarrow HONO_2 \tag{3.6}$$

The product branching ratio ($k_{3.5}/k_{3.6}$) is perturbed in favor of increased nitrate production (HNO_3). Butkovskaya et al.[57] showed that at 50% relative humidity production of HNO_3 increased by ~800%. They hypothesized that water forms a mono-hydrated complex with peroxy radicals. An $HO_2{-}H_2O$ complex has been observed experimentally by Suma et al.[55] An analysis of published data by Butkovskaya et al. supports the hypothesis that water complexation of RO_2 leads to increased nitrate production.[57] Figure 3.1 shows the reported product branching ratio by Butkovskaya et al. as a function of the percentage of HO_2 that is complexed with water vapor. The complexation percentage is calculated using the equilibrium constant reported by Kanno et al.[67] Figure 3.1 shows a clear relationship between increased nitrate production and complexation with water.

Previous work[51] demonstrates that organic peroxy radicals form water complexes and it is proposed that their reactions with NO can lead to increased production of organic nitrates in the troposphere. In a recent high level *ab initio* study, Clark et al.[51] demonstrated theoretically the existence of other peroxy radical-water complexes. Perturbation to the product branching ratio favoring formation of $RONO_2$ is speculated to occur because of the formation of a radical-molecule complex. The production of NO_2 is caused by NO removing oxygen from the peroxy radical at the nitrogen site. The NO bond is formed when the NO_2 rotates to attach to RO. It is proposed that a water complex provides a chaperone whereby the NO_2 is maintained close to the RO through hydrogen bonding. The longer the NO_2 has to interact with the RO at close proximity, the more likely the formation of $RONO_2$. The work presented in Chapter 2 with the β-HEP self-reaction supported the theory that complexation of peroxy radicals with water increases the rate of reaction. Although this discovery is of importance to the atmospheric science community, the perturbation of the branching ratio of β-HEP + NO towards more organic nitrate formation has more direct effects on the atmosphere due to the ability to pollute pristine environments through long-range transport.

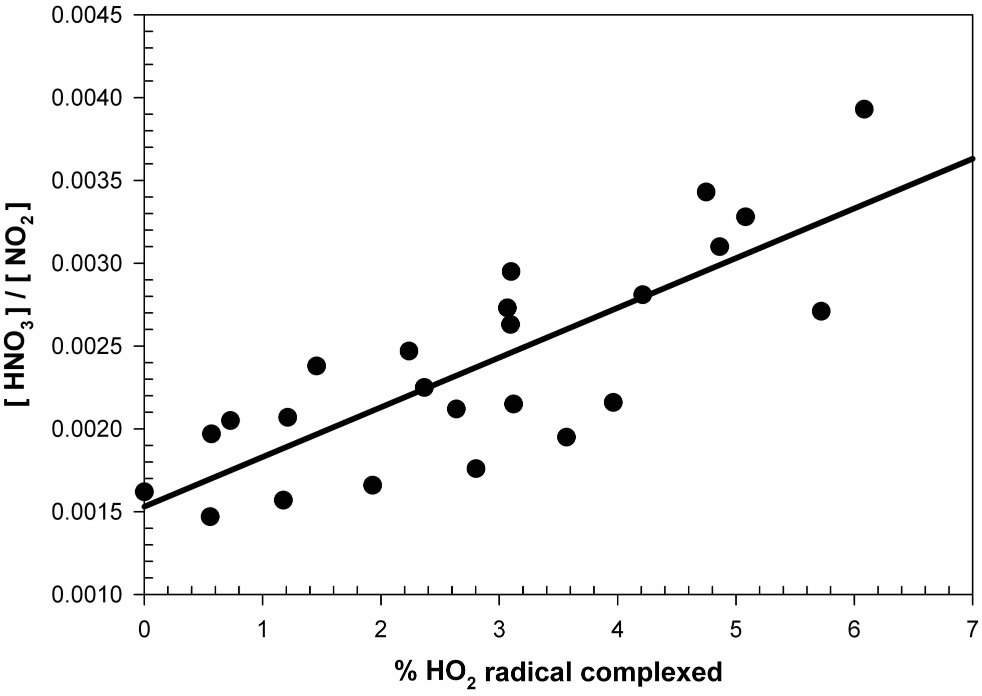

Figure 3.1: Product branching ratio ($[HNO_3]/[NO_2]$) plotted vs. the percentage of HO_2 complexed with water. (Calculated from Butkovskaya et. al.)

3.4 Kinetic Model

A kinetic model of the reaction mechanism was built to aid in the analysis of the kinetic data. Secondary chemistry must be explored to assure that significant sources or sinks of analyte molecules are accounted for in rate calculations.

$$\mathrm{HOCH_2CH_2 + O_2 \rightarrow HOCH_2CH_2O_2} \tag{3.7}$$

$$\mathrm{HOCH_2CH_2O_2 + HOCH_2CH_2O_2 \rightarrow 2HOCH_2CH_2O + O_2} \tag{3.8}$$

$$\mathrm{HOCH_2CH_2O_2 + HOCH_2CH_2O_2 \rightarrow HOCH_2CH_2OH + HOCH_2CHO + O_2} \tag{3.9}$$

$$\mathrm{HOCH_2CH_2O + M} \rightarrow HCHO + \mathrm{CH_2OH + M} \tag{3.10}$$

$$\mathrm{CH_2OH + O_2 \rightarrow HCHO + HO_2} \tag{3.11}$$

$$\mathrm{HOCH_2CH_2O + O_2 \rightarrow HOCH_2CHO + HO_2} \tag{3.12}$$

$$\mathrm{HOCH_2CH_2O_2HO_2 \rightarrow Products} \tag{3.13}$$

$$\mathrm{HO_2 + HO_2 \rightarrow H_2O_2 + O_2} \tag{3.14}$$

$$\mathrm{HOCH_2CH_2O_2 + NO \rightarrow HOCH_2CH_2O + NO_2} \tag{3.15}$$

$$HOCH_2CH_2O_2 + NO \rightarrow HOCH_2CH_2ONO_2 \tag{3.16}$$

The ideal reaction produces a peroxy radical that reacts completely with NO to form two possible products (reactions 3.15 and 3.16). The reactions outlined above constitute the reactions used in the model. Reactions 3.8 and 3.9 produce alkoxy radicals that are subsequent sources of HO_2 via reactions 3.10, 3.11, and 3.12. Reactions 3.13 and 3.14 are sinks for HO_2, but reaction 3.13 is less probable than reaction 3.14 because of the minimal concentrations of HO_2 and $HOCH_2CH_2O_2$ existing at the same time. This model allows data to be fit and analyzed for determination of the rate constant, and also aids in predicting probable effects from water vapor. Other considerations can be placed into the model, most importantly the reaction of Cl radicals with all of the above chemicals. These reactions are a small sample to demonstrate the complexity inside the cell. To minimize effects from undesired chemistry, the concentration of $HOCH_2CH_2Cl$ is introduced into the cell orders of magnitude smaller than $[O_2]$ and [NO]. This will produce pseudo first-order conditions whereby the relative concentrations of O_2 and NO will remain unchanged. Kinetic data is fit to the above kinetic model using SCIENTIST 3.0, a kinetic modeling program.

3.5 Methods

The kinetics of the β-HEP self-reactions was previously investigated with laser flash photolysis/UV time-resolved spectroscopy/diode laser spectroscopy. The experimental setup is described in Chapter 2 of this dissertation. A versatile instrument is required to measure the kinetics over a range of atmospherically relevant conditions including pressure (50–760 Torr) and temperature (250 K–300 K). The detection methods must include sufficient selectivity, sensitivity, and response time to obtain the necessary kinetic information. It is necessary to measure the time-resolved concentration of the reactants and products simultaneously. Preliminary work has been completed using such an instrument. The instrument combines laser flash photolysis with detection by UV time-resolved spectroscopy and near IR (NIR), two-tone frequency-modulated diode laser spectroscopy (TTFMS). This instrument has been modified to include two additional detection cells; one for measuring laser-induced fluorescence (LIF) of NO_2 and another for cavity ringdown spectroscopy to measure organic nitrates ($RONO_2$). This instrument and method facilitate the initiation of radical formation and allow for the probe of the kinetics from microseconds to tens of milliseconds.

Figure 3.2 illustrates the setup of the system. The instrument is composed of a long-path (∼200 cm) reaction cell. The temperature is controlled by a chiller that circulates methanol through a jacket on the outside of the cell. A pulsed excimer laser is fired at 0.33 Hz at either 248 nm or 193 nm to produce the radical of interest. The energy of the excimer laser is typically 200–400 mJ pulse^{-1}. The excimer can photolyze either 2-iodoethanol (248 nm) or 2 chloroethanol (193 nm) to produce approximately 1–5 $\times$ 10^{14} molecules cm^{-3} of $HOCH_2CH_2$ radicals. In the presence of excess oxygen, $HOCH_2CH_2$ is rapidly converted into β-hydroxyethyl peroxy radical ($HOCH_2CH_2O_2$) on a near instantaneous timescale relative to the rate of decay from self-reaction.

UV time-resolved absorption spectroscopy is used to detect $HOCH_2CH_2O_2$ analogous to the description in Chapter 2. To measure the absorption of $HOCH_2CH_2O_2$, a 40-W deuterium lamp is directed to propagate coaxially with the excimer laser through the photolysis cell. UV light is detected by use of a spectrograph (Andor SR-303i-B) and with either an intensified CCD camera (Andor DH720i-18H-03) or by a photomultiplier tube (Electron Tubes). This design allows for the collection of absorption spectra between 210–350 nm, minus a ±10 nm region centered around the dichroic maximum reflectance wavelength, with delay times that range between 1 μs–100 ms. Delay times are triggered from a photodiode that collects scatter from the excimer beam as it is directed through the cell. Typically 300 shots are averaged at each delay time collected by the CCD to produce a spectrum with sufficient signal-to-noise. Light collected with the PMT is collected time dependently and averaged 500 times with a digital oscilloscope.

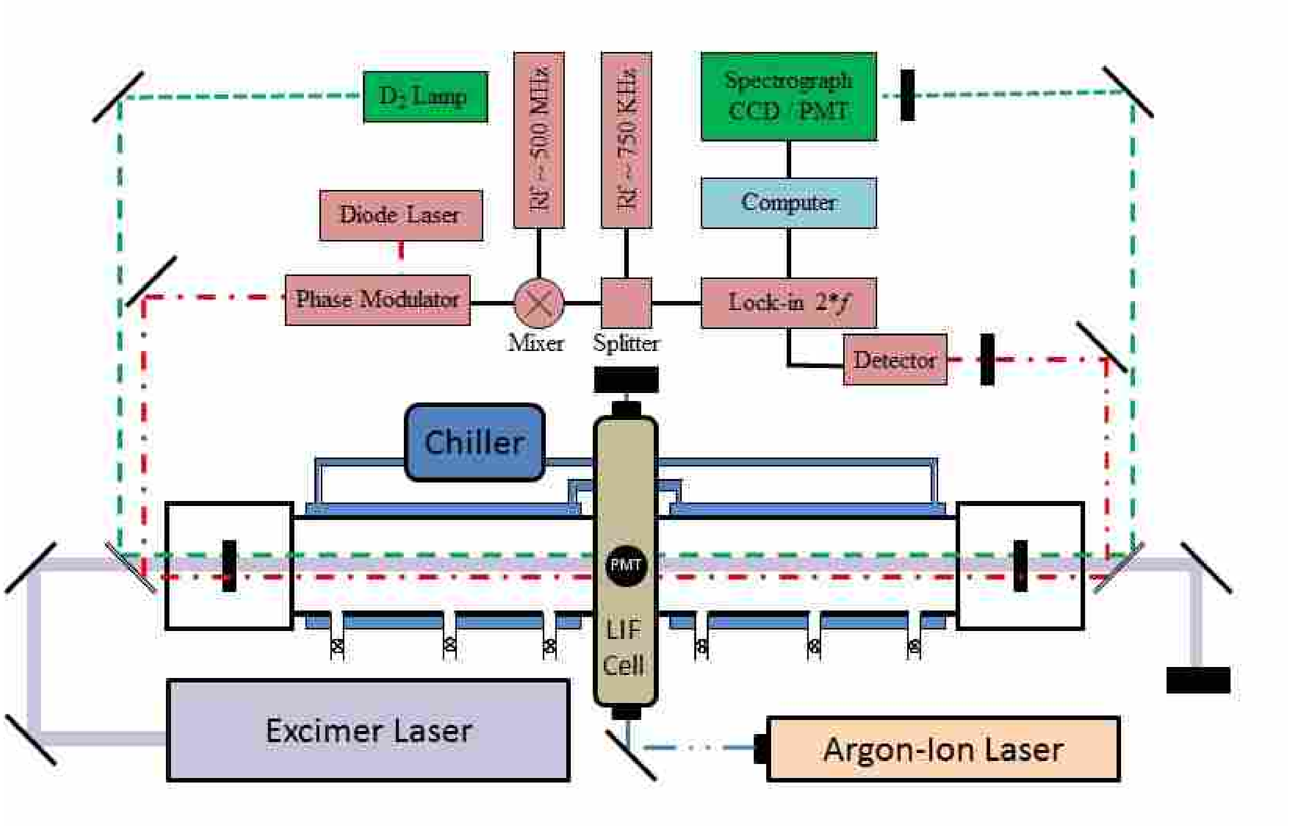

Figure 3.2: Schematic of flash-photolysis system. Purple lines show path of excimer laser pulse to initiate radical chemistry. Green path and boxes show the equipment needed for UV-absorption spectroscopy. Red path and boxes show equipment needed for TTFMS.

It is imperative that the water vapor concentration in the cell be precisely known. Two-tone frequency modulated spectroscopy (TTFMS) can measure either water vapor or HO_2 radical concentrations at sub-ppt. Significant effects of water vapor on the kinetics of $HOCH_2CH_2O_2$ + NO are not expected to occur until ~3 Torr of water is introduced into the cell. This assumption is based on the water vapor effects observed on the self-reaction of HO_2 and β-HEP.[64] Water vapor is introduced into the cell by bubbling N_2 through water that is maintained at a constant temperature. Absorption spectroscopy is dependent on path length; the longer the path length, the greater the absorption. The path length in this experiment is extended by reflecting the laser beam back and forth through the reaction mixture in a Harriett cell configuration. Figure 3.3 is the recent design of new optics for a Harriett cell that facilitates 35–120 passes of the probe laser before exiting the cell. These optics have a 1-inch hole cut from the center enabling the excimer beam to pass cleanly through the optics without being clipped or scattered. This design increases the overlap between the photolysis laser and the IR probe beam compared to previous designs in which two optics were placed above and below the plane of the excimer pulse. The intersection of the diode laser with the excitation pass occurs because each pass of the laser crosses through a focal point in the center of the cell and reflects off the other mirror back through the excitation path in the manner described in Figure 3.4.

The frequency of a near infrared (NIR) laser is modulated by mixing two frequencies (500 MHz and 750 kHz) in a MgO:LiNbO3 crystal housed in an external resonant cavity. Water absorbs at ~6600 cm^1 and is attributed to the first O-H overtone in H_2O. The wavelength of the NIR-laser is set at the frequency of the absorption feature. The mixing of two frequencies causes the laser to dither back and forth across the absorption feature. The unbalancing of the modulated frequency generates a beat frequency on the detector. The amplitude of the beat frequency is proportional to the absorption. 2f-Heterodyne detection is employed using a lock-in amplifier (Stanford Research System SR844) at 2 times the intermodulation frequency ($750\ \text{kHz} \times 2 = 1.5\ \text{MHz}$). The signal is digitized and stored using an in-house LabVIEW

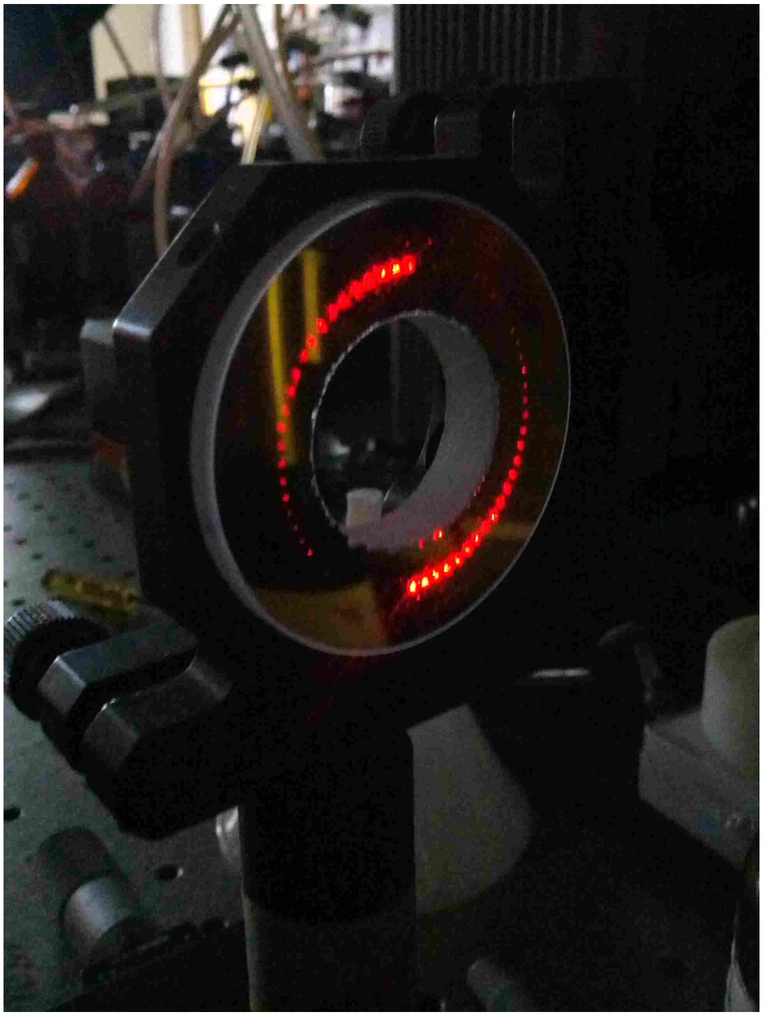

Figure 3.3: Custom Harriot cell optics facilitating excimer light pass through and 35–100 laser passes intersecting the excimer photolysis region.

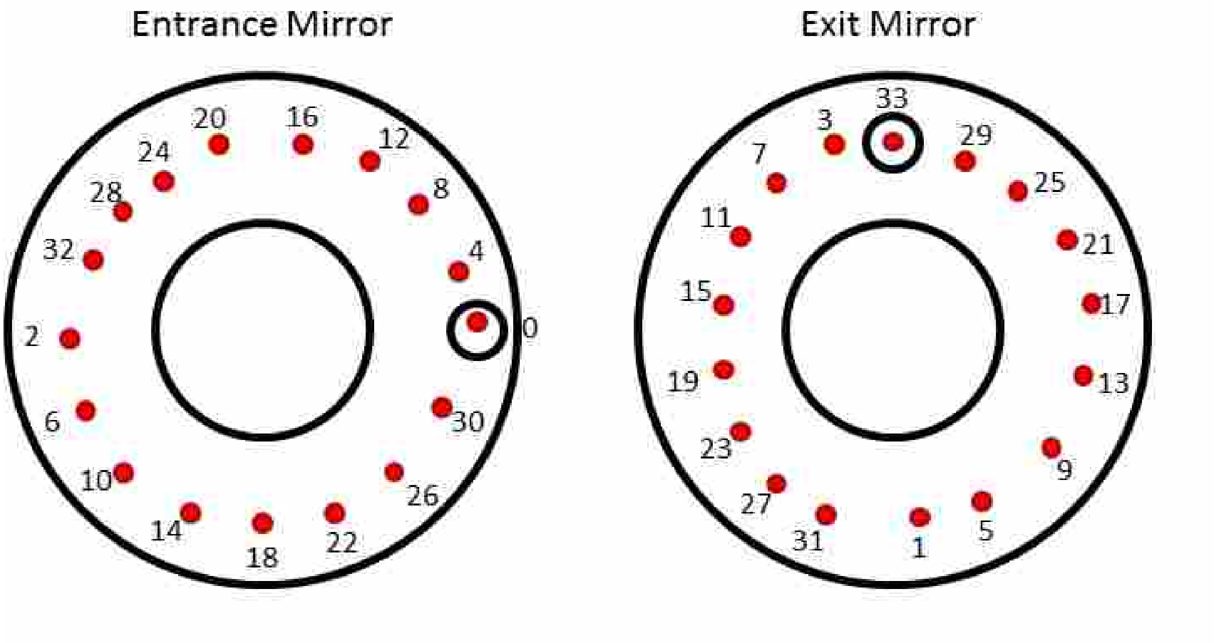

Figure 3.4: Harriot cell mirrors demonstrating laser-light path through the cell.

program. The absorption data must be correlated to a concentration with absorption cross sections. Cross sections in the infrared are more subject to experimental conditions of pressure and temperature than UV cross-sections. Therefore, every experimental setup requires the measurement of the cross section for the O-H overtone of water. Laser-induced fluorescence detection and cavity ringdown are described in detail in the preliminary and proposed work while the techniques established previously in our laboratory are described in Chapter 2.

3.6 Present work and detection limits

An LIF detection system for NO_2 has been designed from information obtained from the literature. Abundant physical data for NO_2 was established in the 1960's and 1970's.[96–104] NO_2 has irregularities compared to other small molecules because it has an unpaired electron in its ground state. Absorption of light at wavelengths < 370 nm will completely dissociate NO_2 into NO and O.[96] Light between 370 nm and 436 nm promotes NO_2 to a predissociative state,[98,104] of which the quantum yield for dissociation varies from 1.0 to 0.01. The full potential energy diagram of the excited states of NO_2 in the region of 420 nm to 800 nm is yet to be discovered. More than one state overlaps in this region and significant inter-system crossing occurs. Upon excitation with 488 nm or 514.5 nm light, three different lifetimes have been observed: 3, 28, and 75 μs[102]. Evidence suggests that at these wavelengths NO_2 is excited into the $^2B_1$ state and rapidly crosses into the $^2B_2$ state. If the molecule relaxes from the $^2B_1$ state, it has a short radiative lifetime of 3 μs opposed to the longer radiative lifetimes of 28 and 75 μs if the molecule relaxes from the $^2B_2$ state.

Fluorescence of NO_2 excited at 488 nm, is emitted between 398 and 750 nm[98]. No structural features appear in the spectrum above 0.1 Torr of pressure. Because of the broad spectrum of fluorescence from NO_2, a continuous-wave (cw) excitation source combined with optical filtering collects the maximum fluorescence per unit time. The best S/N fluorescence signal was collected by optically filtering so that only light between 550 nm to 900 nm was measured. A 550 nm long-pass filter restricts laser scatter from being detected and a 900 nm short-pass filter restricts higher wavelength emissions of the laser from being measured. additionally, a 488 nm bandpass filter is used to reject spontaneous plasma emission from the argon-ion laser. Raman scattering from O_2 and N_2 is small compared to the signal from fluorescence but radiates at 528.1 nm and 550.6 nm, most of which would not reach the detector. The long radiative lifetime of NO_2 provides substantial time for fluorescence quenching at pressures above 1 Torr[99]. The challenge in the proposed work is to detect NO_2 at pressures as high as 200 Torr in the presence of strong quenchers such as O_2, N_2, and H_2O vapor.

Recent work has demonstrated the use of LIF for the *in-situ* detection of NO_2 at tens of ppt.[105–107] The cell described in this chapter provides three advantages for detecting LIF. First, baffles along the excitation path aid to reject stray light and pass collimated light. Second, extraneous light is filtered so it fails to reach the detector. And lastly, optics are used to collimate fluorescence through the filters and then focus the light onto the detector. These designs require a variety of working conditions but generally require pressures near 1 Torr, which is much lower than the desired operating pressure (50–200 Torr). Figure 3.5 is a LIF-cell that has been constructed and tested. The cell is based on the design of Dari-Salisburgo et al.[107] The excitation path is defined by the longest axis in Figure 3.5 and is filled with optically black baffles to collimate the probe beam and to reject diverging light. Orthogonal to this axis are two cover plates that allow for experiments to be performed without integration into the rest of the slow-flow photolysis system. These plates are easily removed, which allows the cell to be integrated quickly into the photolysis cell. Perpendicular to both cover plate axis and excitation axis, the fluorescence signal is detected. The argon-ion laser is vertically polarized; therefore scattered light is most intense 90 degrees to the left and right and the least intense 90 degrees up and down. The side opposite of the PMT on the detection axis contains an aluminum-coated mirror to reflect fluorescence back towards the telescoping optics.

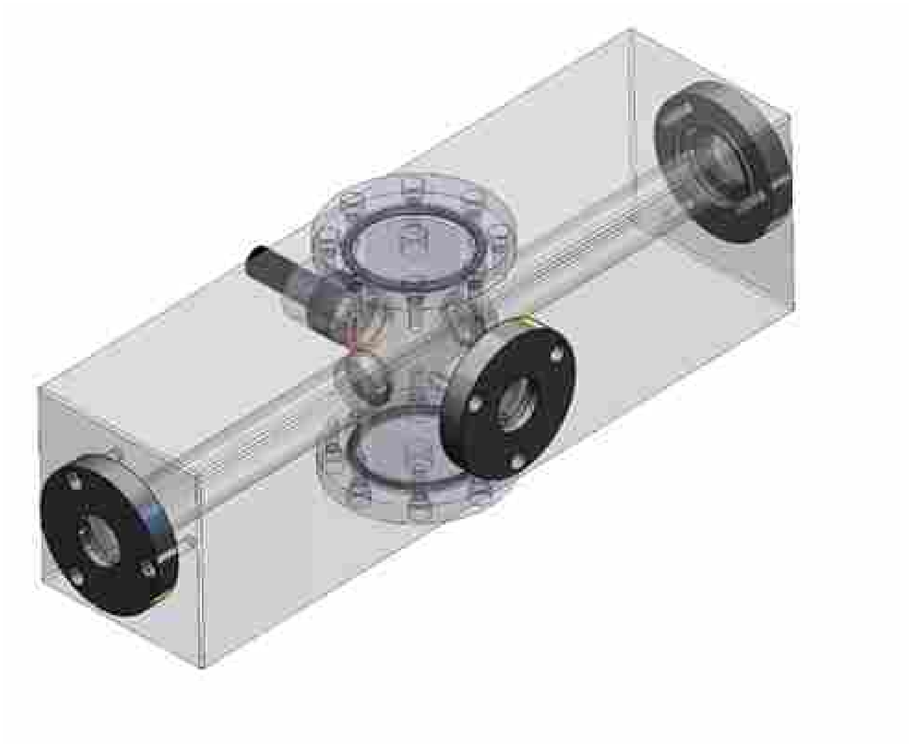

Figure 3.5: LIF cell needed to detect NO_2 *in situ* during kinetic experiments.

A detection telescope with filters enhances the collection of fluorescence. Figure 3.6 shows two lenses and four filters that work to collimate, filter, and focus light onto the PMT. Figure 3.7 shows the results of fluorescence quenching by N_2 as a function of pressure as well as fluorescence from NO_2. The data in Figure 3.7a was collected on an un-anodized cell without the filtering/focusing light assembly described previously. The data for Figure 3.7b was collected on the anodized system with the aid of the filter/focusing assembly.

From Figure 3.7, it is observed that at our desired operating pressures (50-200 Torr), the first experiment showed a signal-to-noise ratio of less than 1. Figure 3.7b shows a dramatic increase in the signal-to-noise over Figure 3.7a. Further reduction of noise can be achieved by placing an iris over the PMT to restrict the angle of light reaching the detector. This enhances the S/N because the light passing through the filters is not collimated completely because the laser is a line source not a point source. The success of the cell design is shown first in the S/N obtained and then again with linear fits of calibration curves of the fluorescence of NO_2.

Calibrations of NO_2 in O_2 and N_2 using the system shown in Figures 3.5 and 3.6 are plotted in Figure 3.8. A standard cylinder containing 48.8 ppm NO_2 in 1000 ppm O_2 with N_2 as backfill was systematically diluted with N_2 from 48.38 ppm to 73.43 ppb. Each dilution was mixed at higher pressures (∼300–400 Torr) and then evacuated to observe fluorescence signal at 50, 25, 5, and 1 Torr. Each pressure showed a good linear fit, and although the signal was higher at lower pressures the sensitivity was relatively constant. The small difference in the fluorescence signal collected between 25 Torr and 50 Torr indicates the possibility that NO_2 can be detected at pressures as high as 200 Torr.

3.7 Future Work

3.7.1 β-$HOCH_2CH_2O_2$ Self-reaction and reaction with HO_2

The effects of water vapor on the $HOCH_2CH_2O_2$ self-reaction must be understood before a complete kinetic model can be built to fit data from the reaction of $HOCH_2CH_2O_2$ with NO. The $HOCH_2CH_2O_2$ is created by photolyzing $HOCH_2CH_2Cl$ with 193 nm light from

Figure 3.6: Filter tower designed to collimate fluorescence, filter noise, and then focus light onto PMT detector.

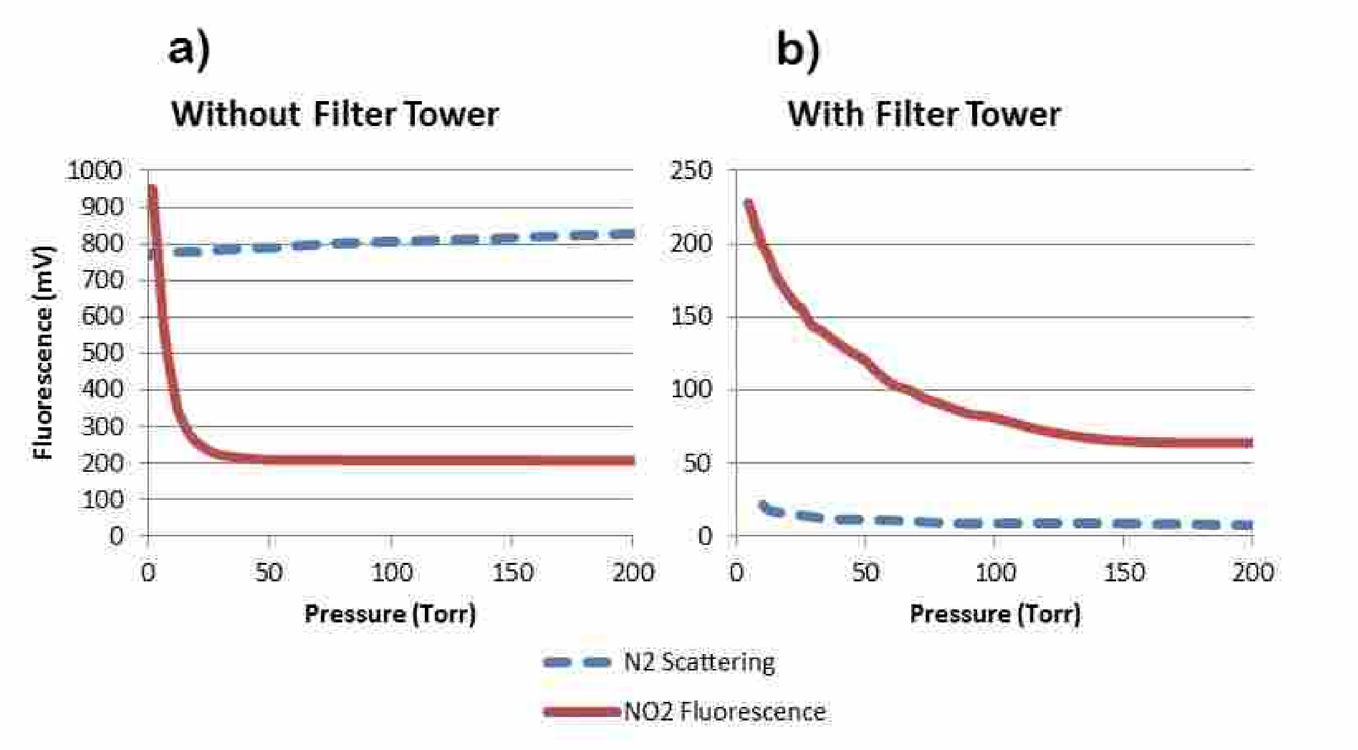

Figure 3.7: Plots of fluorescence of NO_2 and scattering of N_2 vs. total pressure in the newly designed cell. (Figure 3.5)

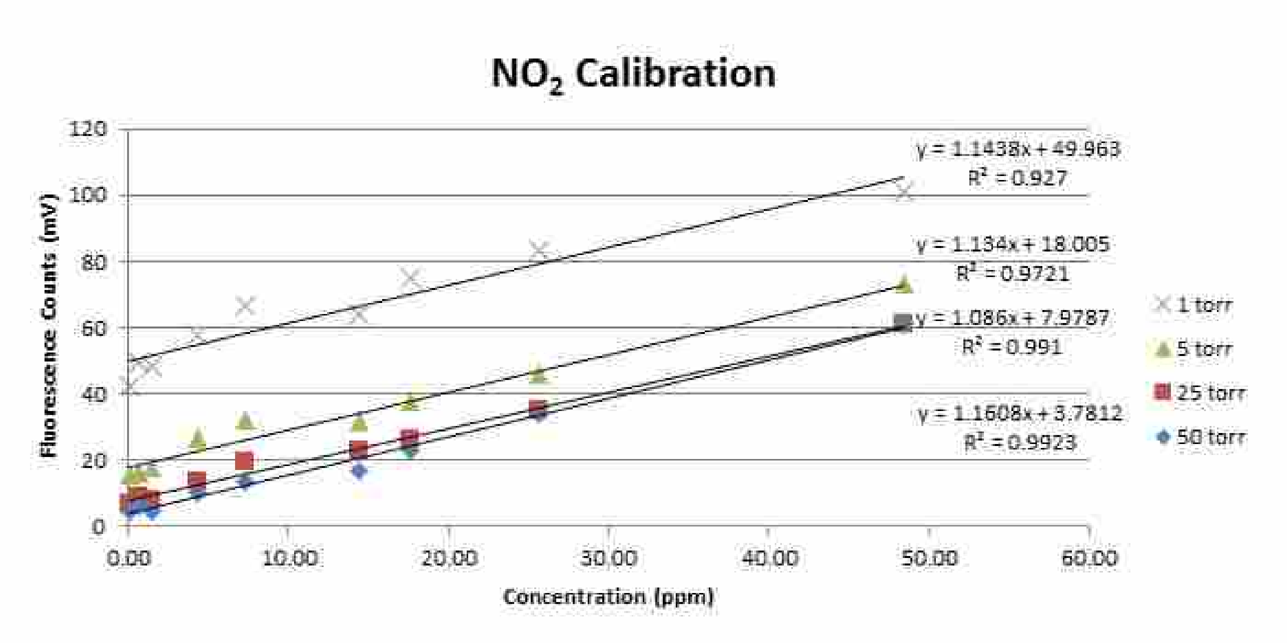

Figure 3.8: Calibration curves of NO$_2$ fluorescence with N$_2$ as backfill gas.

an ArF excimer and then reacting with excess O_2. Absorption spectra were collected on an intensified CCD camera at varying time-delays (50 s–300 ms). The entire spectrum was collected from 210–350 nm at each time delay. Because the cross section has been reported[67] analysis of the entire spectrum can determine contaminating species that would be caused by secondary chemistry. This is completed by fitting the data to our kinetic model and observing differences without the presence of water vapor. Time-concentration profiles are generated using a PMT for collection at a specified wavelength with a known cross section from the literature. The addition of HO_2 to the reaction cell further complicates the model as well as the experiment. HO_2 is also produced through photolysis, but conveniently can be initiated by the photolysis of $HOCH_2CH_2Cl$ as shown in reaction 3.17 and 3.18 and is produced as secondary chemistry demonstrated by reactions 3.10 and 3.11.

$$\mathrm{Cl + CH_3OH \rightarrow CH_2OH + HCl} \tag{3.17}$$

$$\mathrm{CH_2OH + O_2 \rightarrow HO_2 + CH_2O} \tag{3.18}$$

3.7.2 Product branching ratio by LIF of NO_2

Once the effects of water vapor on the self-reaction of $HOCH_2CH_2O_2$ and reactions with HO_2 are established the product branching ratio of $HOCH_2CH_2O_2$ with NO can be studied through LIF. Now that the LIF cell has been built and its capabilities in static experiments have been verified it can be integrated into the photolysis cell. Calibrations are necessarily retaken in the full setup to verify if linear curves and sufficient sensitivity exist. Approximate detection limits and sensitivities needed to observe the effect of water vapor have been calculated. Figure 3.9 shows the production of NO_2 as a function of time using the kinetic model under pseudo-first order conditions ([NO]>>[$HOCH_2CH_2O_2$]). The initial concentrations of both NO and $HOCH_2CH_2O_2$ are 3.0×10^{15} molecules cm^3 and 3.0×10^{14} molecules cm^3 respectively. The reaction rate coefficient $k_{3.16}$ was increased between 0 and 50% of

$k_{3.15}$ while keeping $k_{3.15}$ constant. The time-concentration traces in black represent the NO_2 concentration as a function of increasing values of $k_{3.16}$ (the production of $HOCH_2CH_2ONO_2$). The red traces represent the time-concentration profile for production of $HOCH_2CH_2ONO_2$ as a consequence of increasing $k_{3.16}$ as a function of $k_{3.15}$.

Examination of Figure 3.9 shows that the equilibrium concentrations of NO_2 are reached ~100 ms after the reaction begins. The figure also shows that as the rate constant used for $k_{3.16}$ increases, the concentration of NO_2 produced decreases. When $k_{3.16} = 0$ cm^3 molecule^{-1} s^{-1}, the yield of NO_2 is ~2.8 × 10^{14} molecules cm^{-3}. When $k_{3.16}$ is increased to 30% of $k_{3.15}$ the yield of NO_2 decreases to 2.2 × 10^{14} molecules cm^{-3}, a decrease of ~9 ppm. Currently, the LIF system allows for the measurement of ± 1.7 ppm at 50 Torr (total pressure). Consequently the LIF system currently in use will allow for the effect of water vapor on the product branching ratio ($k_{3.15}/k_{3.16}$) to be measured assuming that any loss in NO_2 formation is followed with an equal increase in $HOCH_2CH_2ONO_2$ production.

3.7.3 Product branching ratio by CRDS of $HOCH_2CH_2ONO_2$

The Hansen group propose to design, construct, and use a cavity ringdown system (CRDS) to measure organic nitrate production in conjunction with the system outlined above. Cavity ring-down spectroscopy is a specialized long-path absorption spectroscopy technique.[108–111] This technique measures the rate of decay of light intensity as it reflects between two parallel mirrors. In the absence of any absorbing species, the rate of decay is dependent only on the characteristics of the cavity (i.e., the distance between the mirrors and the reflectivity of the mirrors). With each pass of the light, a small fraction of intensity is lost to transmission through the mirrors. The measured decay rate is deemed the ringdown time. In the presence of an absorbing species the rate of decay increases in a manner that correlates with the concentration of the species in the cavity.

In CRDS, the limit of detection is determined by a combination of the path length, minimum detectable differences in rate decay, and the absorption cross-section of the molecule.

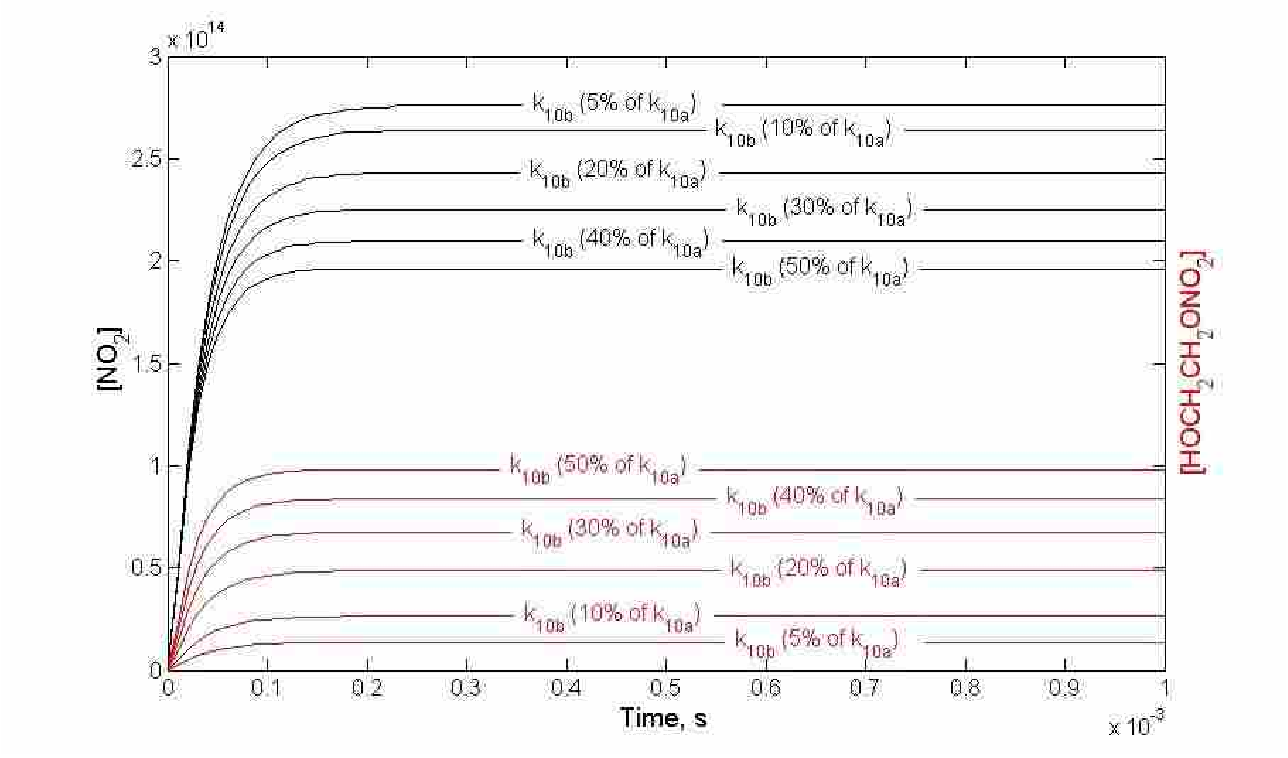

Figure 3.9: Calculated production of NO_2 and $HOCH_2CH_2O_2$ as a function of time ($k_{3.16}$ was varied from 0 to 50% of $k_{3.15}$).

Path length is limited by the reflectivity of the mirrors and the distance between them. Reflectivities of mirrors used in CRDS are typically $R > 0.9999$. Mirror separations greater than a few meters become increasingly difficult to align, but only small separations are needed to create extremely long optical-path lengths. As an example, a cavity with a mirror separation of 100 cm and reflectivity of 0.9999 has a ringdown time of 33 μs and an effective path length of $\sim$10 km. With a minimum detectable difference in decay rate of 1% of the ringdown time, the minimum absorption coefficient is 1×10^{-8} cm^{-1}.

In this proposed work, mirror separation is limited to the horizontal width of the excimer laser beam ($\sim$24 mm). With mirror reflectivities of 0.9999 and detectable change of 0.01, the ringdown time is calculated to be 8×10^{7} s with a pathlength of 240 m. These parameters bring the minimum absorption coefficient to 4.1×10^{7}. To improve this value, higher mirror reflectivities are needed. Increasing the mirror reflectivities to 0.99999, the ringdown time, pathlength and minimum absorption coefficient all improve by a factor of 10. The minimum detectable change in ringdown can also be improved. Brown et al.[112] demonstrated detectable changes observed at 6×10^{-4} absorption. With a detectable difference of 0.001, the minimum absorption coefficient in this experiment will be 2.5×10^{9}. Because the typical infrared absorption cross section is $\sim 1.0 \times 10^{-20}$ cm^{2} molecule^{-1}, the limit of detection for $HOCH_2CH_2ONO_2$ under these conditions will be $\sim$10 ppb. The expected maximum concentration of $HOCH_2CH_2ONO_2$ is 10 ppm. This difference in limit of detection and expected concentration provides sufficient dynamic range to measure the kinetics of the production of $HOCH_2CH_2ONO_2$ and other organic nitrates.

The CRDS cavity will be constructed with an aim to detect many different organic nitrates for future experiments. The main difficulty lies in obtaining mirrors for the cavity with high reflectivity over a range of wavelengths. This range can be much smaller than for other detection systems because each analyte contains the same $R{-}O{-}NO_2$ functional group. The fundamental transitions for the asymmetrical and symmetrical stretches of NO_2 in methyl nitrate are 1672 cm^{-1} and 1287 cm^{-1}, respectively[113]. The study of other

Table 3.1: Calculated stretches of NO_2 in various nitrate molecules and NO_2.

Molecule	Anti-symmetric Stretch (cm^{-1})	Symmetric Stretch (cm^{-1})
NO_2	1705.2	1394.6
CH_3NO_2	1717.6	1327.7
$CH_3CH_2NO_2$	1711.6	1321.9
$CH_3CH_2CH_2NO_2$	1711.0	1318.9
$CH_3CH_2CH_2CH_2NO_2$	1706.6	1335.8
$HOCH_2CH_2O_2$	1706.8	1320.9

more complex organic nitrates by Finlayson-Pitts et al.[114] showed that the asymmetrical stretch for these molecules absorb at 1635 ± 5 cm^{-1} and the symmetrical stretch absorbs at 1280 ± 2 cm^{-1}. *Ab initio* geometry and frequency calculations were performed in an effort estimate the needed wavelength range for the CRDS mirrors. Table 3.1 lists several organic nitrate geometry optimizations and the associated symmetric and asymmetric stretches from the nitrate groups. These calculations were performed with Gaussian03 with the B3LYP/aug-cc-pVDZ method/basis set combination. Analysis of Table 3.1 shows that the symmetric stretches in NO_2 are within 11 cm^{-1} of one another. If we combine these calculations with the experimental frequencies of methyl nitrate, we predict that small-chained hydrocarbon (less than 6 carbons) organic nitrates will absorb at 1672 ± 20 cm^{-1}. High reflectivity mirrors are readily available in the IR with typical wavelength ranges of 100–200 nm. This designed CRDS system will measure the kinetic production of a variety of organic nitrates to assist in measuring the complete kinetic effects of water vapor on the reaction of RO_2 + NO.

Chapter 4

Method for Evaluating Anaerobic Digester Performance

4.1 Disclaimer

The work presented in this chapter has been published in Bioresource Technology.[115] It is presented in its entirety with minor changes.

4.2 Abstract

The degradation rate and efficiency of digestion processes is typically measured by introducing a substrate or pollutant into a digester and then monitoring the effluents for the pollutant or substrate, a costly and slow process. A new method for rapid measurement of the rates and efficiencies of anaerobic degradation of pollutants and lignocellulose substrates from various pretreatments is described. The method uses micro-reactors (10 to 30 mL) containing a mixed culture of anaerobic bacteria obtained from a working anaerobic digester. The rate of degradation of pollutants and metabolic heat rate are measured in parallel sets of micro-reactors. Measurement of metabolic rate and pollutant degradation simultaneously is an effective means of rapidly examining pollutant degradation on a micro-scale. Calorimetric measurements alone allow rapid, relative evaluation of various substrate pretreatment methods.

4.3 Introduction

The degradation efficiency of digestion processes (aerobic or anaerobic) is typically measured by doping a waste stream with the chemical of interest and then monitoring the effluent for evidence of the compound. This type of analysis can be problematic due to the necessity of using concentrations of effluent exceeding the limit of detection of an analytical technique and because of matrix effects that demand intricate sample preparation methods. Another problem is the large amount of pollutant necessary to do the analyses.

Isothermal heat-conduction calorimetry is an effective tool for measuring the rate of heat production from slow reactions. Many exothermic reactions take place during anaerobic degradation, and the rates and total heat from these reactions can easily be measured to provide data on growth of bacteria. This manuscript presents a combined analytical and calorimetric method for rapid measurement of the rate and efficiency of degradation of PCBs as an example of a pollutant that is recalcitrant to aerobic digestion. The chemical analysis provides the rate of degradation of the pollutant and calorimetry provides information on the effects of the pollutant on the bacterial culture. Data applicable to the degradation of pollutants in anaerobic digesters is thus rapidly obtained with minimal amounts of material. The calorimetric method can also be used to determine the efficiency of various pretreatment methods for digestion of cellulose and lignocellulosic material as shown by measurements with a mixed culture of anaerobic bacteria obtained from a working induced-blanket reactor (IBR).

Anaerobic digestion has recently been suggested as a method to degrade organic pollutants. In comparison, composting, or aerobic degradation, which has been widely used as a strategy for biodegradation of organic pollutants is a slower process, and recalcitrant pollutants are not degraded and remain functional.[116] Induced Bed Reactors (IBR) have recently been developed as anaerobic bioreactors and have the advantage of more rapid throughput and higher solids density than previous designs of anaerobic reactors.[117] These advantages make the IBR an attractive possibility for green energy production. In an IBR, a sludge blanket is initially formed as bacteria attach to the waste particles in the wastewater.[118] If the sludge blanket is operating properly it will be comprised primarily of living bacteria. Organic waste is pumped through the sludge blanket where it is brought into contact with the mixed culture and consequently broken down by a consortium of anaerobic bacteria. The bioreactor usually involves a cylindrical tank 4-5 meters in diameter and 9-10 meters tall where wastewater containing a high concentration of organic matter is passed through. The organic matter may be byproducts of farming, food processing, or slaughterhouse waste, for example. A partition or septum is positioned within the tank about two-thirds up the tank. The septum allows biogas to rise to the top of the tank where it is separated from the solids and subsequently removed and used for energy production.

Anaerobic digesters have the added benefit of more rapid degradation than aerobic digestion, and also have the potential of producing substantial amounts of biogas as a product. Recent studies of anaerobic reactors for degradation of organic pollutants have shown variable, but promising progress.[119–121] However, measurements of the rates and efficiencies of degradation of pollutants, even in small laboratory scale digesters is a costly and slow process. Analyses that may be necessary include: (a) Biochemical methane potential (BMP), the maximum amount of methane that can be produced from 1 g of chemical oxygen demand (COD) in wastewater which indicates how amenable the wastewater is to anaerobic treatment. BMP is therefore an indicator of the kinetics and efficiency of the anaerobic digestion process.[122] (b) Specific methane activity (SMA), which measures the rate at which the COD in wastewater is converted to methane. SMA can be used to evaluate the methanogenic metabolic activity of the starter sludge and to determine the potential loading capacity of an upflow anaerobic sludge blanket (UASB) reactor.[123] (c) Nutrient deficiency (ND), which is employed to determine if the wastewater has enough nutrients to allow anaerobic bacteria to grow. (d) Anaerobic toxicity assay (ATA), which indicates whether the wastewater is toxic to anaerobic bacteria. And (e), cation inhibition (CI), which is used to investigate the effect of cation concentration on the performance of anaerobic bacteria and if a pH control is required for anaerobic technology. The BMP analysis by itself can take 40 to 60 days and requires additional tests including at least chemical oxygen demand in and out of the BMP vessel.[124]. While not addressing all of the information available from these tests, the micro-method presented in this manuscript allows for the rapid measurement of the relative rates and efficiencies of the degradation of pollutants and potential feedstocks.

4.4 Materials and Methods

4.4.1 PCB Degradation

Samples were prepared by adding 1.5 mL of a 1000 μg/mL solution of PCB in methanol (Aroclor 1260 PCB standard) obtained from Sigma-Aldrich to a 30 mL, glass, serum vial. The methanol was allowed to evaporate at room temperature overnight. The sample was re-solvated by adding 1.5 mL of 95% ethanol to the vial. Preliminary experiments showed that methanol was toxic to the culture so it was replaced with ethanol. Twenty mL of sludge (mixed culture) collected from an operating IBR were added to the sample vial. Previous work has shown the mixed culture of anaerobic bacteria to include *Clostridium, Flavobacterium, Bacteroides, Spirochaeta, Methanobrevibacter*, and *Methanosarcina* as well as several species whose roles are not completely understood in the breakdown mechanism of an IBR.[125] These include *Dehalococcoides, Planctomyces, Aequorivita,* and *Sedimentibacter* species. The sample was divided into twenty, 1-mL aliquots, purged with dry N_2 and sealed. These vials were placed in a constant temperature bath maintained at 37.5°C. At increasing times, vials were removed from the constant temperature bath and placed into a freezer, which suspended all bacterial activity. The first few vials were removed at 30 min intervals, followed by 1-hour intervals, and finally 1-day intervals to capture the decreasing concentration of PCBs caused by reaction with the mixed culture.

Extraction of PCBs from the organic matrix was accomplished by allowing the samples to warm to room temperature, adding 500 μL of a 2:1 chloroform:methanol solution, shaking the mixture, allowing the solvent to separate, and collecting the supernatant. This procedure was repeated 3 times for each sample, each time removing the organic layer prior to the addition of the subsequent extraction solvent. The extractant solution was then placed in an oven at 50°C to evaporate all solvent. Prior to GC-MS analysis, 500 L of n-hexane was used to re-dissolve the sample. GC-MS data were obtained with a double sector electron ionization (EI) instrument operating with 70 eV electron ionization. A 30 meter long, 250 μm diameter, 50% phenyl polysilpenylene-siloxane column was used (SGE Analytical Sciences). The injector port was maintained at 100°C. After injection, the temperature was raised 20°C min^{-1} to 286°C, after which it was held at this temperature for 6 min. A mass range of 325 to 375 m/z was chosen to observe the constitutional isomers of $C_{12}H_4Cl_6$.

Simultaneous samples matching the undivided samples for chemical analysis were prepared for calorimetric measurements, the 30-mL vial was purged with dry N_2 and it was sealed with a silicone rubber seal. Samples were run isothermally at 37.5°C in a Calorimetry Sciences isothermal micro calorimeter (IMC) (currently TA Instruments, Lindon, UT). This calorimeter runs three samples and one reference simultaneously. The reference chamber contained a serum bottle filled with glass beads for these experiments. Heat rates were obtained as a function of time for typically 5 days.

4.4.2 Cellulose and Algae Pretreatment Methods

The IMC was used to evaluate the effectiveness of H_2O_2 as a pretreatment for digestion of cellulose and lignocellulosic materials. Powdered Whatman filter paper was used as a pure cellulose feedstock by pretreatment with 30% H_2O_2 in a ratio of 2:1 (mL H_2O_2/g filter paper) and enough distilled, deionized water to form a slurry. After dilution with water, the final concentration of peroxide was approximately 3%. The slurry was continuously mixed and allowed to react for 12 h. The slurry was then vacuum filtered and washed to remove any unreacted H_2O_2. Three samples were prepared and run in parallel. One sample was prepared by mixing 1 g of pretreated cellulose with 10 mL of active culture obtained from a working IBR and 10 mL of distilled, deionized water. A second sample was prepared by mixing untreated cellulose with 10 mL of culture and 10 mL of water. A third sample was prepared by mixing only culture and water together. The samples were thermally equilibrated for about 1 h and inserted into the measuring chambers of the IMC at 37.5°C. Heat rates were measured as a function of time for 5 days.

A variety of pretreatment techniques were tested for their ability to break down algae. Five, 10-g aliquots of wet algae obtained from the Cache County (Utah) sewage treatment retention ponds were added to bubblers containing the following chemical oxidants: 0.50 g $FeCl_3$, 500 mL 30% H_2O_2, 0.50 g MnO_2, 0.50 g KI, 500 mL 3% NaOCl. Room air was drawn through the bubblers for 24 h at a rate of approximately 30 sccm. Additionally, 10 g of wet algae were placed in an electrolysis cell and stirred overnight at 0.5 A and 12 V between iron and nickel electrodes immersed in the sample. A seventh sample was irradiated with a total of 122 grays of gamma radiation (661 keV) from a Cs-137 source during 60 min. An untreated blank sample was also prepared. After pretreatment, approximately 0.5 g of each sample was added to 5 g of sludge obtained from a working IBR and flame sealed in 20 mL glass vials.

Samples were run in an 8-cell microcalorimeter at 37°C (TAM-AIR, TA Instruments, Lindon, UT). Heat rates were obtained as a function of time for typically 5 days. This calorimeter runs 8 samples and 8 reference samples simultaneously. The reference chamber contained distilled water in a flame sealed vial.

4.5 Results and Discussion

4.5.1 PCB Degradation

Figure 4.1 shows the time dependence of the breakdown of PCBs by reaction with the mixed culture. Within the first 200 min the concentration decreased by 66%, from 200 to 68 ppm. The concentration continued to decrease after this time but at a much slower rate of 1.5 ppm h^{-1}. Figure 4.2 shows the thermograms for three samples analyzed in the calorimeter.

The control sample vial contained only 1.5 mL ethanol and 20 mL of mixed culture. A second sample vial contained 200 ppm PCB, 1.5 mL ethanol and 20 mL of the same mixed culture. A third sample vial contained 1.5 mL ethanol, 20 mL of the same mixed culture and

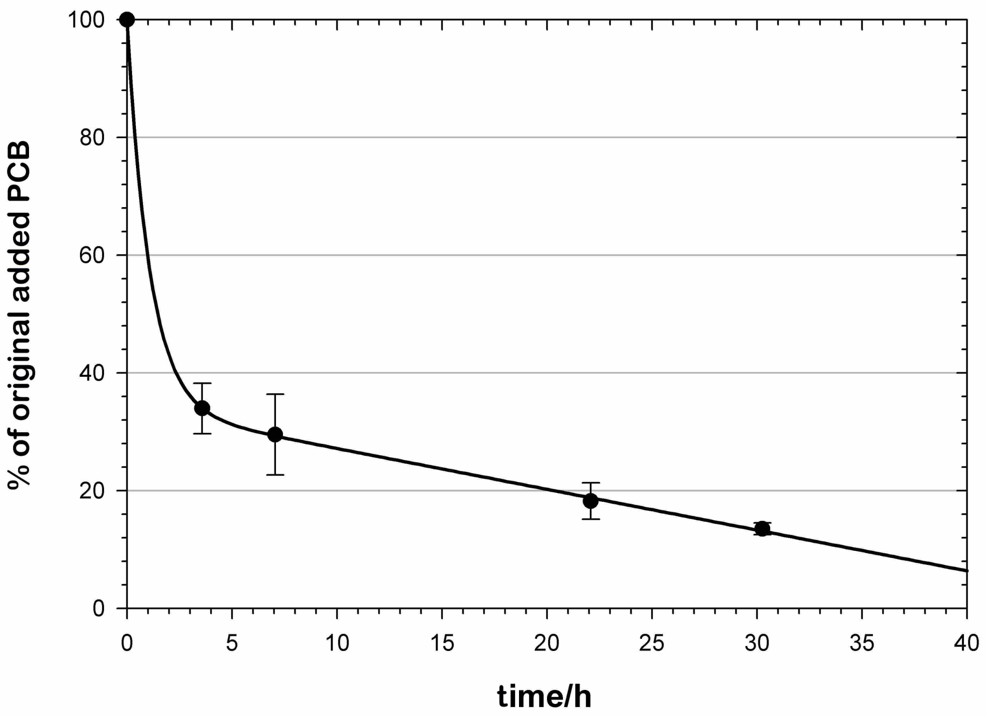

Figure 4.1: Degradation of PCBs by a mixed culture of anaerobic bacteria obtained from an operating IBR.

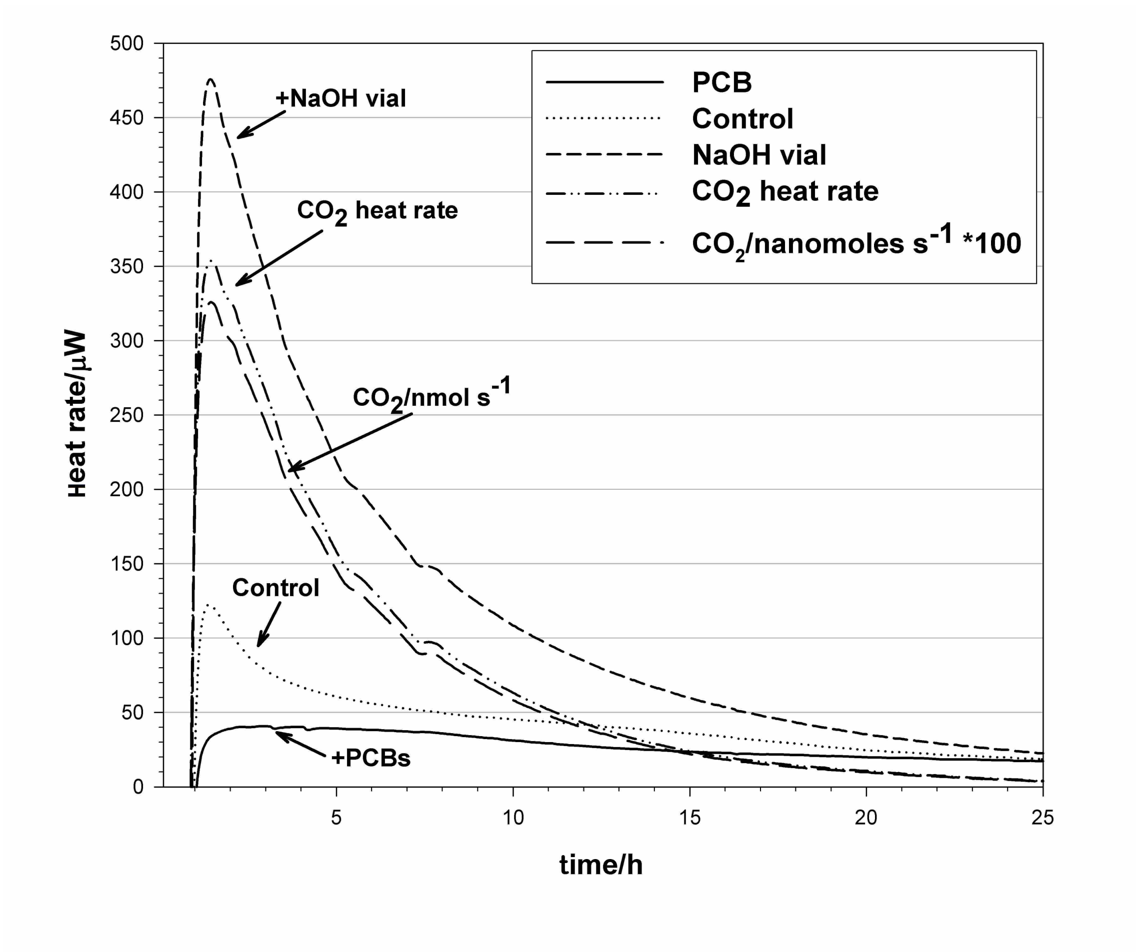

Figure 4.2: Thermograms for degradation of PCBs by a mixed culture of anaerobic bacteria. The solid line is the heat rate for the reaction of PCB/ethanol mixture with the mixed culture. The dotted line is the heat rate from the control sample (95% ethanol) reacting with the mixed culture. The short dashed line is the heat rate from a sample containing 95% ethanol and a separate vial containing NaOH. The difference in heat rates between this sample and the control is shown by the dash-dot-dot line and represents the rate of CO_2 production. The long dashed line is the rate of CO_2 production in nmol s^{-1} (scaled by 100 for ease in viewing).

a separate vial containing 1.5 mL of 0.4 M NaOH solution. At early times, all three samples showed a rapid rise in the heat rate caused by the samples equilibrating in the calorimeter as well as reacting with the substrate. The maximum heat rate of the control sample is 100 μW; the sample containing the NaOH vial, peaked at 470 μW. The difference between these two signals represents the CO_2 production rate due to the mixed culture reacting with ethanol. The enthalpy of reaction for CO_2 + NaOH (-108.5 kJ mole^{-1}) is used to calculate the CO_2 production rate. The rapid rise in the measured heat rate followed by an exponential decay indicates that ethanol is readily consumed by the mixed culture. The PCB containing sample peaks at approximately the same time as the non-PCB containing samples, but does so at a much reduced heat rate ($\sim$25 μW) showing that the presence of PCBs affects the ability of the mixed culture to consume the ethanol in the sample. Instead of an exponential decay, as observed in the non-PCB containing samples, the heat rate remains constant for about 5 h and then decays exponentially.

The analytical data indicate PCB concentrations decreased due to anaerobic treatment. Over a 3 day period, the total PCB concentrations were reduced from 200 ppm to 30 ppm, an approximately 85% decrease. The lower limit of detection for the PCBs by the GC-MS method used in this study is 14 ppm. Calorimetric data confirmed that bacterial growth and activity occurred over the same time frame when contaminant concentrations decreased. Simultaneous measurement of contaminant degradation and metabolic rate by independent methods is an effective means of rapidly examining a complex process. In applying this combined analytical/calorimetric method to a pollutant, it is critical that an analytical procedure with the appropriate detection limit be available to determine the concentration of pollutant in the analytical samples that are analyzed in parallel with the calorimetric samples. Because the culture evolves over time it is not reproducible and thus it is necessary to run a control in parallel with the analytical/calorimetric samples in each experiment. What is exploited in this method is the ability to measure calorimetric differences between the control and the polluted samples. Our experience indicates that calorimetric differences caused by the added pollutant are readily apparent in the thermograms. While the total amount of heat can be quantified by integrating the thermograms, the pattern of the thermograms contains significant information. But as yet there is no standardized way to quantify the differences in the patterns or to ascribe these differences to any particular metabolic process. In response to recent data from the EPA, these methods are being applied to the degradation of clopyralid and ibuprofen as examples of pollutants that pass through aerobic digestion.[126]

4.5.2 Cellulose and Algae Pretreatment Methods

Figure 4.3 displays the thermograms of the cellulose samples. The sample containing only bacteria remains near the baseline throughout the entire trial. The sample pretreated with H_2O_2 shows a rapid rise in the measured heat rate at early times, reaching a maximum of 2.5 mW. The initial rapid rise in heat rate is attributed to the sample equilibrating in the calorimeter as well as reacting with the substrate. This peak develops a shoulder that begins at ~ 7.2 h and continues for 1.8 h with a heat rate of 1.6 mW before it begins to tail off. This shoulder is consistent with the production of a digestible substrate by bacteria in the culture followed by consumption of this product by another set of bacteria. The heat rate from the control sample (non-treated cellulose) peaks much later, at 83 h with a heat rate of 0.95 mW. Integrating the area under the curves shows that 1.5 times more heat (136 J) is liberated from the nontreated sample than from the pretreated sample (90 J), but much of the heat from the pretreated sample may have been produced before the calorimetric measurement began. The early rise in the heat rate suggests that the pretreated sample contains a more easily digestible substrate than the untreated sample. Quantifying the absolute amount of degradation would require the determination of the carbon balance, but since the conditions (i.e., mixed culture and amount of substrate) in each sample vial are identical, the relative amount of degradation is directly proportional to the total heat produced. Therefore. the experiments reported here provide a relative measure of the amount of each substrate degraded.

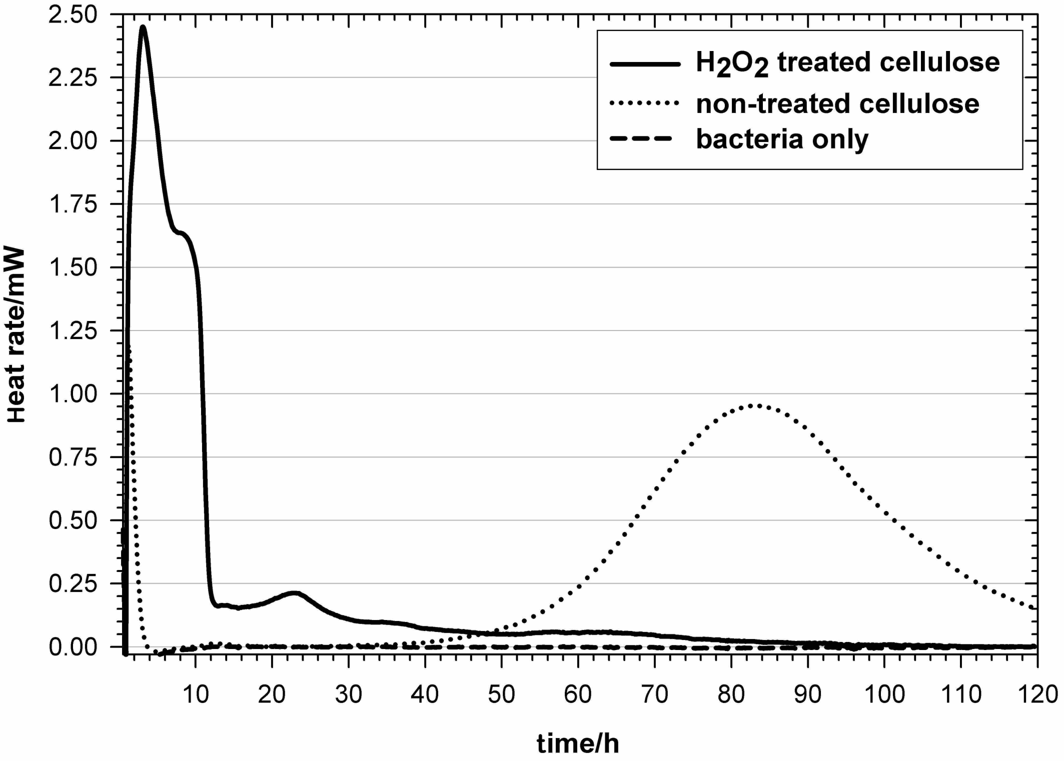

Figure 4.3: Thermograms for the digestion of untreated and pretreated cellulose by H_2O_2. The solid line is the heat rate for pretreated cellulose reacting with the mixed culture of anaerobic bacteria. The dotted line represents the heat rate for reaction of untreated cellulose with the mixed culture. The dashed line is the heat rate for the sample containing only the mixed culture with no added substrate.

Figure 4.4 shows thermograms for the various pretreated algae samples analyzed calorimetrically. The 1.3 h delay in the measurement of the heat rates is due to sample equilibration to the temperature of the calorimeter (37.5°C), and measured heat rates during this equilibration time must be disregarded. Although significant reactions may be occurring during the first 1.3 h, it is not possible to obtain meaningful data during this time. Integration of the peak areas and normalizing for the amount of algae in the sample shows that the blank liberated the most heat (44 J). Undoubtedly, as shown by the initial rapid rise in heat rate, most of the pretreatment methods produce a substrate that is more easily consumed by the consortium of bacteria found in an IBR. However, when pretreating with H_2O_2, any residual unreacted peroxide must be removed prior to introducing the sample into an anaerobic digester. Hydrogen peroxide is an antibacterial agent and the presence of peroxide with bacterial peroxidases causes rapid breakdown of H_2O_2 and sterilization of the bacteria. Washing and filtering the pretreated sample after reaction removes unreacted peroxide and produces influent that can be introduced into an anaerobic digester, but washing and filtering also removes soluble and easily digestible components of the algae. The removal of these components accounts for much of the reduction in total heat observed in Figure 4.4. In addition to a reduced amount of substrate, the reduced heat rate of samples pretreated with $FeCl_3$, KI, NaOCl, and MnO_2 relative to the blank is also likely due to inhibition of bacterial action by residual chemical in the pretreated sample. The reason for the reduced total heat observed for the algae sample irradiated with gamma radiation is unclear. Neither washing nor filtering is required for this sample, and residual chemical is also not present.

Calorimetric data were collected and used to measure the effectiveness of various pretreatment methods for digestion of cellulose and algae by a mixed culture commonly found in anaerobic digesters. The described method allowed for the rapid and quantitative evaluation of various pretreatment methods with a minimal amount of sample preparation.

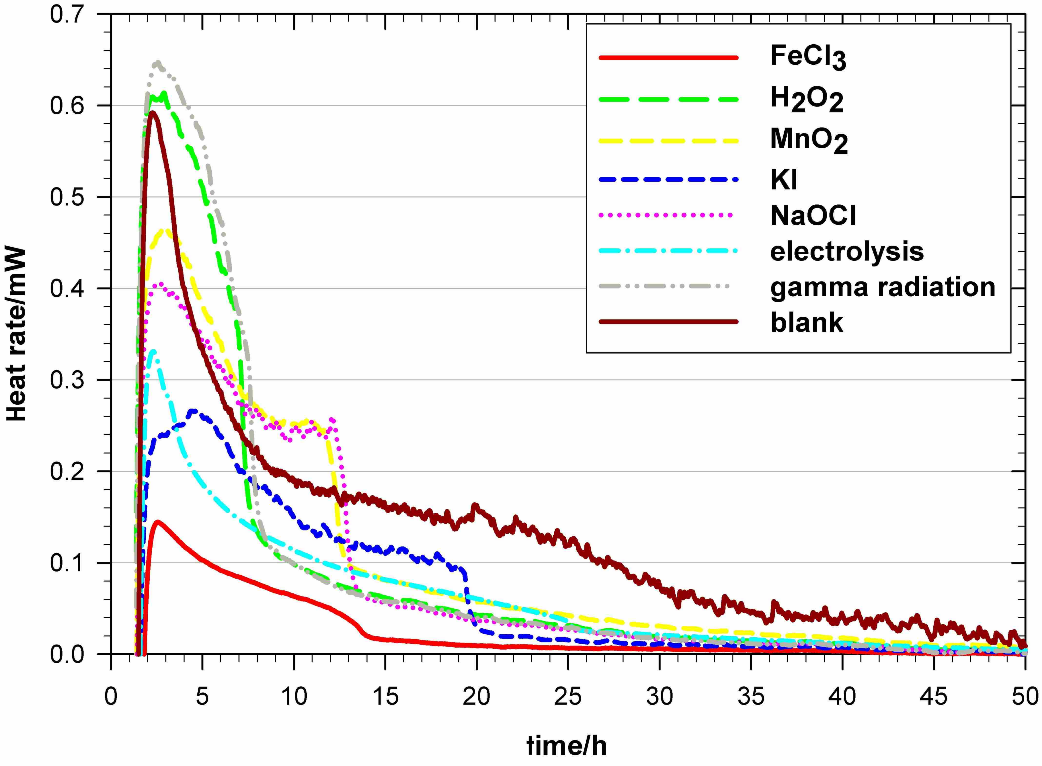

Figure 4.4: Thermograms for the reaction of algae, pretreated by a variety of techniques, reacting with a mixed culture of anaerobic bacteria obtained from an operating IBR.

4.6 Conclusions

These methods are applicable for the analysis of the breakdown rates for a wide range of pharmaceuticals, pesticides, herbicides, and halogenated organic compounds present in wastewater streams and water supplies. Measurement of metabolic rate and contaminant degradation simultaneously is an effective means of rapidly examining a complex process. The described method also allows for the rapid and quantitative evaluation of various pretreatment methods.

Chapter 5

Thermal and Photolytic Degradation of Promethazine Hydrochloride Solutions

5.1 Disclaimer

The work presented in this chapter has been submitted for publication in The International Journal of Pharmacology. It is presented in its entirety with minor changes.

5.2 Abstract

Promethazine hydrochloride is a medication that is commonly used as an antihistamine, a sedative, an antiemetic, and to treat motion sickness. Perivascular extravasation, unintentional intra-arterial injection and intraneuronal or perineuronal infiltration may lead to irreversible tissue damage if the drug is not properly diluted or is administered too quickly. Data on the stability of promethazine hydrochloride diluted in sodium chloride 0.9% are lacking. This study evaluates the thermal and photolytic degradation of promethazine hydrochloride concentrations of 250 μg/mL and 125 μg/mL diluted in sodium chloride 0.9% over a period of 9 days. Degradation rates of promethazine hydrochloride were determined under UV-light and fluorescent light and when it was protected from light at various temperatures and concentrations to determine medication stability. The shelf-life (<10% degradation) at 25°C and under normal fluorescent lights is 4.9 days, at 25°C protected from light, 6.6 days, and at 7°C in the dark, 8.1 days. These results may increase patient safety by improving current protocols for intravenous promethazine administration.

5.3 Introduction

Promethazine has a long history of being a cost effective and therapeutically efficacious medication. Promethazine possesses antihistamine, sedative, anti-motion sickness, and antiemetic effects.[127] It is most commonly used as an antiemetic but with its unique anti-histaminergic mechanism of action, it is also FDA approved for allergic conditions, motion sickness, and sedation.[127,128] Promethazine is FDA approved for oral, intramuscular, rectal, and intravenous administration, with deep intramuscular injection being preferred.[128] While being both efficacious and cost effective, injectable promethazine is also a known vesicant that is highly caustic to the vasculature and surrounding tissues.[127] Perivascular extravasation, unintentional intra-arterial injection and intraneuronal or perineuronal infiltration of promethazine may lead to irreversible tissue damage.[129] However, when properly administered, intravenous(IV) administration is well tolerated.[128] Several safety precautions concerning the administration of IV promethazine have been established by the Institute for Safe Medication Practices (ISMP) to prevent or minimize tissue damage: (1) limit the concentration available to 25 mg/mL, (2) consider limiting initial doses to 6.25–12.5 mg, (3) Further dilute the 25 mg/mL strength into 10–20 mL of normal saline and administer through a large bore vein (not hand or wrist), (4) Administer via running IV line at port farthest from patient's vein, (5) Consider administering over 10–15 min, and (6) instruct patients to immediately report signs of pain or burning.[128] The possibility of adverse events is increased when the drug is not properly diluted or is administered too quickly.

A recent case report published by the American Journal of Emergency Medicine[130] cited a cluster of three cases of promethazine-related tissue toxicity. Two cases experienced permanent complications, one with gangrene which required amputation, and the other was left with chronic pain and decreased range of motion. Failures to follow the ISMP recommendations have led to an increase in adverse outcomes for patients as well as increased litigation against physicians, hospitals, and drug companies.[130] The FDA has labeled promethazine with a black box warning based on their analysis of post-marketing reports and current prescribing information.[129] In 2006, the ISMP requested eliminating the IV route completely.[127] However, there are potential problems caused by eliminating the intravenous route; including inability to substitute for an alternative during drug shortages, inability to treat a number of FDA approved indications, safety concerns with other agents, and less efficacy of other agents.

A possible solution would be to appropriately pre-dilute promethazine injectable solution in an IV bag and make the bags readily available on hospital units. This will minimize delays in patient care and ensure that the medication is correctly diluted and appropriate for delivery via intravenous pump administered over 10–15 min.[127] This solution is currently impractical because available stability data suggests promethazine at 21°C and protected from light is only stable for up to 24 h.[131] If the actual stability is greater than 24 h, and could match the current sterility time, then compounded promethazine could warrant up to a 9 day shelf life.

According to the United States Pharmacopeia (USP) Chapter 797[132], the maximum allowed beyond use date based on sterility for promethazine stored under refrigeration is 9 days and, without refrigeration, 30 h. Some studies[133–136] have shown photodegradation and oxidative degradation to be slower than the study[131] claiming only 24 h of stability, but these studies were performed at non-ideal hospital conditions, i.e. low pH, high temperatures, and additional chemicals. The purpose of this study is to determine the rate of degradation of promethazine hydrochloride diluted in sodium chloride(0.9% by both chemical and photolytic reactions over a period of nine days permitted by lack of bacterial growth at conditions that may be encountered in a hospital.

5.4 Materials and Methods

Promethazine hydrochloride (98% powder) was purchased from Sigma Aldrich (Lot : #129K1789V St. Louis, MO) and was used without further purification. Additionally, promethazine HCl 1-mL injection samples were obtained from Amerinet Choice at USP (25 mg/mL, Lot: 010335z

NDC 10019-097-01, St. Louis, MO). Saline solution (0.9 % in 100 mL PVC bags) was obtained from Braun, Bethlehem, PA.

Solutions of promethazine hydrochloride in sodium chloride (0.9 %) were prepared at 250 μg/mL from 98% solid promethazine hydrochloride. Two 20-mL aliquots of the 250 μg/mL solution were sealed under air in 30-mL serum bottles with double-crimped seals for isothermal calorimetric measurements at 37°C in an isothermal microcalorimeter from Calorimetry Sciences, Lindon, UT (Model # 5024, S/N 102). Thirty-two 2-mL aliquots of the 250 μg/mL solution were sealed in 5-mL glass vials to be assayed over time after exposure to various conditions. 8 vials were held under normal fluorescent lighting at room temperature, 8 vials were kept in the dark at room temperature, 8 vials were kept in the dark at 7°C, and 8 vials were kept at room temperature under UV lamps (0.83 mW/cm^2, 350–400 nm with peak radiation at 368 nm). For the first 3 days, samples were analyzed every 8 to 14 h and daily thereafter for 5 days. Five replicate analyses were done on each vial. An additional 250 μg/mL solution in 0.9% sodium chloride was prepared from 1-mL injection samples protected from light and stored at 7°C. At 12 h intervals over 10 days, two 0.6-mL aliquots were removed and immediately placed in a freezer below 0°C. These samples were thawed and analyzed after 10 weeks of storage. Additional solutions of 250 μg/mL and 125 μg/mL were prepared in PVC bags of 0.9% sodium chloride stored at 25°C protected from light to determine if degradation rates were concentration dependent. These solutions were maintained at room temperature wrapped in amber bags to protect them from light.

Although previous studies[133–138] of degradation of promethazine were performed with HPLC, sample analysis using capillary electrophoresis substantially reduced analysis time with no loss in precision or detection limit compared with HPLC. Capillary electrophoresis instruments began to be commercialized in the early 2000s and are now common instruments in analytical laboratories where they may replace HPLC. Solutions were analyzed by capillary zone electrophoresis, CZE[139], with a UV-vis absorption detector and 31 cm capillary cooled with a perfluoro-n-alkyl morpholine solution (Beckman Coulter P/ACE MDQ Capillary

Electrophoresis System, S/N 967742, Brea, CA). The UV-vis absorption detector measures absorption from 220 to 350 nm resulting in 3 parameters: migration time, absorption, and wavelength. Multidimensionality of the data facilitates discovery of co-eluting species. The spectral data confirmed that no degradation products co-eluted and thus interfered with the promethazine determination. The separation buffer was 0.4% boric acid and 0.3% sodium borate. Separations were done at 30 kV with an injection time of 0.3 s at 0.5 psi. The sample eluted from the capillary in 4 min. Caffeine was used as an internal standard in each sample. The linear dynamic range of the calibration curve was 25 to 487 μg/mL promethazine.

To determine the products of photolysis, 100 mL of a 1 g/L promethazine hydrochloride solution in water was photolyzed for three days with a 450 W mercury arc immersion lamp (Hanova 451-050). Water was removed from the resulting purple slurry with a rotary vacuum evaporator, and the product characterized by proton NMR, diffuse reflectance IR, and UV-vis spectrophotometry.

5.5 Results

Calorimetrically measured heat rates were less than 2 μW (i.e., less than the detection limit), indicating no measurable rate of oxidation under air in the dark at 37°C. By Thornton's rule (455 kJ/mol O_2), the rate of oxygen uptake was less than 0.2 μmol of oxygen per day or the rate of oxidation of promethazine was less than 2% per day.

Degradation rates measured by CZE are given in Table 5.1. The degradation rate of promethazine is constant with time and showed no dependency on concentration. As expected, increasing temperature and light showed small, but significant, increases in the degradation rate. Frozen solutions exhibited no evidence of degradation over ten weeks. Comparing the degradation rates of solutions that were prepared and then aged followed by immediate analysis (Table 5.1, experiment 4) to samples that were prepared, aged and then frozen for future analysis (Table 5.1, experiment 5) showed no statistical difference in their degradation rates.

Table 5.1: Degradation rates of promethazine.

Experiment #	Conditions	Decay rate/% per day
1	25 °C, fluorescent lighting, 250 μg/mL, glass	2.04±0.20
2	37 °C, dark, 250 μg/mL, glass	<2
3	25 °C, dark, 250 μg/mL, glass	1.52±0.16
4	7 °C, dark, 250 μg/mL, glass	1.24±0.36
5	7 °C, dark, then frozen, 250 μg/mL, amber bag	1.44±0.40
6	25 °C, dark, 250 μg/mL, amber bag	2.28±0.51
7	25 °C, dark, 125 μg/mL, amber bag	2.39±0.18

uncertainties are given as the 95% confidence interval

Figure 5.1 shows the rate of degradation in glass vials at room temperature under intense UV light. The decay is first order in promethazine concentration with a rate constant of 9.7 x 10^{-6} s^{-1}. The NMR spectrum of promethazine has peaks centered at 7.25, 7.03, 4.75, 3.91, 3.75, 2.77, and 1.52 ppm. The NMR spectrum of promethazine photodegradation products has peaks similar to those in the spectrum of pure promethazine (7.24, 7.04, 4.71, 3.94, 3.72, 2.75, and 1.51 ppm) along with an additional peak at 5.30 ppm. The peaks at 7.24 and 7.04 ppm have significantly larger relative areas (5.69 and 5.09, respectively) and a different ratio, 1.1, compared with the pure promethazine peaks (4.30 and 3.84, respectively, and a ratio of 1.2). The diffuse reflectance IR spectrum of promethazine has a prominent feature at 2550 cm^{-1} with a small shoulder peak centered at 2400 cm^{-1}. These two transitions are characteristic of an aromatic sulfur stretch (ArS) and a sulfhydryl stretch (SH), respectively. The IR spectrum of the photodegradation product has two similar transitions, but the 2550 cm^{-1} transition has shifted to 2500 cm^{-1} and decreased in intensity.

The NMR spectra of promethazine and the photodegradation products are similar except for the additional peak at 5.30 ppm in the spectrum of the photodegradation product that corresponds to a sulfhydryl group. The peaks centered at 7.24 and 7.04 ppm in each spectrum are larger in the spectrum of the photodegradation products indicating gain of an aromatic hydrogen. The IR spectra also demonstrate a loss in Ar-S intensity and a gain in S-H intensity. From these observations we conclude that the dominant photodegradation product is from cleavage of one of the aromatic sulfur bonds with formation of a sulfhydryl group. These structures are shown in Figure 5.2.

5.6 Discussion

The results indicate that the oxidation rate of promethazine hydrochloride in 0.9% sodium chloride protected from light at 375.1C is less than 2% per day. Decreasing storage temperature in the dark causes a small decrease in the oxidation rate while normal fluorescent lighting causes a small increase in the degradation rate. UV light is responsible for the majority of

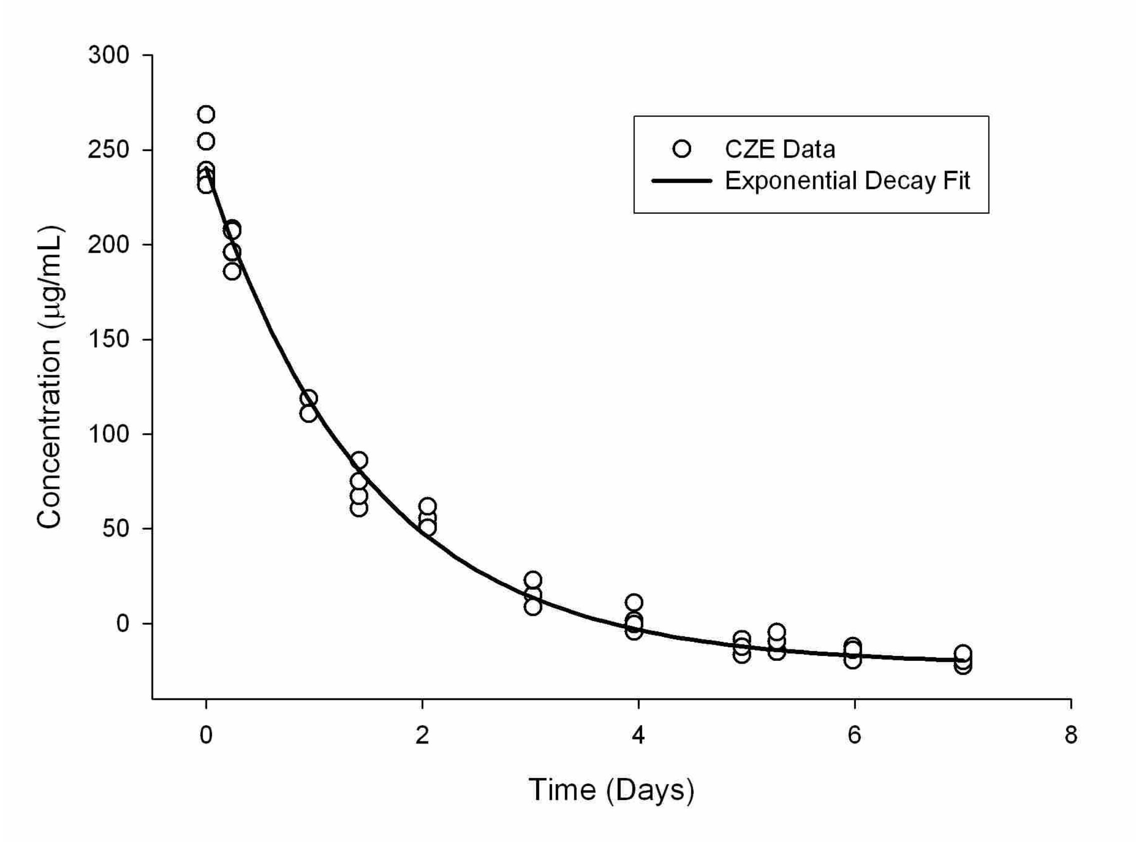

Figure 5.1: Exponential decay of promethazine under UV-light, 350–400 nm, 0.83 mW cm^{-2}.

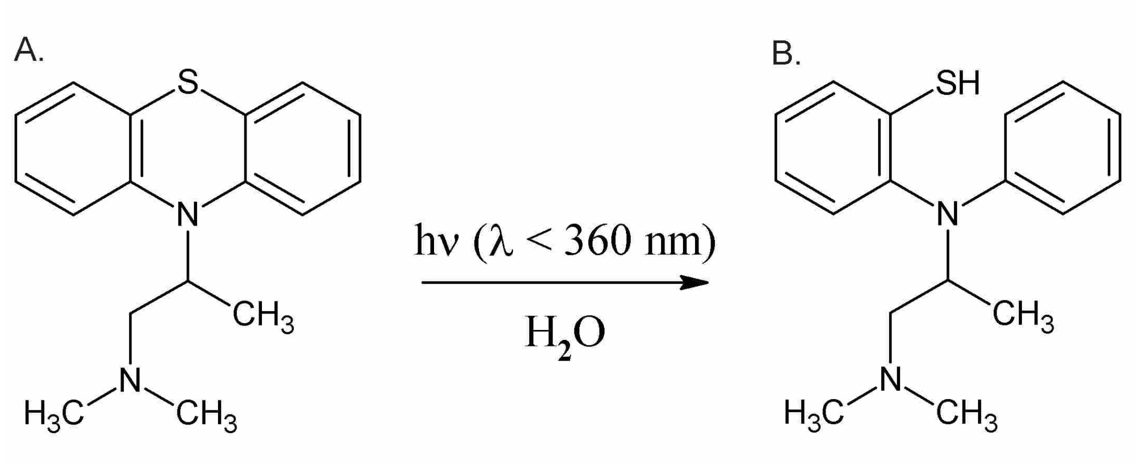

Figure 5.2: Proposed reaction scheme for photolytic degradation of promethazine to a 2-benzenethiol.

degradation because the oxidation rate is comparatively very slow. UV light rapidly degrades promethazine, and the use of techniques to limit UV light exposure during preparation will prolong shelf-life.

The UV spectrum of promethazine has two broad absorption features: one centered at 210 nm and the other with a broad maximum from 280 to 320 nm. Light at wavelengths shorter than 260 nm causes degradation toward the product shown in Figure 5.2. The structural data indicate the degradation mechanism is photolysis/hydrolysis to a structure with a free sulfhydryl group which is susceptible to oxidation to a dimer joined with a disulfide bond. The oxidation mechanism in the dark is more complicated than photolysis but produces a drastically different product as reported elsewhere.[138] Previous work[135] on the degradation of promethazine under intense UV light did not publish a rate or the concentrations used but showed a 90% decrease in promethazine after 1.5–2.5 days in pH 5 whereas under similar conditions a 90% loss occurred after 3 days in pH 7 buffer. Data in the previous study[135] show a decreasing rate of decomposition with increasing pH which can be extrapolated to pH 7 to match the degradation rate found in this work. Additionally, the experiments reported earlier[128] determined the oxidation rate at temperatures exceeding 60°C, where the half-life at pH 5 is 55 h. The half-life reported here at room temperature is substantially longer as expected. No literature on the effects of promethazine photodegradation/oxidation products on biological systems is available.

The most significant result for the pharmaceutical and medical community is the approximate shelf-life of promethazine under these different conditions. The degradation rate is concentration independent, and promethazine solutions can be stored indefinitely if kept frozen in the dark. Explicit studies were not performed to determine degradation in frozen states, but the degradation rates of the two cold, dark experiments were the same even though one experiment analyzed samples immediately and the other were frozen for several weeks.

That promethazine breaks down by a photolytic reaction rather than oxidation is shown by the analysis of promethazine under different environmental conditions. When protected from light, the amount of time to a 10% loss in drug concentration at room temperature is approximately 6.6 d, whereas when exposed to light that resembles conditions of day to day hospital practice, the time to 10% drug loss drops to 4.9 d. Promethazine was proven to be most stable (8.1 d to 10% drug loss) when stored under refrigeration at 5 ± 3°C and protected from light. These conditions could be mimicked in a hospital setting by storing promethazine solutions in an amber bag in a refrigerator. The increased length of stability that this research found allows sufficient time to batch promethazine in an IV preparation room, store it on the floors in an amber bag under refrigeration, and administer it when needed via an intravenous pump. This would decrease the chance of tissue damage due to extravasation. Also, samples could be frozen and thawed when needed.

5.7 Conclusions

The data from this study show that solutions can be stored in amber bags at room temperature for 4 d and in a refrigerator for 8 d. It is not the intention of this research to guide drug therapy, but only to provide stability information that is currently unavailable. This long term stability data will allow for the possibility that pre-diluted promethazine bags can be provided in hospital unit refrigerators for immediate and safe administration.

Chapter 6

Summary

This dissertation is written to present several studies related to the fields of environmental and atmospheric chemistry. The first portion outlines the motives for probing the water vapor dependence on important atmospheric reactions and present the results of a series of experiments designed to measure this effect. The β-HEP self-reaction results, combined with the work from Butkovskaya[57] on water enhancement of HO_2 + NO, provides motivation for further investigation into the effects of water on other peroxy radical reactions. Investigation should focus on reactions important in atmospheric chemistry and include radicals that form strong complexes with water, e.g., peroxy radical derivatives of terpenes and isoprene.[58]. Subsequent work in the Hansen group will study the cross reaction of β-HEP and HO_2 as well as changes to the product branching ratio of β-HEP + NO in the presence of water. As evidenced from the work of Stockwell[56], small changes in the reaction rates of HO_2 lead to dramatic differences in predicted and measured HO_2 concentrations. To correctly predict pollution levels, atmospheric models need to be adjusted to include the rate enhancements demonstrated in this work. The implications of these findings promote the path of further discovery of peroxy radical self-reaction and cross reaction enhancements through the formation of pre-reactive complexes between radicals and polar molecules such as water, methanol, and ammonia. Furthermore, water vapor catalysis will become increasingly more significant in light of global warming inducing increased water vapor concentrations in the troposphere.

The new analysis of anaerobic digestion performance through calorimetric methods is applicable for the analysis of the breakdown rates for a wide range of pharmaceuticals, pesticides, herbicides, and halogenated organic compounds present in waste water streams and water supplies. Measurement of metabolic rate and contaminant degradation simultaneously is an effective means of rapidly examining a complex process. The described method also allows for the rapid and quantitative evaluation of various pretreatment methods. Current research in the Hansen lab uses these techniques to study breakdown of cellulose and lignin-cellulose by the photo-active catalyst TiO_2 as a pre-treatment method. These techniques lead to the discovery of more efficient methods of harnessing renewable energy from organic waste.

Degradation rates of promethazine hydrochloride were determined under UV-light and fluorescent light, and when protected from light at various temperatures and concentrations to determine medication stability. The shelf-life (<10% degradation) at 25°C under normal fluorescent lights is 4.9 d, at 25°C protected from light, 6.6 d, and at 7°C in the dark, 8.1 d. These results may increase patient safety by improving current protocols for intravenous promethazine administration. It is recommended that solutions may be stored in amber bags at room temperature for up to 4 d and in a refrigerator for up to 8 d. The long term stability data presented will allow for the possibility that pre-diluted promethazine bags can be provided in hospital unit refrigerators for immediate and safe administration, reducing both risk to patients and overall hospital waste.

References

[1] Leighton, P. A. In *Photochemistry of Air Pollution*; Hutchinson, E., Van Rysselberghe, P., Eds.; Academic Press New York and London, 1961.

[2] Finlayson-Pitts, B. J.; Pitts, J. N. J. *Chemistry of the Upper and Lower Atmosphere: Theory, Experiments and Apllications*; Academic Press: San Diego, 2000.

[3] Crosley, D. *Journal of Atmospheric Science* **1995**, *52*, 3299–3314.

[4] Schonbein, C. *Ber. Verh. Nat. Ges. Basel* **1840**, *4*, 58.

[5] Leeds, A. *Annals of the New York Academy of Sciences* **1880**, *3*, 363–391.

[6] Andrews, T. *Annales de Chimie et de Physique* **1868**, *13*, 474–477.

[7] Schonbein, C. *Ber. Verh. Nat. Ges. Basel* **1849**, *8*, 4–5.

[8] Cornu, M. *Comptes Rendus* **1879**, *88*, 1101–1108.

[9] Hartley, W. *Chemical News* **1880**, *Nov. 26*, 268.

[10] Fabry, C.; Buisson, H. *Journal de Physique* **1913**, *5*, 196–206.

[11] Strutt, R. *Proceedings of the Royal Society of London* **1918**, *94*, 260–268.

[12] Wallington, T. J.; Dagaut, P.; Kurylo, M. J. *Chemical Reviews* **1992**, *92*, 667–710.

[13] Haagen-Smit, A. *Industrial and Engineering Chemistry Research* **1952**, *44*, 1342–1346.

[14] Haagen-Smit, A.; Bradley, C.; Fox, M. *Industrial & Engineering Chemistry Research* **1953**, *45*, 2086–2089.

[15] Marshall, A. *The Journal of Physical Chemistry* **1926**, *30*, 1078–1099.

[16] Foner, S.; Hudson, R. *The Journal of Chemical Physics* **1953**, *21*, 1608–1609.

[17] Rubin, M. B. *Bulletin for the History of Chemistry* **2001**, *26*, 40–56.

[18] Monks, P. *Chemical Society Reviews* **2005**, *34*, 376–395.

[19] Creasy, D. J.; Evans, G. E.; Heard, D. E.; Lee, J. D. *Journal of Geophysical Research* **2003**, *108*, 4475.

[20] Monks, P. S. *Chemical Society Reviews* **2005**, *34*, 376–395.

[21] Roehl, C. M.; Orlando, J.; Tyndall, G.; Shetter, R.; Vasquez, G.; Cantrell, C.; Calvert, J. *The Journal of Physical Chemistry* **1994**, *98*, 7837–7843.

[22] Wayne, R.; Barnes, I.; Biggs, P.; Burrows, J.; Canosa-Mas, C.; Hjorth, J.; Lebras, G.; Moortgat, G. K.; Perner, D.; Poulet, G.; Restelli, G.; Sidebottom, H. *Atmospheric Environment* **1991**, *25A*, 1–203.

[23] Orlando, J.; Tyndall, G. *Chemical Society Reviews* **2012**, *41*, 6294–6317.

[24] DeSain, J.; Ho, A.; Taatjes, C. *Journal of Molecular Spectroscopy* **2003**, *219*, 163–169.

[25] Taatjes, C.; Oh, D. *Applied Optics* **1997**, *36*, 5817–5821.

[26] Christensen, L.; Okumura, M.; Sander, S.; Freidl, R.; Miller, C.; Sloan, J. *The Journal of Physical Chemistry A* **2004**, *108*, 80–91.

[27] Christensen, L.; Okumura, M.; Hansen, J.; Sander, S.; Francisco, J. *The Journal of Physical Chemistry A* **2006**, *110*, 6948–6959.

[28] Noell, A.; Alconcel, L.; Robichaud, D.; Okumura, M.; Sander, S. *The Journal of Physical Chemistry A* **2010**, *114*, 6983–6995.

[29] Grieman, F.; Noell, A.; Van-Atta, C.; Okumura, M.; Sander, S. *The Jounral of Physical Chemistry A* **2011**, *115*, 10527–10538.

[30] Friedrichs, G. *Zeitschrift fur Physikalische Chemie* **2008**, *222*, 1–30.

[31] Avetisov, V.; Kauranen, P. *Applied Optics* **1996**, *35*, 4705–4723.

[32] D'Amato, F.; DeRosa, M. *Optics and Lasers in Engineering* **2002**, *37*, 533–551.

[33] Johnson, T.; Wienhold, F.; Burrows, J.; Harris, G. W. *Journal of Physical Chemistry* **1991**, *95*, 6499–6502.

[34] Janik, G.; Carlisle, C.; Gallagher, T. *Journal of The Optics Society of America* **1986**, *3*, 1070–1074.

[35] Thiebaud, J.; Fittschen, C. *Applied Physics B: Lasers and Optics* **2006**, *85*, 383–389.

[36] Ibrahim, N.; Thiebaud, J.; Orphal, J.; Fittschen, C. *Journal of Molecular Spectroscopy* **2007**, *242*, 64–69.

[37] Mazurenka, M.; Orr-Ewing, A.; Peverall, R.; Ritchie, G. *Annual Reports on the Progress of Chemistry, Section C: Physical Chemistry* **2005**, *101*, 100.

[38] Paldus, B.; Kachanov, A. *Canadian Journal of Physics* **2005**, *83*, 975.

[39] Berden, G.; Peeters, R.; Meijer, G. *International Review of Physcial Chemistry* **2000**, *19*, 565.

[40] Brown, S. *Chemical Reviews* **2003**, *103*, 5219.

[41] Pushkarsky, M.; Zalubovsky, S.; Miller, T. *Journal of Chemical Physics* **2000**, *112*, 10695–10698.

[42] Atkinson, D.; Spillman, J. *The Journal of Physical Chemistry A* **2002**, *106*, 8891–8902.

[43] Gu, G.; Adler, R. *International Journal of Climatology* **2011**, *32*, 1782–1791.

[44] Du, J.; Cooper, F.; Fueglistaler, S. *Journal of Geophysical Research* **2012**, *117*, 1–10.

[45] Hamilton, E. J. *Journal of Chemical Physics* **1975**, *63*, 3682–3683.

[46] Cox, R. A.; Burrows, J. P. *Journal of Physical Chemistry* **1979**, *83*, 2560–2568.

[47] Demore, W. B. *Journal of Physical Chemistry* **1979**, *83*, 1113–1118.

[48] Hamilton, E. J.; Lii, R. R. *International Journal of Chemical Kinetics* **1977**, *9*, 875–885.

[49] Kircher, C. C.; Sander, S. P. *Journal of Physical Chemistry* **1984**, *88*, 2082–2091.

[50] Lii, R. R.; Gorse, R. A.; Sauer, M. C.; Gordon, S. *Journal of Physical Chemistry* **1980**, *84*, 813–817.

[51] Sander, S. P.; Peterson, M.; Watson, R. T.; Patrick, R. *Journal of Physical Chemistry* **1982**, *86*, 1236–1240.

[52] Kanno, N.; Tonokura, K.; Tezaki, A.; Koshi, M. *Journal of Physical Chemistry A* **2005**, *109*, 3153–3158.

[53] Tang, Y. X.; Tyndall, G. S.; Orlando, J. J. *Journal of Physical Chemistry A* **2010**, *114*, 369–378.

[54] Stone, D.; Rowley, D. M. *Physical Chemistry Chemical Physics* **2005**, *7*, 2156–2163.

[55] Suma, K.; Sumiyoshi, Y.; Endo, Y. *Science* **2006**, *311*, 1278–1281.

[56] Stockwell, W. R. *Journal of Geophysical Research-Atmospheres* **1995**, *100*, 11695–11698.

[57] Butkovskaya, N.; Rayez, M. T.; Rayez, J. C.; Kukui, A.; Le Bras, G. *Journal of Physical Chemistry A* **2009**, *113*, 11327–11342.

[58] Clark, J.; English, A. M.; Hansen, J. C.; Francisco, J. S. *Journal of Physical Chemistry A* **2008**, *112*, 1587–1595.

[59] Hansen, J. C.; Francisco, J. S. *Chemphyschem* **2002**, *3*, 833–840.

[60] Kramer, Z. C.; Takahashi, K.; Skodje, R. T. *Journal of the American Chemical Society* **2010**, *132*, 15154–15157.

[61] Vaida, V. *Journal of Chemical Physics* **2011**, *135*, 8.

[62] Sennikov, P. G.; Ignatov, S. K.; Schrems, O. *Chemphyschem* **2005**, *6*, 392–412.

[63] Staikova, M.; Donaldson, D. J. *Physics and Chemistry of the Earth Part C-Solar-Terrestial and Planetary Science* **2001**, *26*, 473–478.

[64] English, A. M.; Hansen, J. C.; Szente, J. J.; Maricq, A. M. *Journal of Physical Chemistry A* **2008**, *112*, 9220–9228.

[65] Aloisio, S.; Francisco, J. S. *Journal of Physical Chemistry A* **1998**, *102*, 1899–1902, Aloisio, S Francisco, JS.

[66] Sawada, S.; Totsuka, T. *Atmospheric Environment* **1986**, *20*, 821–832.

[67] Murrells, T. P.; Jenkin, M. E.; Shalliker, S. J.; Hayman, G. D. *Journal of the Chemical Society-Faraday Transactions* **1991**, *87*, 2351–2360.

[68] Bauer, D.; Crowley, J. N.; Moortgat, G. K. *Journal of Photochemistry and Photobiology A-Chemistry* **1992**, *65*, 329–344.

[69] Jenkin, M. E.; Cox, R. A. *Journal of Physical Chemistry* **1991**, *95*, 3229–3237.

[70] Jenkin, M. E.; Hayman, G. D. *Journal of the Chemical Society-Faraday Transactions* **1995**, *91*, 1911–1922.

[71] Jenkin, M. E.; Hurley, M. A.; Wallington, T. J. *Journal of Physical Chemistry A* **2010**, *114*, 408–416.

[72] Anastasi, C.; Muir, D. J.; Simpson, V. J.; Pagsberg, P. *Journal of Physical Chemistry* **1991**, *95*, 5791–5797.

[73] Lightfoot, P. D.; Cox, R. A.; Crowley, J. N.; Destriau, M.; Hayman, G. D.; Jenkin, M. E.; Moortgat, G. K.; Zabel, F. *Atmospheric Environment Part A-General Topics* **1992**, *26*, 1805–1961.

[74] Vohringer-Martinez, E.; Hansmann, B.; Hernandez, H.; Francisco, J. S.; Troe, J.; Abel, B. *Science* **2007**, *315*, 497–501.

[75] Gerber, R. B.; McCoy, A. B.; Garciavela, A. *Annual Review of Physical Chemistry* **1994**, *45*, 275–314.

[76] Bogumil, K.; Orphal, J.; Hormann, J.; Voigt, S.; Speitz, P.; Fleischmann, O.; Vogel, A.; Hartmann, M.; Kromminga, H.; Bovensmann, H.; Frerick, J. *Journal of Photochemistry and Photobiology A-Chemistry* **2003**, *157*, 2–3.

[77] Crowley, J.; Simon, F.; Burrows, J.; Moortgat, G.; Jenkin, M.; Cox, R. *Journal of photochemistry and photobiology A-Chemistry* **1991**, *60*, 1–10.

[78] Keller-Rudek, H.; Moortgat, G. *MPI-Mainz-UV-Vis Spectral Atlas of Gaseous Molecules*; Max-Planck Intitut fur chemie, Atmospheric Chemistry Division, 2013.

[79] Rothman, L. S. et al. *Journal of Quantitative Spectroscopy and Radiative Transfer* **2009**, *110*, 533–572.

[80] Boyd, A. A.; Lesclaux, R. *International Journal of Chemical Kinetics* **1997**, *29*, 323–331.

[81] Orlando, J. J.; Tyndall, G. S.; Bilde, M.; Ferronato, C.; Wallington, T. J.; Vereecken, L.; Peeters, J. *Journal of Physical Chemistry A* **1998**, *102*, 8116–8123.

[82] Grotheer, H.; Reiekeryt, G.; Meier, U.; Just, T. *Physical chemistry chemical physics* **1985**, *89*, 187–191.

[83] Hintsa, E. J.; Zhao, X. S.; Lee, Y. T. *Journal of Chemical Physics* **1990**, *92*, 2280–2286.

[84] Atkinson, R.; Baullch, D.; Cox, R.; Crowley, J.; Hampson, R.; Kerr, J.; Rossi, M.; Troe, J. **2001**, 1–56.

[85] Atkinson, R.; Baulch, D. L.; Cox, R. A.; Crowley, J. N.; Hampson, R. F.; Hynes, R. G.; Jenkin, M. E.; Rossi, M. J.; Troe, J. *Atmospheric Chemistry and Physics* **2007**, *7*, 981–1191.

[86] Sander, S. P.; Friedll, R. R.; Golden, D. M.; Kurylo, M. J.; Moortgat, G. K.; Keller-Rudek, H.; Wine, P. H.; Ravishankara, A. R.; Kolb, C. E.; Molina, M. J.; Finlayson-Pitts, B. J.; Huie, R. E.; Orkin, V. L. *Chemical kinetics and photochemical data for use in atmospheric studies*; 2006; Vol. JPL 06-2.

[87] Caralp, F.; Forst, W.; Rayez, M. T. *Physical Chemistry Chemical Physics* **2003**, *5*, 476–486.

[88] Frisch, M. J. et al. Gaussian 03, Revision C.02. Gaussian, Inc., Wallingford, CT, 2004.

[89] Clark, J.; Call, S.; Austin, D.; Hansen, J. *Journal of Physical Chemistry A* **2010**, *114*, 6534–6541.

[90] McQuarrie, D.; Simon, J. *Physical Chemistry: A Molecular Approach*; University Science Books, 1997.

[91] McClurg, R.; Flagan, R.; Goddard, W. *Journal of Chemical Physics* **1997**, *106*, 6675–6680.

[92] Curtiss, L.; Raghavachari, K.; Redfern, P.; Rassolov, V.; Pople, J. A. *The Journal of Chemical Physics* **1998**, *109*, 7764–7777.

[93] M., M.; Benson, S. *International Journal of Chemical Kinetics* **1985**, *17*, 787–807.

[94] Lesclaux, R. In *Peroxy Radicals*; Alfassi, Z., Ed.; John Wiley and Sons, 1997.

[95] Wallington, T.; Nielsen, O.; Sehested, J. In *Peroxy Radicals*; Alfassi, Z., Ed.; John Wiley and Sons, 1997.

[96] Pitts, J. N.; Chan, S. I.; Sharp, J. H. *Journal of Chemical Physics* **1964**, *40*, 3655–3665.

[97] Lee, E. K. C.; Uselman, W. M. *Faraday Discussions* **1972**, *53*, 125–131.

[98] Uselman, W. M.; Lee, E. K. C. *Chemical Physics Letters* **1975**, *30*, 212–214.

[99] Gelbwach.Ja,; Birnbaum, M.; Fincher, C. L.; Tucker, A. W. *Journal of the Optical Society of America* **1972**, *62*, 1368–1368.

[100] Neuburger, D.; Duncan, A. *Journal of Chemical Physics* **1975**, *22*, 208.

[101] Parra, J.; George, L. A. *Applied Optics* **2009**, *48*, 3355–3361.

[102] Paech, F.; Schmiedl, R.; Demtroder, W. *Journal of Chemical Physics* **1975**, *63*, 4369–4378.

[103] Solarz, R.; Levy, D. H. *Journal of Chemical Physics* **1974**, *60*, 842–845.

[104] Creel, C. L.; Ross, J. *Journal of Chemical Physics* **1976**, *64*, 3560–3566.

[105] Thorton, J.; Wooldridge, P.; Cohen, R. C. *Analytical Chemistry* **2000**, *72*, 528.

[106] Day, D. A.; Wooldridge, P. J.; Dillon, M. B.; Thornton, J. A.; Cohen, R. C. *Journal of Geophysical Research-Atmospheres* **2002**, *107*, 14.

[107] Dari-Salisburgo, C.; Di Carlo, P.; Giammaria, F.; Kajii, Y.; D'Altorio, A. *Atmospheric Environment* **2009**, *43*, 970–977.

[108] Friedrichs, G.; Fikri, M.; Guo, Y.; Temps, F. *Journal of Physical Chemistry A* **2008**, *112*, 5636–5646.

[109] Paldus, B.; Zare, R. In *Absorption Spectroscopies: from early beginnings to cavity-ring down spectroscopy*; Paldus, B., Zare, R., Eds.; Oxford University Press, 1997.

[110] Busch, K.; Busch, M. In *Introduction to Cavity Ringdown Spectroscopy*; Busch, K., Busch, M., Eds.; Oxford University Press, 1999.

[111] Thompson, J. E.; Smith, B. W.; Winefordner, J. D. *Analytical Chemistry* **2002**, *74*, 1962–1967.

[112] Brown, S. S.; Stark, H.; Ravishankara, A. R. *Applied Physics B-Lasers and Optics* **2002**, *75*, 173–182.

[113] Brand, J. C. D.; Cawthon, T. M. *Journal of the American Chemical Society* **1955**, *77*, 319–323.

[114] Bruns, E. A.; Perraud, V.; Zelenyuk, A.; Ezell, M. J.; Johnson, S. N.; Yu, Y.; Imre, D.; Finlayson-Pitts, B. J.; Alexander, M. L. *Environmental Science & Technology* **2010**, *44*, 1056–1061.

[115] Cline, T.; Thomas, N.; Shumway, L.; Yeung, I.; Hansen, C. L.; Hansen, L.; Hansen, J. *Bioresource Technology* **2010**, *101*, 8623–8626.

[116] Harrad, S. J.; Sewart, A. P.; Alcock, R.; Boumphrey, R.; Burnett, V.; Duartedavidson, R.; Halsall, C.; Sanders, G.; Waterhouse, K.; Wild, S. R.; Jones, K. C. *Environmental Pollution* **1994**, *85*, 131–146.

[117] Hansen, C., C.L. Hansen Induced sludge bed anaerobic reactor. 2005.

[118] Dustin, J. Fundamentals of operation of the induced bed reactor (IBR) anaerobic digester. Ph.D. thesis, 2010.

[119] Battersby, N. S.; Wilson, V. *Applied and Environmental Microbiology* **1989**, *55*, 433–439.

[120] Lin, J. G.; Ma, Y. S.; Chao, A. C.; Huang, C. L. *Bioresource Technology* **1999**, *68*, 187–192.

[121] Wang, J. L.; Chen, L. J.; Shi, H. C.; Qian, Y. *Chemosphere* **2000**, *41*, 1245–1248.

[122] Semple, K. T.; Reid, B. J.; Fermor, T. R. *Environmental Pollution* **2001**, *112*, 269–283.

[123] Ince, O.; Ince, B. K.; Yenigun, O. *Journal of Chemical Technology and Biotechnology* **2001**, *76*, 573–578.

[124] Franson, M. *Standard Methods for the Examination of Water and Wastewater.*, 21st ed.; American Water Works Association and Water Environment Federation, 2005.

[125] Cheong, D. Studies of High Rate Anaerobic Bio-conversion Technology For Energy Production During Treatment of High Strength Organic Wastewaters. Ph.D. thesis, 2005.

[126] Agency, U. E. P. Priority Pollutants. 2010.

[127] Practices, I. f. S. M. *Medication Safety Alert Action Needed to Prevent Serious Tissue Injury with IV Promethazine*; 10 Aug 2006.

[128] Baxter, Phenergan (Promethazine Hydrochloride) injection, soultion. 2009.

[129] Food,; Administration, D. Severe Tissue Injury with IV Promethazine. 2008.

[130] Paula, R.; Peckler, B.; Nguyen, M. Catastrophic complications of intravenous promethazine. 2010.

[131] Martens, H. J.; Degoede, P. N.; Vanloenen, A. C. *American Journal of Hospital Pharmacy* **1990**, *47*, 369–373.

[132] Formulary, T. U. S. P.; National, USP31-NF26. 2007.

[133] Stevens, J.; Meakin, B. J.; Davies, D. J. G. *Journal of Pharmacy and Pharmacology* **1972**, *24*, P133–&.

[134] Peek, B. T.; Webster, K. D.; da Camara, C. C. *American Journal of Health-System Pharmacy* **1999**, *56*, 1835–1838.

[135] Stavchansky, S.; Wallace, J. E.; Wu, P. *Journal of Pharmaceutical Sciences* **1983**, *72*, 546–548.

[136] Underberg, W. J. M. *Journal of Pharmaceutical Sciences* **1978**, *67*, 1128–1131.

[137] Meakin, B. J.; Davies, D. J. G.; Cox, N.; Stevens, J. *Analyst* **1976**, *101*, 720–727.

[138] Underberg, W. J. M. *Journal of Pharmaceutical Sciences* **1978**, *67*, 1133–1138.

[139] Pazourek, J.; Revilla, A. L.; Gajdogova, D.; Havel, J. *Drug Development and Industrial Pharmacy* **2004**, *30*, 125–134.

Chapter 7

Appendix

7.1 Experimental Instructions and LabVIEW Code

Operation of Slow-Flow Flash Photolysis System

The following instructions are for use of equipment and wiring diagrams to facilitate changes for future experiments. LabVIEW instructions are meant for those with at least an introductory knowledge of virtual instruments.

7.2 Andor SOLIS Software

Andor SOLIS is the operating software for the spectrograph built by Andor. SOLIS has many capabilities to perform experiments independently but more complicated experiments for radical experiments require the use of LabVIEW. The Andor software is still needed to set parameters for wavelength collection while LabVIEW is used for acquisition timings and data averaging.

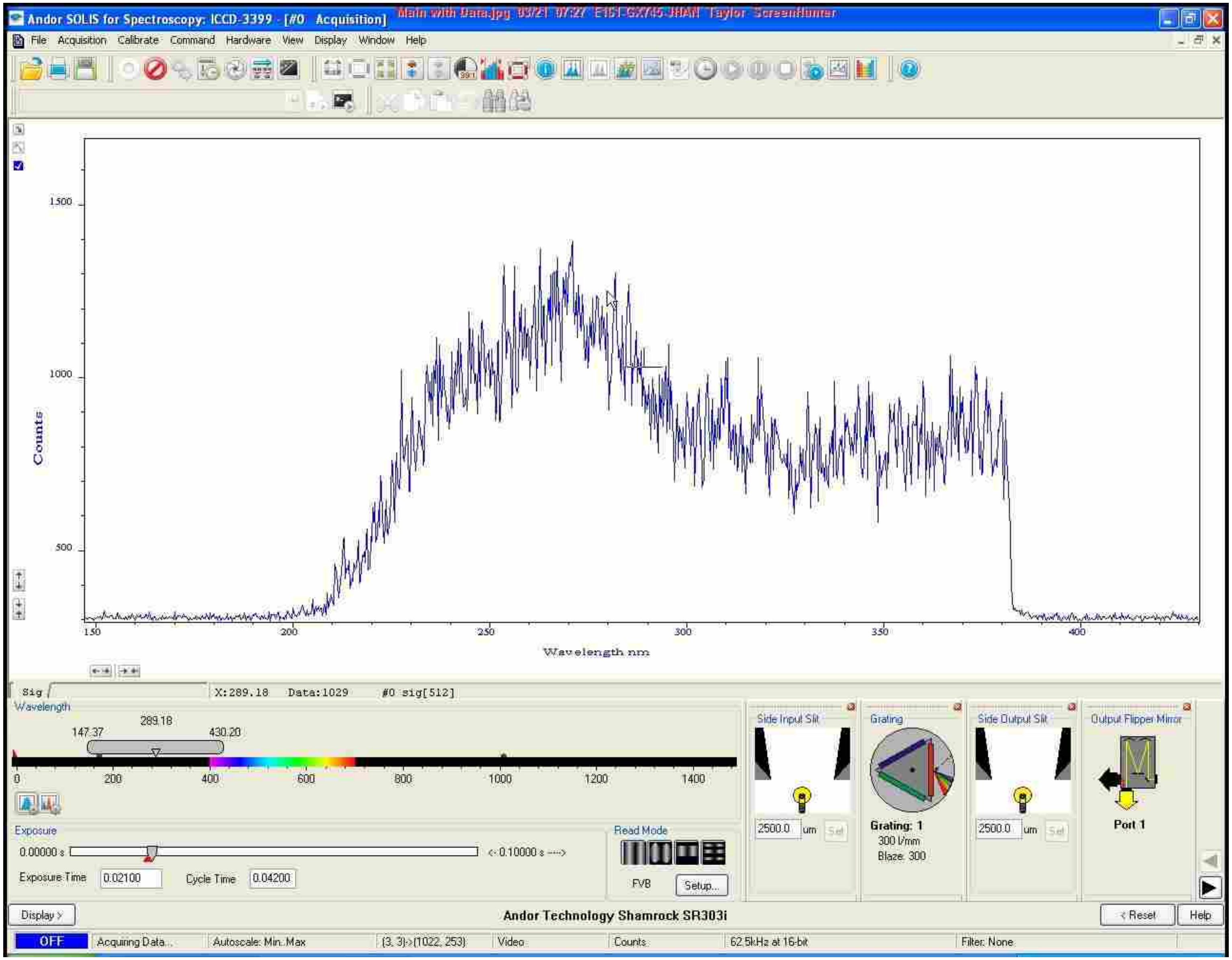

X:289.18 Data:1029 #0 sig[512]

Exposure Time 0.02100 Cycle Time 0.04200

Side Input Slit: 2500.0 um

Grating: 1
300 l/mm
Blaze: 300

Side Output Slit: 2500.0 um

Acquiring Data... | Autoscale: Min..Max | (3, 3)->(1022, 253) | Video | Counts | 62.5kHz at 16-bit | Filter: None

This is the Andor SOLIS software to control the Spectrograph and Camera. The PCI capture card interface for the camera isn't compatible on Windows 7+ so it is installed on windows XP. If on startup it says "Camera not detected" Exit the program and restart the computer. This typically happens when the program is left for several hours without using the camera.

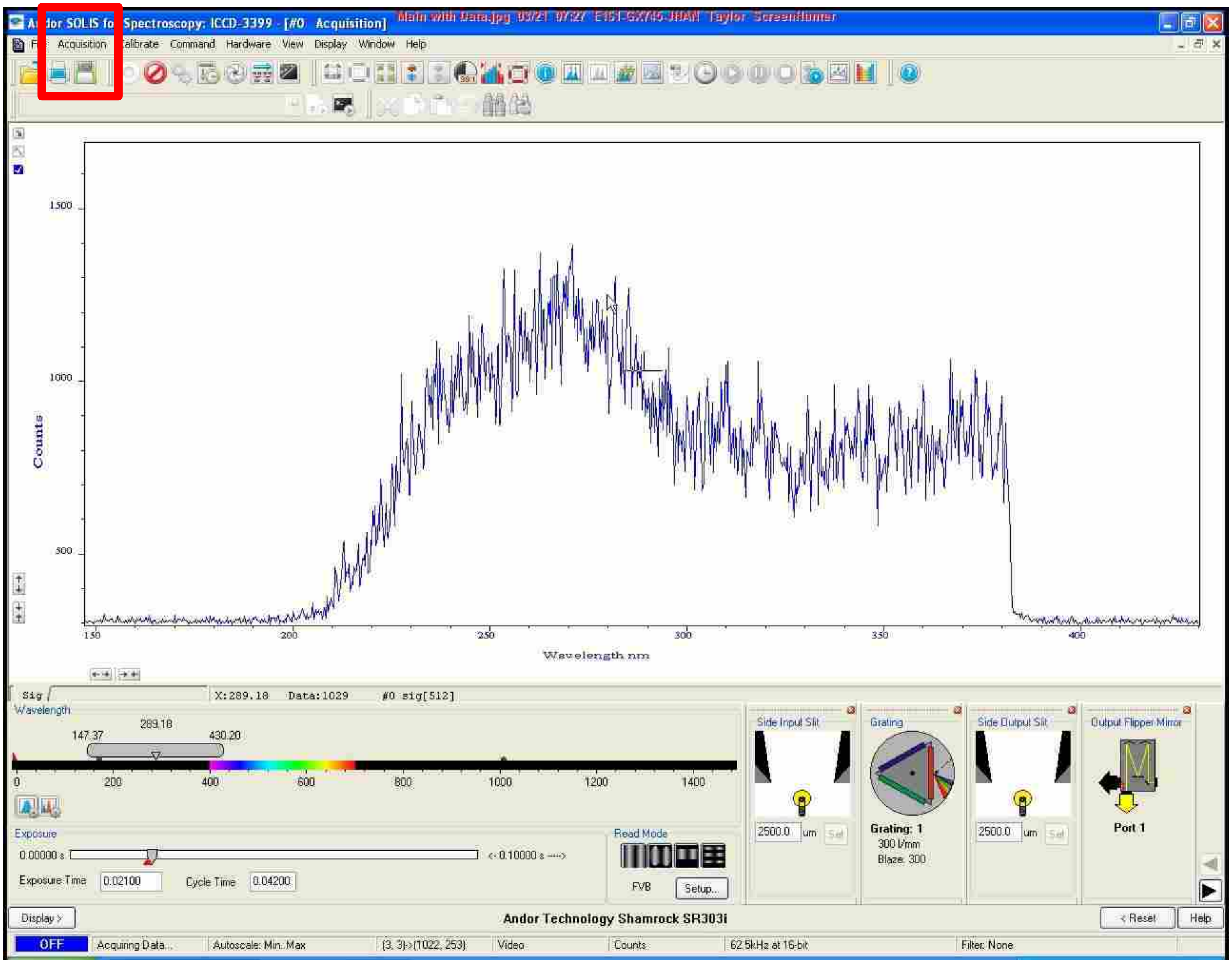

X:289.18 Data:1029 #0 sig[512]

147.37 289.18 430.20

0.00000 s <- 0.10000 s --->

Exposure Time 0.02100 Cycle Time 0.04200

2500.0 um Set

Grating: 1
300 l/mm
Blaze: 300

2500.0 um Set

Acquiring Data... | Autoscale: Min..Max | (3, 3)->(1022, 253) | Video | Counts | 62.5kHz at 16-bit | Filter: None

Start by clicking “Acquisition” and then “Setup” the window on the next page will appear. Acquisition setup must be complete prior to operation of the camera but the controls shown at the bottom of the program may be adjusted during camera operation.

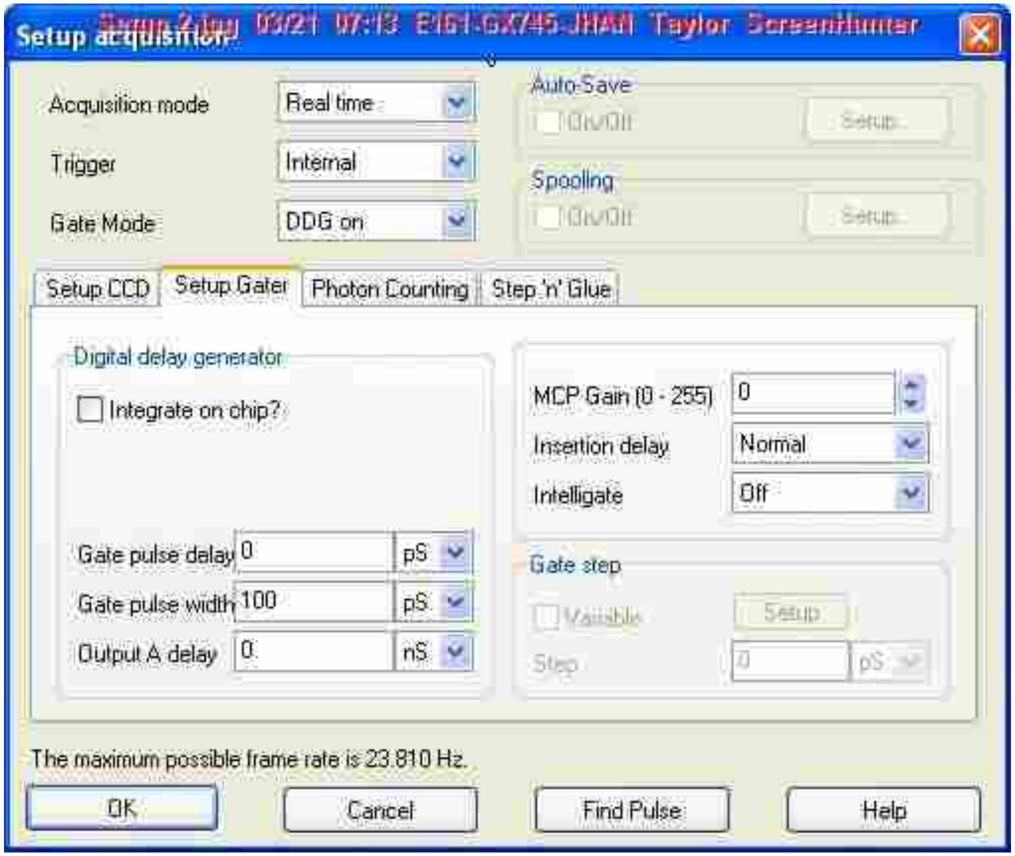

Acquisition mode: Real time

Trigger: Internal

Gate Mode: DDG on

☐ Integrate on chip?

Gate pulse delay: 0 pS

Gate pulse width: 100 pS

Output A delay: 0 nS

MCP Gain (0 - 255): 0

Insertion delay: Normal

Intelligate: Off

☐ On/Off (Auto-Save)

☐ On/Off (Spooling)

☐ Variable

Step: 0 pS

The maximum possible frame rate is 23.810 Hz.

The “Gate pulse width” needs to be set to 5 micro seconds and the “MCP Gain” to 100. These settings match the default setting in the CCD LabVIEW Program for the digital delay generator and may be changed if desired. If the settings are kept constant, alignment is easier because the maximum signal possible under these settings are known.

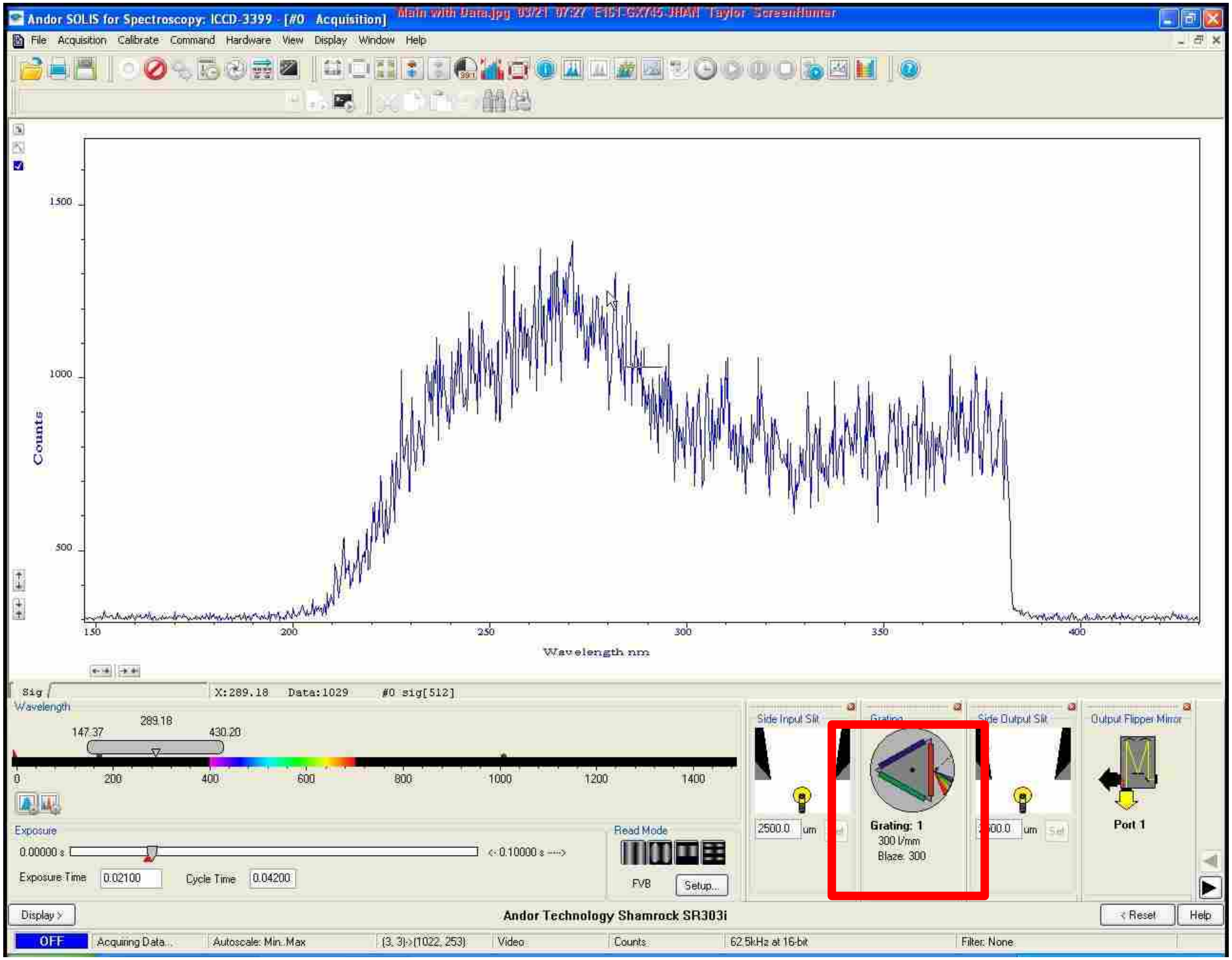

X:289.18 Data:1029 #0 sig[512]

Exposure Time 0.02100 Cycle Time 0.04200

Side Input Slit: 2500.0 um

Grating: 1
300 l/mm
Blaze: 300

Side Output Slit: 2500.0 um

OFF | Acquiring Data... | Autoscale: Min..Max | (3, 3)->(1022, 253) | Video | Counts | 62.5kHz at 16-bit | Filter: None

There are three gratings at 300, 600, and 1800 lines/mm. The greater the resolution of the grating, the smaller the range of wavelength because the light is spread at greater angles. The lower the resolution of the grating, the greater the intensity of light collected by the CCD. Be aware that even though the scale of the wavelengths extends from 147 nm to 430 nm, the CCD is capturing from 200 to 380 nm. This is always the case that less wavelengths are actually recorded. Whatever is displayed in the active plot will be recorded.

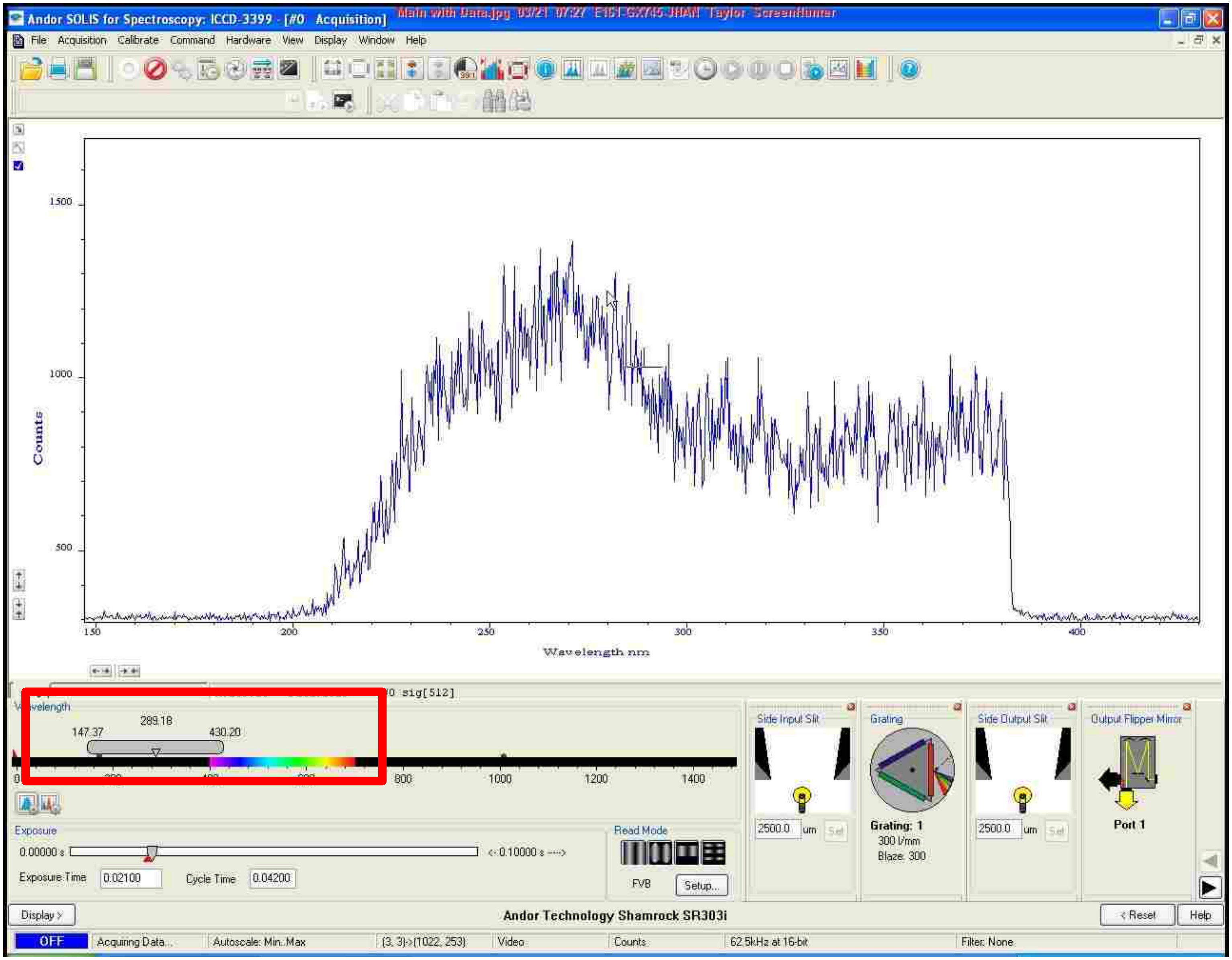

Exposure Time 0.02100

Cycle Time 0.04200

Side Input Slit 2500.0 um

Grating: 1
300 l/mm
Blaze: 300

Side Output Slit 2500.0 um

OFF | Acquiring Data... | Autoscale: Min..Max | (3, 3)->(1022, 253) | Video | Counts | 62.5kHz at 16-bit | Filter: None

The spectrum above is the typical output from the deuterium lamp. The red square is highlighting the Wavelength selector where the range may be adjusted. The range is changed by sliding the bar where desired or clicking on the bar and inputting the center wavelength directly. The size of the range is adjusted with the different gratings.

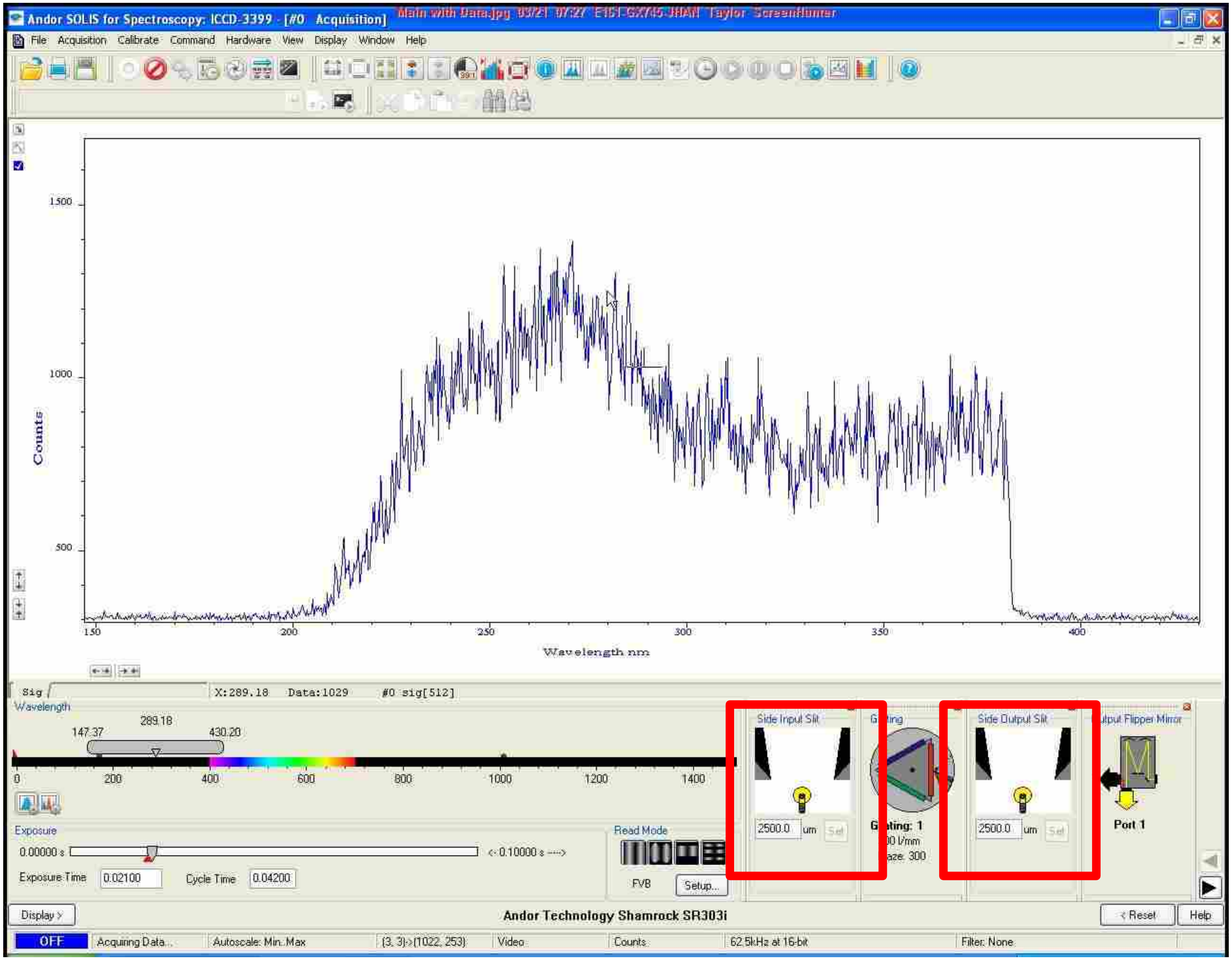

Entrance and exit slit widths are controlled here. The minimum is 1 micron and the maximum is 2500. Slit widths are related to resolution as well. In these experiments the concerned for light intensity outweighs that of resolution especially with the use of the PMT with notch filters to control wavelength selection.

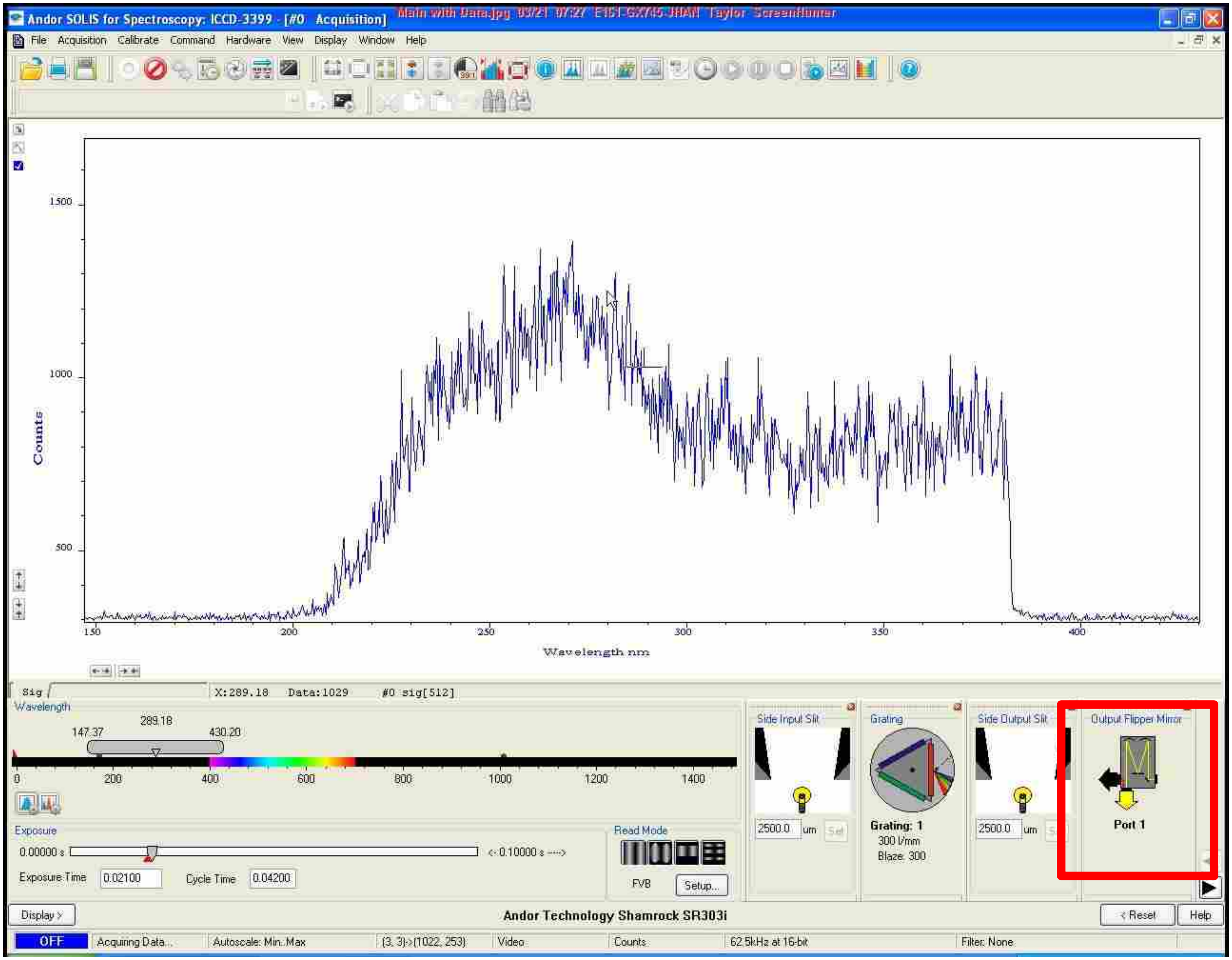

X:289.18 Data:1029 #0 sig[512]

Wavelength: 147.37 – 289.18 – 430.20

Side Input Slit: 2500.0 um

Grating: 1
300 l/mm
Blaze: 300

Side Output Slit: 2500.0 um

Output Flipper Mirror: Port 1

Exposure: 0.00000 s <- 0.10000 s --->

Exposure Time 0.02100 Cycle Time 0.04200

Read Mode: FVB

Andor Technology Shamrock SR303i

OFF | Acquiring Data... | Autoscale: Min..Max | (3, 3)->(1022, 253) | Video | Counts | 62.5kHz at 16-bit | Filter: None

This is the flipper mirror control. It switches the output path from CCD to PMT. Once all settings are correct, stop collection. This program can't be actively collecting data while the LabVIEW CCD program is working because they use the same device. The only time data should be saved is to collect the x-axis for later analysis as LabVIEW will average the y-axis data.

7.3 UV-Vis Absorption with PMT Detection

The PMT detector has no 2-dimentional discrimination like the CCD. Only one output signal is collected where with the CCD there are 1024 collection bins that collect differing wavelengths depending on the grating lines/mm and angle. If multiple species absorb in the same wavelength region deconvolution is necessary. With a PMT deconvolution can only be facilitated by collecting multiple wavelengths. Since there is no discrimination the experiment must be repeated multiple times at differing wavelengths. The UV-Vis 2011.vi program is described in the following pages to perform such an experiment and deconvolution.

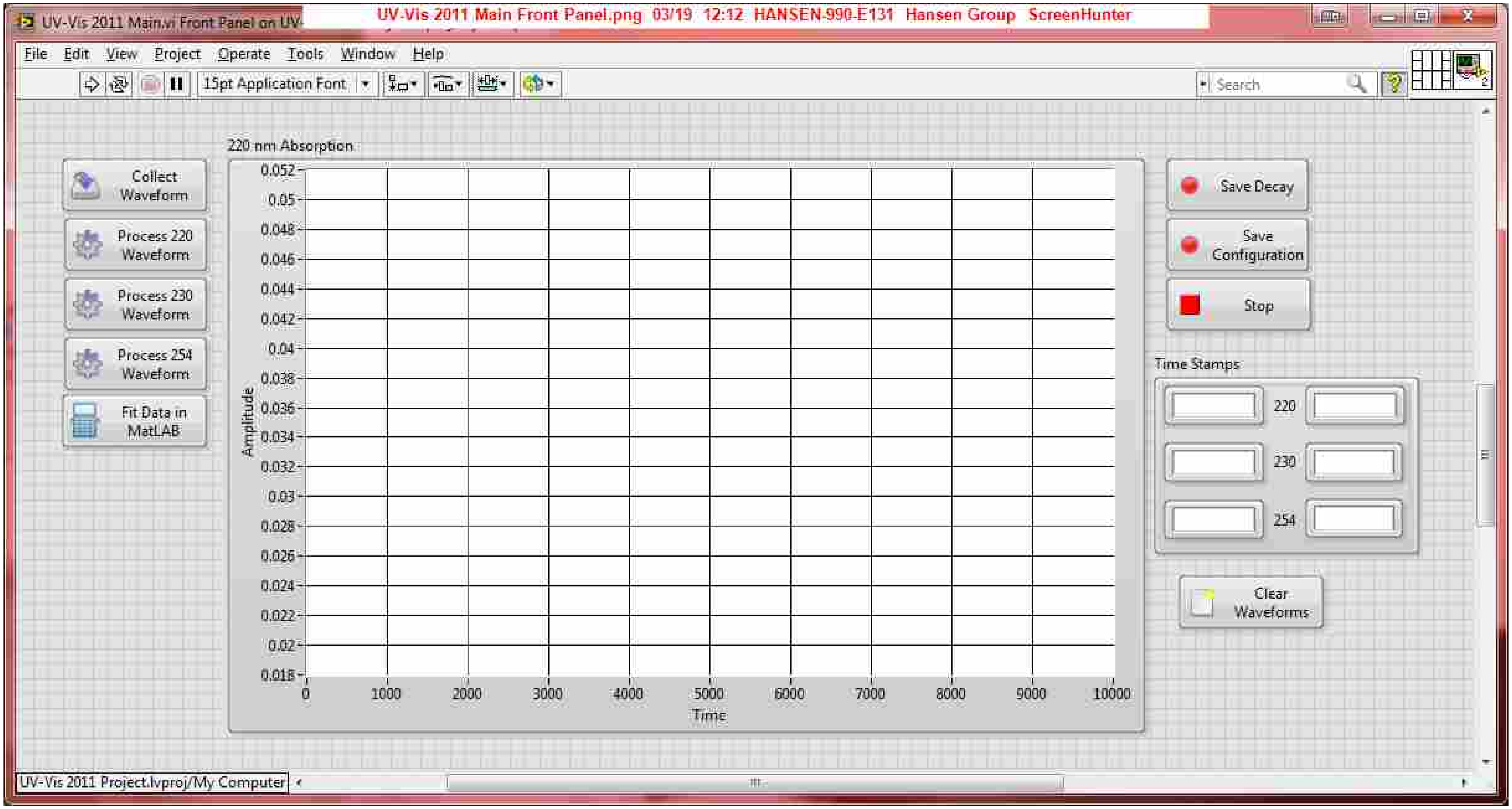

This is the main Vi (Virtual Instruments) and additional Vi's will appear when certain buttons are pressed. This VI is used to analyze data collected on the oscilloscope. Additionally the Andor Software is needed to control the spectrograph to change between collection wavelengths.

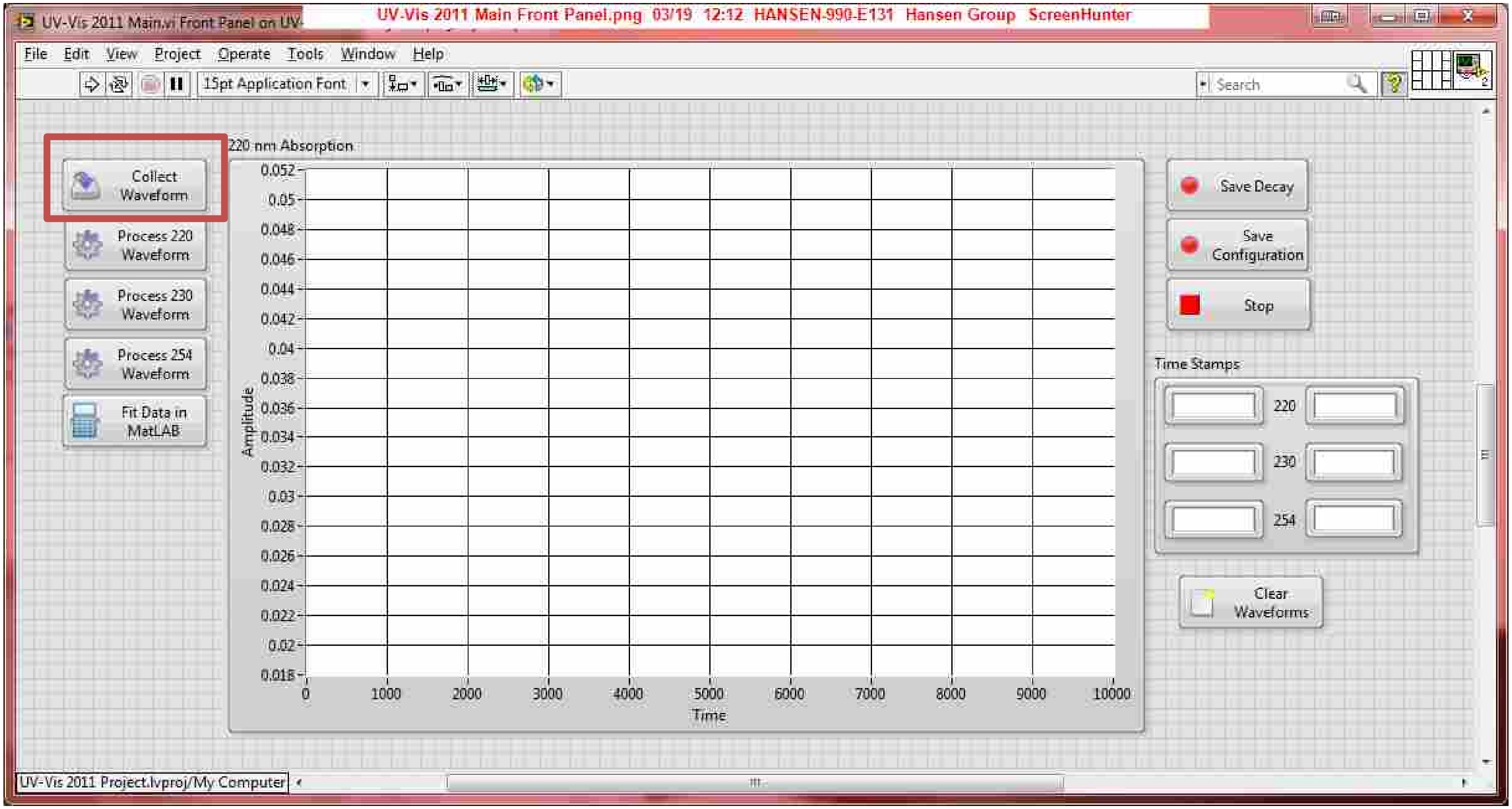

The data must first be collected and averaged on the oscilliscope before collected inot LabVIEW. Once a decay has averaged sufficiently (max is 512 but fewer may be collected depending on the experimental conditions) press “Collect Waveform”. An additional program will appear (next page) and assist you in collecting and assigning the decay.

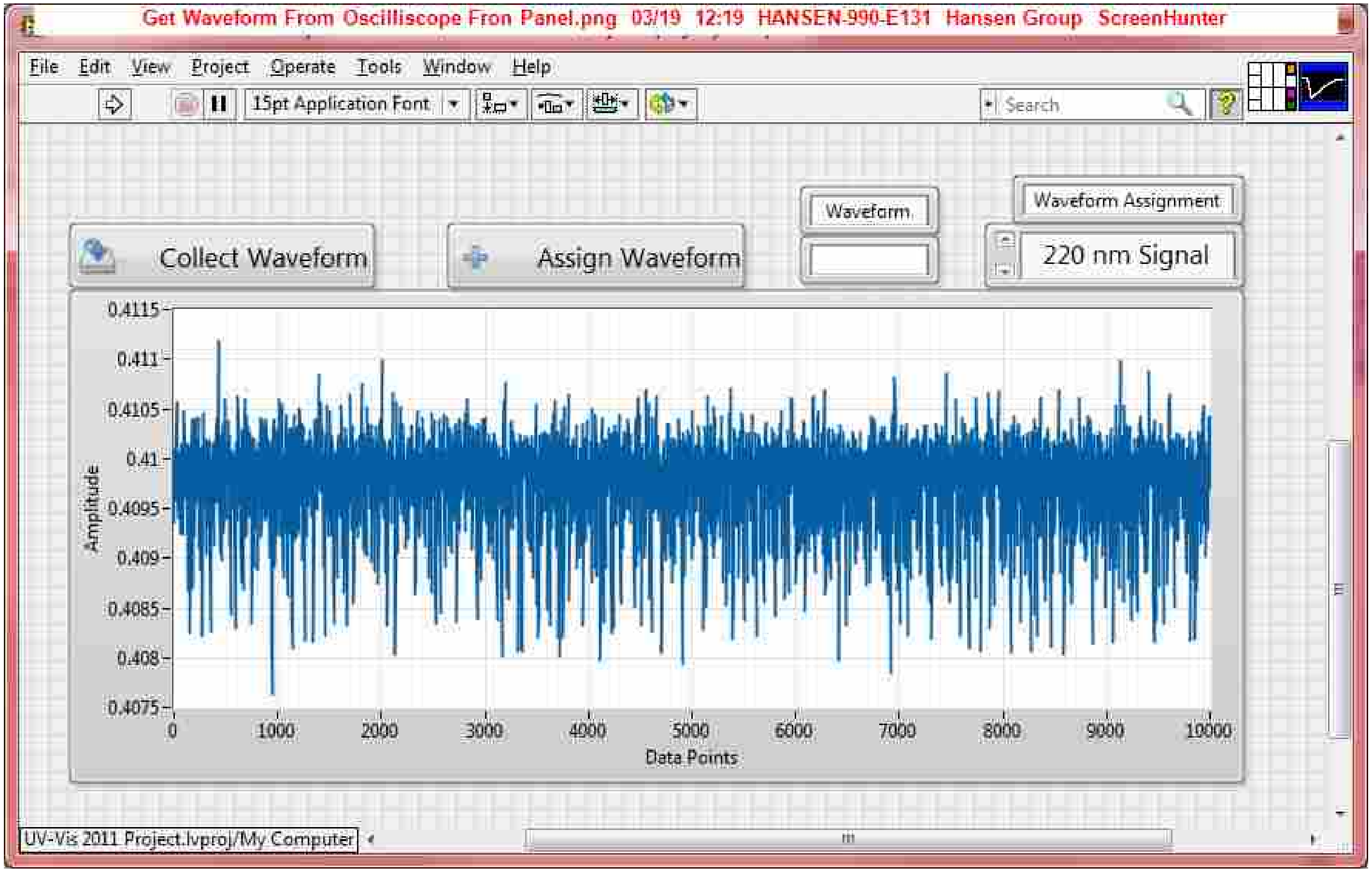

Waveform Assignment: 220 nm Signal

When the "Collect Waveform" button is pressed, whatever is displayed on the oscilloscope will be recorded and displayed here. If the waveform is unsatisfactory another one may be collected again without closing. To save the waveform, click the waveform assignment drop menu and select the appropriate designation. To complete analysis you must collect three decays and associated background/dark counts. Once the designation is properly displayed, press "Assign Waveform" and the waveform will be stored and this window will close.

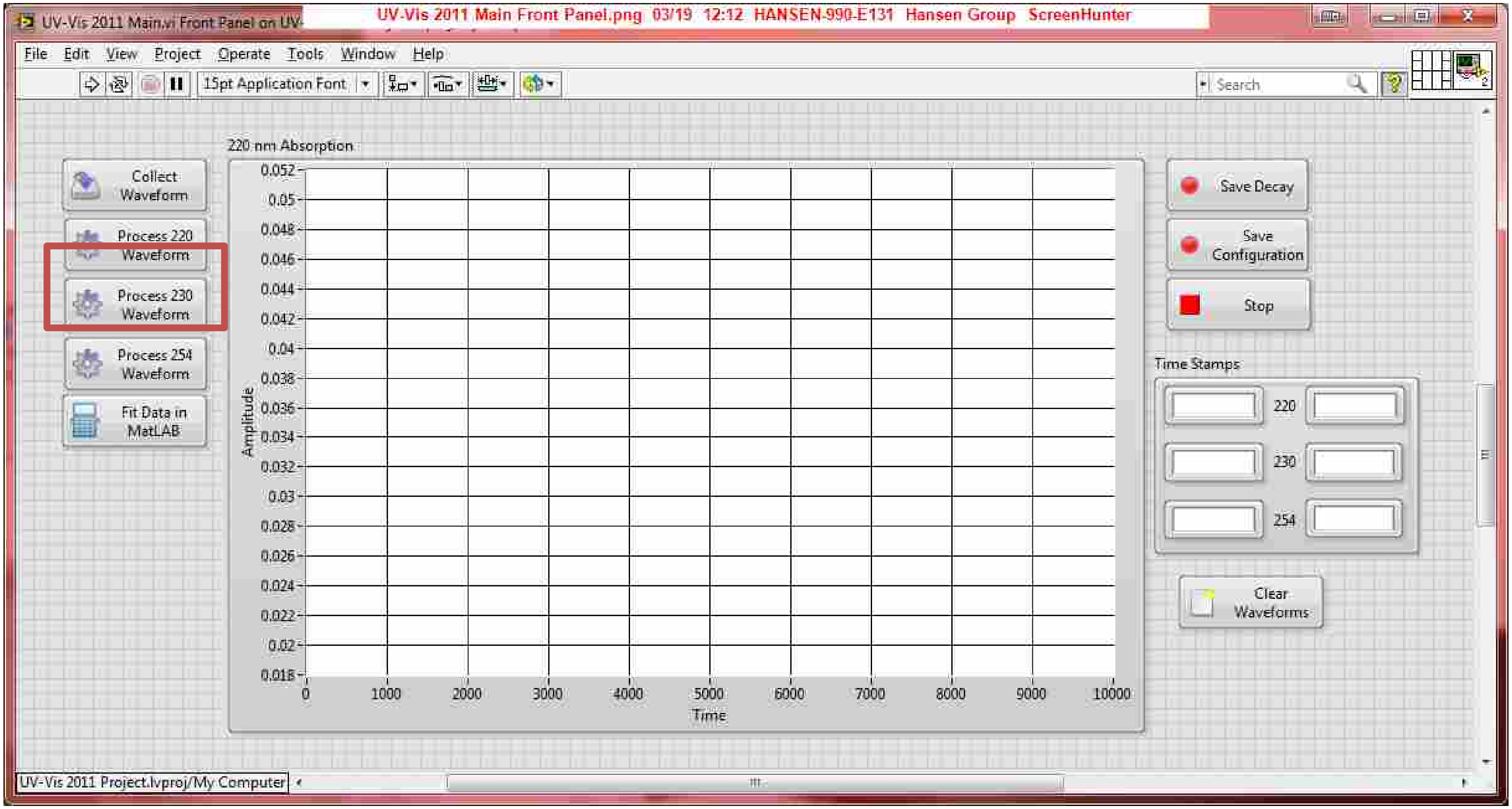

You will need to repeat the previous steps for each wavelength and dark counts for each. If care is taken to not adjust any parameters on the oscilloscope then the background counts will be the same at each wavelength. This takes some practice since each wavelength has different intensities that don't all fit in the same range of the oscilloscope but it is a good idea to learn how to get equal intensity for each wavelength by adjusting slit widths of the monochromator and grating.

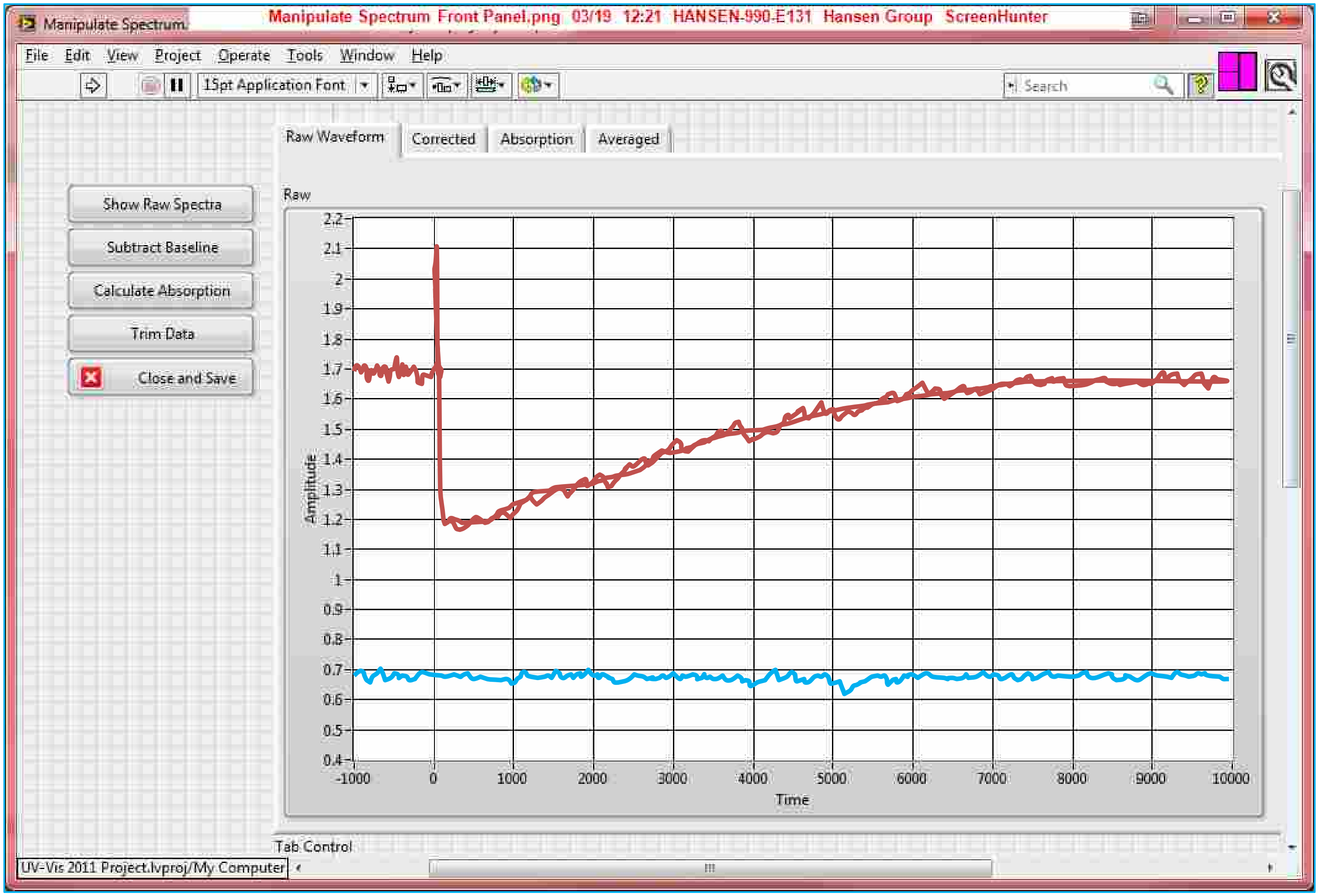

This window appears when the "Process Waveform" button is pressed. If there is not both a background waveform and signal waveform this window will not open and the user will be informed of the error. A complete analysis requires each of the buttons on the left pressed in order from top to bottom. A task is required after each button is pressed and each are discribed in the following pages.

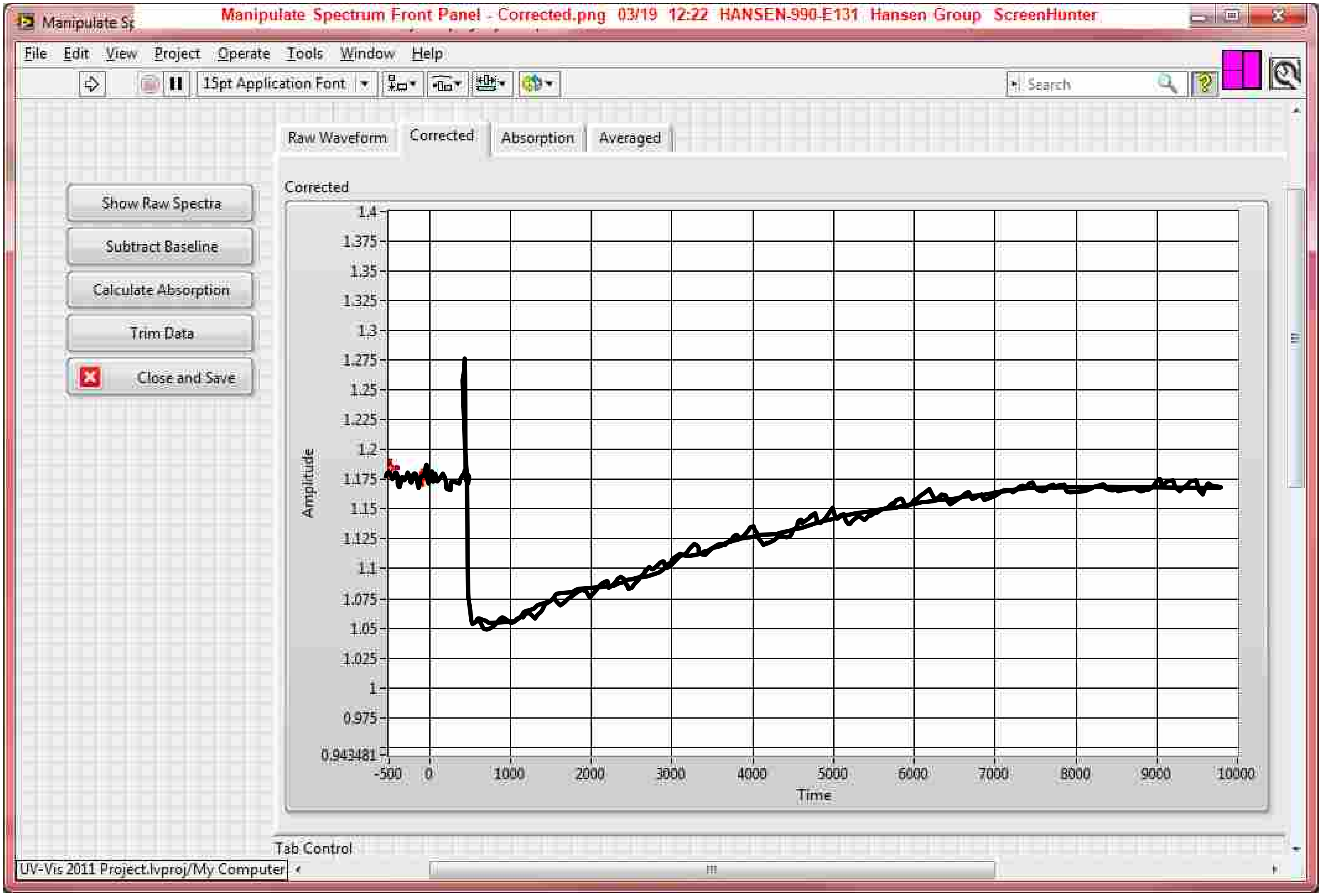

Press “Subtract Baseline” and it will simply subtract the two waveforms and leave display the corrected signal. The two red crosshairs are then used to select the I_o. The region before the laser fires is used as I_o because the region is the absence of absorbers. When the selected region is satisfactory press “Calculate Absorption”.

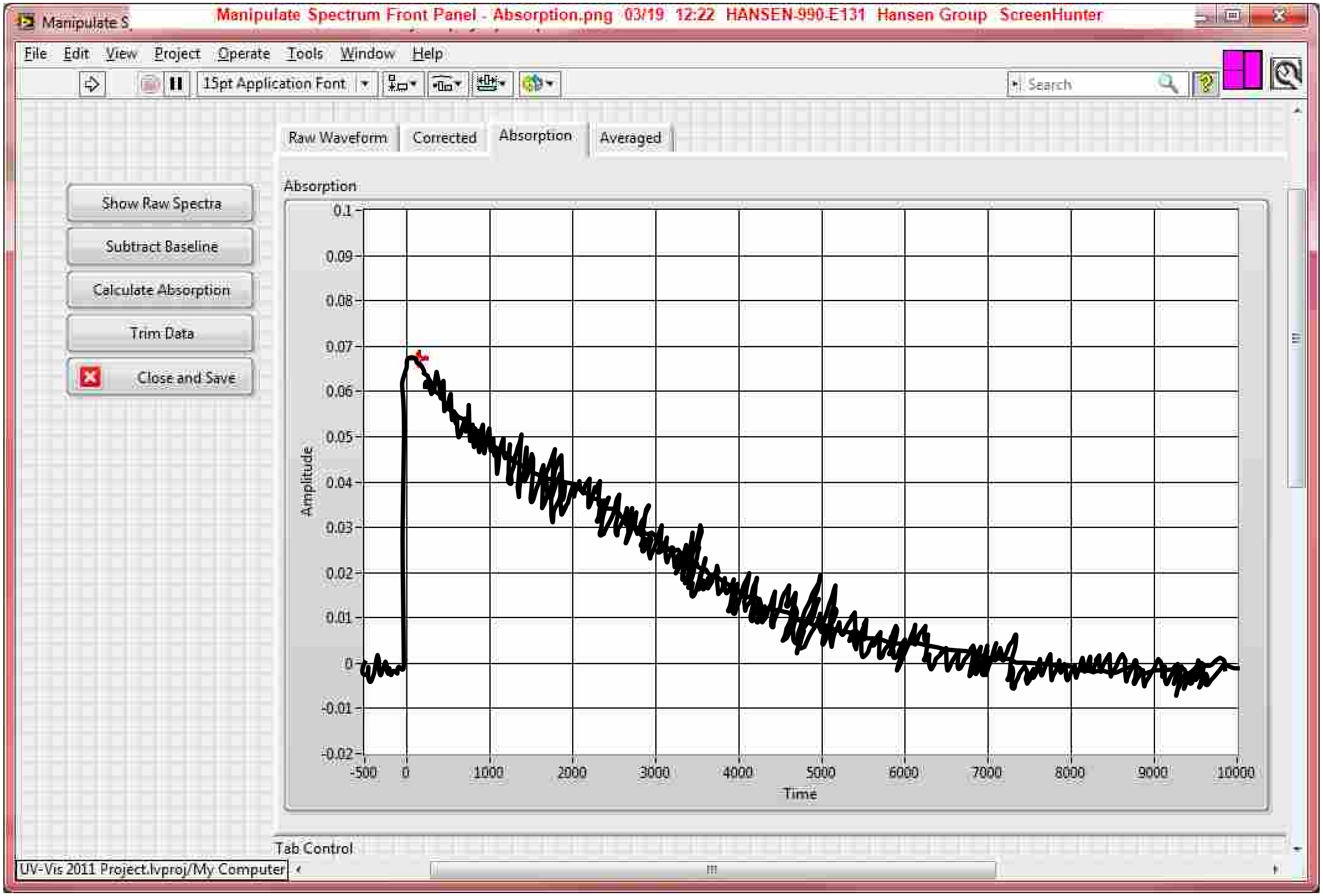

The single crosshair here is to select where to cutoff data. Analysis and data fitting require the data to be trimmed from before the laser fires or the time it takes for the radical to be formed. So data is cut off after the signal turns over and begins to decay. After selection press “Trim Data”.

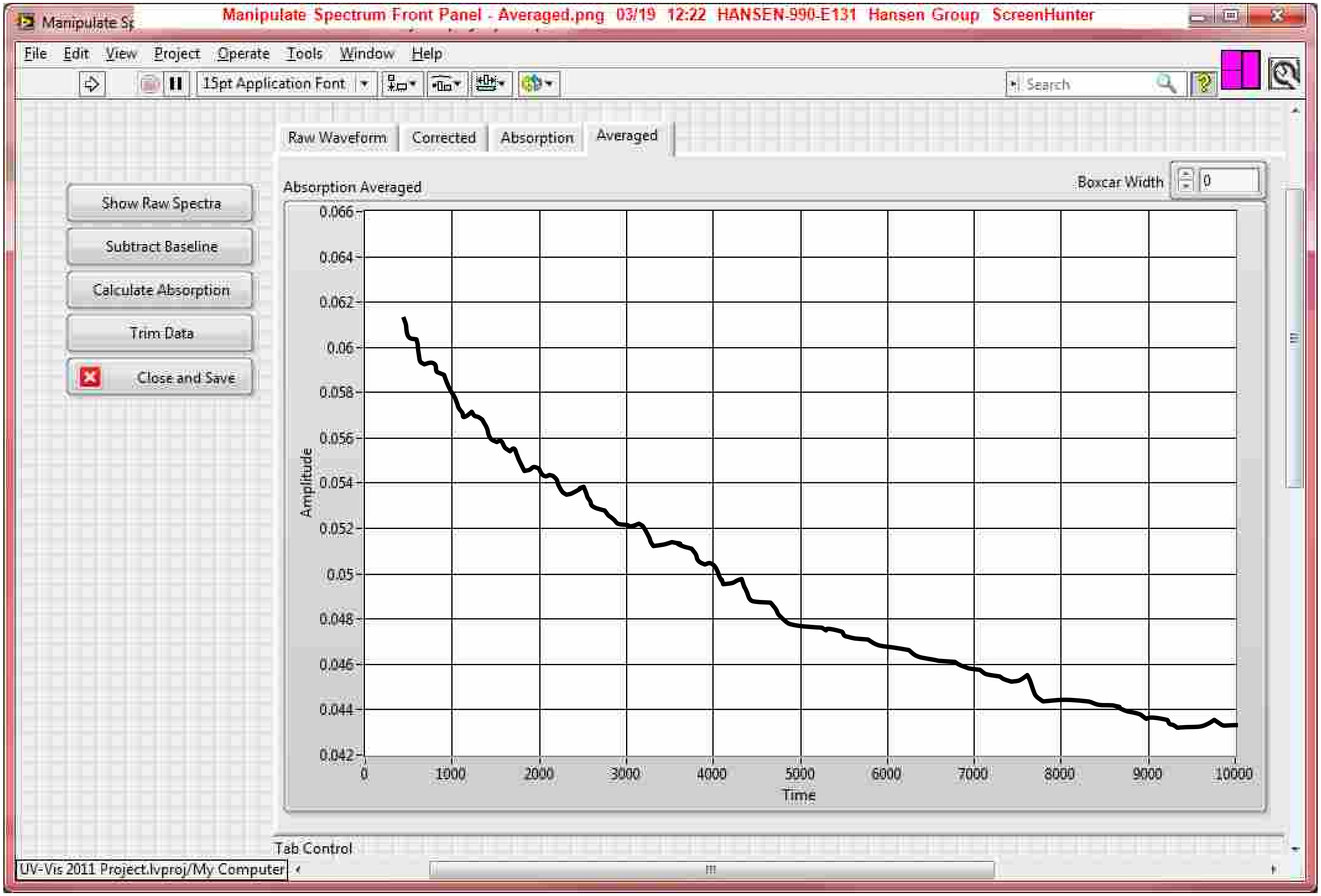

This last tab is used to average the decay before saving. Use the incrementer on the right side to adjust the boxcar width. This is a moving boxcar and is described within the block diagrams later. Each time the boxcar width value is changed the plot will update so you may be adjusted until satisfied. If satisfied press “Close and Save”. This will exit the window and the decay saved. If any steps were performed incorrectly just press “Show Raw Spectra” and go through the steps again.

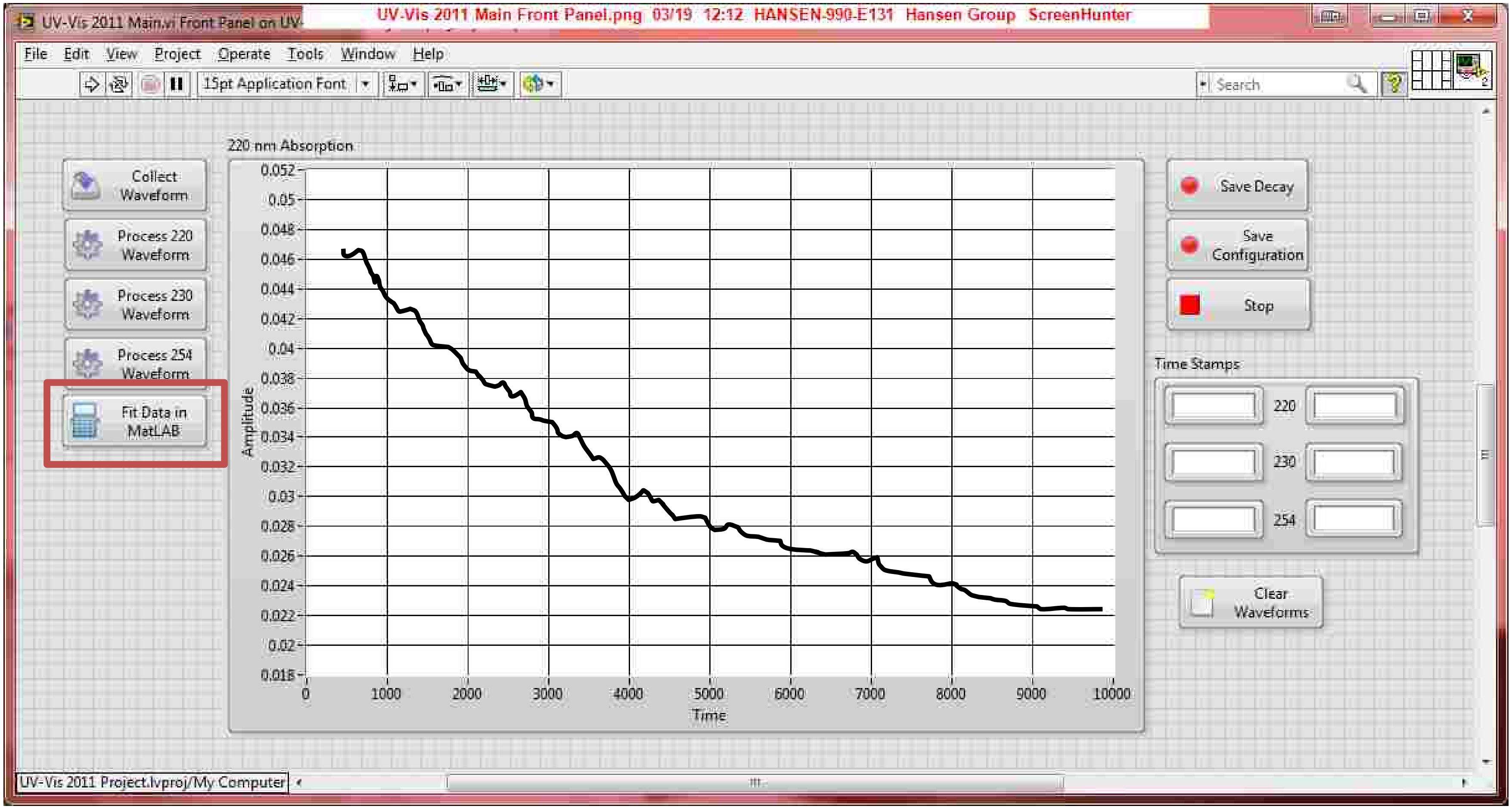

Once a decay is processed for each wavelength you can press “Fit Data in Matlab” and the VI will deconvolve the three decays into a concentration-time profile for both HEP and O_3. Now press “Save Decay”. At any time during an experiment pressing “Save Configuration” brings up a new window described on the next page.

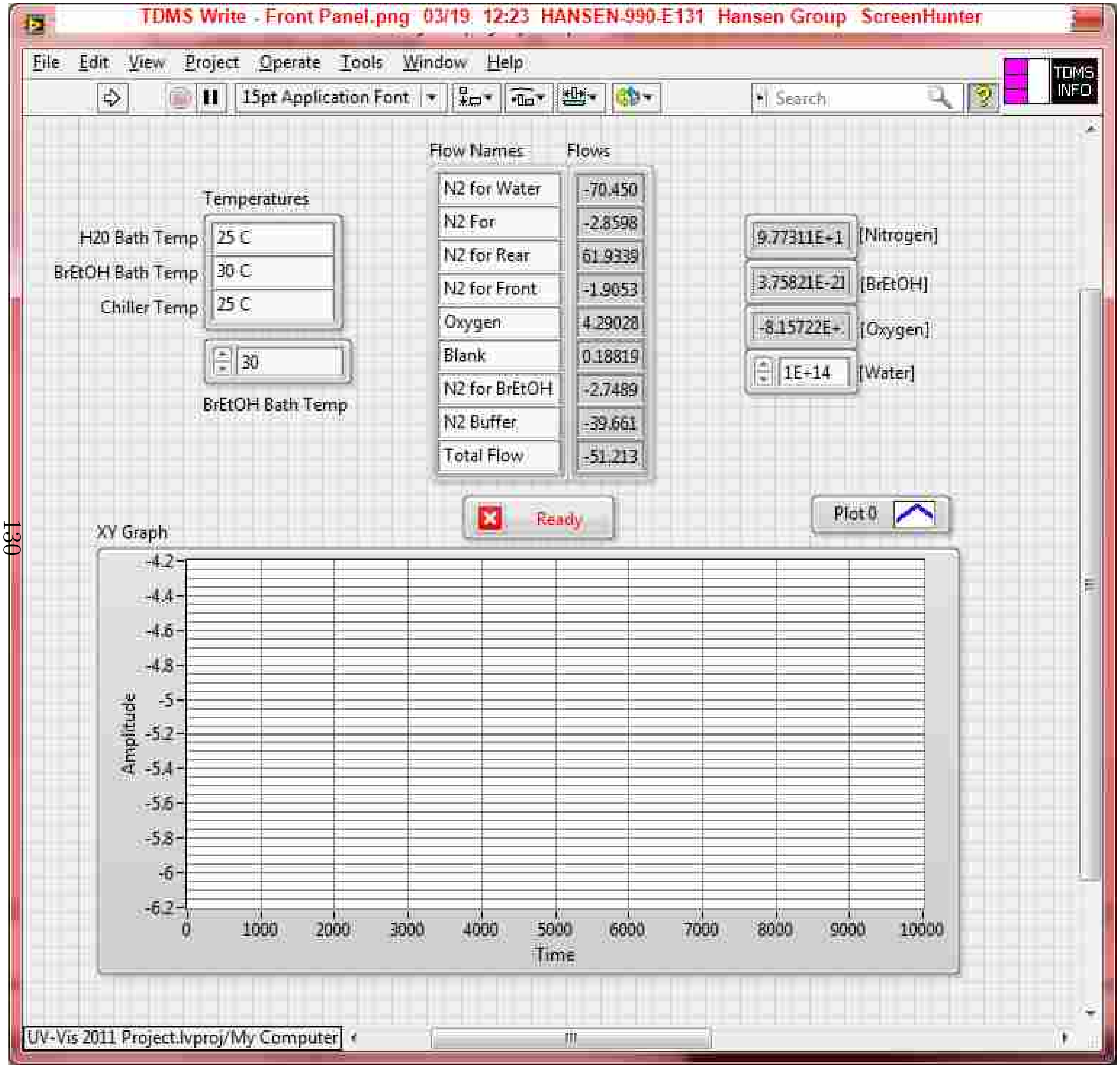

H20 Bath Temp: 25 C
BrEtOH Bath Temp: 30 C
Chiller Temp: 25 C
BrEtOH Bath Temp: 30

Flow Names	Flows
N2 for Water	-70.450
N2 For	-2.8598
N2 for Rear	61.9339
N2 for Front	-1.9053
Oxygen	4.29028
Blank	0.18819
N2 for BrEtOH	-2.7489
N2 Buffer	-39.661
Total Flow	-51.213

[Nitrogen]: 9.77311E-1
[BrEtOH]: 3.75821E-21
[Oxygen]: -8.15722E-
[Water]: 1E+14

This is used to create a TDMS file. The flows are collected automatically but the temperatures and water vapor are inputs. When all inputs are correct press “Ready” and a comment box will appear.

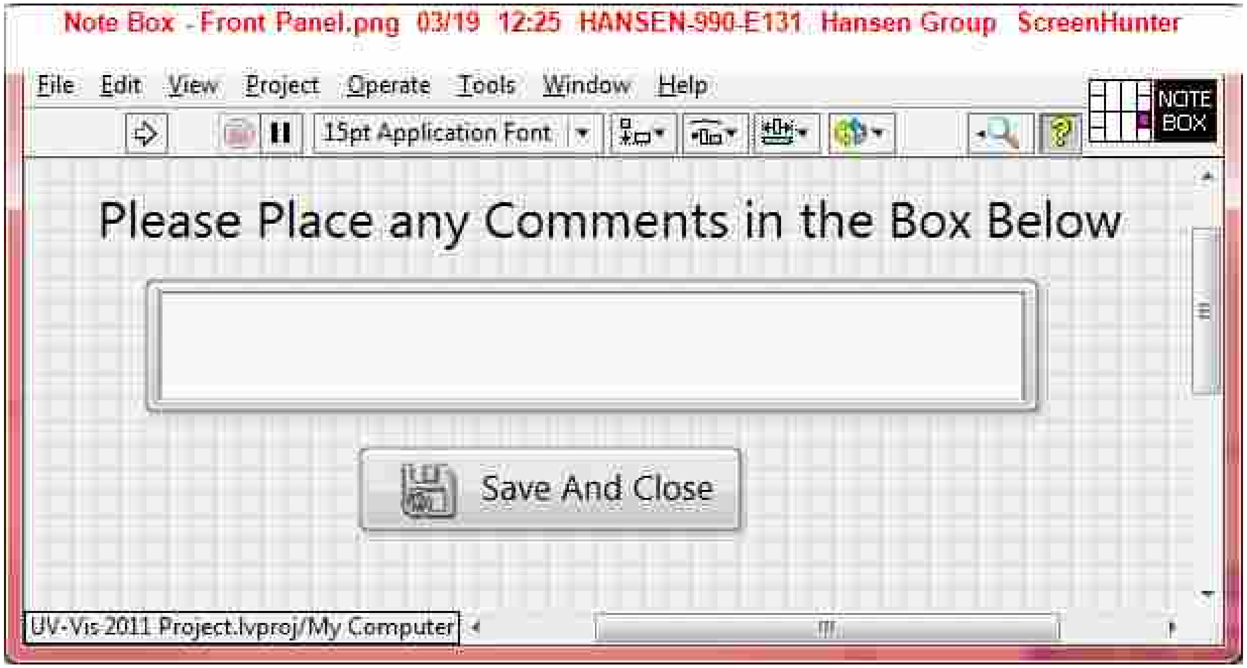

Place here any length comment and it will be saved along with all the data. The saved data will not include the deconvolved decay but will contain the raw data from the three wavelengths before any processing. The file will be saved as the current date and time automatically and both windows will close and return to the main VI. Then continue collecting decays. A trick is to also collect three decays and fit then replace one of the decays and fit again. Three new decays are not needed each time similar to a running average.

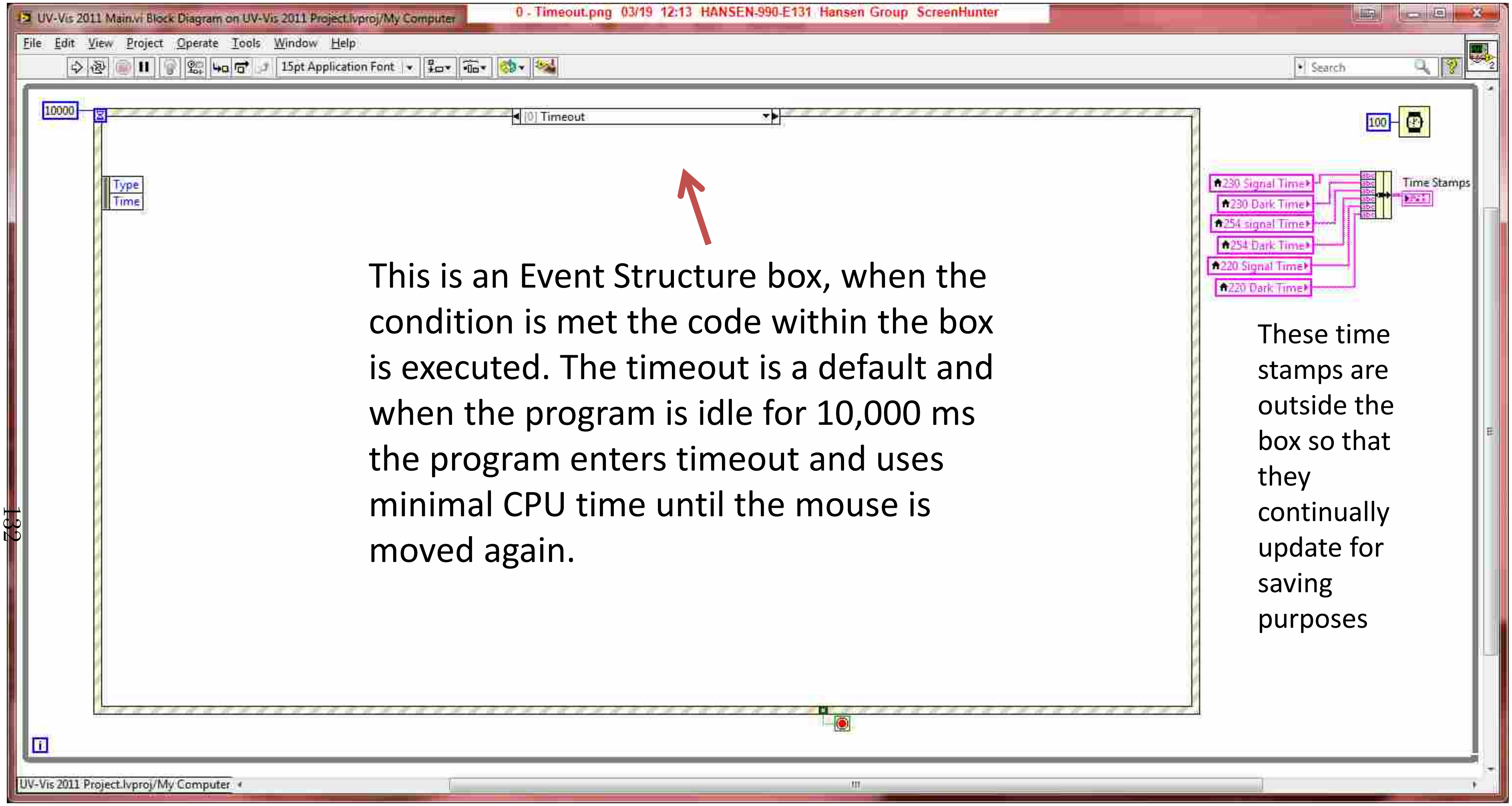

This is an Event Structure box, when the condition is met the code within the box is executed. The timeout is a default and when the program is idle for 10,000 ms the program enters timeout and uses minimal CPU time until the mouse is moved again.

These time stamps are outside the box so that they continually update for saving purposes

In the following pages the block diagrams or programming behind the front panel controls are described in brief. This is in case adjustments are needed for different experiments. For new users of LabVIEW this will help but initial instruction is needed as this is not a LabVIEW guide but a UV-VIS main.vi guide. Be wise and save a copy before any manipulation.

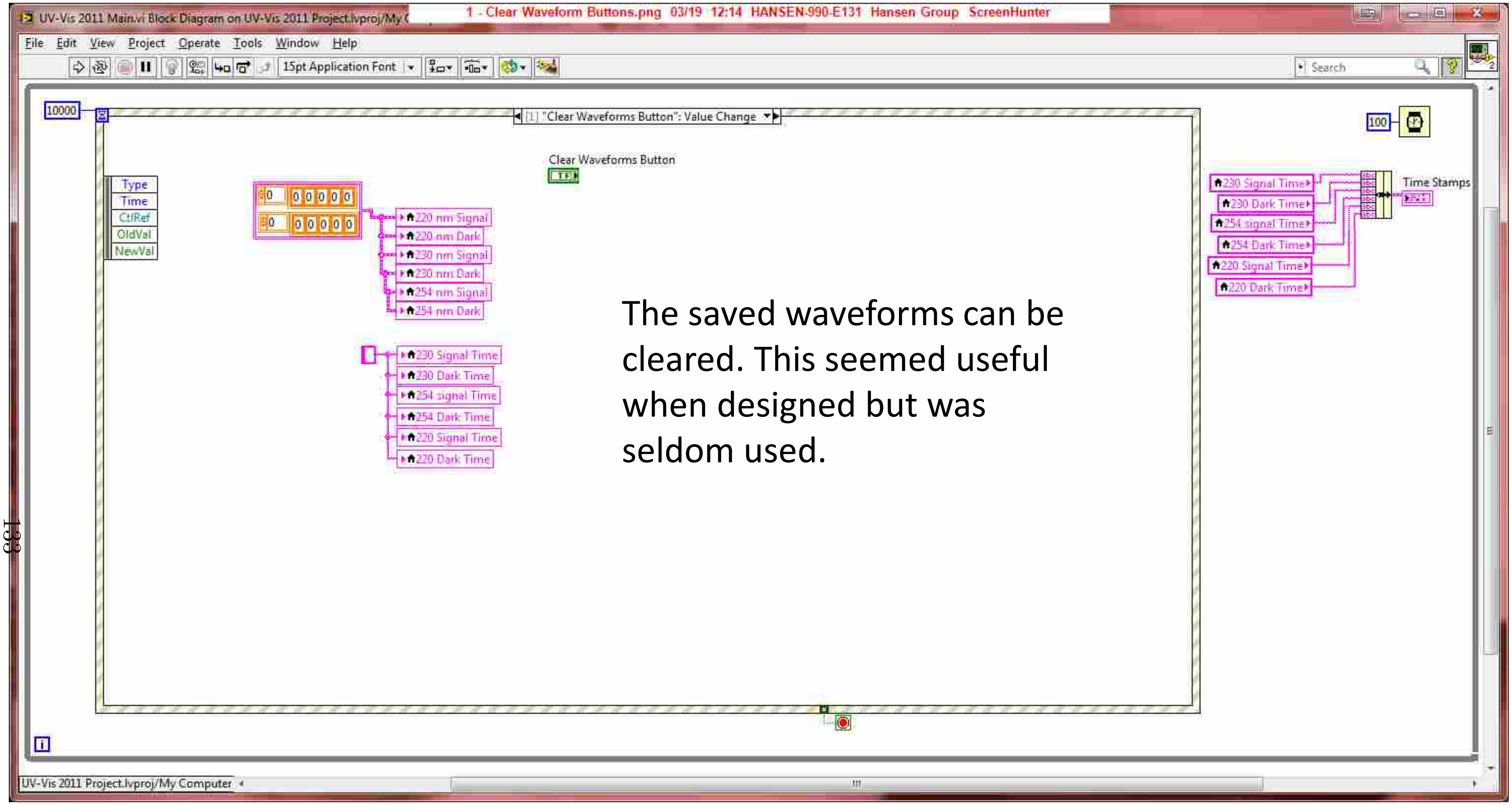

The saved waveforms can be cleared. This seemed useful when designed but was seldom used.

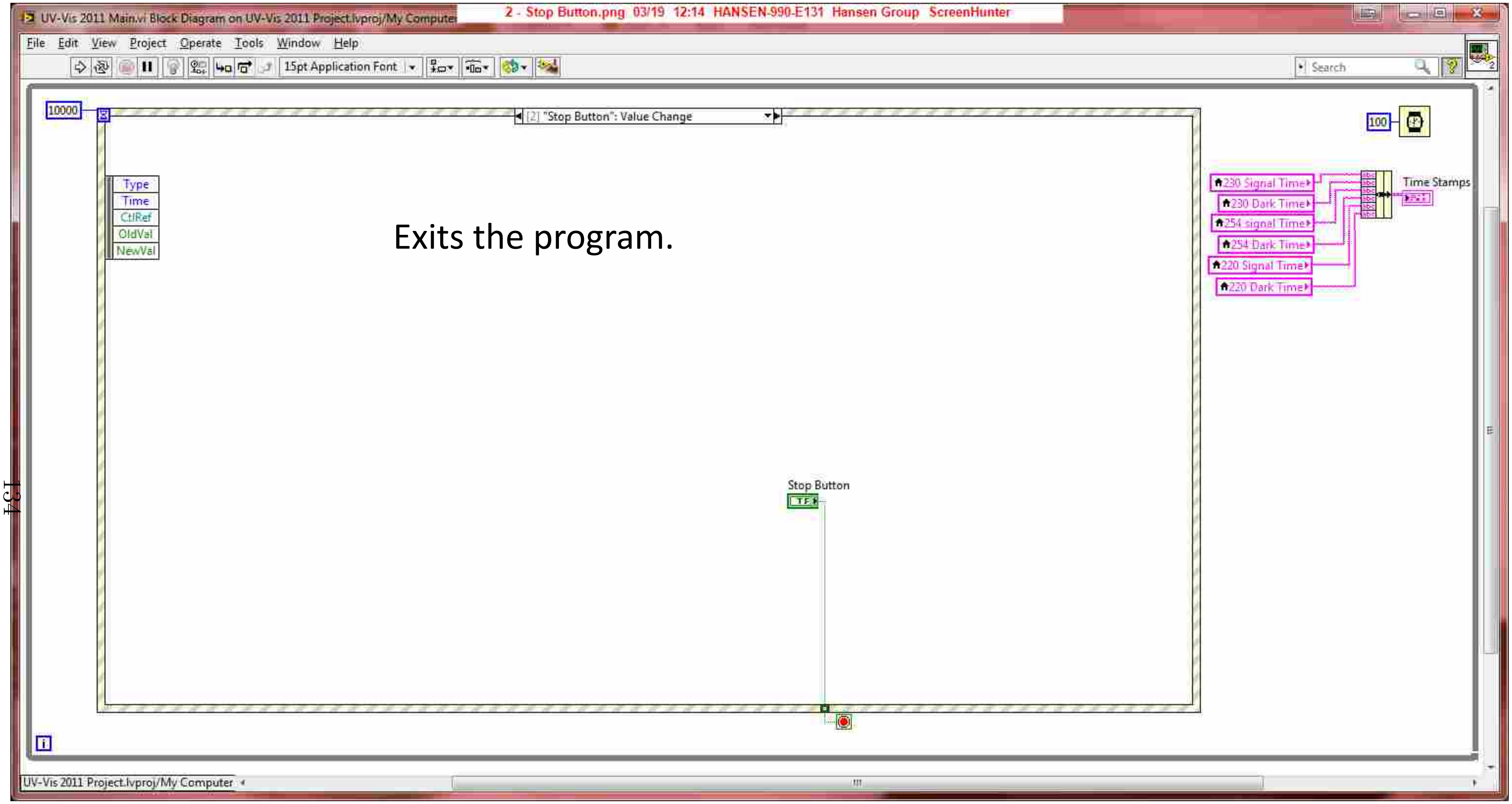

Exits the program.

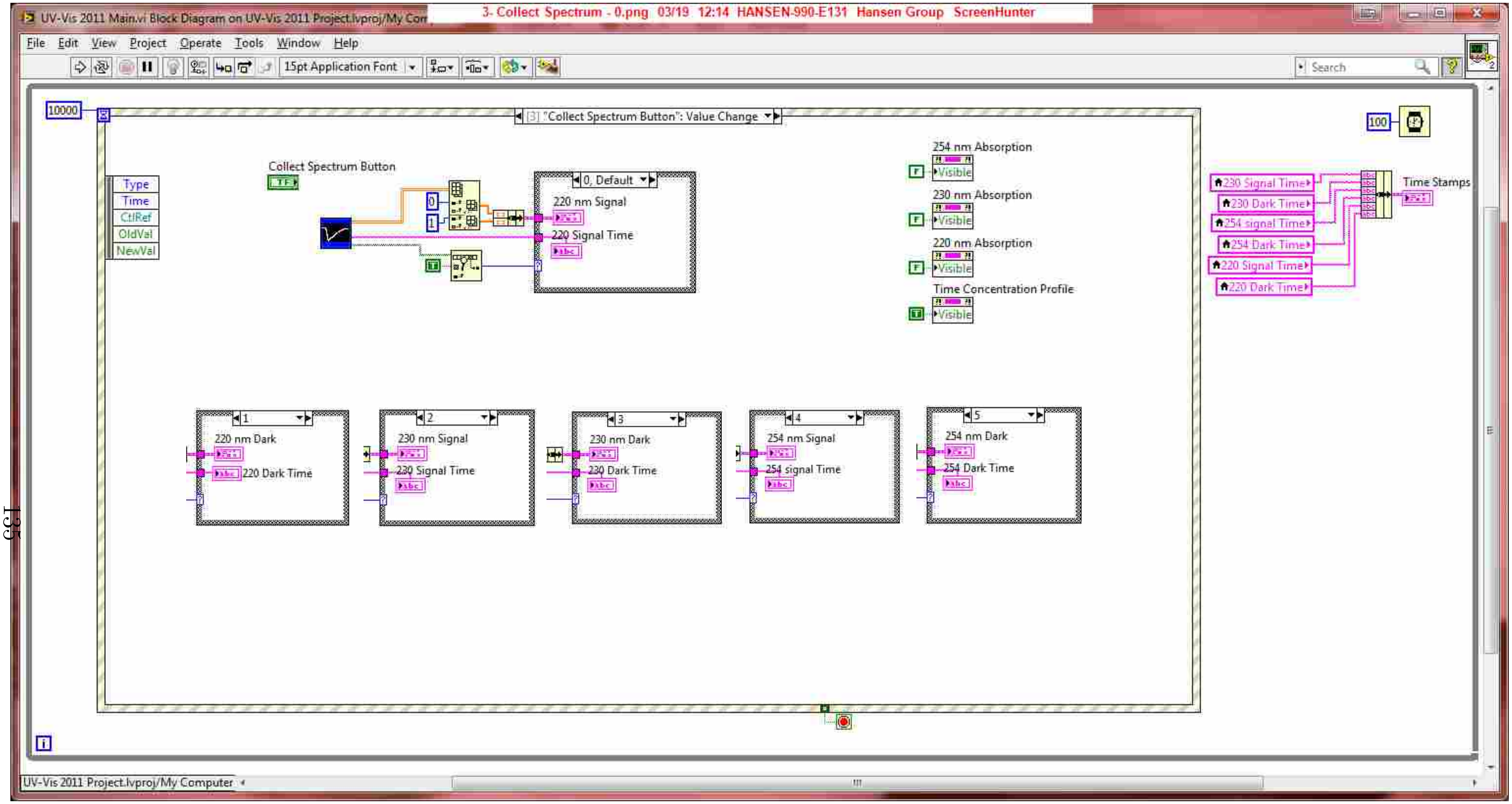

This box will open the "Collect Waveform" VI and then depending on the selection within the VI this box will properly assign the waveform as desired. Each of the cases of the case structure are pasted here to save space but one must click through the box to see the different cases.

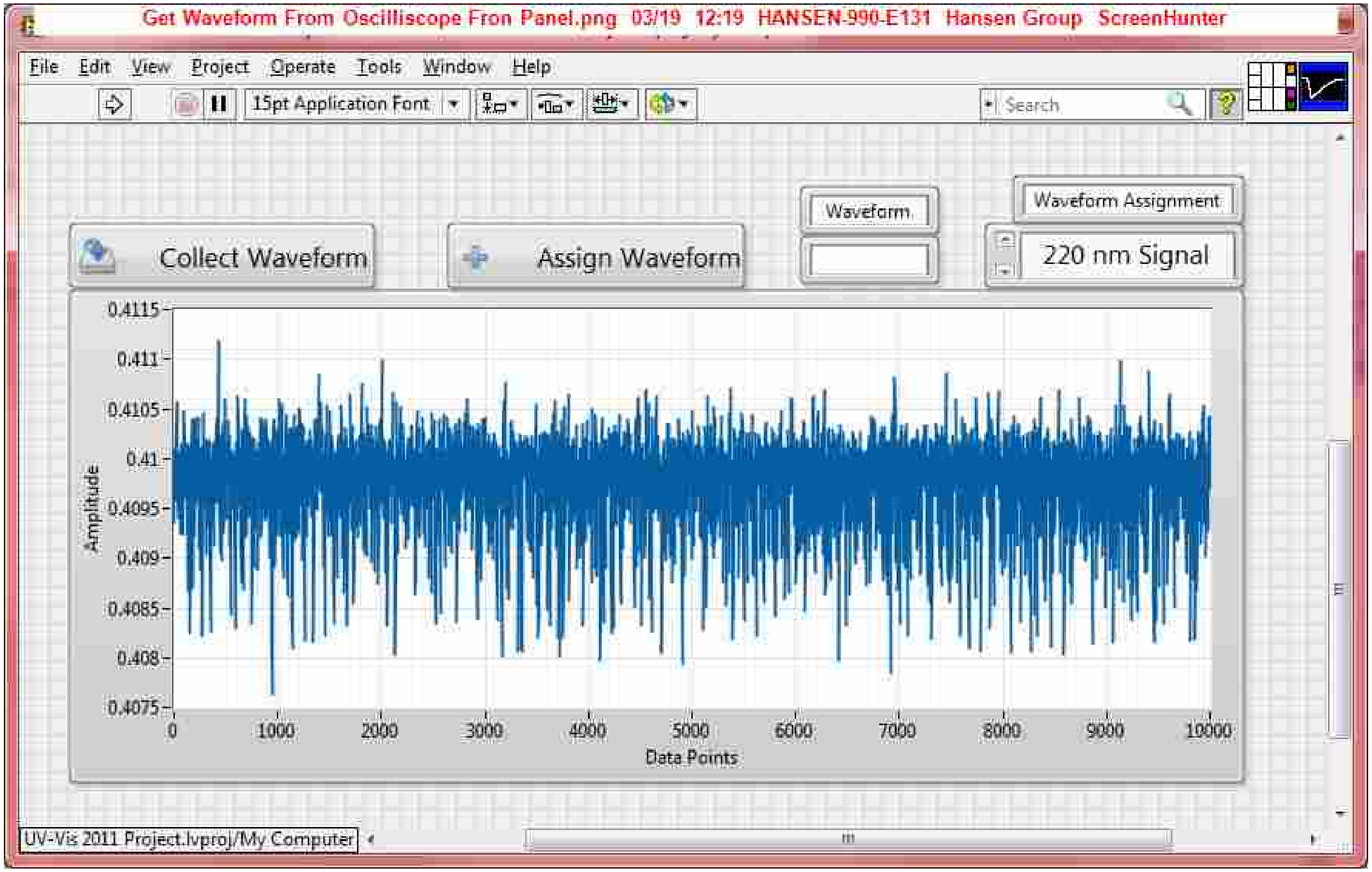

Waveform Assignment: 220 nm Signal

The Get Waveform VI is placed here because this is the place it is called in the main VI

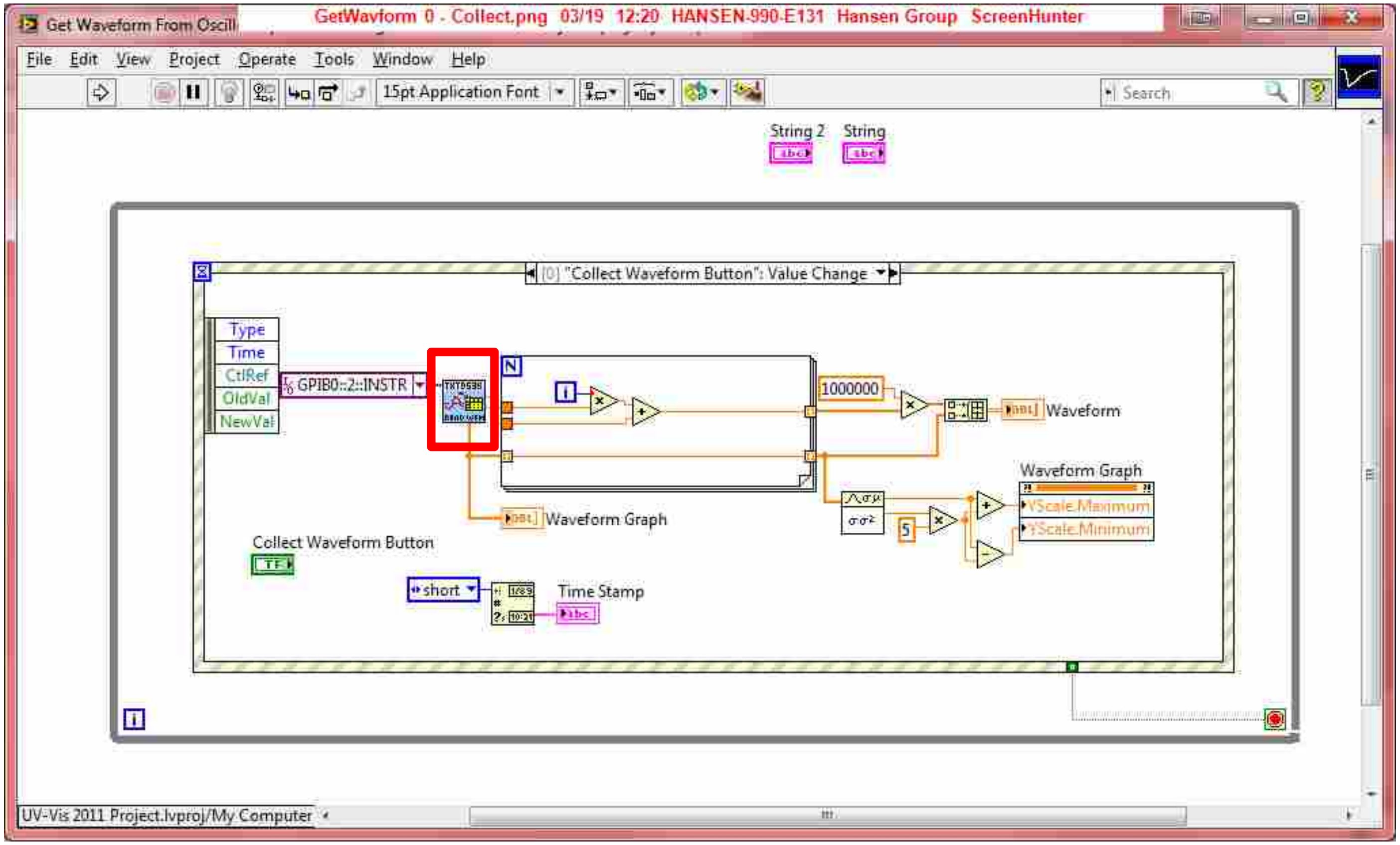

The sub-vi designated in red is an instrument driver for the oscilloscope. (Instrument drivers are VI's usually built by the manufacturer of the instrument and posted on NI.com) It collects what is displayed on the oscilloscope. The "for loop" is used to build a 2-D array for saving. Then the part to the far right is used to adjust the scale of the plot in a view of my preference that may need to be adjusted in the future.

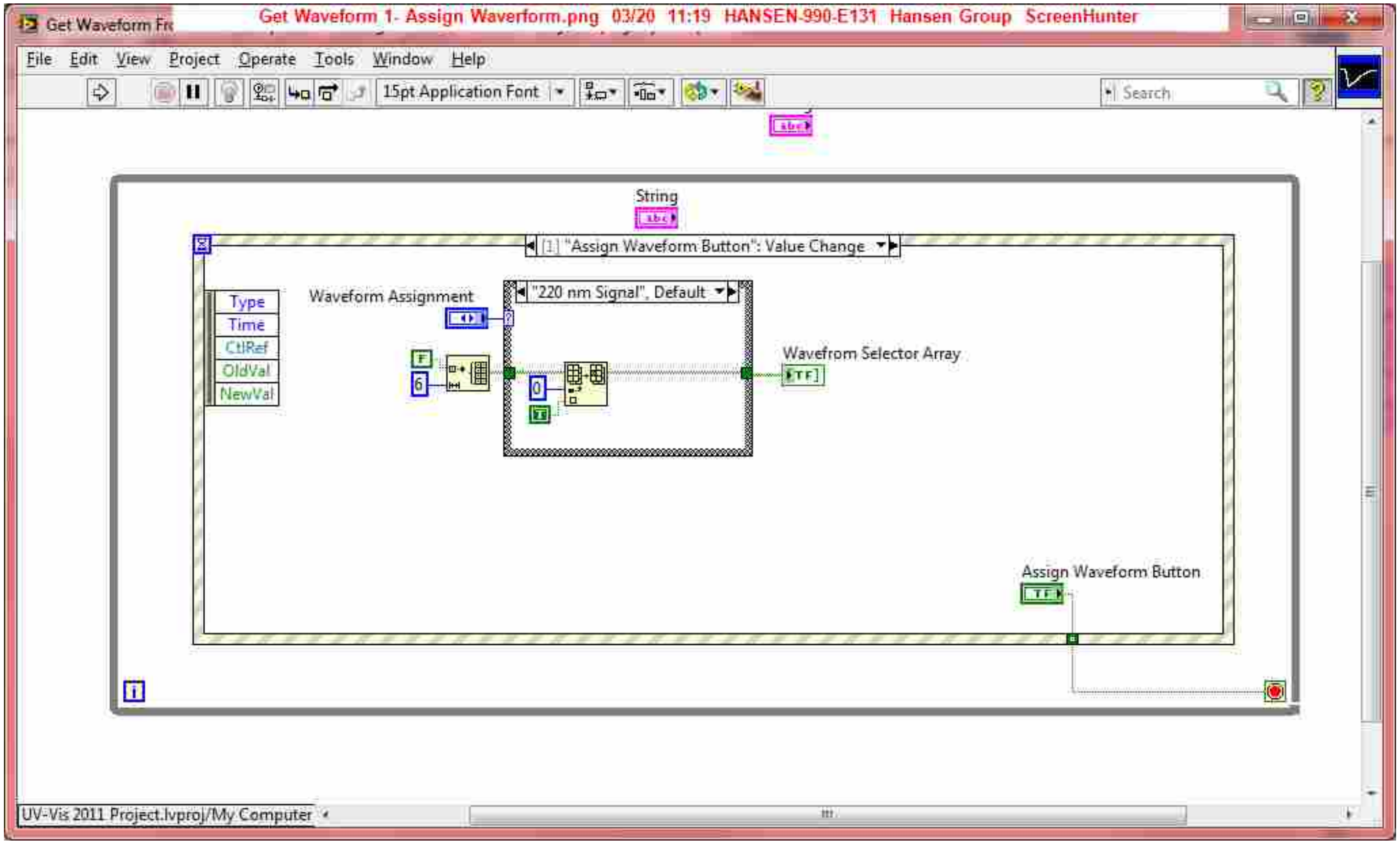

This assigns the waveform to transfer back to the main VI

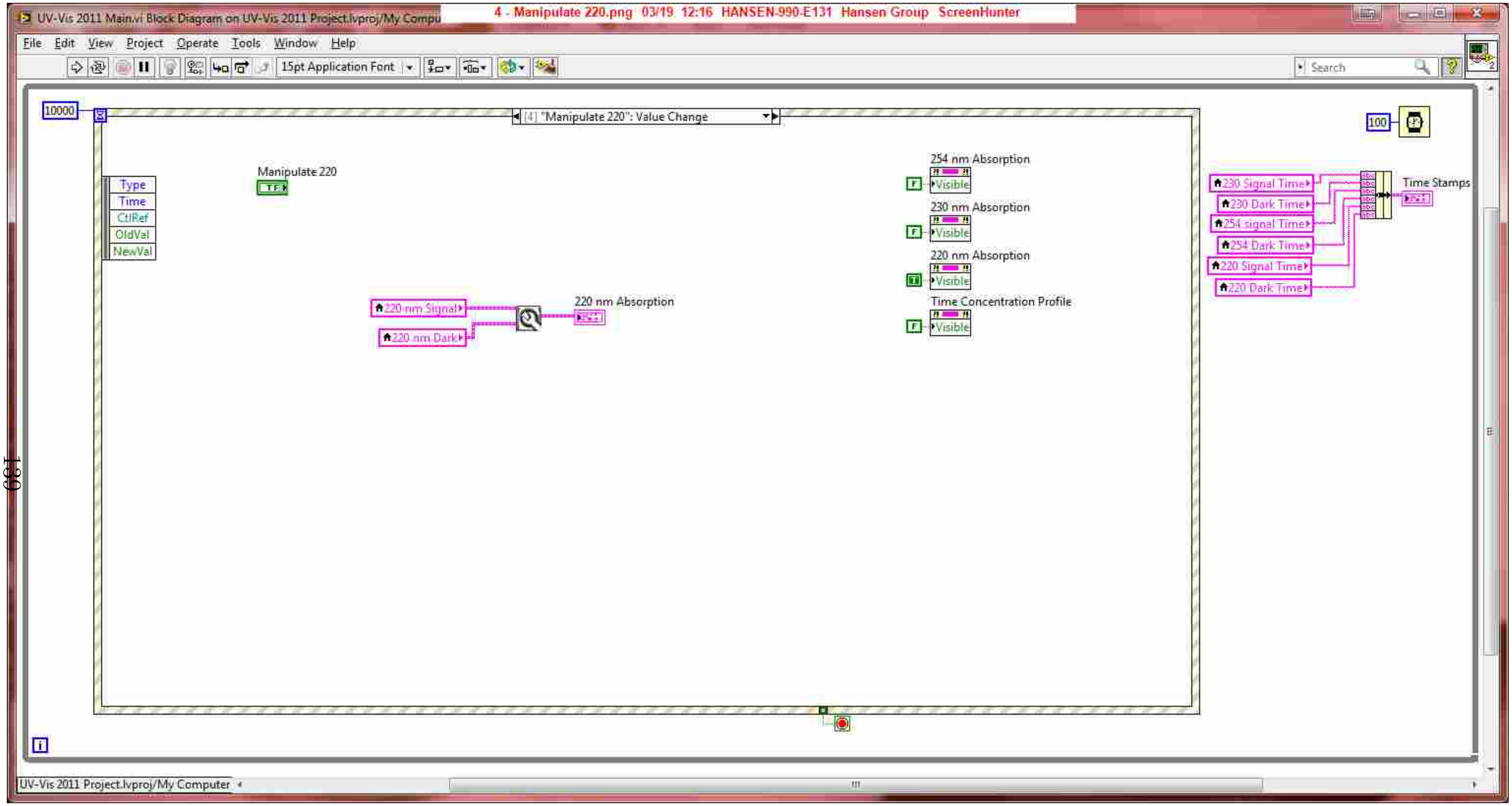

This event triggers the manipulate waveform VI.

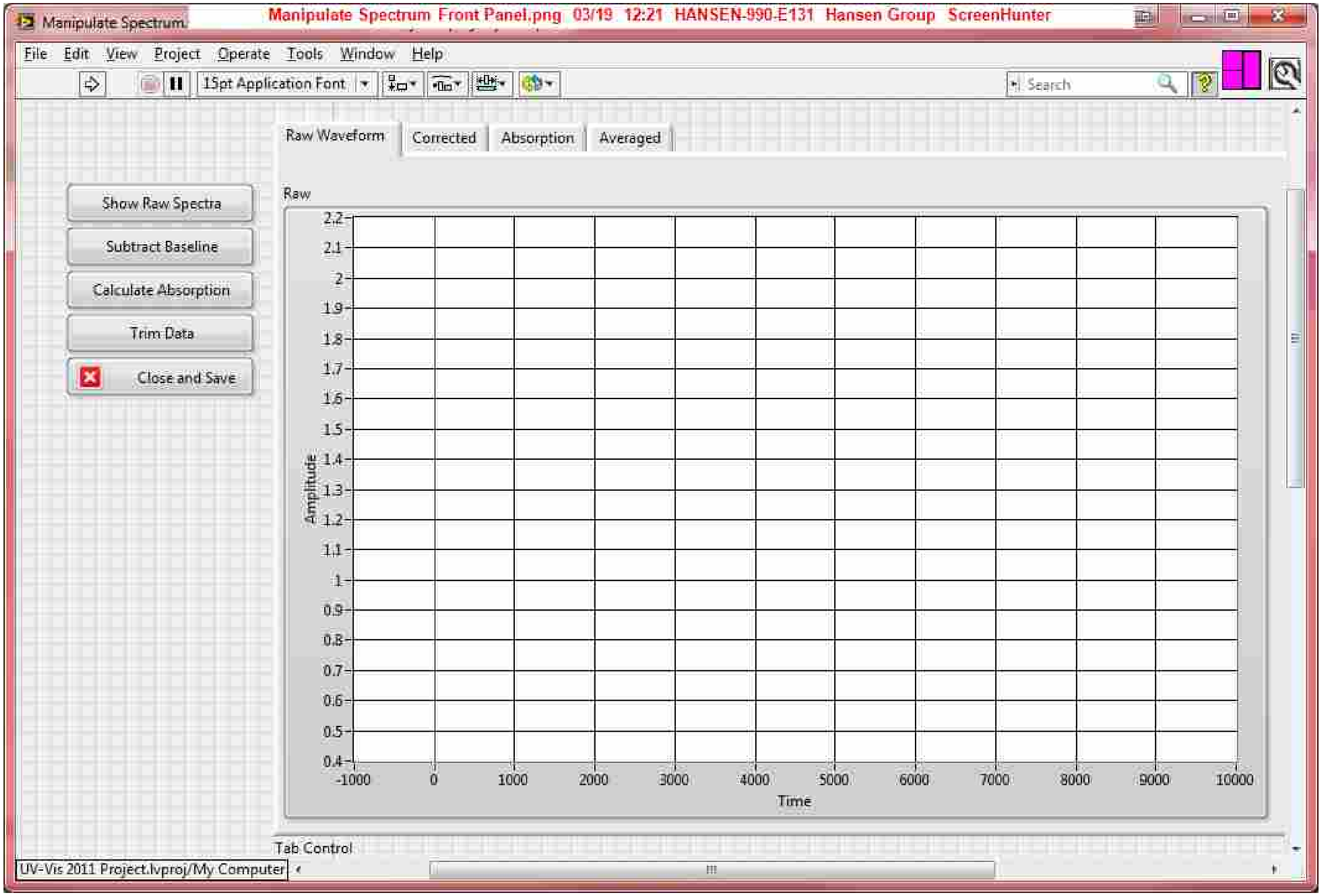

As seen before this is the Manipulate Waveform VI what follows is the associated block diagram

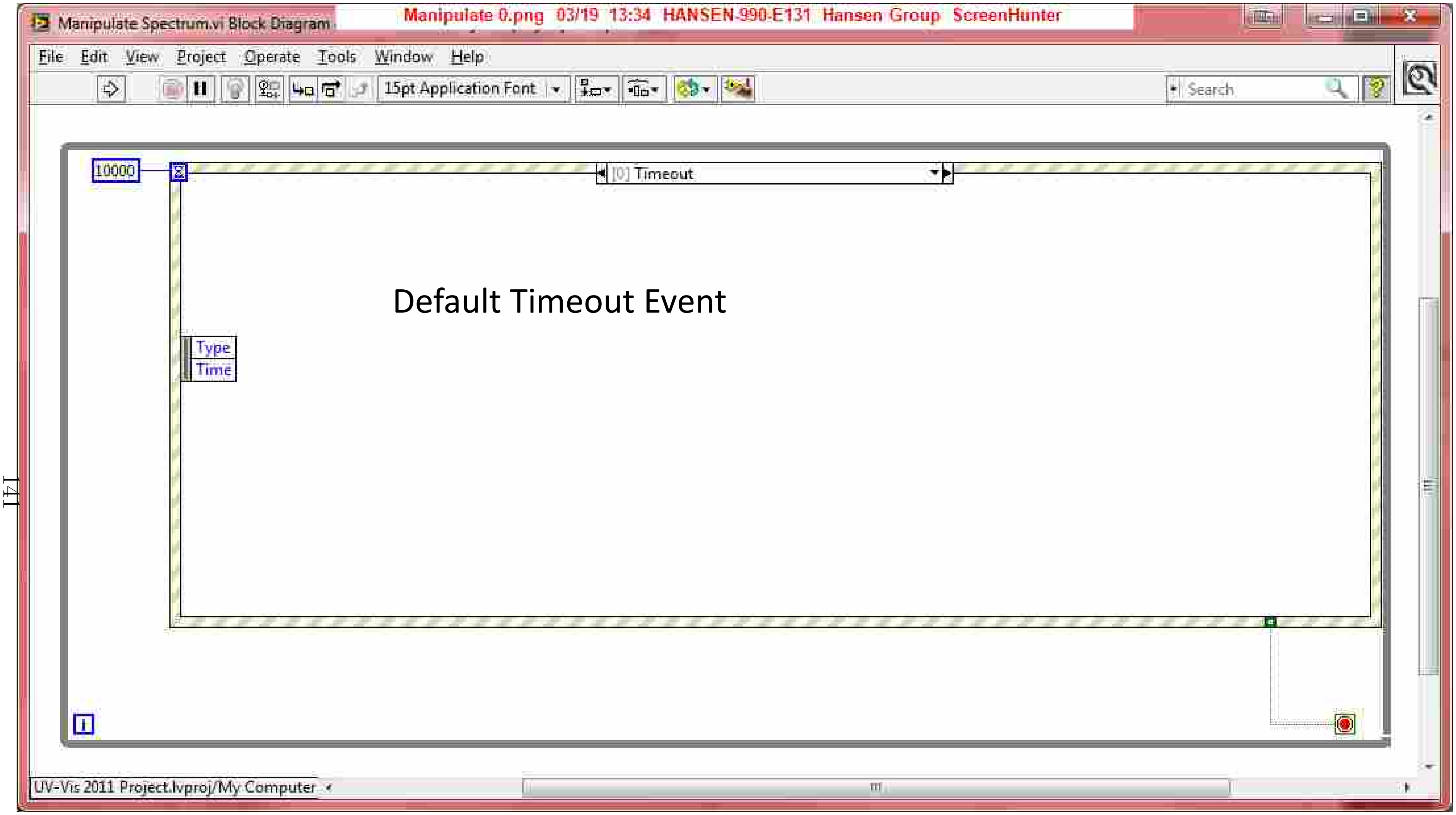
Manipulate Spectrum.vi Block Diagram
Manipulate 0.png 03/19 13:34 HANSEN-990-E131 Hansen Group ScreenHunter
File
Edit
View
Project
Operate
Tools
Window
Help
15pt Application Font
Search
10000
[0] Timeout
Default Timeout Event
Type
Time
i
UV-Vis 2011 Project.lvproj/My Computer

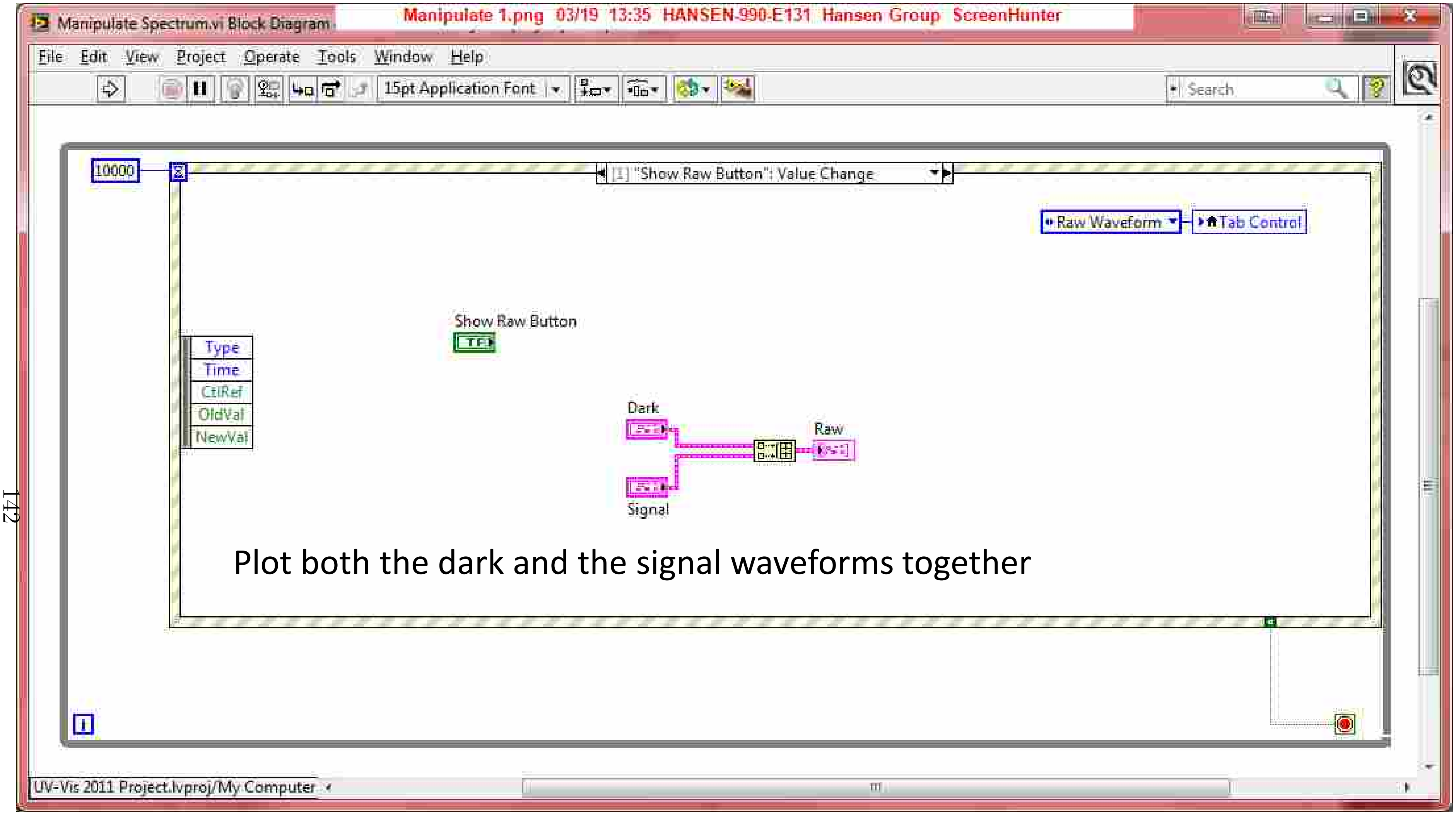

Plot both the dark and the signal waveforms together

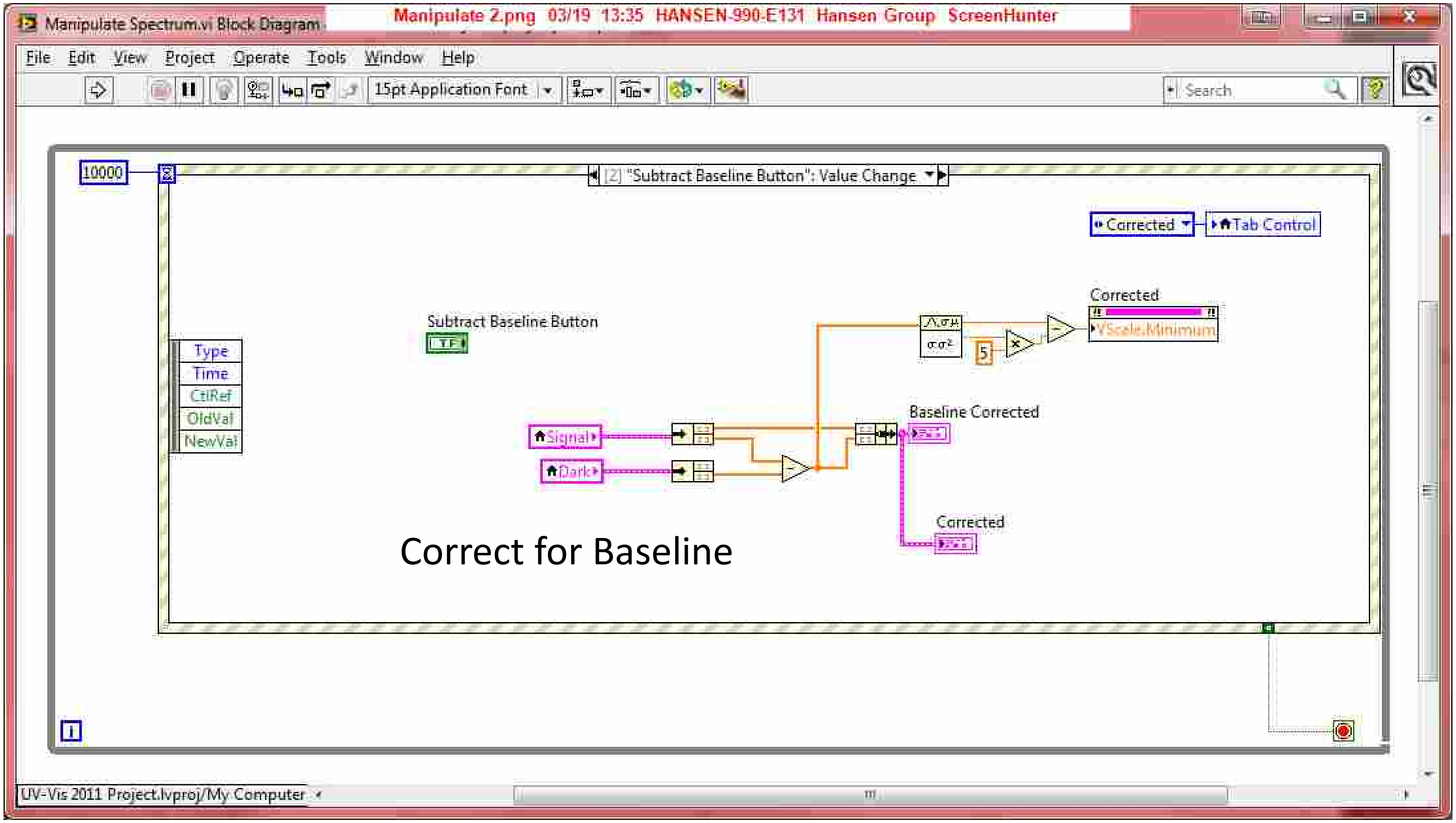
Manipulate Spectrum.vi Block Diagram
Manipulate 2.png 03/19 13:35 HANSEN-990-E131 Hansen Group ScreenHunter
File Edit View Project Operate Tools Window Help
15pt Application Font
Search
10000
[2] "Subtract Baseline Button": Value Change
Corrected
Tab Control
Corrected
VScale.Minimum
Subtract Baseline Button
TF
Type
Time
CtlRef
OldVal
NewVal
5
Baseline Corrected
Signal
Dark
Corrected
Correct for Baseline
i
UV-Vis 2011 Project.lvproj/My Computer

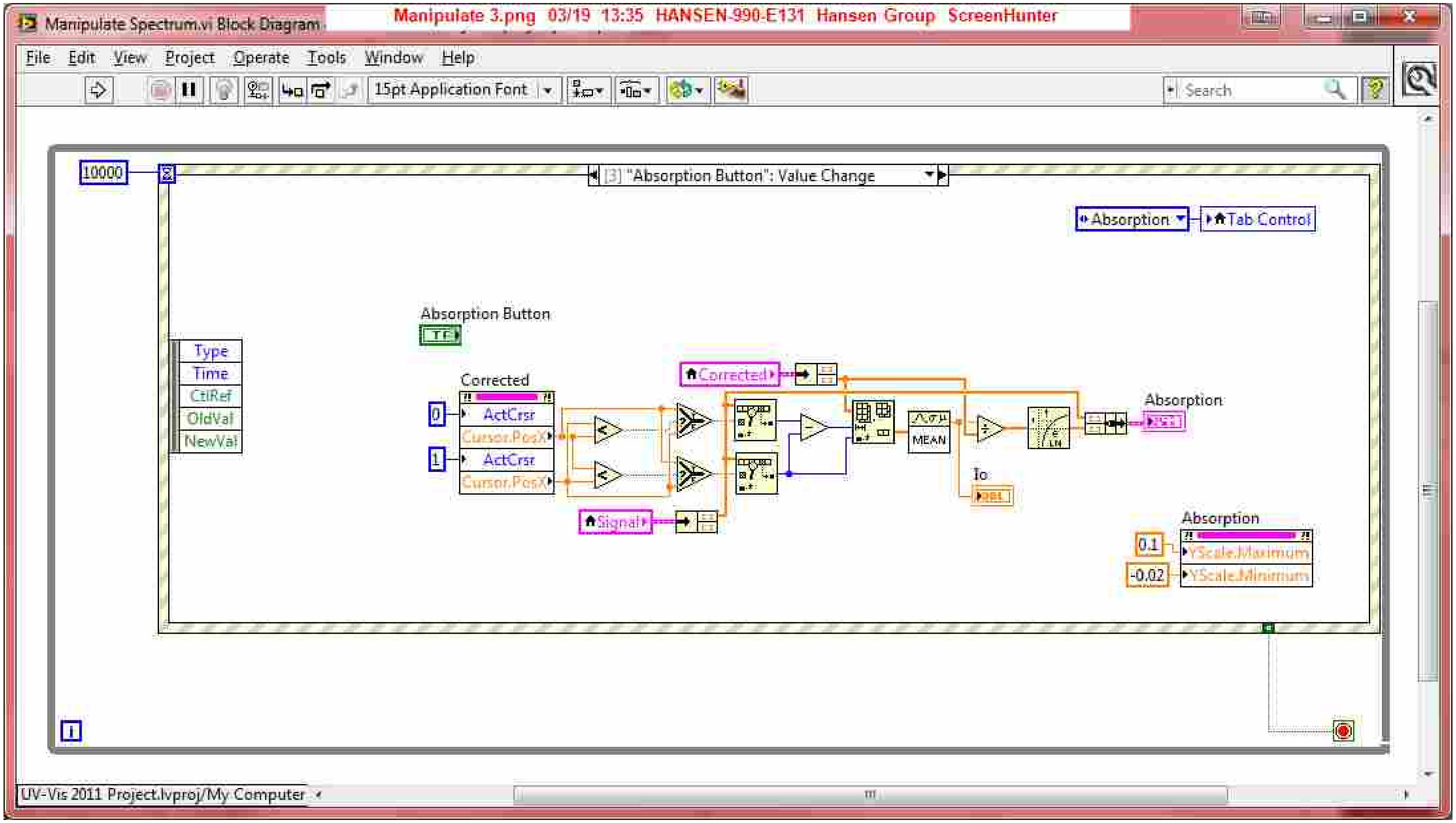

This is a bit complicated but it allows for to use of active cursors on plots to select the I_o region. The complication comes from the ability to swap the two cursors and it corrects itself. The program then takes the mean of all data points between the cursors and calculates absorption.

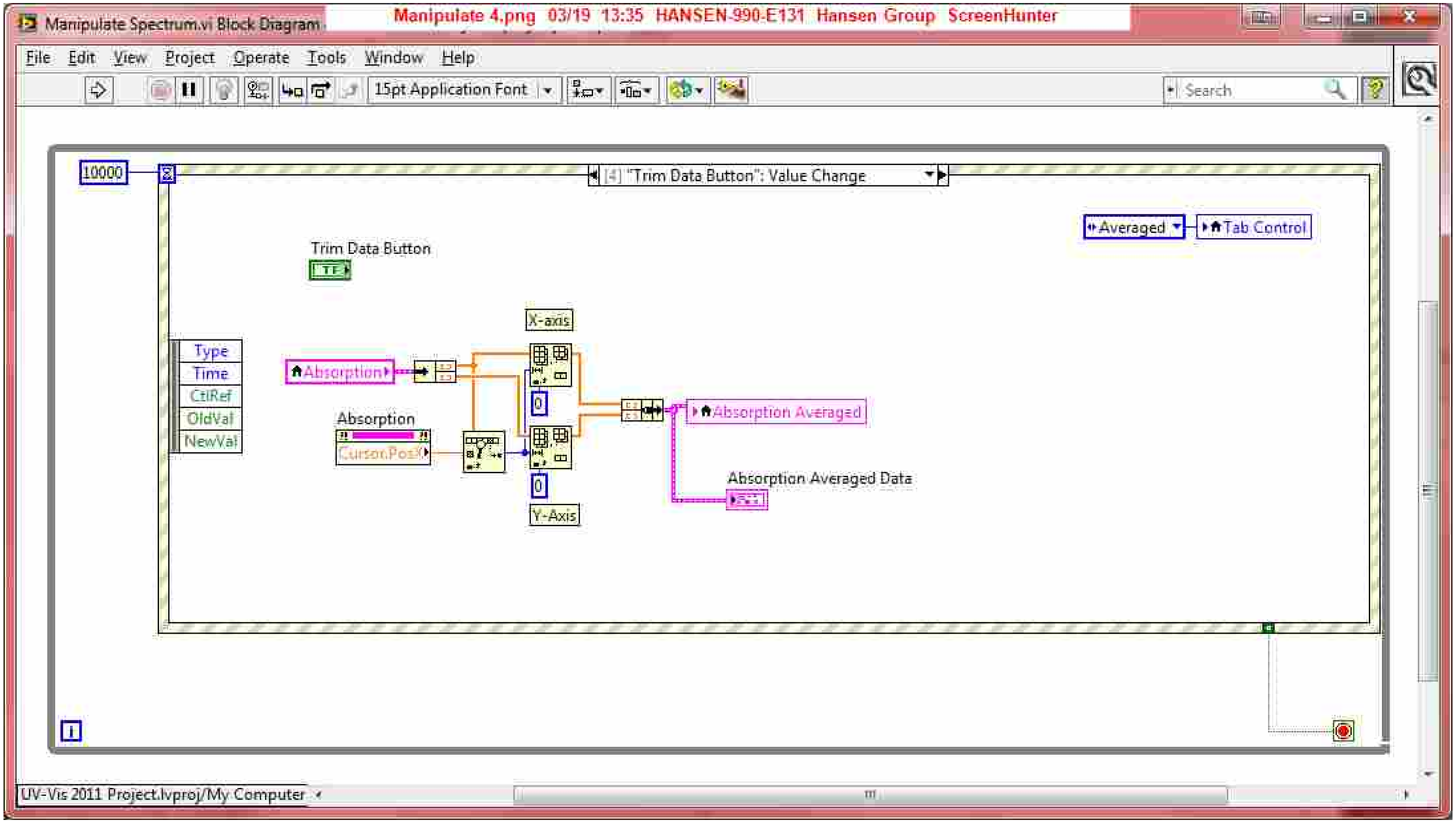

This is similar to the last slide but with one cursor. Data is trimmed at the cursor.

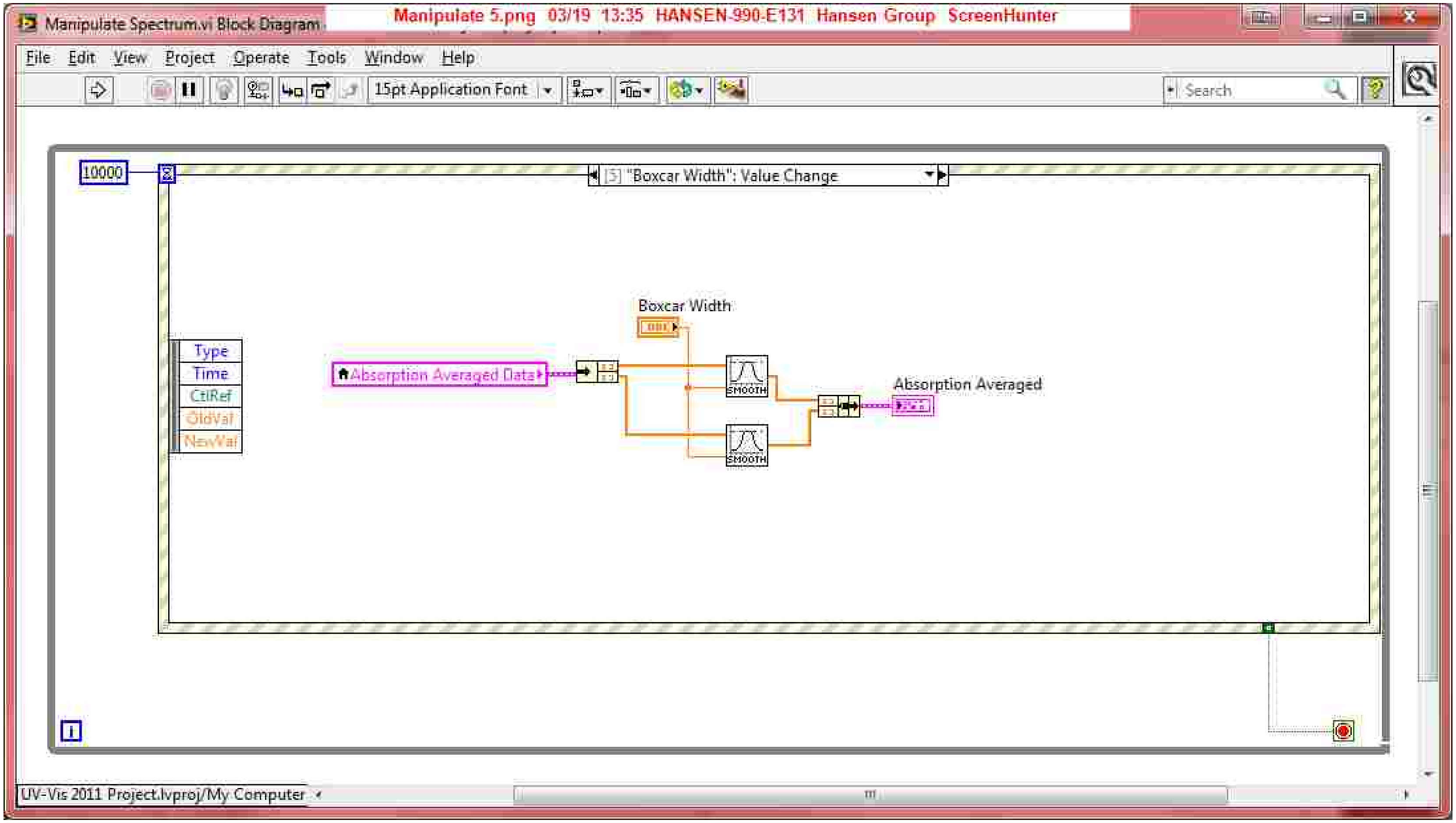

A boxcar averager is used to smooth the decay. Notice the top of the event structure says the event is triggered by a value change in the boxcar width which is a control on the front panel so it updates every time a new value is selected.

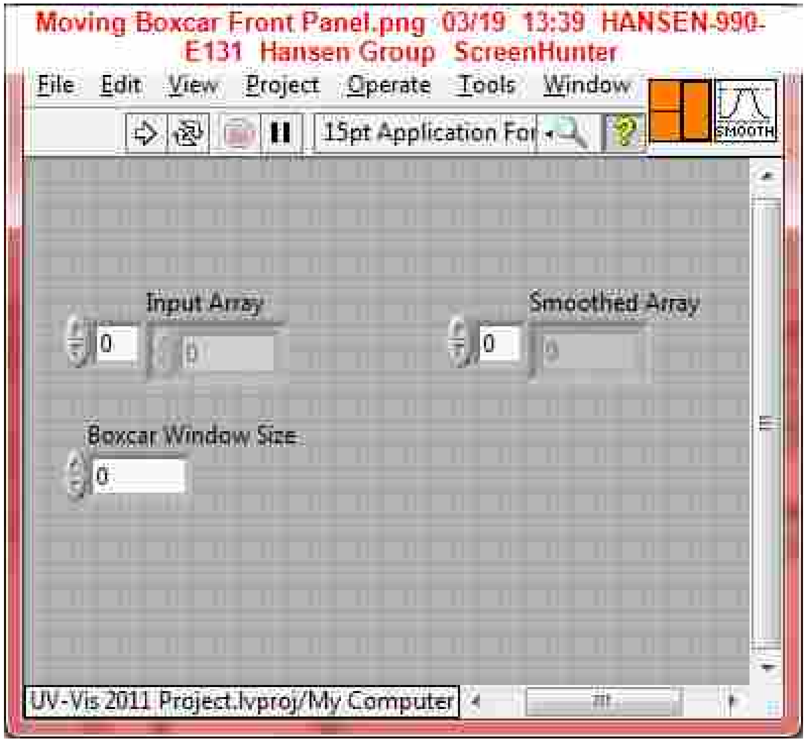

Moving Boxcar Front Panel.png 03/19 13:39 HANSEN-990-E131 Hansen Group ScreenHunter

Input Array 0 0

Smoothed Array 0 0

Boxcar Window Size 0

UV-Vis 2011 Project.lvproj/My Computer

Moving Boxcar interface, the block diagram follows

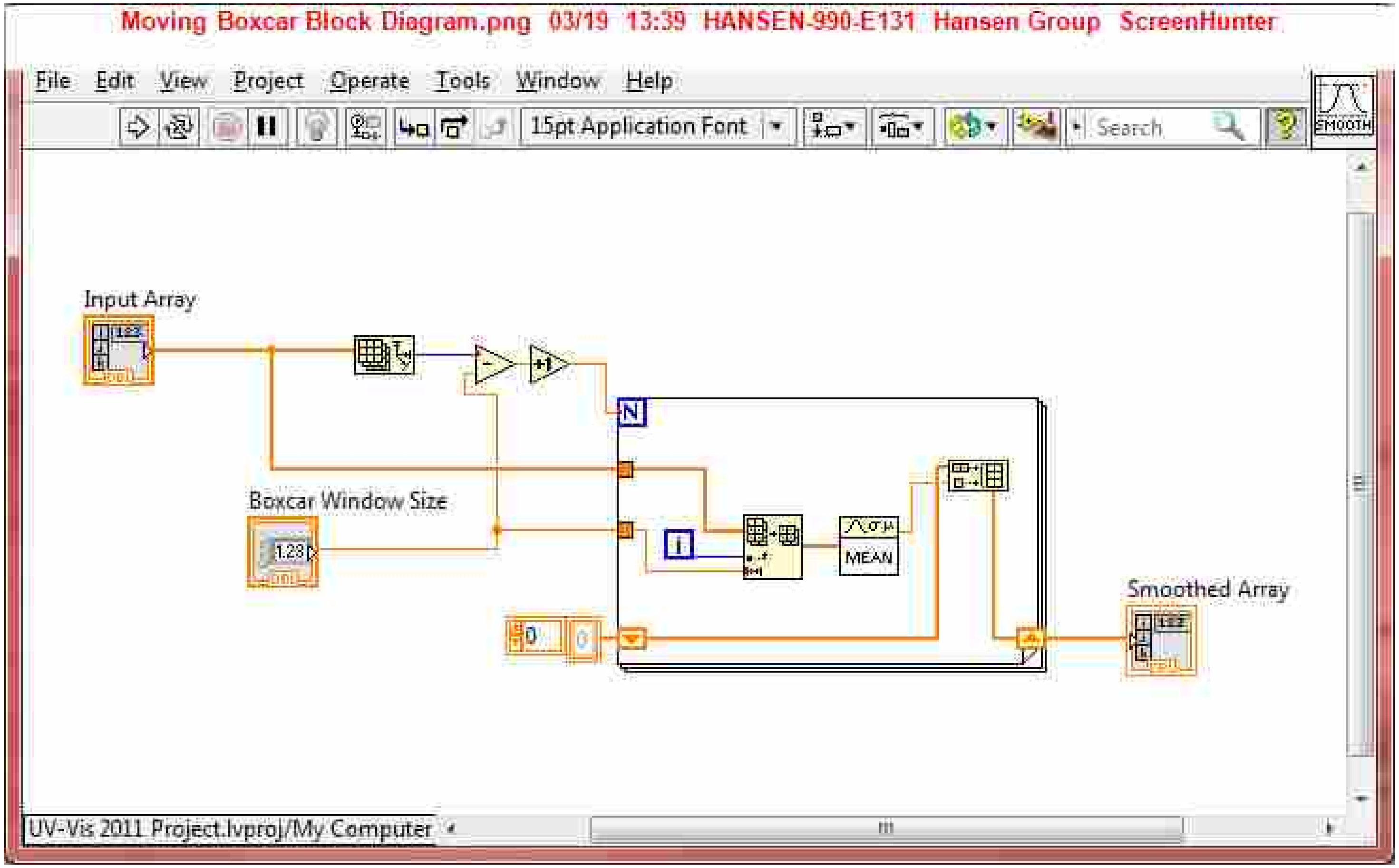

The “for loop” is set to the array size minus the boxcar width plus 1. So if there are 100 data points with a boxcar width of 4 the result will have 97 points. Then we take the array and take the data points from the iteration (i) and all data up to the boxcar width and average them.

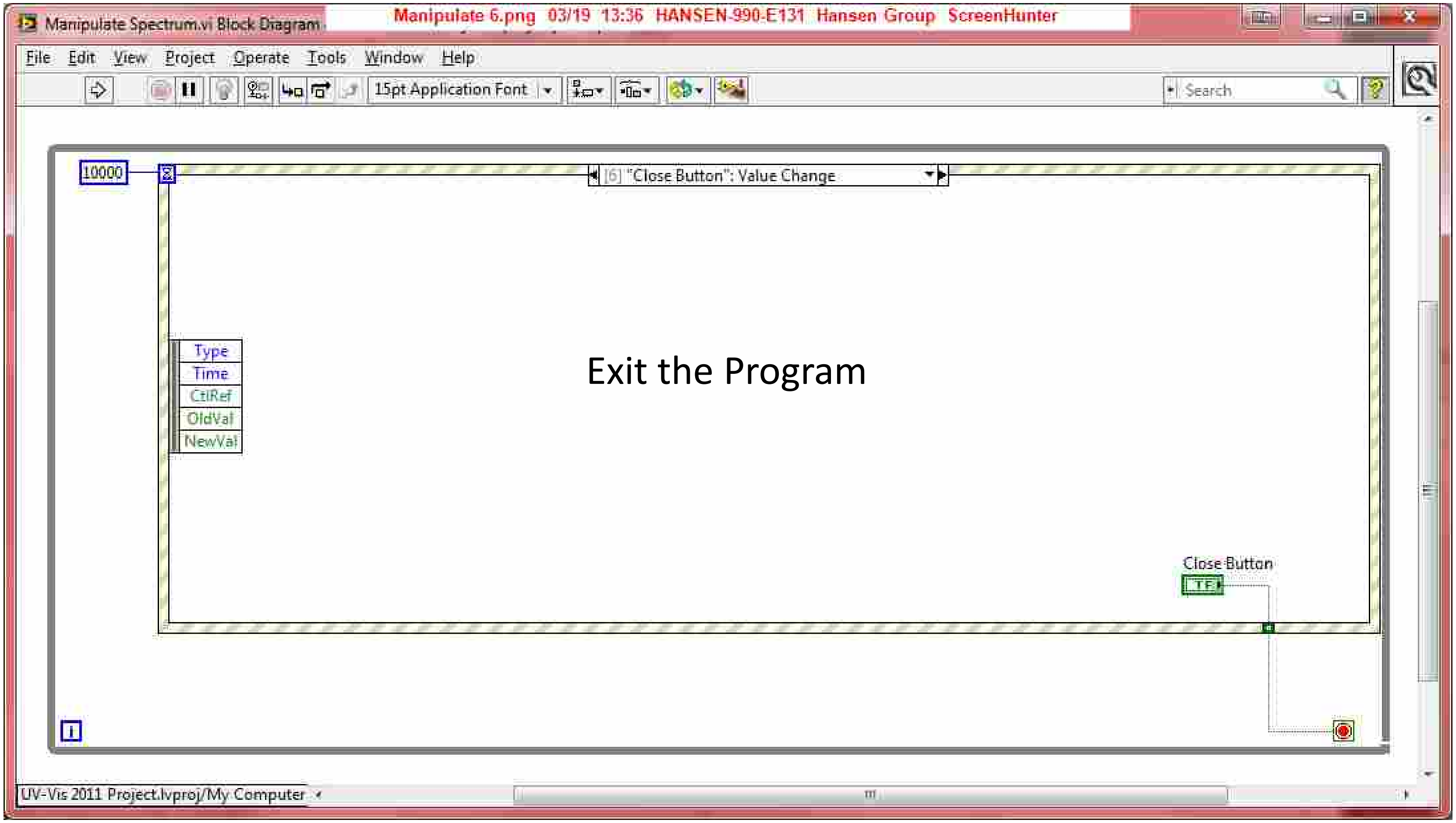

Exit the Program

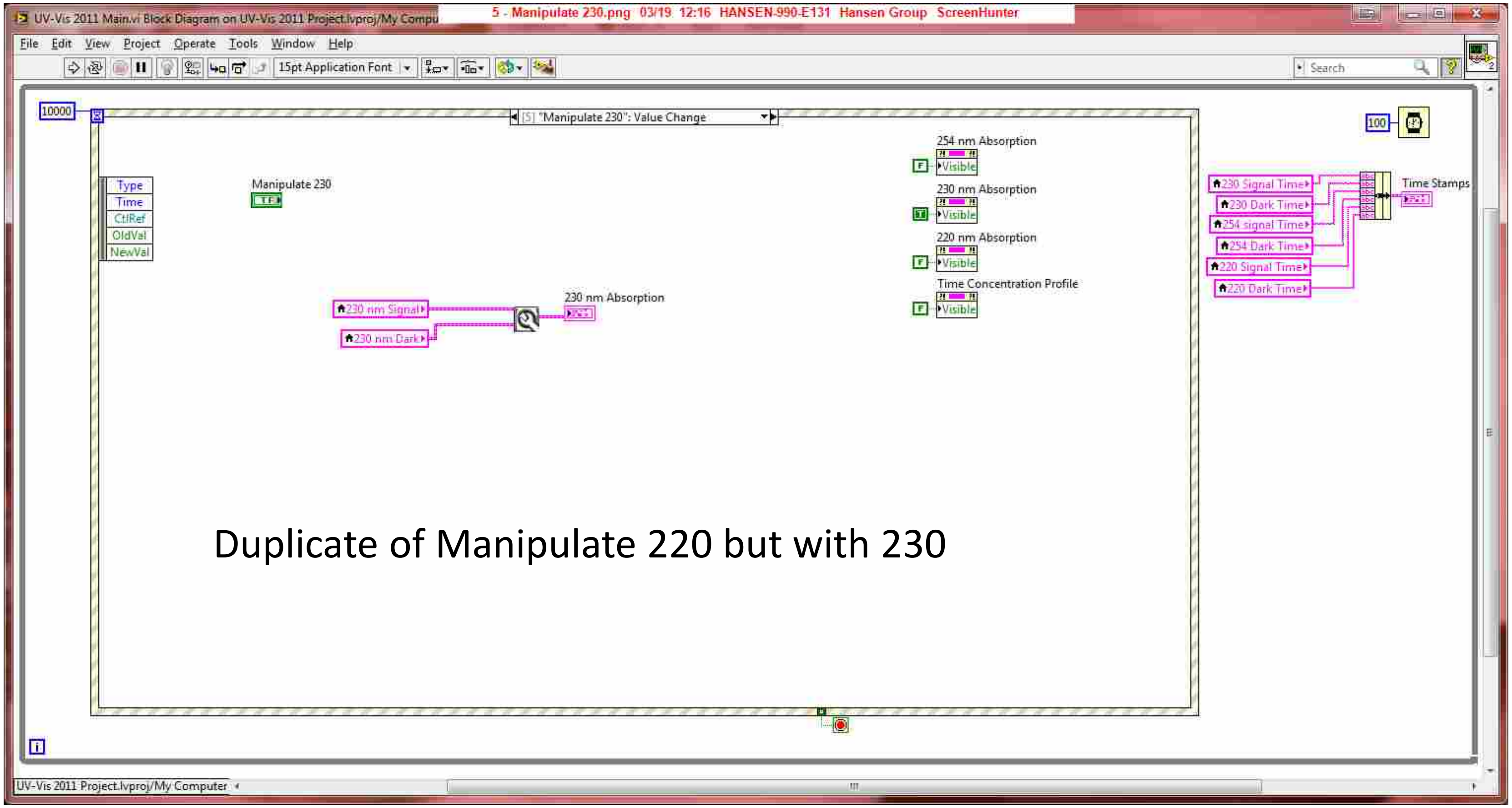

Duplicate of Manipulate 220 but with 230

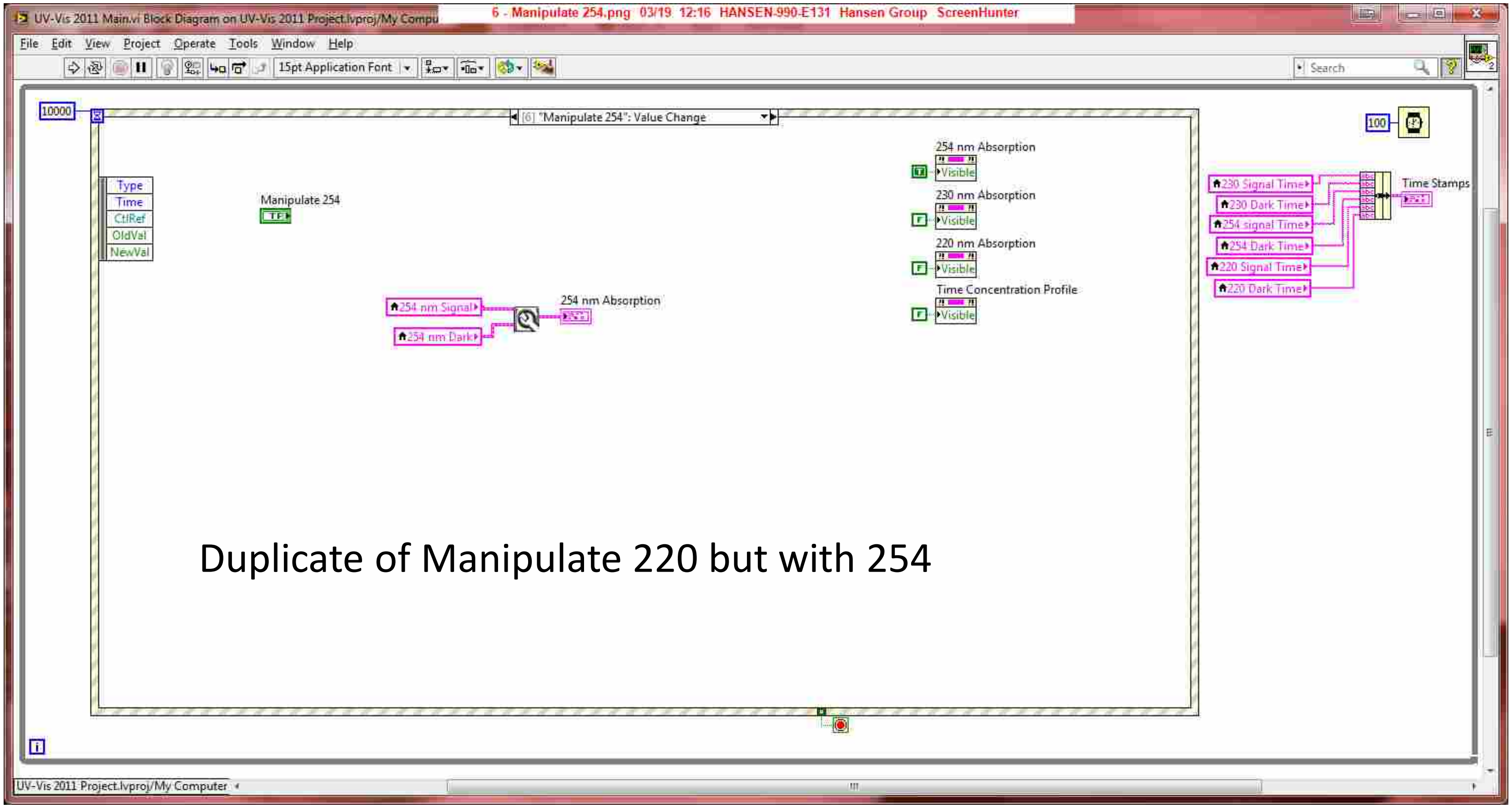

Duplicate of Manipulate 220 but with 254

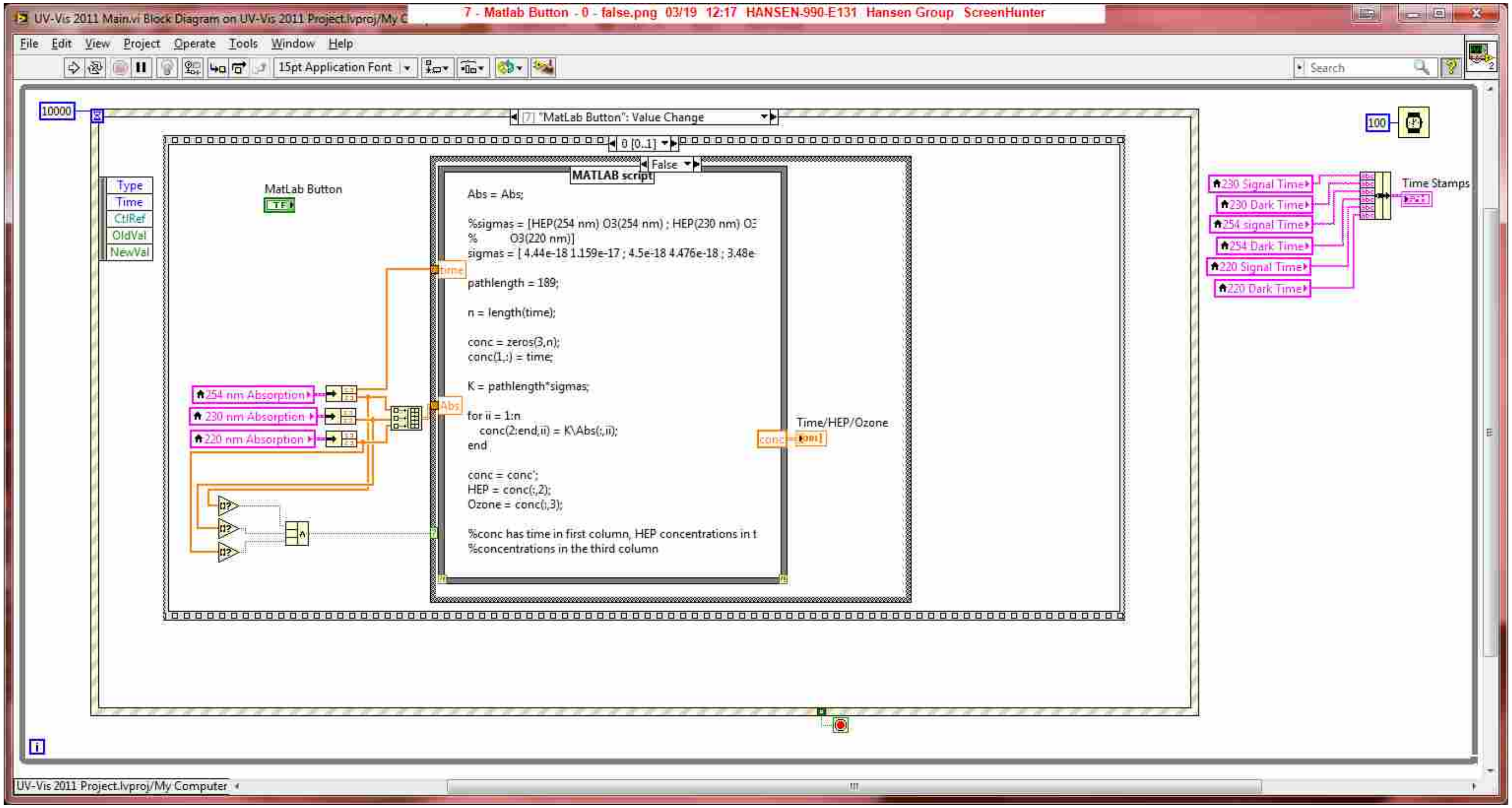

MATLAB script

```
Abs = Abs;

%sigmas = [HEP(254 nm) O3(254 nm) ; HEP(230 nm) O3
%          O3(220 nm)]
sigmas = [ 4.44e-18 1.159e-17 ; 4.5e-18 4.476e-18 ; 3.48e

pathlength = 189;

n = length(time);

conc = zeros(3,n);
conc(1,:) = time;

K = pathlength*sigmas;

for ii = 1:n
   conc(2:end,ii) = K\Abs(:,ii);
end

conc = conc';
HEP = conc(:,2);
Ozone = conc(:,3);

%conc has time in first column, HEP concentrations in t
%concentrations in the third column
```

A Matlab structure is a special download but free. Use Matlab to verify code function and then copy the code into the structure. Here is a least squares regression to the three wavelength decays. The cross sections are built into the code because they are constant. But if this program is adapted to a different experiment then the cross sections need to be updated. The output is a 2-D Array with Time, HEP, and Ozone as columns.

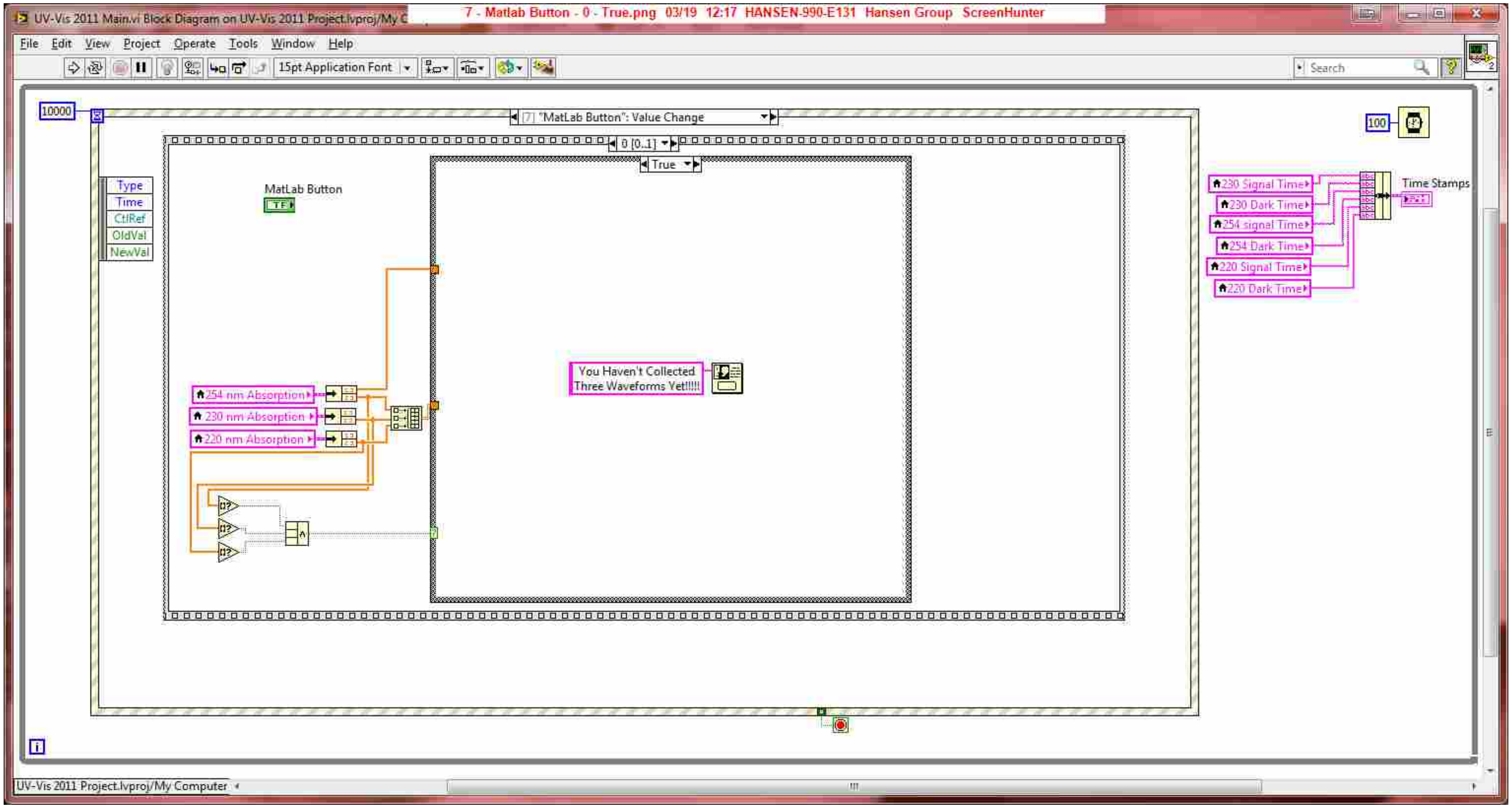

UV-Vis 2011 Main.vi Block Diagram on UV-Vis 2011 Project.lvproj/My C

7 - Matlab Button - 0 - True.png 03/19 12:17 HANSEN-990-E131 Hansen Group ScreenHunter

You Haven't Collected Three Waveforms Yet!!!!!

If three waveforms haven't been collected and adjusted then an error message appears.

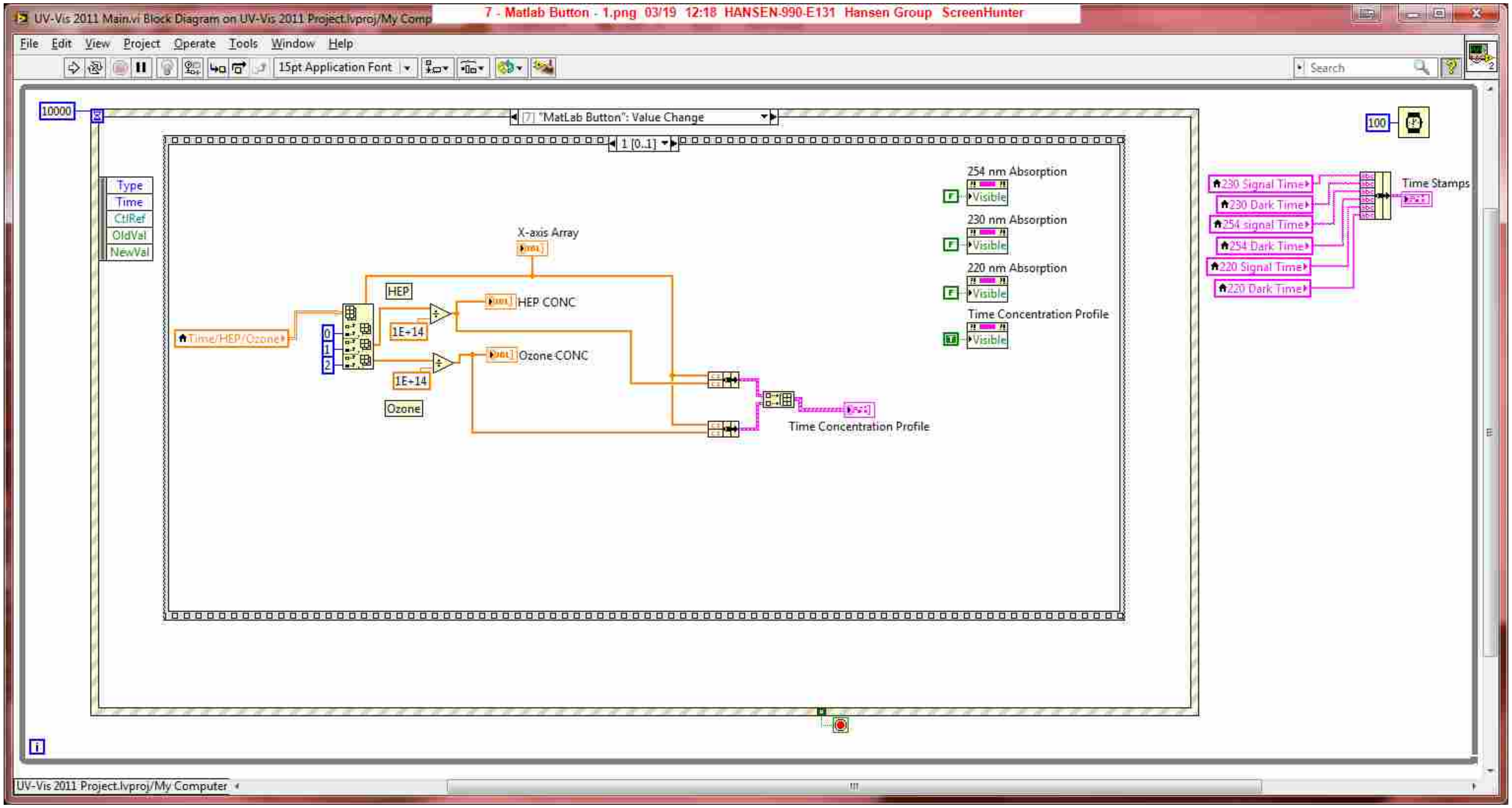

After the matlab least regression this adjusts the units and plots the results

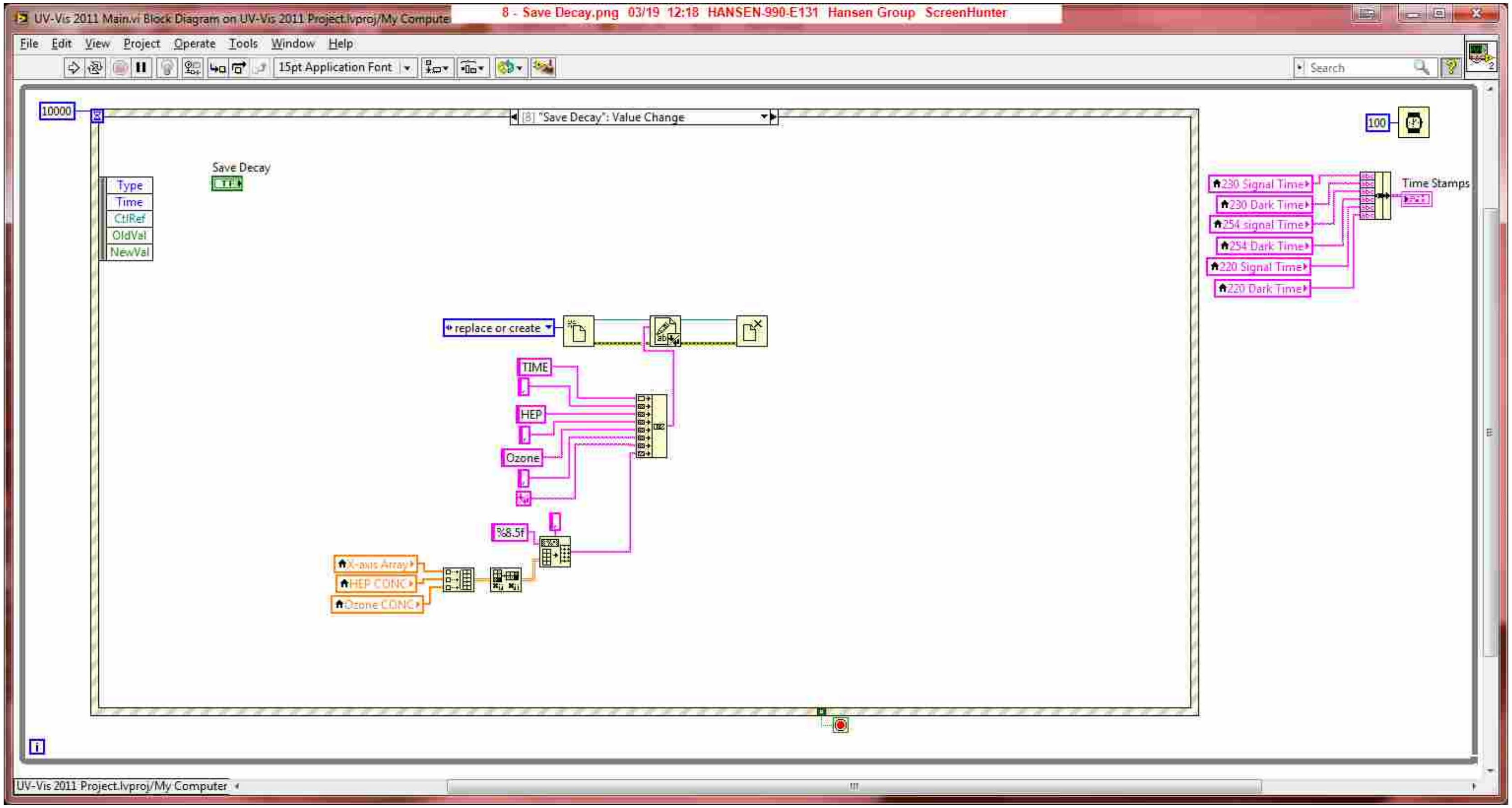

Saves the file with headers as a csv file.

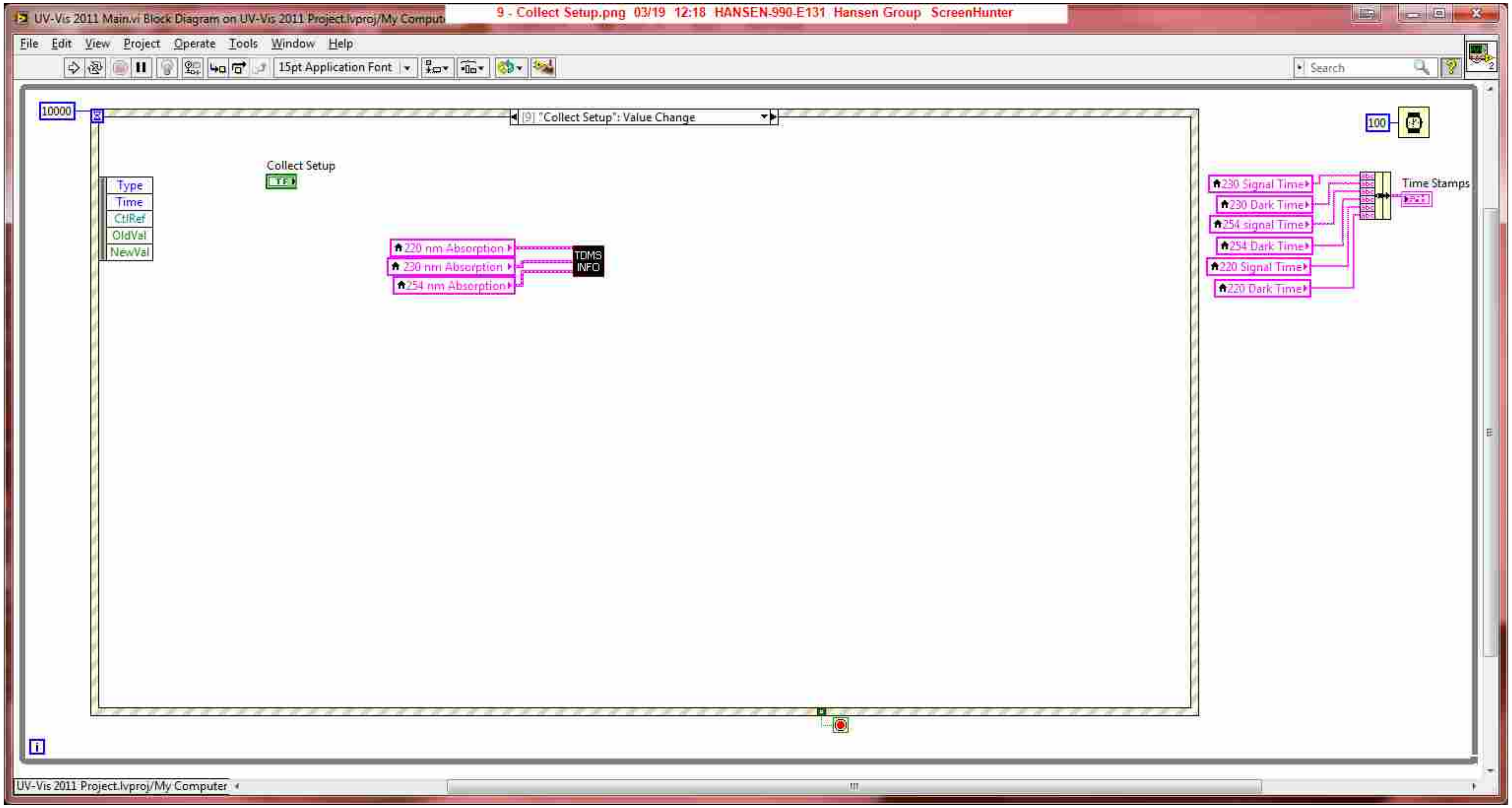

Collect flows, temperatures, and raw data

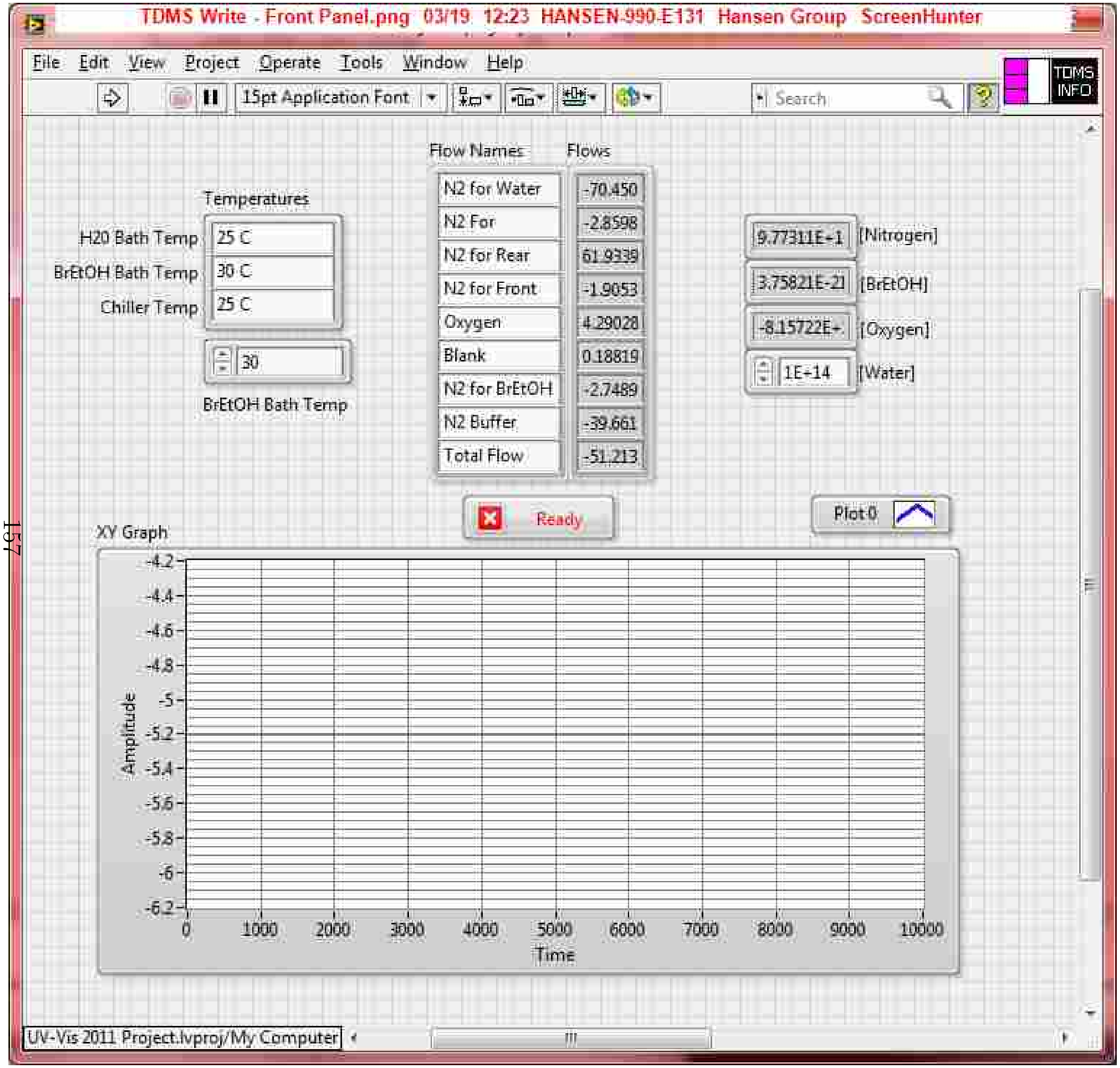

Temperatures

H20 Bath Temp	25 C
BrEtOH Bath Temp	30 C
Chiller Temp	25 C

BrEtOH Bath Temp: 30

Flow Names	Flows
N2 for Water	-70.450
N2 For	-2.8598
N2 for Rear	61.9339
N2 for Front	-1.9053
Oxygen	4.29028
Blank	0.18819
N2 for BrEtOH	-2.7489
N2 Buffer	-39.661
Total Flow	-51.213

9.77311E+1	[Nitrogen]
3.75821E-21	[BrEtOH]
-8.15722E-	[Oxygen]
1E+14	[Water]

TDMS File Saver

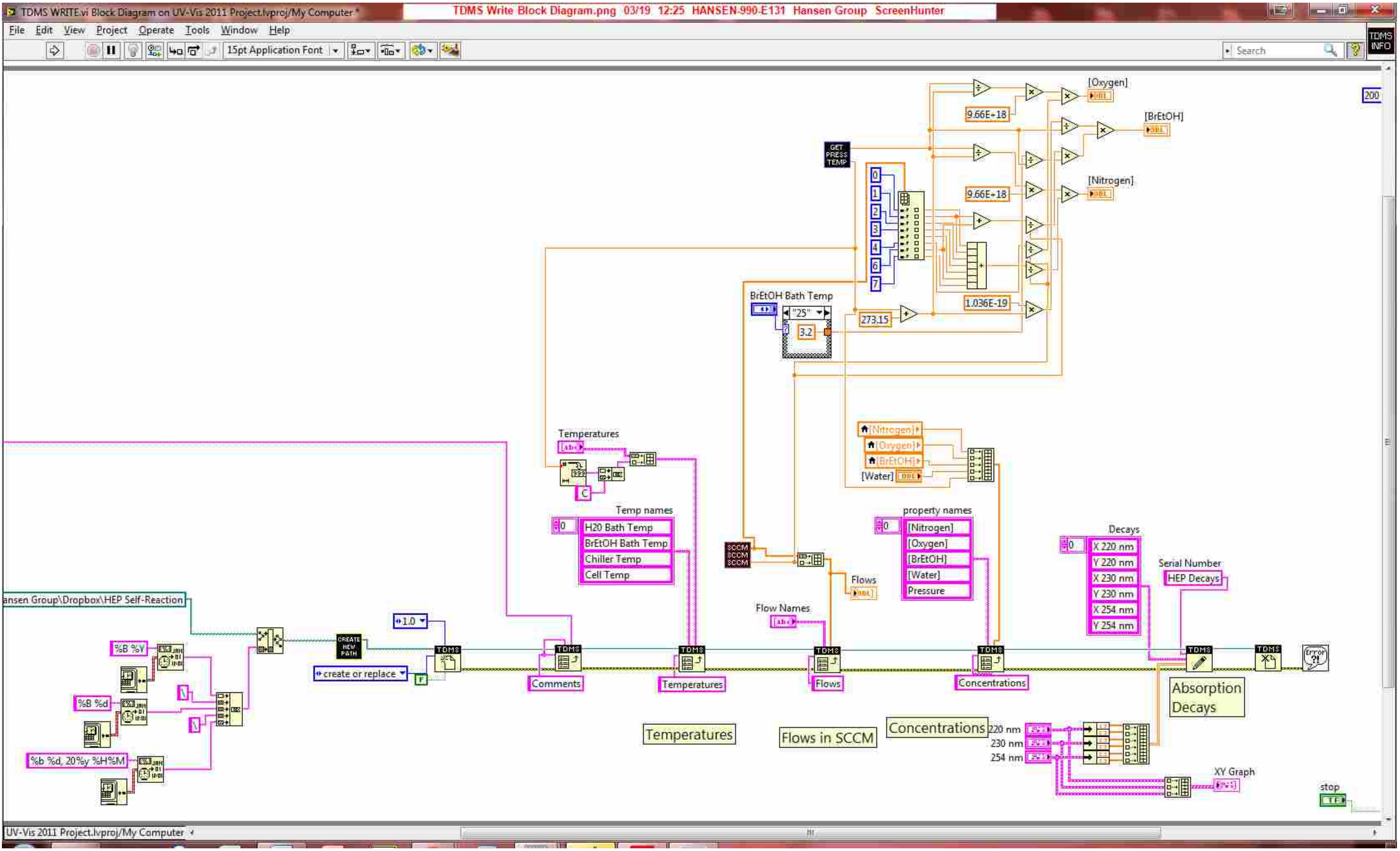

The TDMS file is a complex file but is useful for pooling lots of data sources. It requires a lot of work but here is where problems with the DAQ will occur usually just loose wires.

7.4 UV-Vis Absorption with CCD Detection

The upside of PMT experiments is the time to acquire a self-reaction decay and the difficulty is the loss of wavelength discrimination. The CCD has the opposite figures of merit. The CCD has great discrimination but experiments are very slow. The CCD should be used as an exploratory experiment to discover contaminants in absorption spectra. Then the PMT experiments can be used to measure kinetics. The CCD experiments are more difficult and finicky than the PMT experiments but this is due to the complexity of instruments used. The following will attempt to describe the use of LabVIEW as well as describe the physical wiring needed to connect instruments.

UV-Vis slow-flow flash photolysis using the spectrograph and CCD

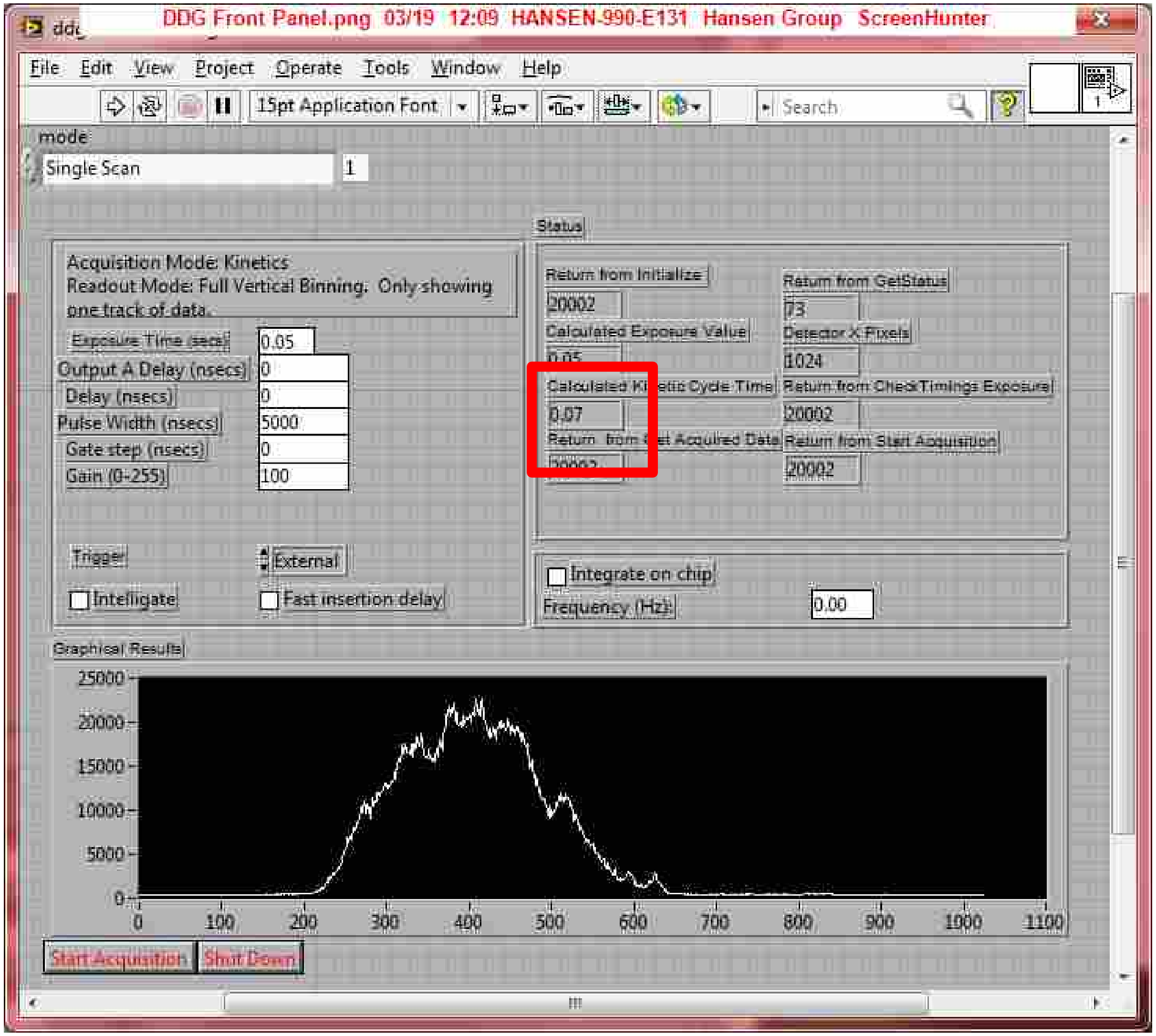

mode: Single Scan 1

Acquisition Mode: Kinetics
Readout Mode: Full Vertical Binning. Only showing one track of data.

Exposure Time (secs): 0.05
Output A Delay (nsecs): 0
Delay (nsecs): 0
Pulse Width (nsecs): 5000
Gate step (nsecs): 0
Gain (0-255): 100

Trigger: External
☐ Intelligate
☐ Fast insertion delay

Return from Initialize: 20002
Calculated Exposure Value: 0.05
Calculated Kinetic Cycle Time: 0.07
Return from Get Acquired Data: 20002
Return from GetStatus: 73
Detector X Pixels: 1024
Return from CheckTimings Exposure: 20002
Return from Start Acquisition: 20002

☐ Integrate on chip
Frequency (Hz): 0.00

This VI is the DDG or digital delay generator. It is used in conjunction with the VI Taylor Main 2.1. Originally these two programs were meant to run as one but worked better as two. They both need to be running and they pass information through a global variable. This VI must be started first. When the white arrow is pressed the program will check with the CCD to see if it's ready. If it communicates properly, the highlighted value will change from 0.07 to 0.08. The other values here remain the same but you can change some variables such as exposure time and gain.

Taylor Main 2.1

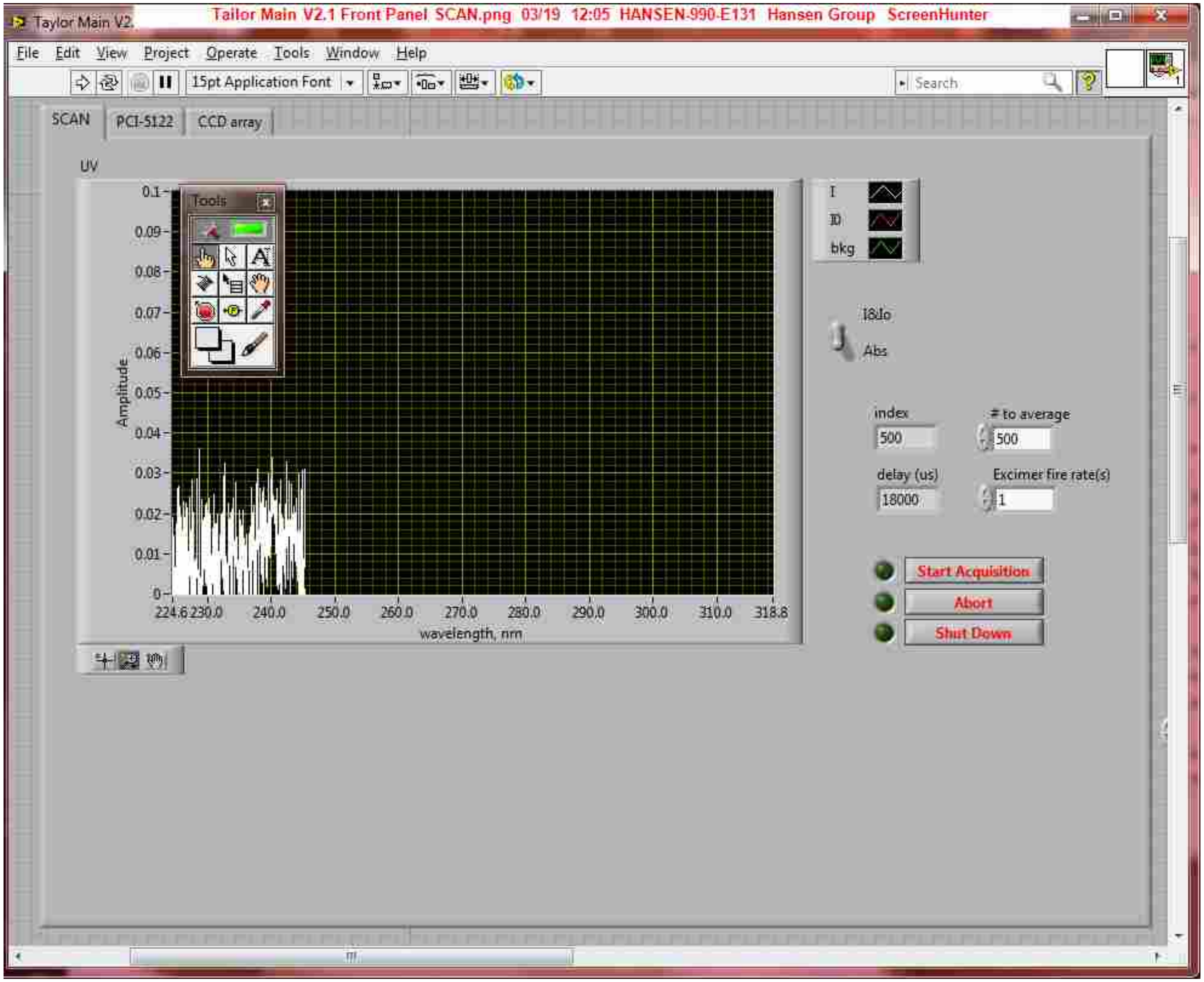

index: 500

to average: 500

delay (us): 18000

Excimer fire rate(s): 1

This VI sets the parameters for the DDG and records the data received back from the DDG. The original file for this VI was created by David Robichaud and is named Main 3-9-09.vi. This one stripped out some bulkiness and simplified other processes.

Overview of Steps

1. The DDG is set with the DDG Vi and is ready to collect data. The Main Vi controls the triggers and sets the delay times.
2. The main.vi starts with first delay time set by the user.
3. The Main Vi triggers both the DDG and the CCD to collect data at the specified delay time which will be I_o.
4. Then the Main Vi triggers the Excimer to fire, a photodiode is triggered from the excimer light that triggers the DDG Vi and the CCD to collect I at the specified delay time.
5. This process is repeated until the requisite number of scans have been collected to average and then moves on to the next delay time until all delay times have been collected.

The DDG is a simple LabVIEW program because it is used to sequentially use SubVi's written by Andor Technology. They collectively are known as Andor Software Development Kit (SDK). In this free kit from the Andor website, it contains over 100 Vi's each with its own function. Most are very simple like SetExposure.vi where you input a number and it sets the Exposure Time as such. Here I will not show pictures of the code rather I will describe each portion of the Vi's in sequential order

SetTrigger

-Set to internal or external
-We set to external so we can collect I and I_o each time the laser is fired.

SetExposureTime

-The amount of time the Intensifier tube is active.
-We set it by default to 50 ms which is more than we'll need for the experiment. The actual exposure time for each delay time is set by the pulse gate width.

SetGain

-Set MCP gain (0 – 250)
-The MCP may be set higher but 100 is consistent so you can recognize problems when aligning.

These three pertain to the SetDDGTimes.vi but as three inputs.

SetDDGTimes – Gate Delay

-What Is the time delay between when the CCD receives a trigger and collects data.

-This is set through a global variable in the Taylor Main.vi. These selected delay times are the focus of these kinetic experiments.

SetDDGTimes – Output Delay

-This is used a delay to compensate for laser trigger offset.

-We set it to zero because we use a trigger from the laser light to trigger the CCD

SetDDGTimes – Pulse Width

-How long is the intensifier active to collect signal.

-We use 5 microseconds but this can be adjusted larger or smaller.

FastInsertionDelay

-Delay in time for the DDG to signal the intensifier tube.

-The two selections are fast and normal. Normal is 26 ns and fast is 16 ns. The fast puts extra strain on the electronics and 26 ns is well within the resolution we work with (5 us)

Intelligate

-Turns MCP and Intensifier on and off together to improve time resolution

-It is recommended not to use this unless necessary. Again our time-resolution isn't an issue so leave this box unchecked.

SetIOC

-Integrate on chip before sending to computer.

-Not necessary. It is best to allow the computer do all processing to not bog down the system.

GetAcqusitionTimings

-This is a check to make sure the times you set for pulse width and also the actual Kinetic Cycle Time.
-The exposure time is set through the pulse width setting and the Kinetic Cycle time is the exposure time plus the time needed to activate each part of the CCD and transfer the information.

GetAcquisitionData

-Returns the data from the last acqusition on the CCD
-This data is passed through a global variable back to the Taylor Main.vi to use in averaging.

Now that your DDG is running you can execute the Taylor Main.vi and began to setup the experiment

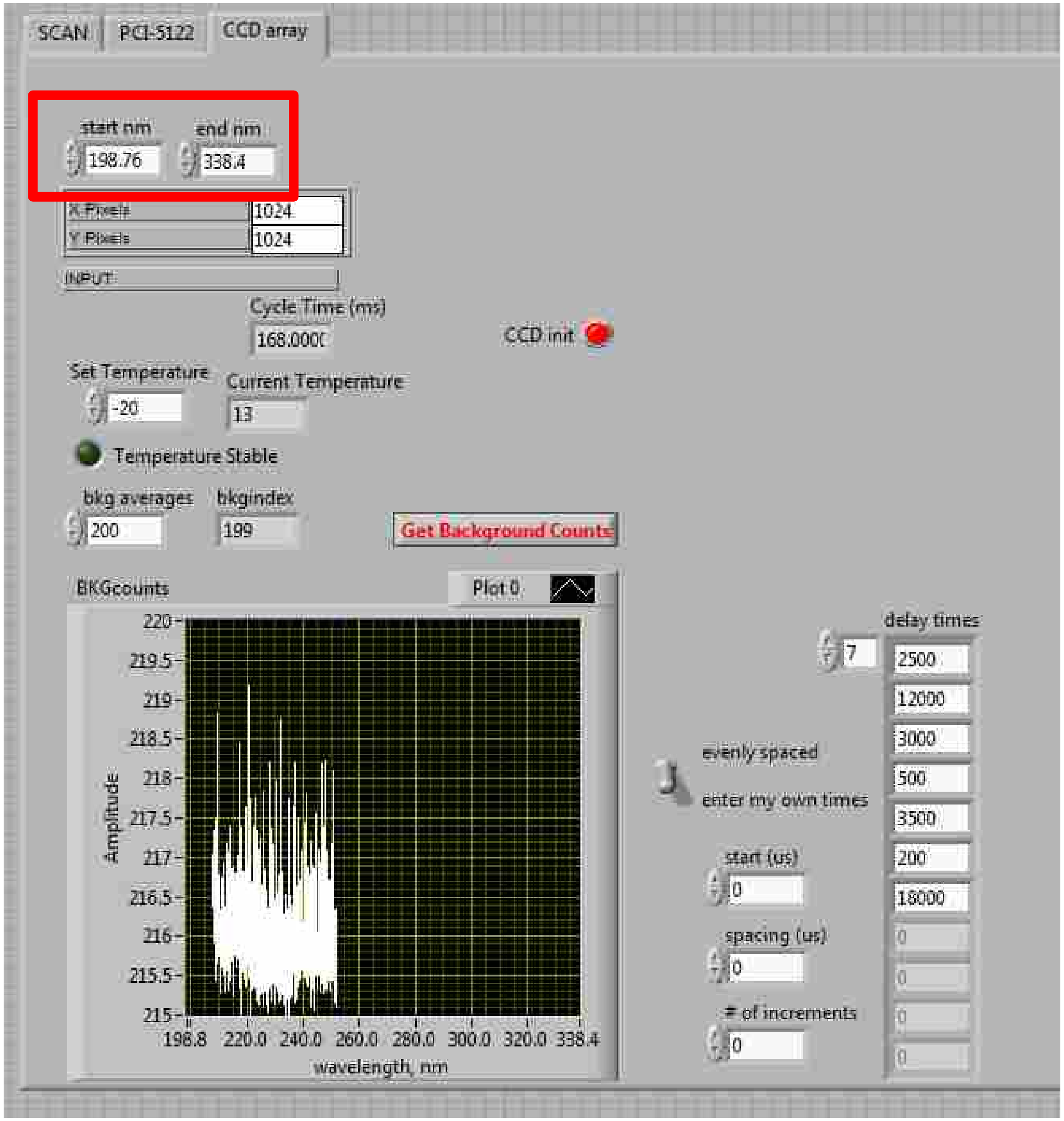

start nm 198.76

end nm 338.4

X Pixels 1024

Y Pixels 1024

Cycle Time (ms) 168.0000

Set Temperature -20

Current Temperature 13

bkg averages 200

bkgindex 199

delay times 7: 2500, 12000, 3000, 500, 3500, 200, 18000, 0, 0, 0, 0

start (us) 0

spacing (us) 0

# of increments 0

Start with the CCD array tab on Taylor Main.vi. The **Start nm** and **End nm** are collected from the Andor Solis software. The wavelength range set in the Solis program must be copied into the Main.vi. The easiest way to find this is by saving the data in the program as an ASC file. Then the x axis will contain the wavelength range.

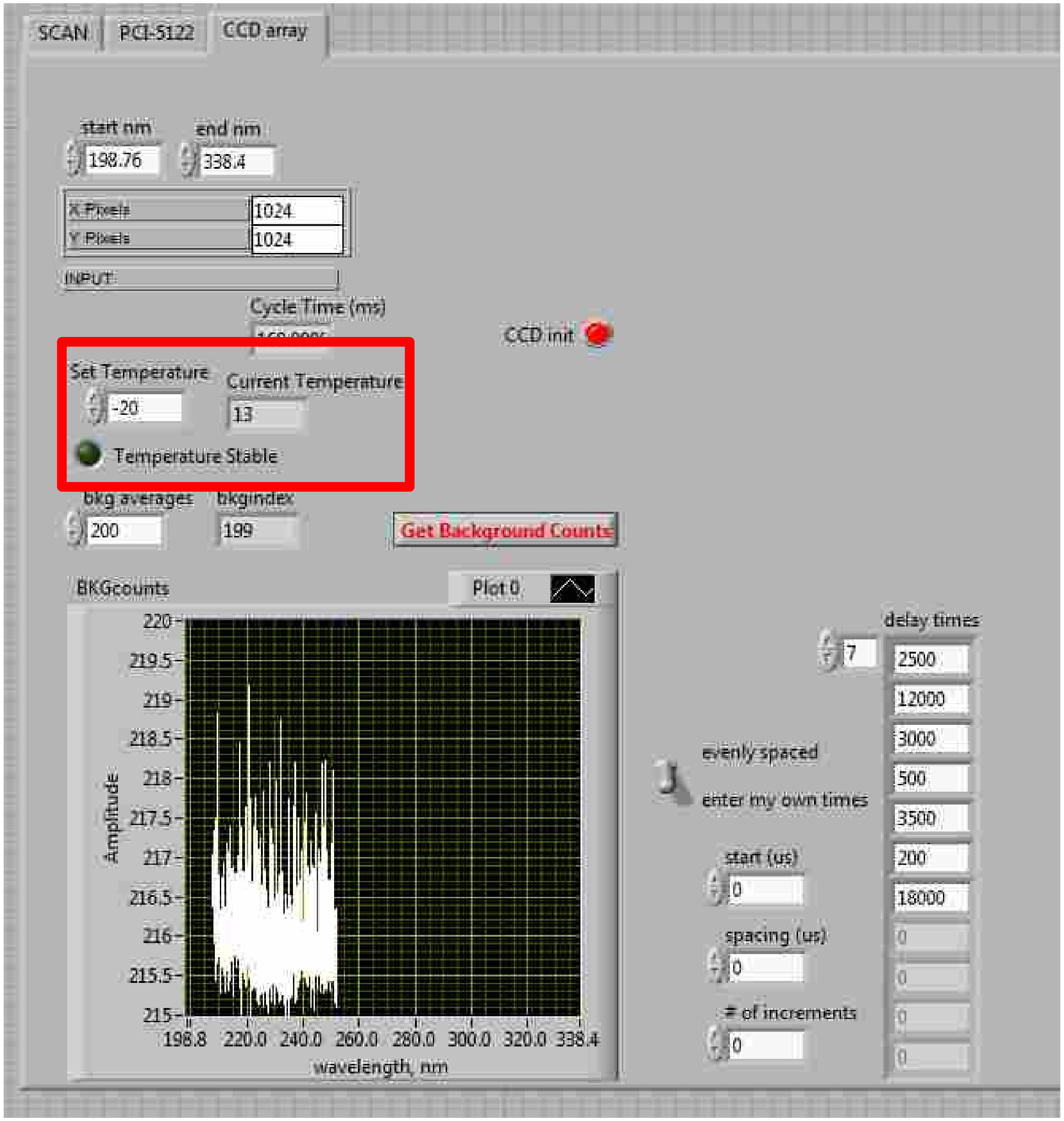

start nm: 198.76
end nm: 338.4
X Pixels: 1024
Y Pixels: 1024
INPUT:
Cycle Time (ms)
Set Temperature: -20
Current Temperature: 13
Temperature Stable
bkg averages: 200
bkgindex: 199
delay times: 7
2500
12000
3000
500
3500
200
18000
0
0
0
0
start (us): 0
spacing (us): 0
# of increments: 0

The CCD temperature is set typically to -10 C. It will take several minutes to cool to the set temperature. Be patient and wait for the Temperature Stable indicator to light up before continuing. The temperature needs to be raised to at least 0 C before shutdown otherwise it may damage the CCD. I recommend keeping the temperature at -10 C until you know the program will work for long periods of time. Avoid having the CCD at –20 C and having the program fault and then the CCD will warm to too quickly.

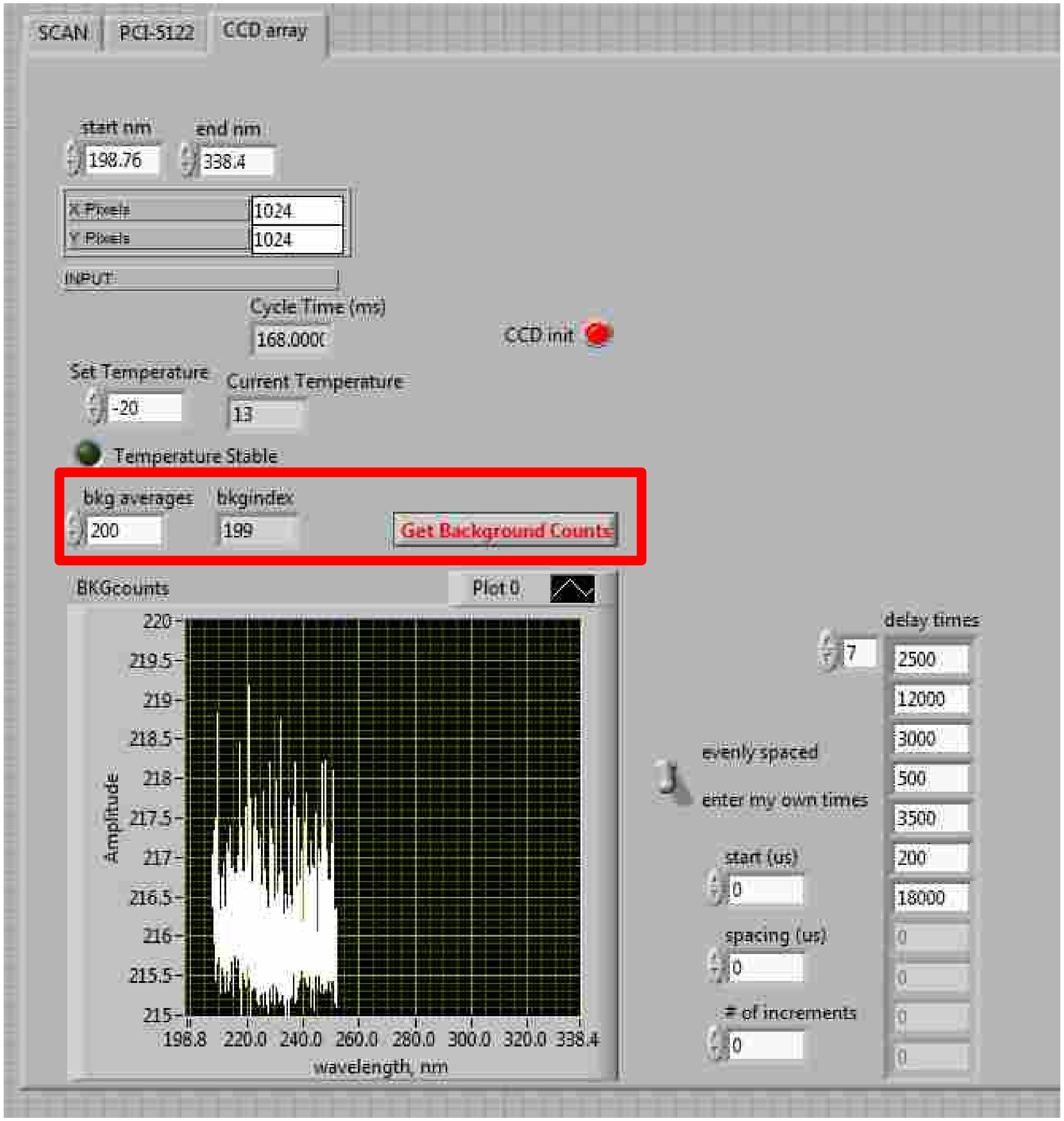

start nm: 198.76
end nm: 338.4
X Pixels: 1024
Y Pixels: 1024
Cycle Time (ms): 168.0000
Set Temperature: -20
Current Temperature: 13
bkg averages: 200
bkgindex: 199
delay times: 7
2500
12000
3000
500
3500
200
18000
0
0
0
0
start (us): 0
spacing (us): 0
# of increments: 0

Once the CCD temperature has stabilized, collect the background counts. The first time "Get Background Counts" is pressed the data doesn't display. Set averages to 10 and collect again. Then set to 200 and and collect once more. 200 is arbitrary, you can decide more or less for yourself. It takes 3 or 4 spectra per second. Be sure to block the Deuterium lamp during collection. To get a glimpse of the D2 spectrum you can collect without blocking the light and then block it and collect again.

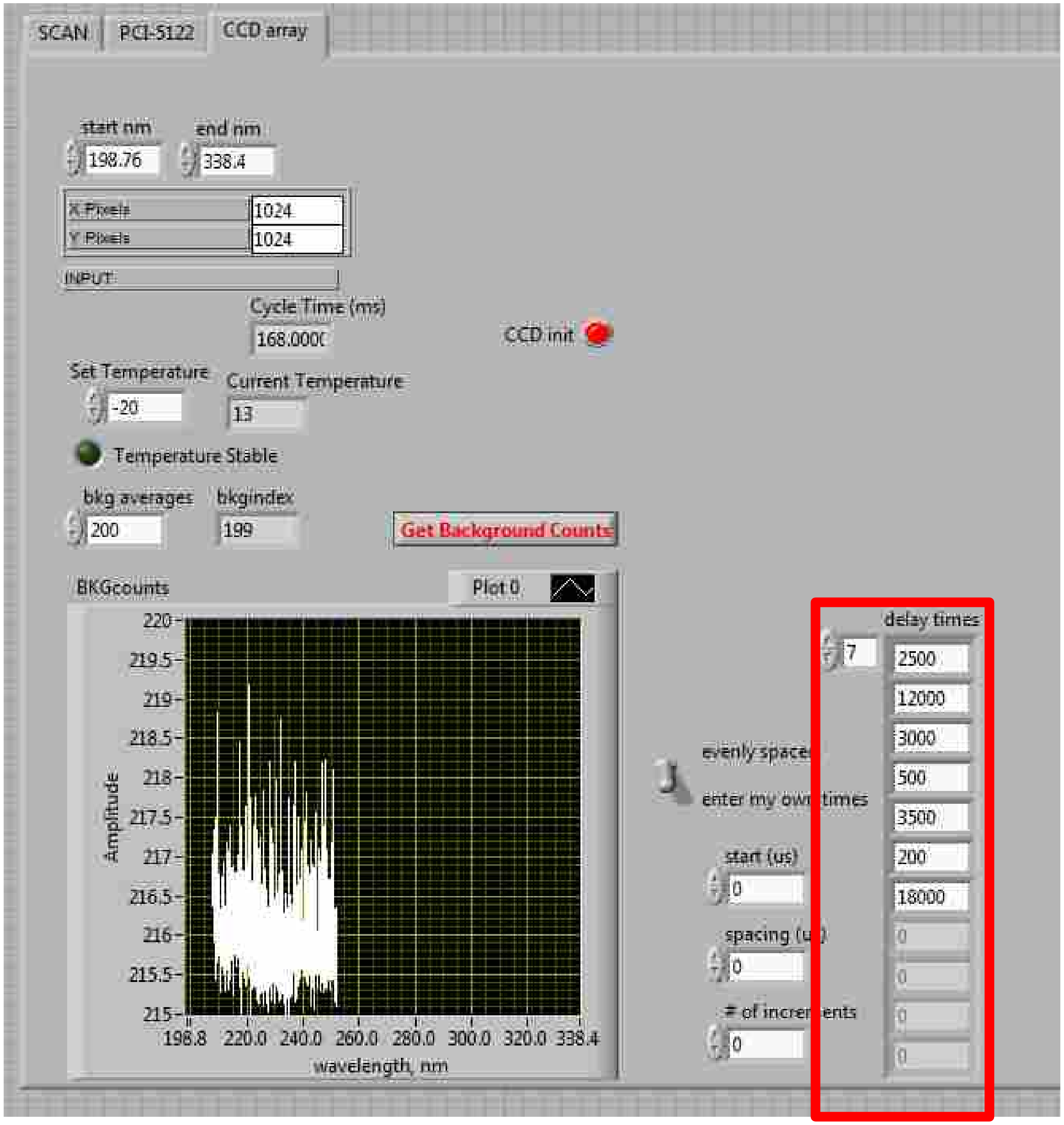

start nm 198.76

end nm 338.4

X Pixels 1024

Y Pixels 1024

INPUT

Cycle Time (ms) 168.0000

Set Temperature -20

Current Temperature 13

Temperature Stable

bkg averages 200

bkgindex 199

delay times 7

2500
12000
3000
500
3500
200
18000
0
0
0
0

start (us) 0

spacing (us) 0

# of increments 0

The selection of delay times is important. Enter as many delay times as desired but be aware that no data is saved until the end of a run. If the program crashes in the middle, the data is unrecoverable. Be judicious in the number of delays selected so data isn't lost. 10 delay times is a good compromise between too many and too few. Once those 10 delays are completed, choose 10 different times and run the experiment again. Stagger the times as shown so that deviations can be corrected over small time periods. Times are in micro seconds. The evenly spaced function works but is not advisable because variations can't be accounted for in any way

Taylor Main 2.1

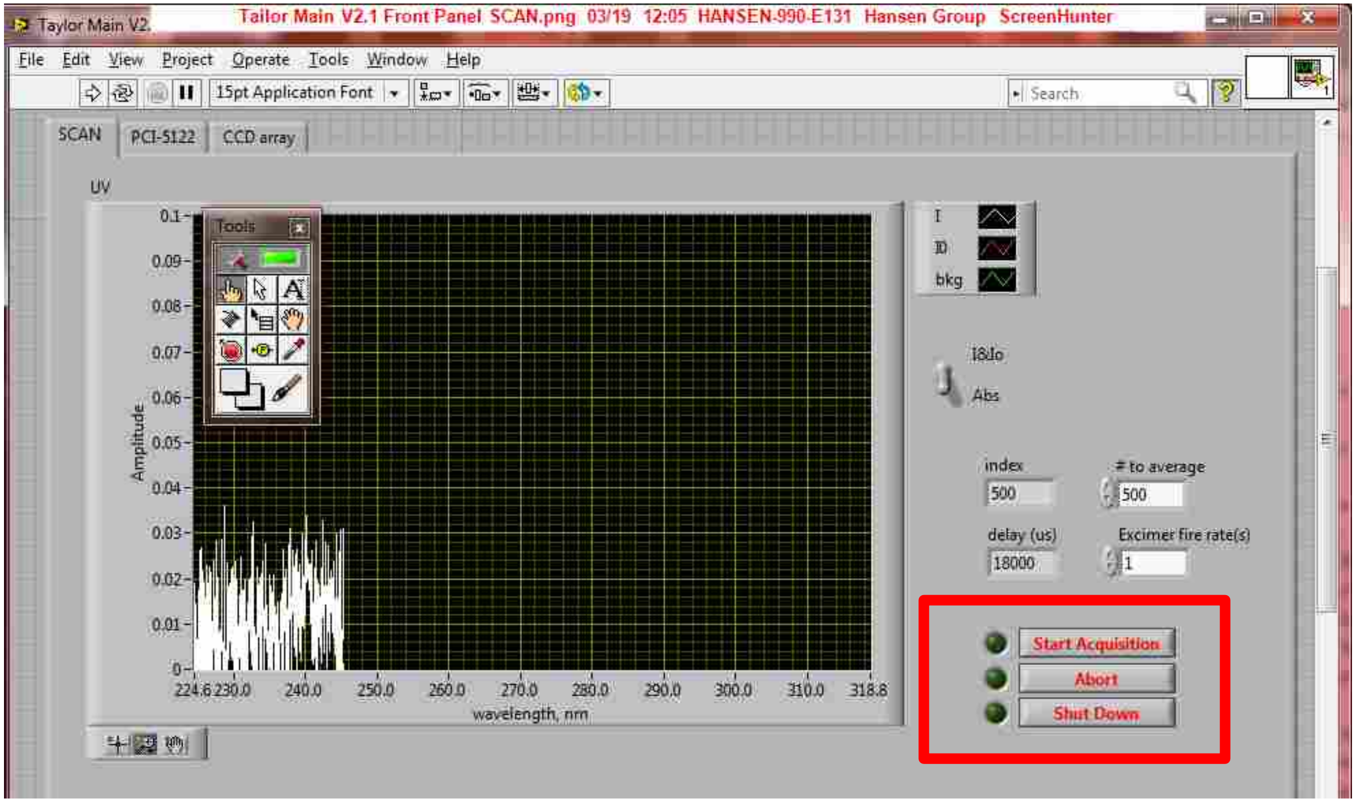

index: 500

\# to average: 500

delay (us): 18000

Excimer fire rate(s): 1

Once the background counts have been selected and the delay times entered the experiment is ready to run. Before pressing Start Acquisition be sure that the D_2 lamp is unblocked and the excimer is warmed up with the high voltage on but with the trigger set to external.

Once in a while the program gets caught waiting for the trigger from the Excimer. You can sometime get it going by pressing **Manual** on the excimer to make it fire. It sometimes takes two or three shots before responding. You cannot **Abort** or **Shutdown** while the Vi is waiting for a trigger. Set the averages and Excimer rep rate before pressing start. One may choose to view either Absorption or the Raw I and Io. It is ok to switch between them during a run, as well as zoom in and out as required.

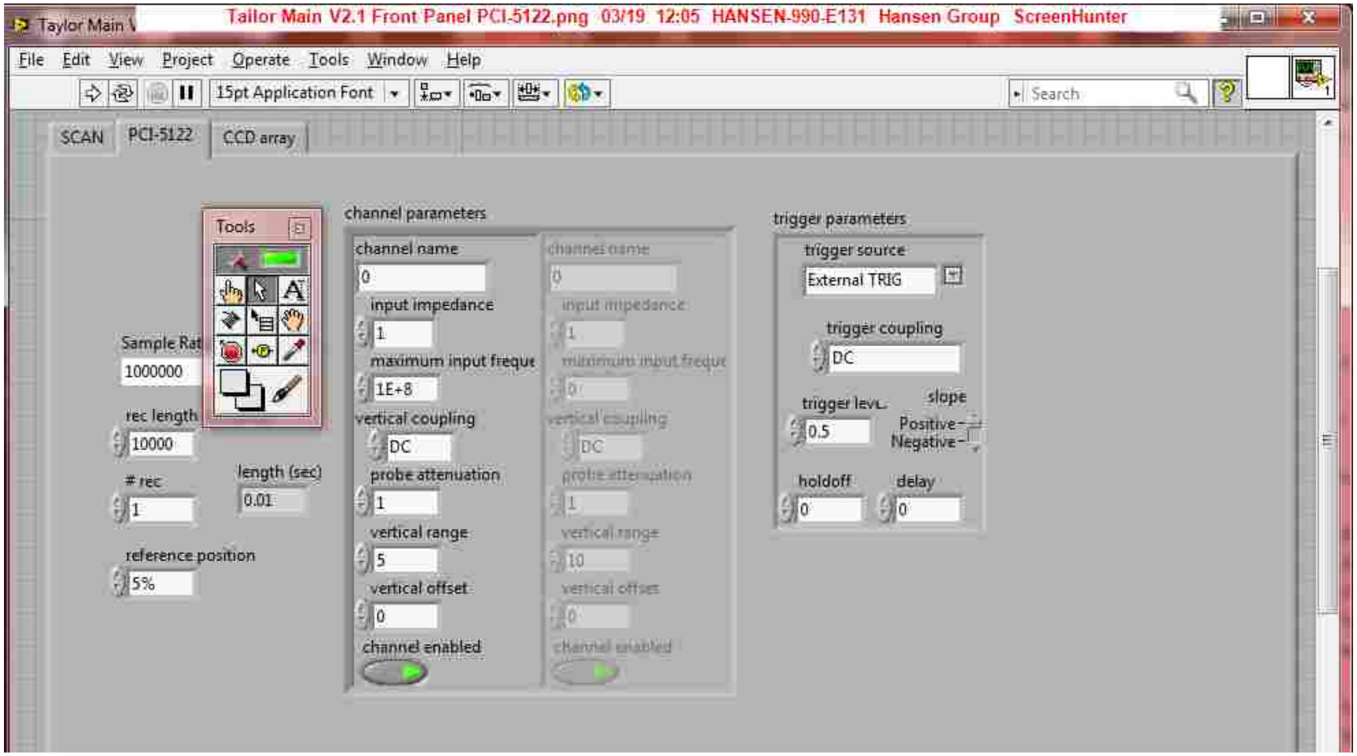

Sample Rat 1000000
rec length 10000
rec 1
length (sec) 0.01
reference position 5%

channel parameters
channel name 0
input impedance 1
maximum input freque 1E+8
vertical coupling DC
probe attenuation 1
vertical range 5
vertical offset 0
channel enabled

channel name 0
input impedance 1
maximum input freque 0
vertical coupling DC
probe attenuation 1
vertical range 10
vertical offset 0
channel enabled

trigger parameters
trigger source External TRIG
trigger coupling DC
trigger leve 0.5
slope Positive Negative
holdoff 0
delay 0

At this point the program should run autonomously until it completes the delay times. The program will prompt to save the data. This will save as a csv file with the first column containing the wavelength values for each vertical bin of the CCD. Each subsequent column will contain, in order of collection, the delay times and associated absorption. A least squares regression with the absorption cross sections of suspected species in your experiment identifies contaminants and isolates important signal. This may be done with SigmaPlot or MatLab. This tab above has to do with the PCI DAQ that has never worked and is non-essential for the CCD. Nothing is changed on this tab and is somewhat of a relic.

These subsequent pages are used to identify the LabView wiring and will be discussed in sequential order.

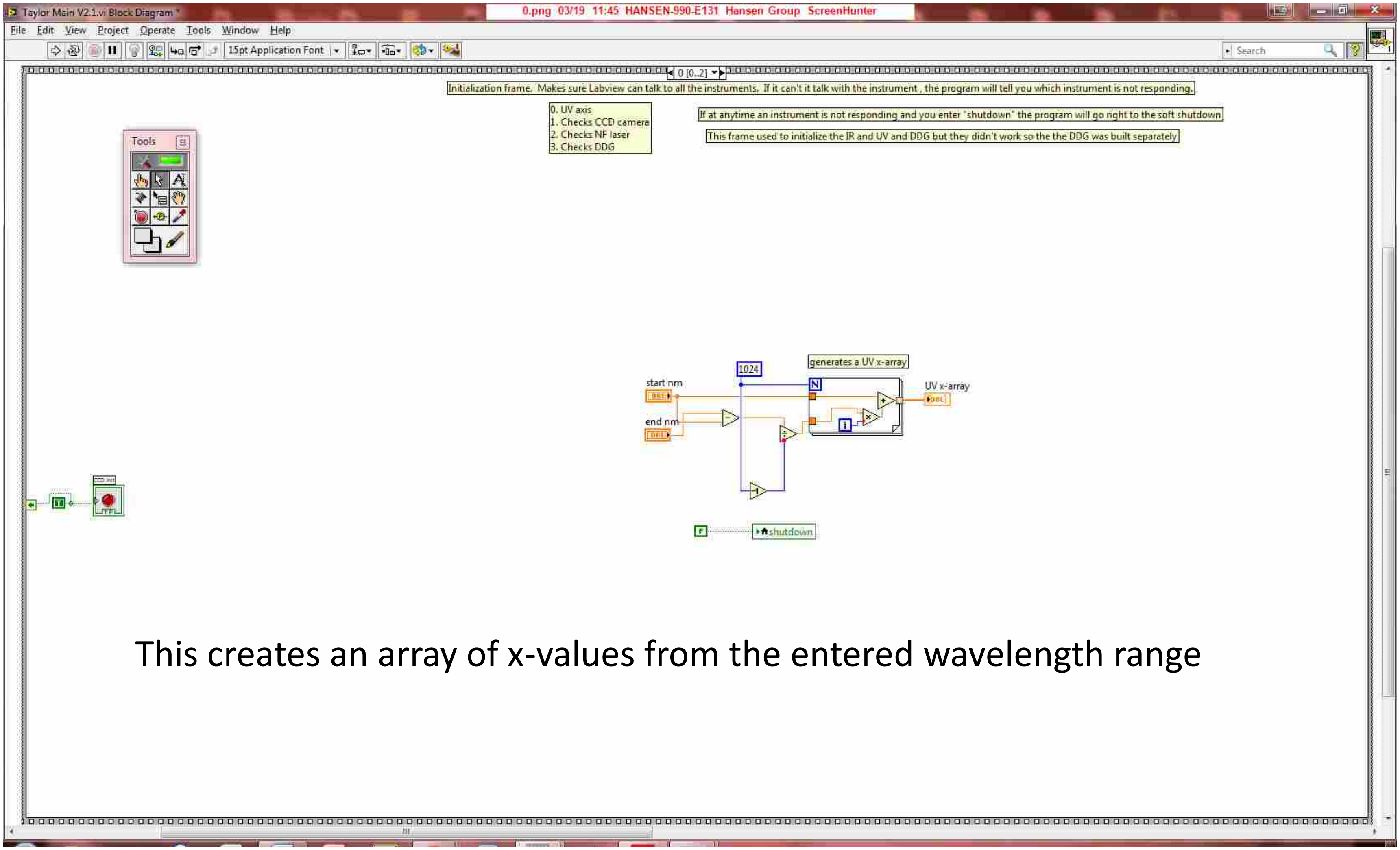

Initialization frame. Makes sure Labview can talk to all the instruments. If it can't it talk with the instrument , the program will tell you which instrument is not responding.

0. UV axis
1. Checks CCD camera
2. Checks NF laser
3. Checks DDG

If at anytime an instrument is not responding and you enter "shutdown" the program will go right to the soft shutdown

This frame used to initialize the IR and UV and DDG but they didn't work so the the DDG was built separately

This creates an array of x-values from the entered wavelength range

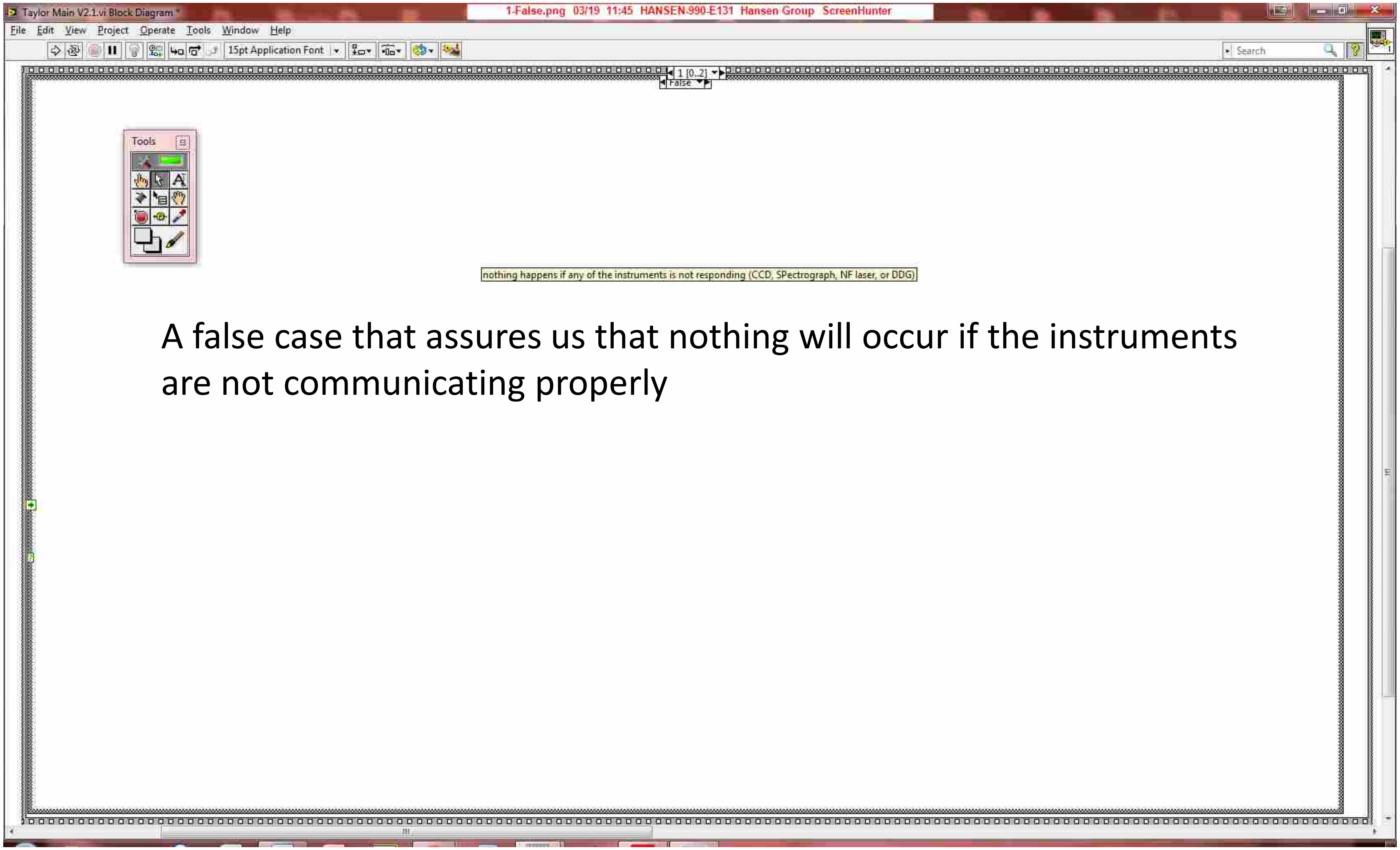

nothing happens if any of the instruments is not responding (CCD, SPectrograph, NF laser, or DDG)

A false case that assures us that nothing will occur if the instruments are not communicating properly

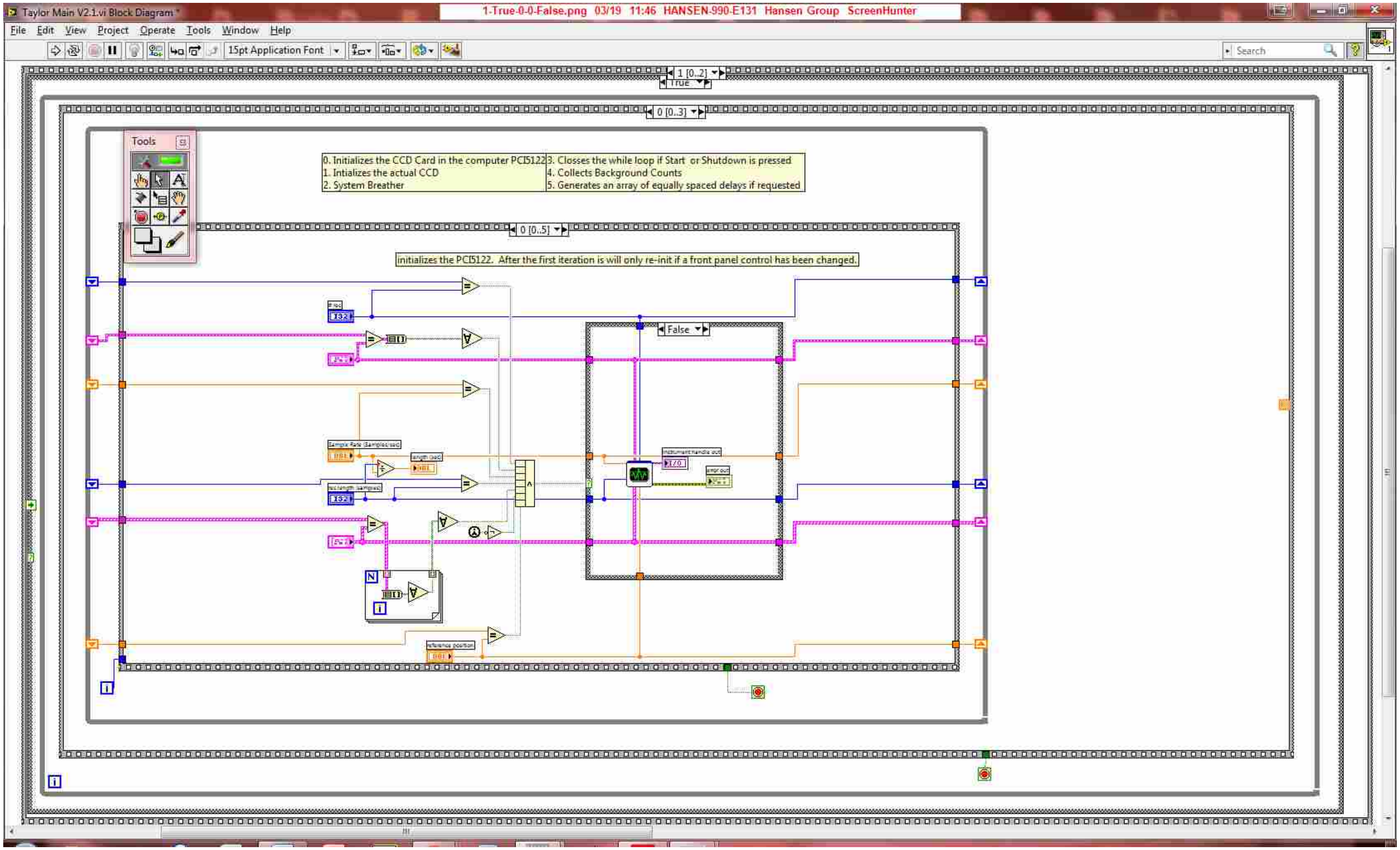

0. Initializes the CCD Card in the computer PCI5122
1. Intializes the actual CCD
2. System Breather
3. Closes the while loop if Start or Shutdown is pressed
4. Collects Background Counts
5. Generates an array of equally spaced delays if requested

initializes the PCI5122. After the first iteration is will only re-init if a front panel control has been changed.

This initializes the PCI5122 Card which currently does not collect data but can be used in IR experiments.

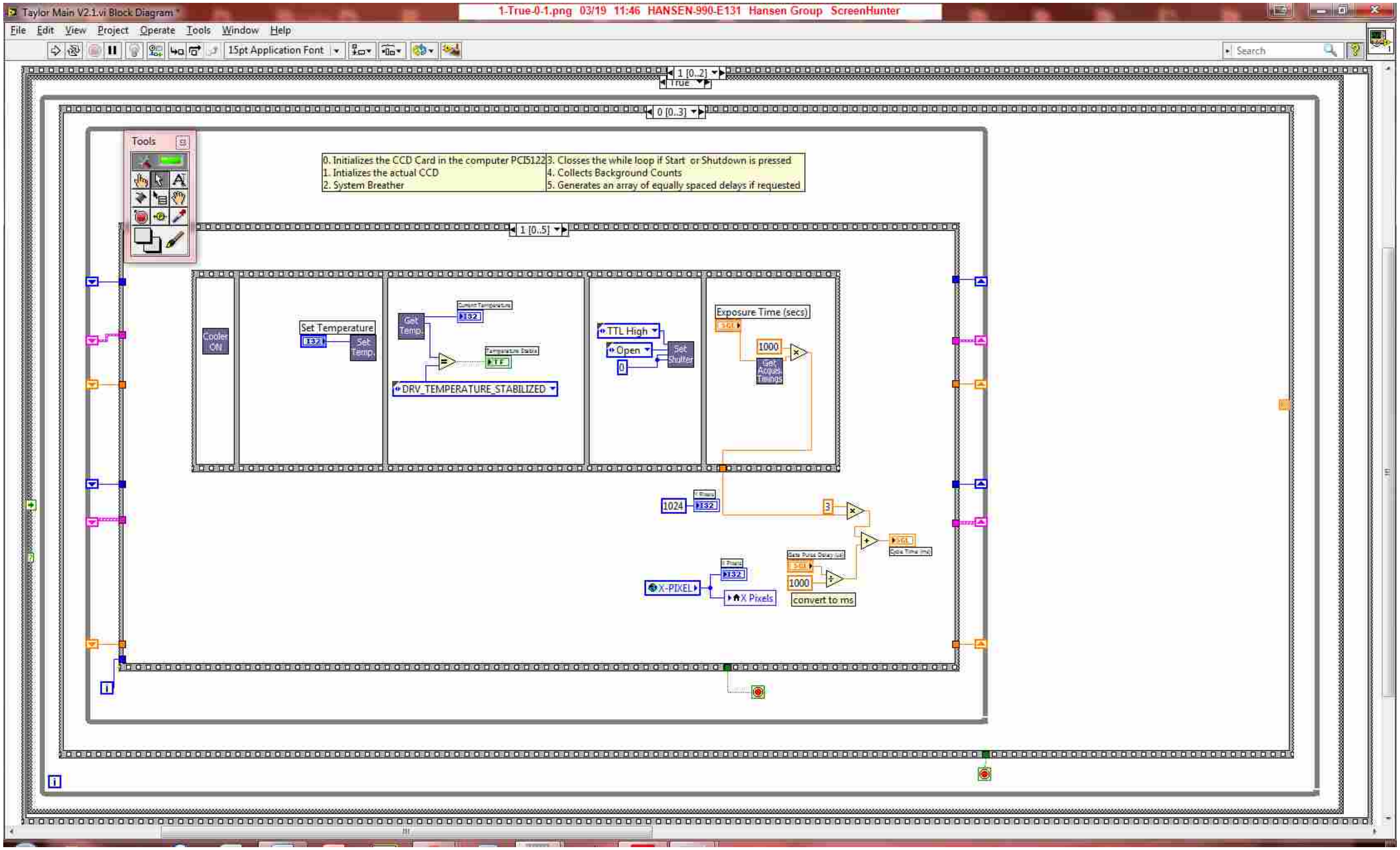

0. Initializes the CCD Card in the computer PCI5122
1. Intializes the actual CCD
2. System Breather
3. Closses the while loop if Start or Shutdown is pressed
4. Collects Background Counts
5. Generates an array of equally spaced delays if requested

This part uses Andor Vi’s to turn the cooler on set the temperature and then check to see if the temperature has stabilized.

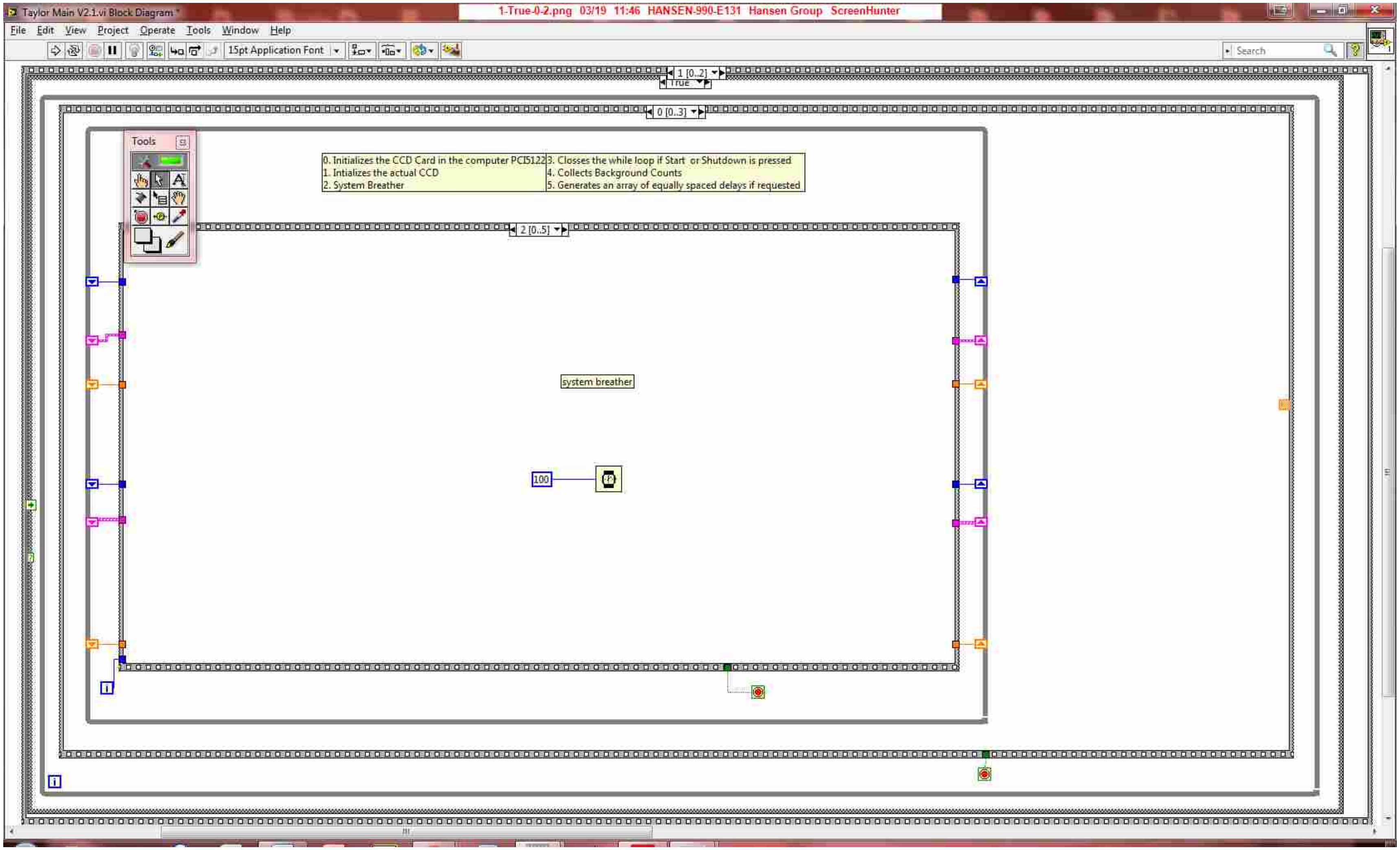

0. Initializes the CCD Card in the computer PCI5122
1. Intializes the actual CCD
2. System Breather
3. Closses the while loop if Start or Shutdown is pressed
4. Collects Background Counts
5. Generates an array of equally spaced delays if requested

System breathers are often placed inside sequences in LabVIEW to make sure each operation runs smoothly. Here the breather is 100 ms.

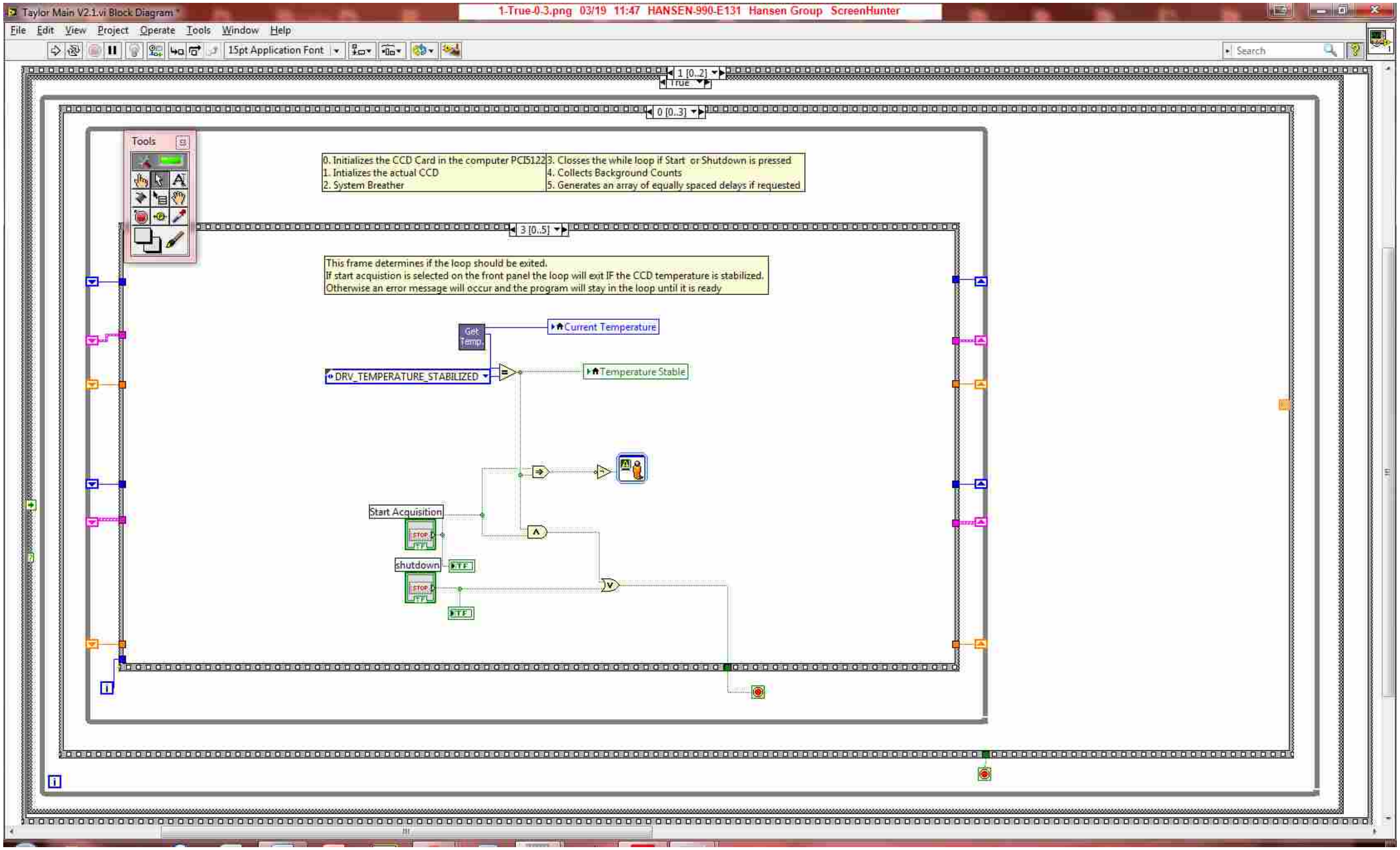

0. Initializes the CCD Card in the computer PCI5122
1. Intializes the actual CCD
2. System Breather
3. Closses the while loop if Start or Shutdown is pressed
4. Collects Background Counts
5. Generates an array of equally spaced delays if requested

This frame determines if the loop should be exited.
If start acquistion is selected on the front panel the loop will exit IF the CCD temperature is stabilized.
Otherwise an error message will occur and the program will stay in the loop until it is ready

When the Start Acquisition is pressed this sequence checks to see if the temperature has stabilized. If it has it will proceed. If it hasn't a warning message will be displayed.

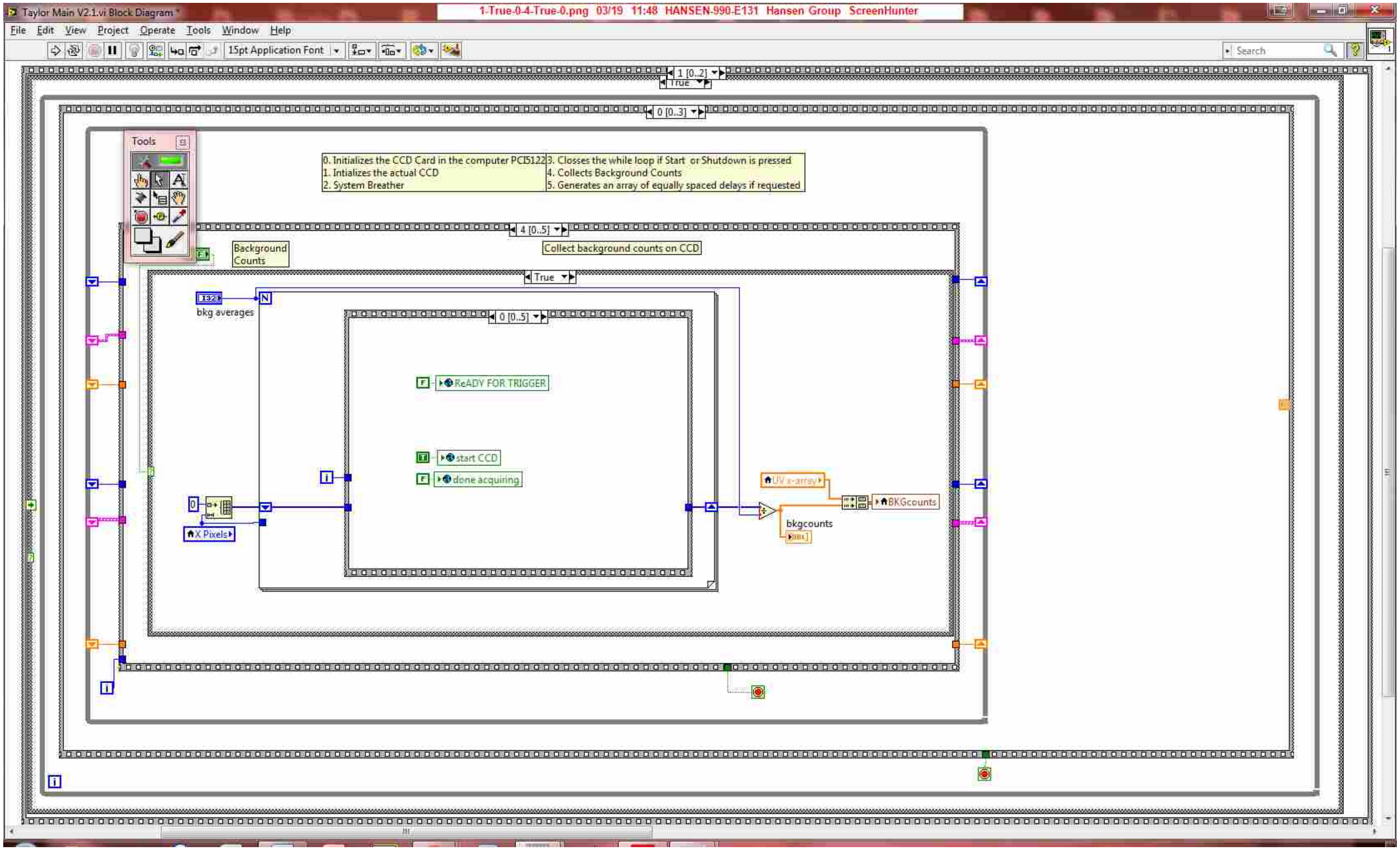

0. Initializes the CCD Card in the computer PCI5122
1. Intializes the actual CCD
2. System Breather
3. Closses the while loop if Start or Shutdown is pressed
4. Collects Background Counts
5. Generates an array of equally spaced delays if requested

Collect background counts on CCD

The sequence within the For Loop will step through the process of triggering and acquiring data from the CCD for background counts. There are three global booleans that we use to pass information to the DDG.vi

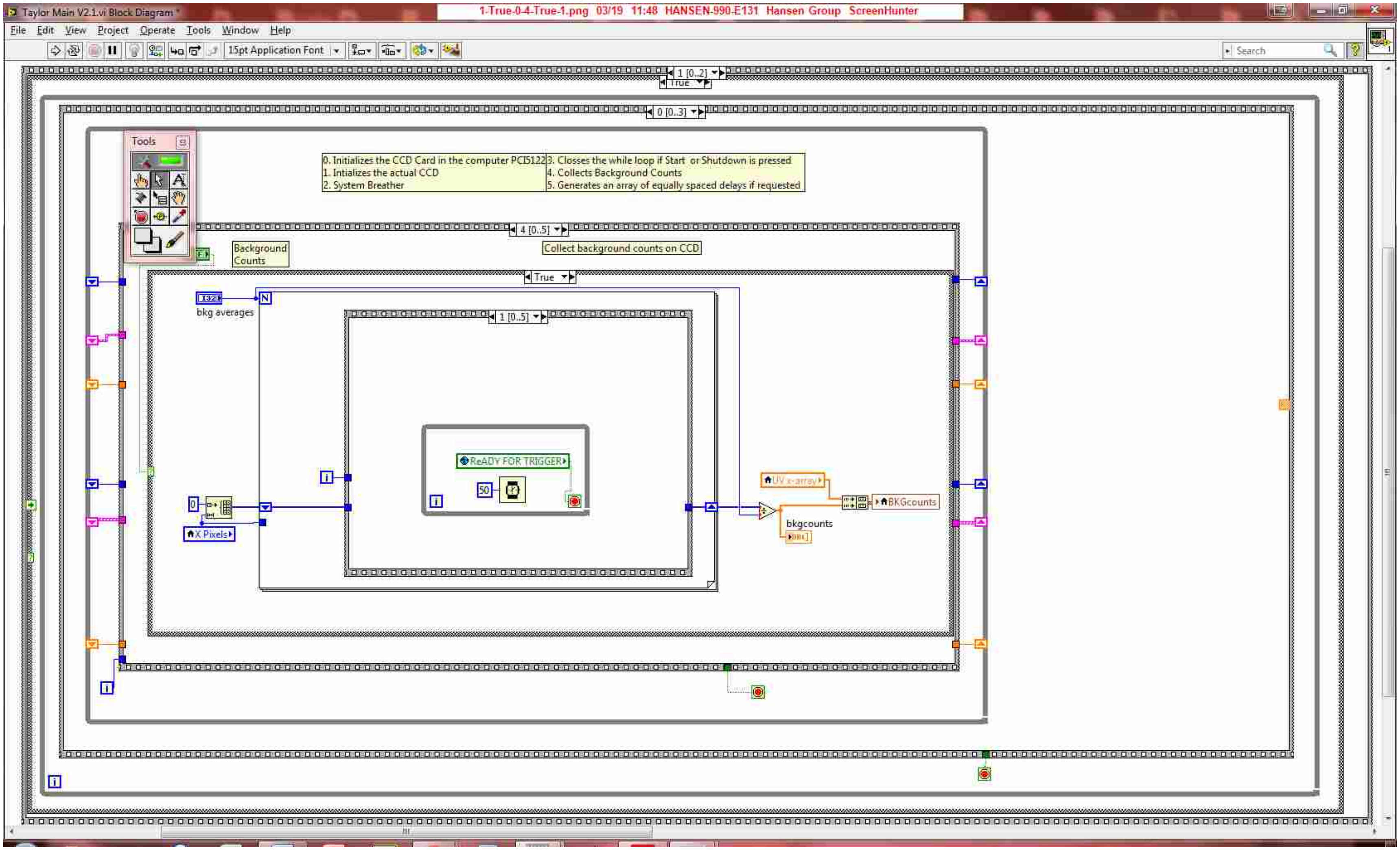

0. Initializes the CCD Card in the computer PCI5122
1. Intializes the actual CCD
2. System Breather
3. Closses the while loop if Start or Shutdown is pressed
4. Collects Background Counts
5. Generates an array of equally spaced delays if requested

Collect background counts on CCD

This waits until the DDG sends a boolean back to the Main.vi that the trigger is ready

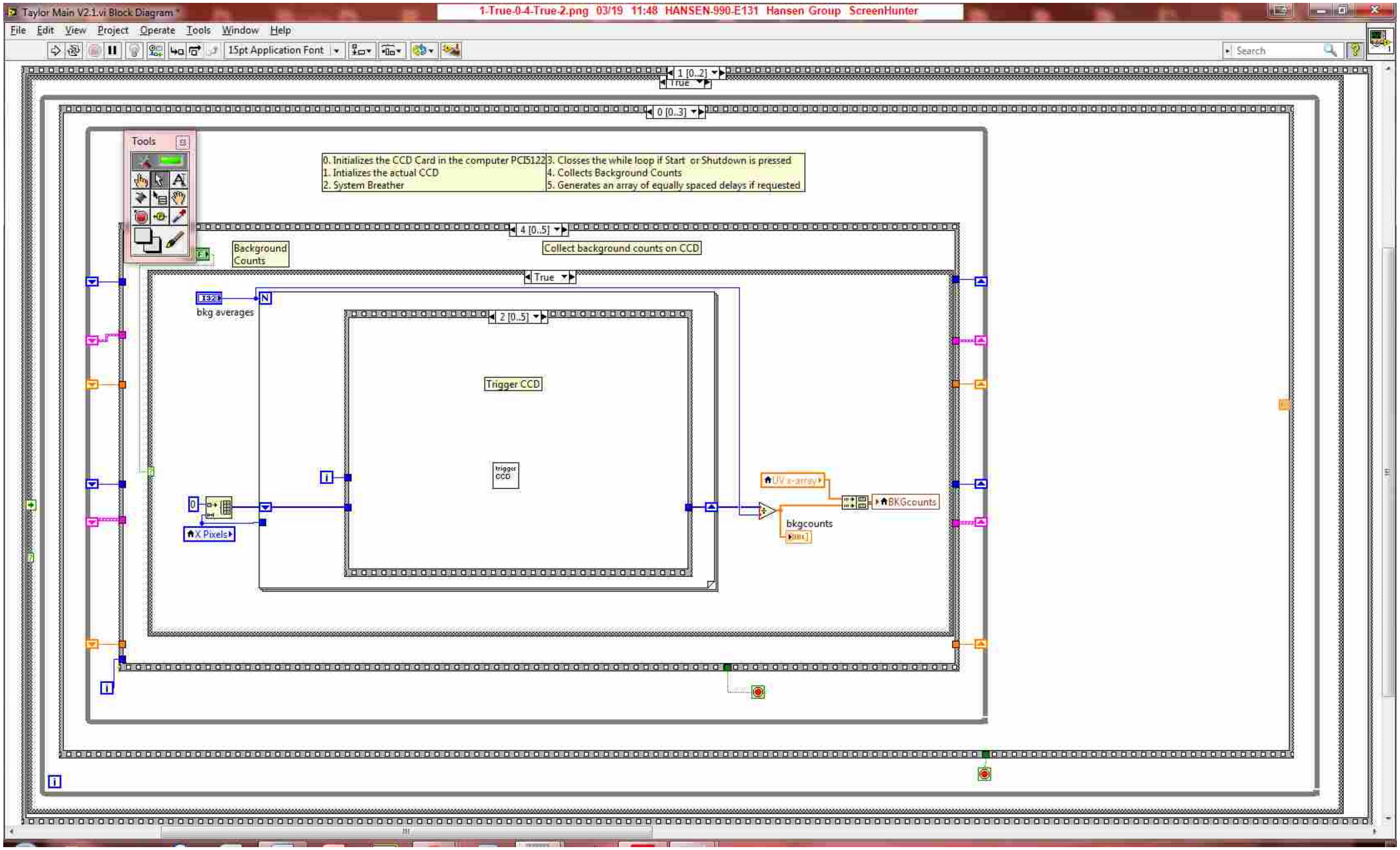

0. Initializes the CCD Card in the computer PCI5122
1. Intializes the actual CCD
2. System Breather
3. Closses the while loop if Start or Shutdown is pressed
4. Collects Background Counts
5. Generates an array of equally spaced delays if requested

Trigger the CCD to collect data

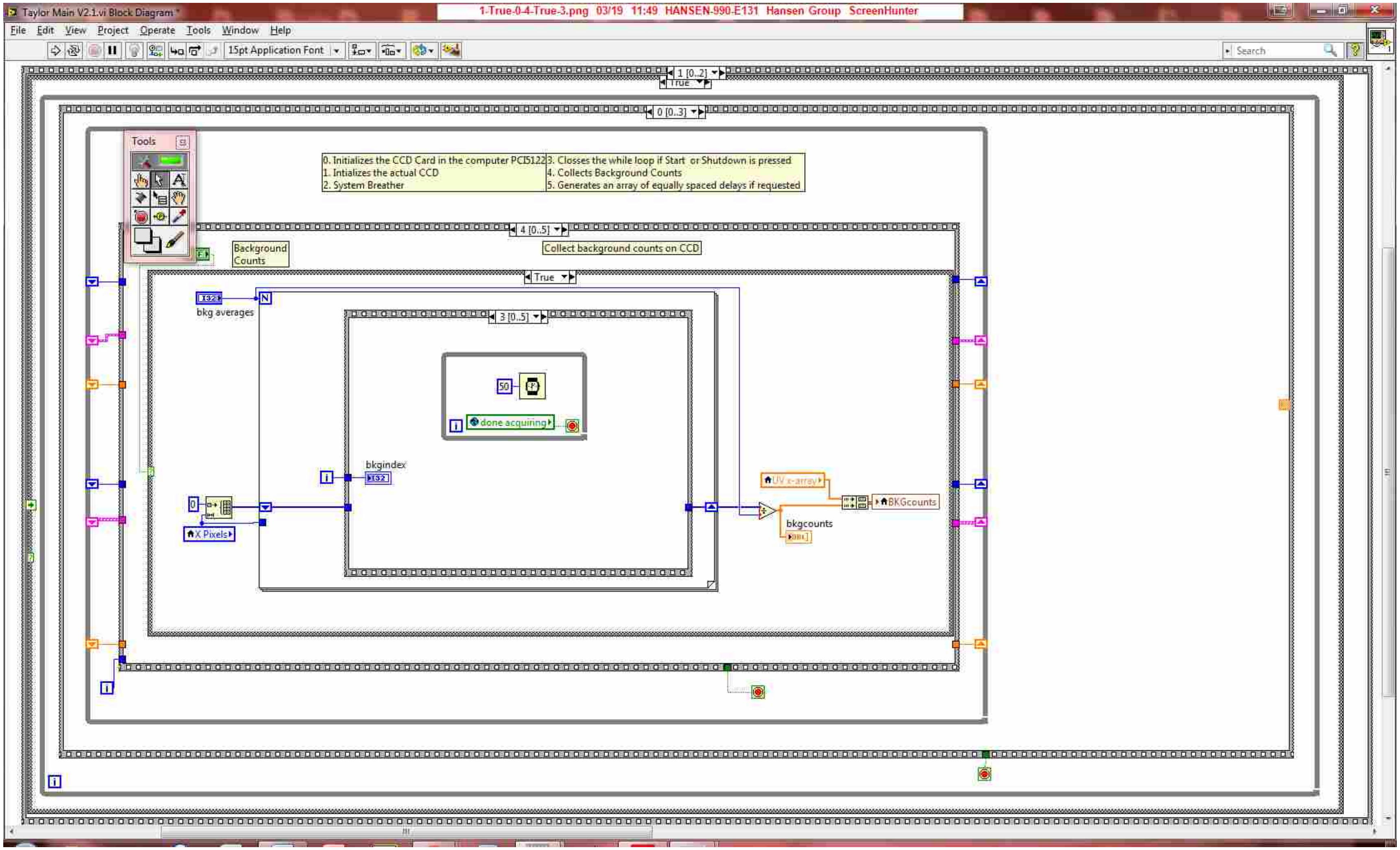

0. Initializes the CCD Card in the computer PCI5122
1. Intializes the actual CCD
2. System Breather
3. Closses the while loop if Start or Shutdown is pressed
4. Collects Background Counts
5. Generates an array of equally spaced delays if requested

Collect background counts on CCD

Wait until the CCD is done acquiring before continuing.

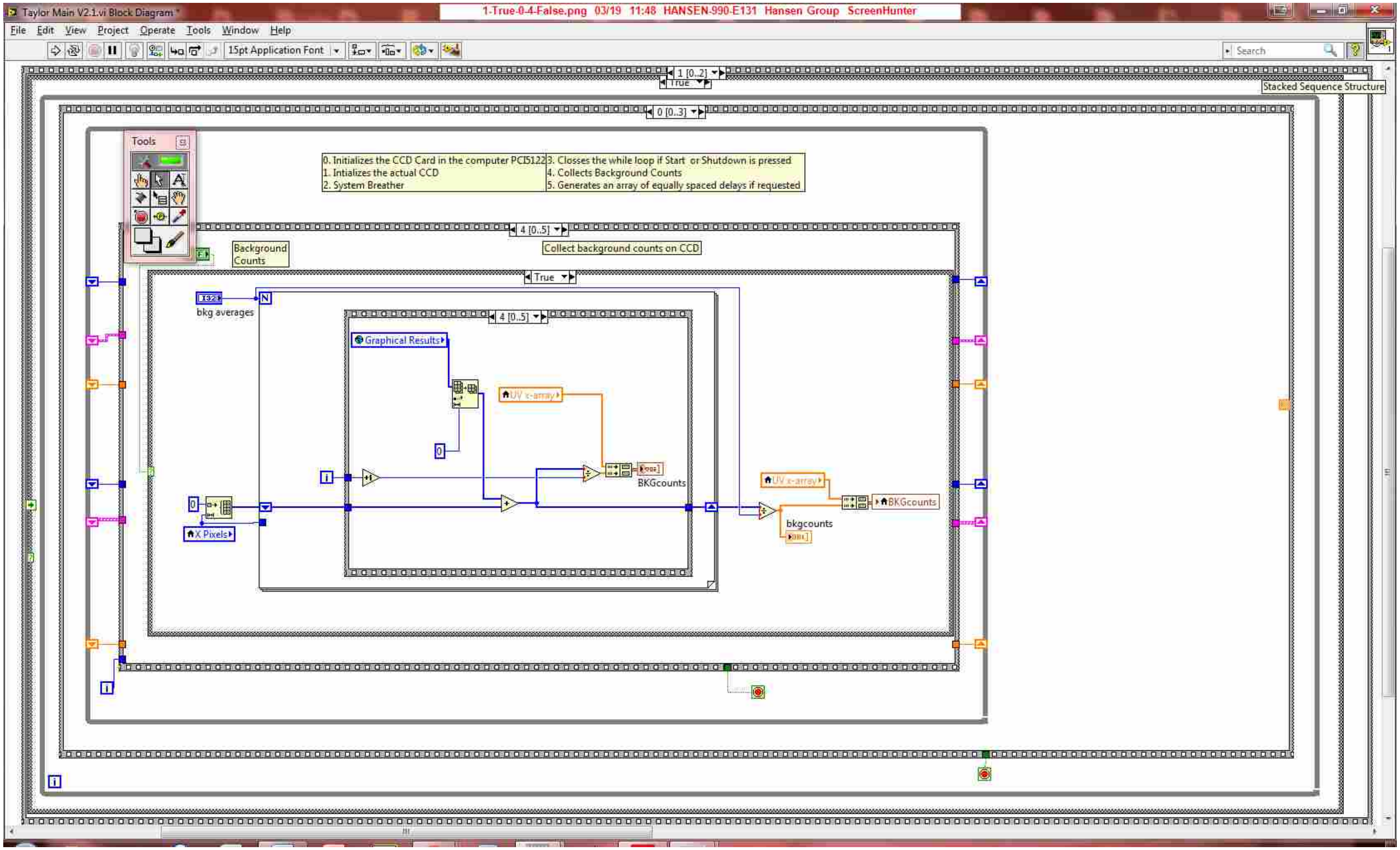

0. Initializes the CCD Card in the computer PCI5122
1. Intializes the actual CCD
2. System Breather
3. Closses the while loop if Start or Shutdown is pressed
4. Collects Background Counts
5. Generates an array of equally spaced delays if requested

Background counts are collected and averaged. The inner For Loop is used to collect counts and update continually the graph on the front panel. The shift register holds all the spectra in case you want the raw data which I never have needed.

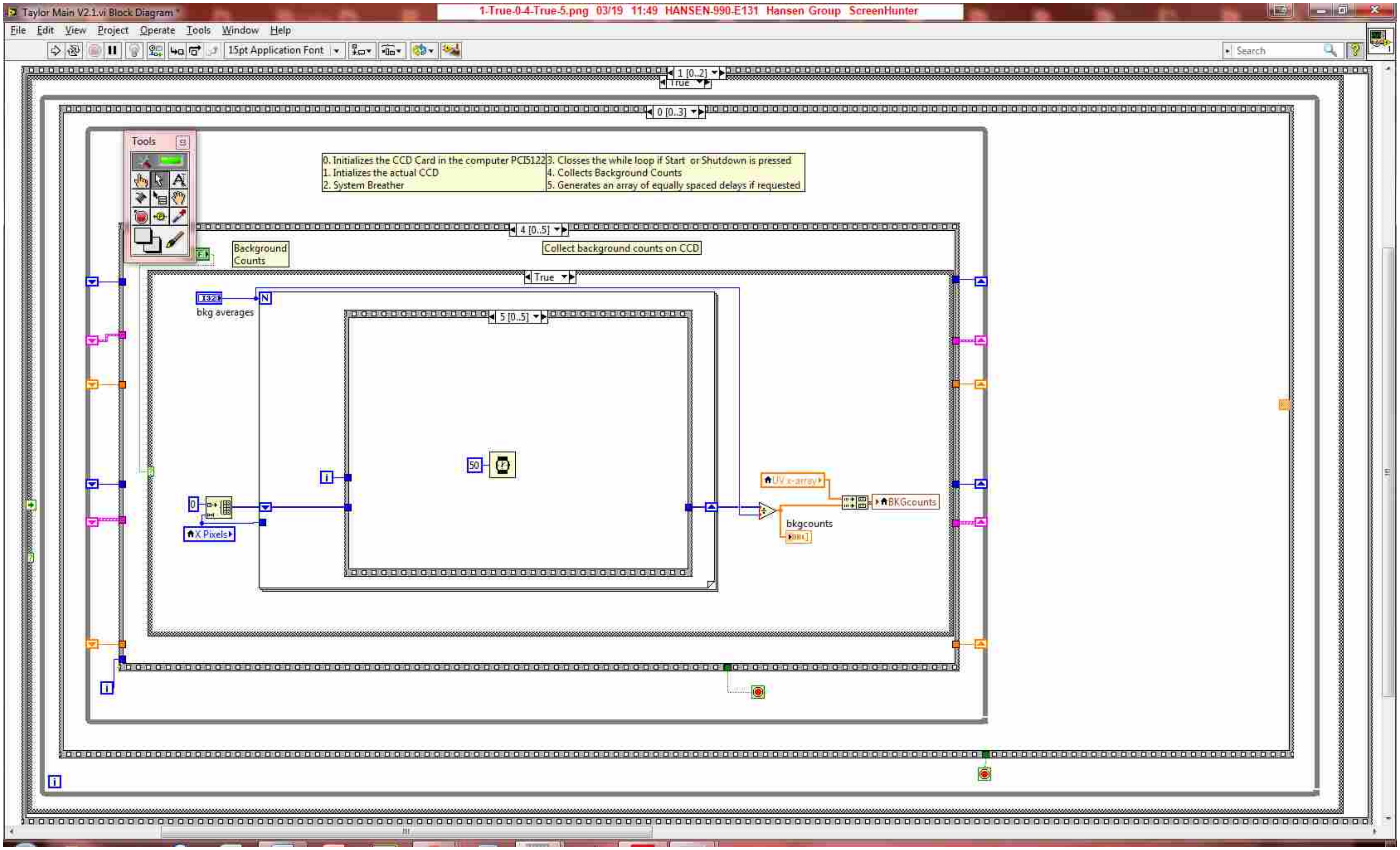

0. Initializes the CCD Card in the computer PCI5122
1. Intializes the actual CCD
2. System Breather
3. Closses the while loop if Start or Shutdown is pressed
4. Collects Background Counts
5. Generates an array of equally spaced delays if requested

Background Counts

Collect background counts on CCD

System Breather before the cycle begins again to acquire the next spectrum

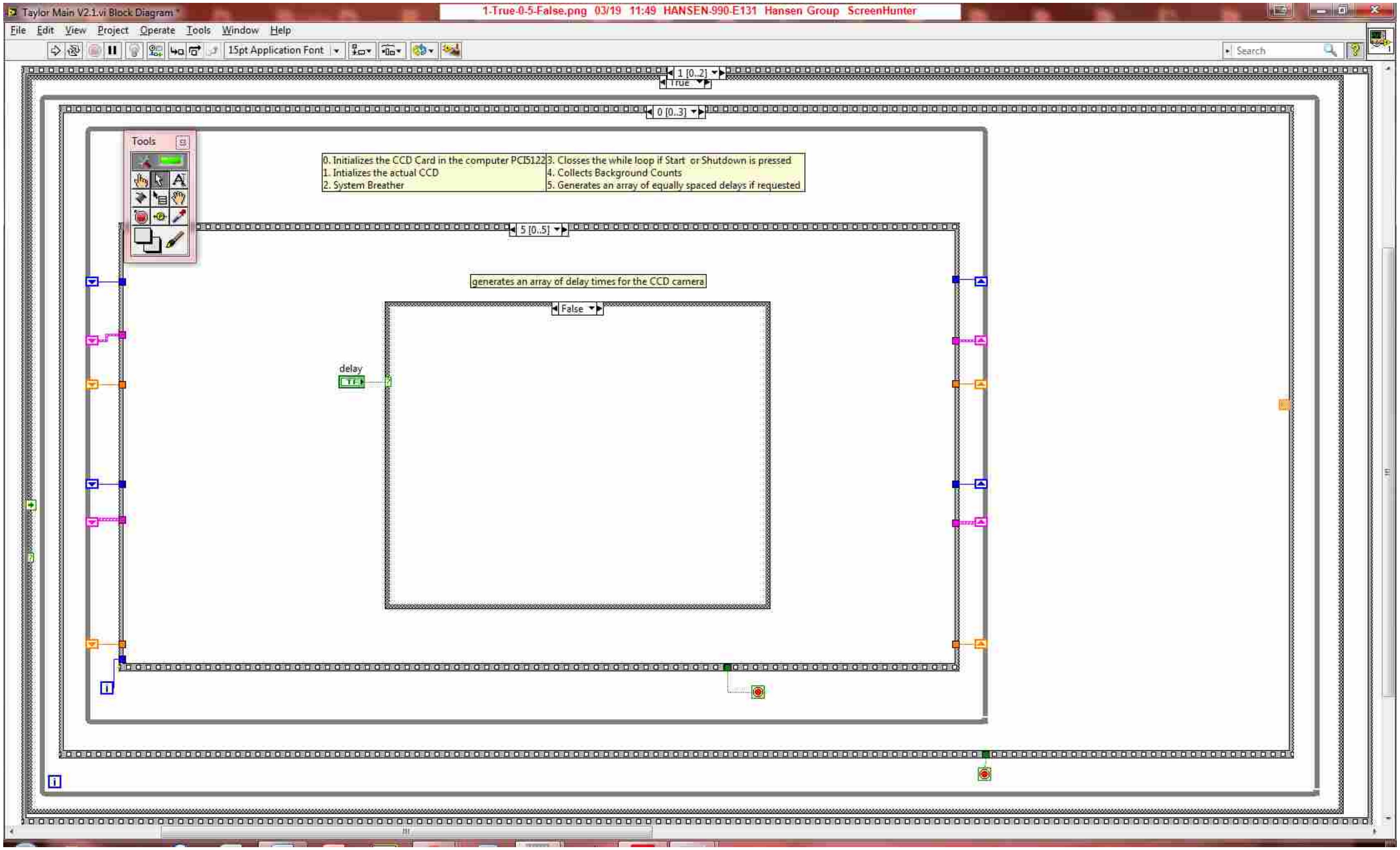

0. Initializes the CCD Card in the computer PCI5122
1. Intializes the actual CCD
2. System Breather
3. Closses the while loop if Start or Shutdown is pressed
4. Collects Background Counts
5. Generates an array of equally spaced delays if requested

generates an array of delay times for the CCD camera

This case structure is connected to the switch on the front panel to use evenly spaced delay times. If false we don’t need to create an array because we will do so manually

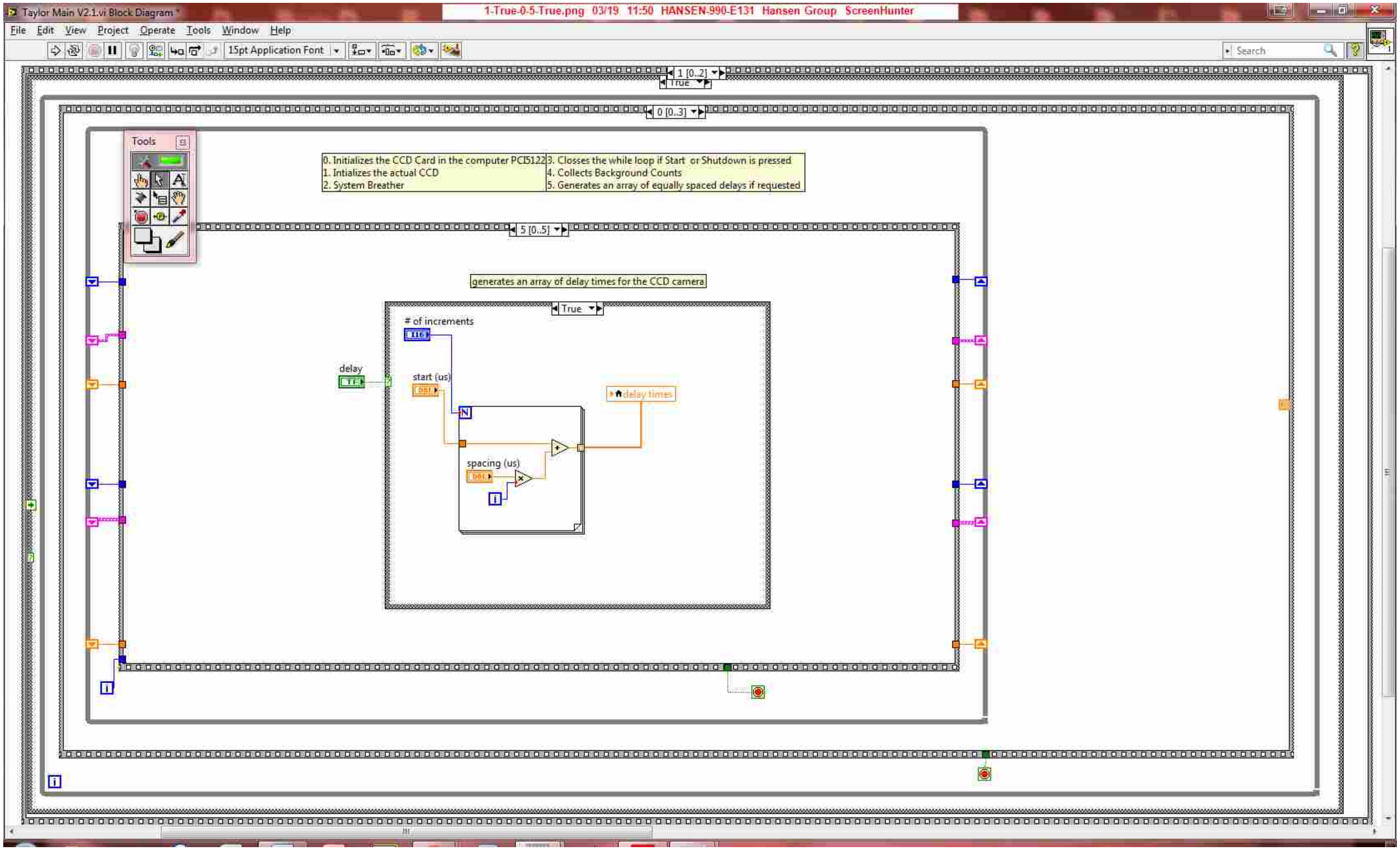

0. Initializes the CCD Card in the computer PCI5122
1. Intializes the actual CCD
2. System Breather
3. Closses the while loop if Start or Shutdown is pressed
4. Collects Background Counts
5. Generates an array of equally spaced delays if requested

generates an array of delay times for the CCD camera

If true then an array is created from the start time, # of increments or delay times, and the designated spacing

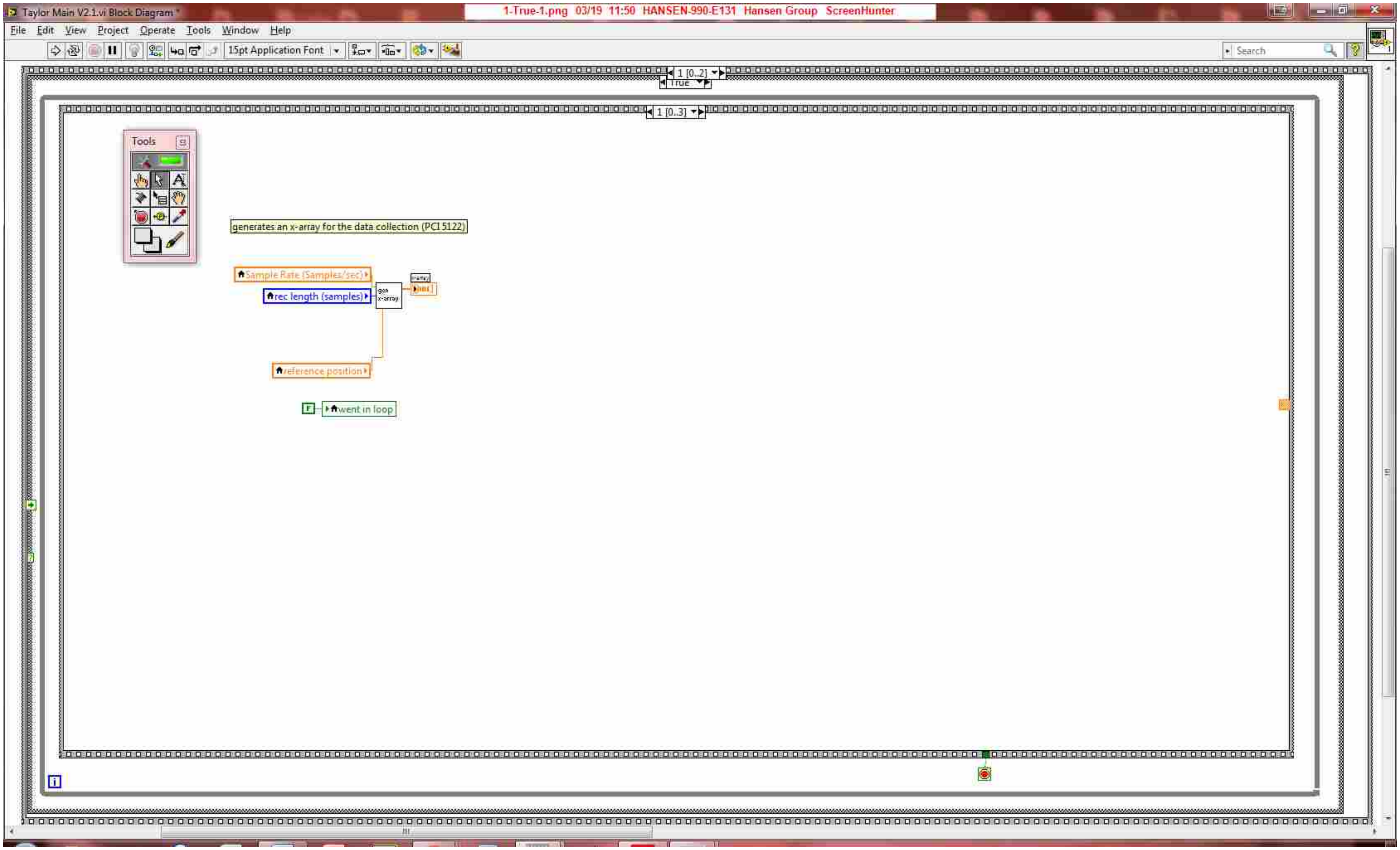

generates an x-array for the data collection (PCI 5122)

Another part of IR collection with the PCI DAQ card to generate an x-array

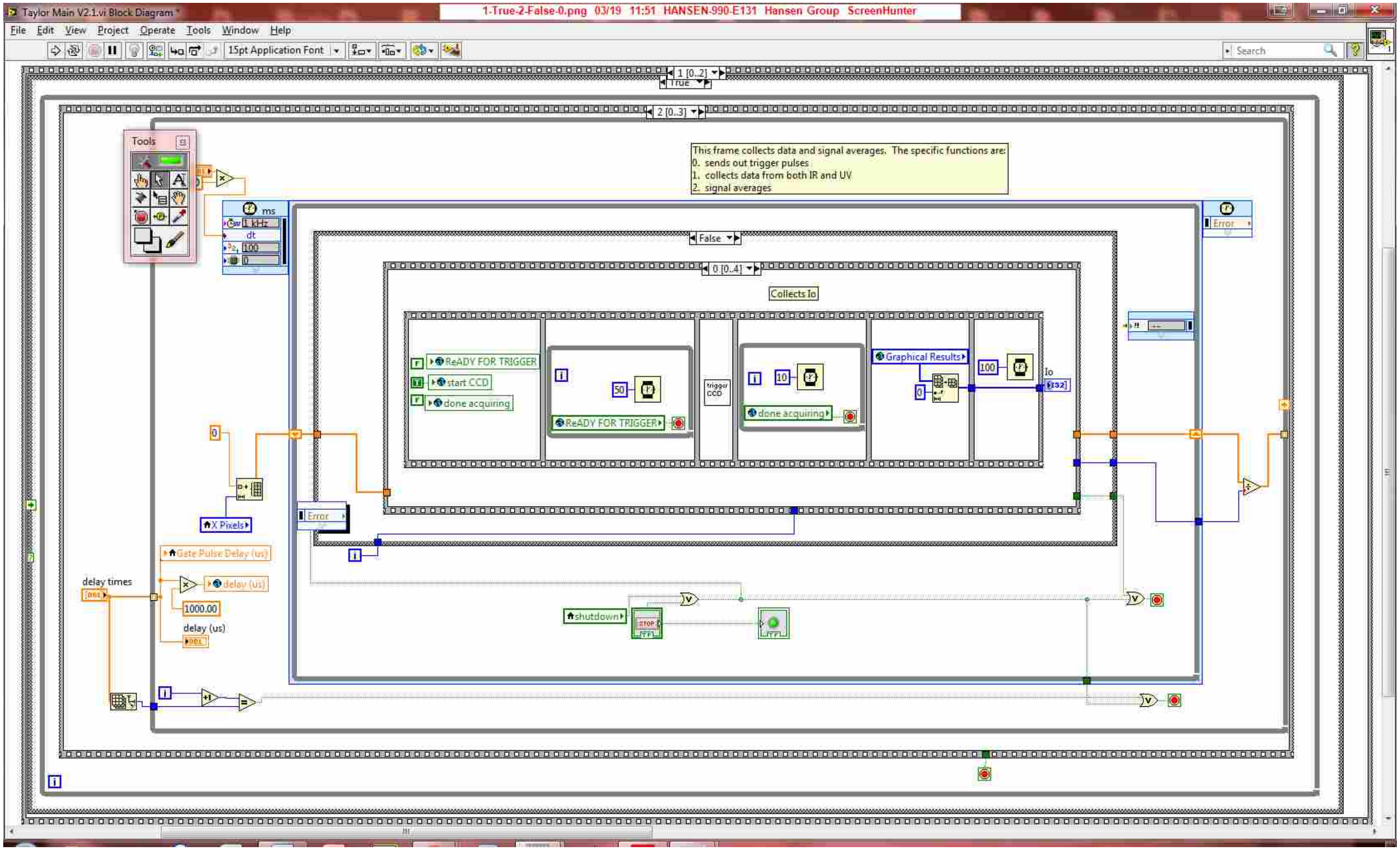

This frame collects data and signal averages. The specific functions are:
0. sends out trigger pulses
1. collects data from both IR and UV
2. signal averages

The inner sequence follows the steps again to collect a spectrum from the CCD. We pass variables to the DDG and await responses. We collect an Io before every laser pulse and I after every laser pulse. This overcomes fluctuations in the D2 lamp by having I and Io collected as close together as possible. The outer loops are used to cycle through both the averaging procedure and stepping through each designated delay time.

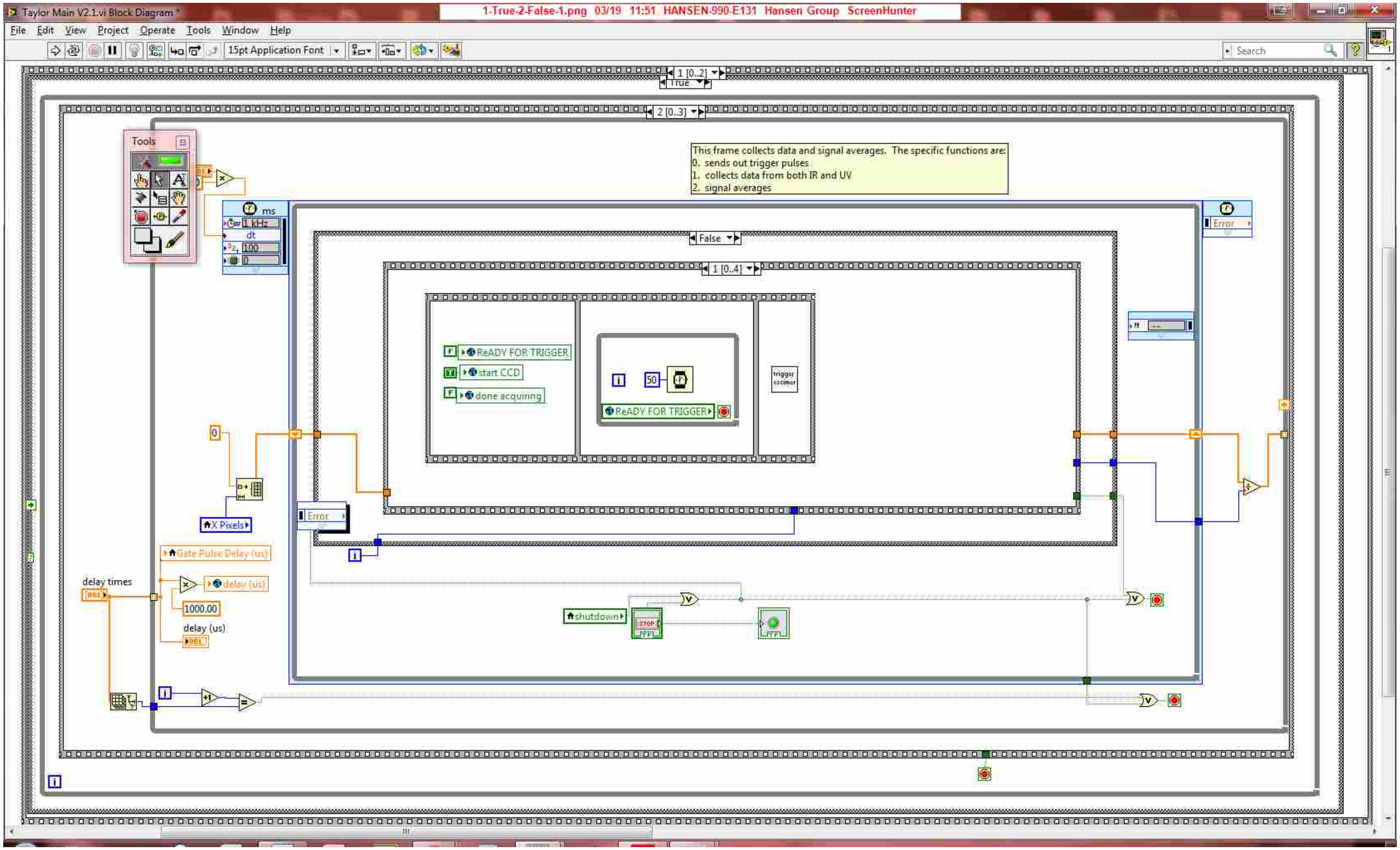

This frame collects data and signal averages. The specific functions are:
0. sends out trigger pulses
1. collects data from both IR and UV
2. signal averages

Now trigger the Excimer that will in turn trigger a photodiode that triggers the CCD

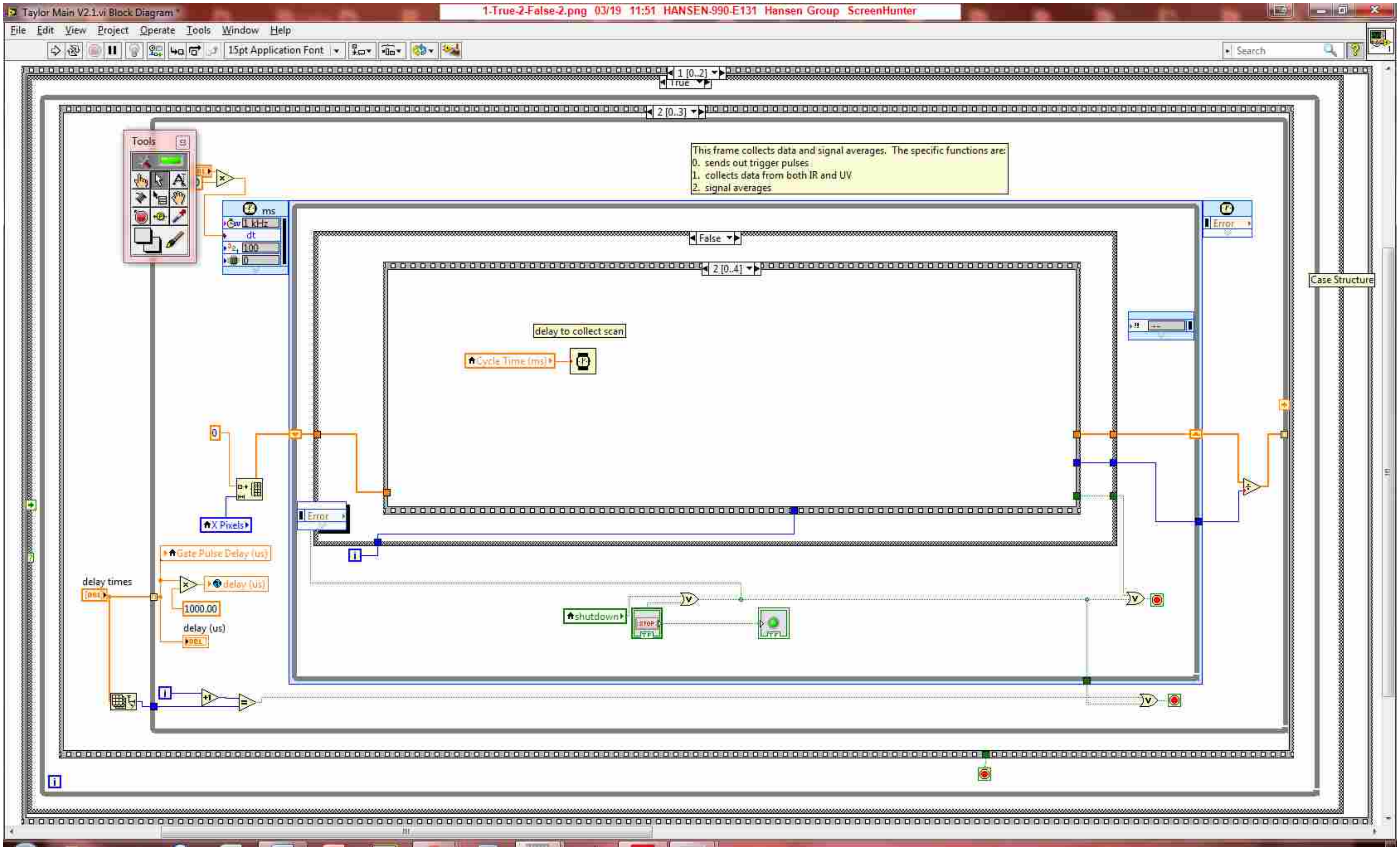

This frame collects data and signal averages. The specific functions are:
0. sends out trigger pulses
1. collects data from both IR and UV
2. signal averages

Delay by the cycle time of the CCD to allow it time to collect data

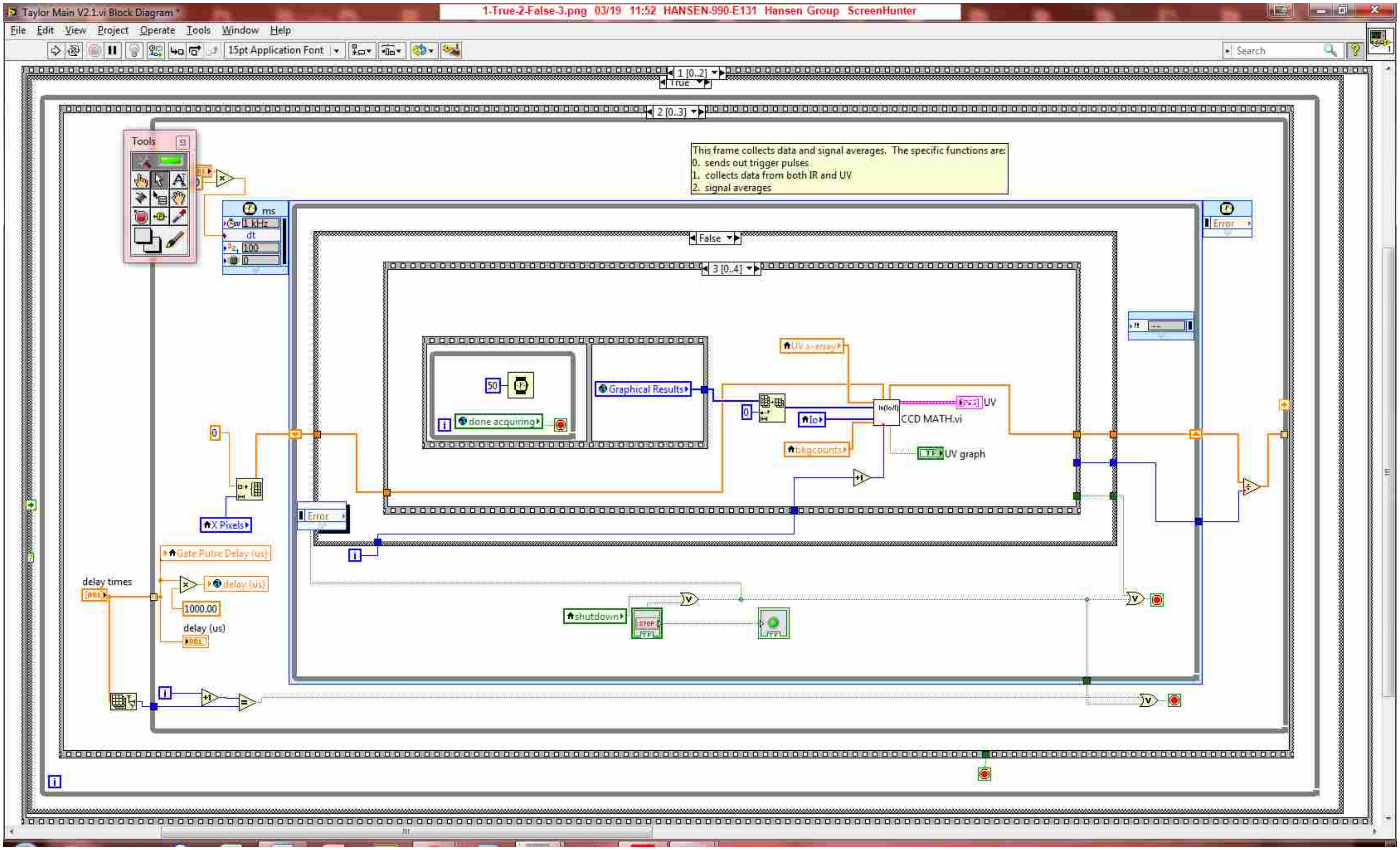

This frame collects data and signal averages. The specific functions are:
0. sends out trigger pulses
1. collects data from both IR and UV
2. signal averages

Return the signal from the CCD and use the previously collected Io to create the absorption spectrum

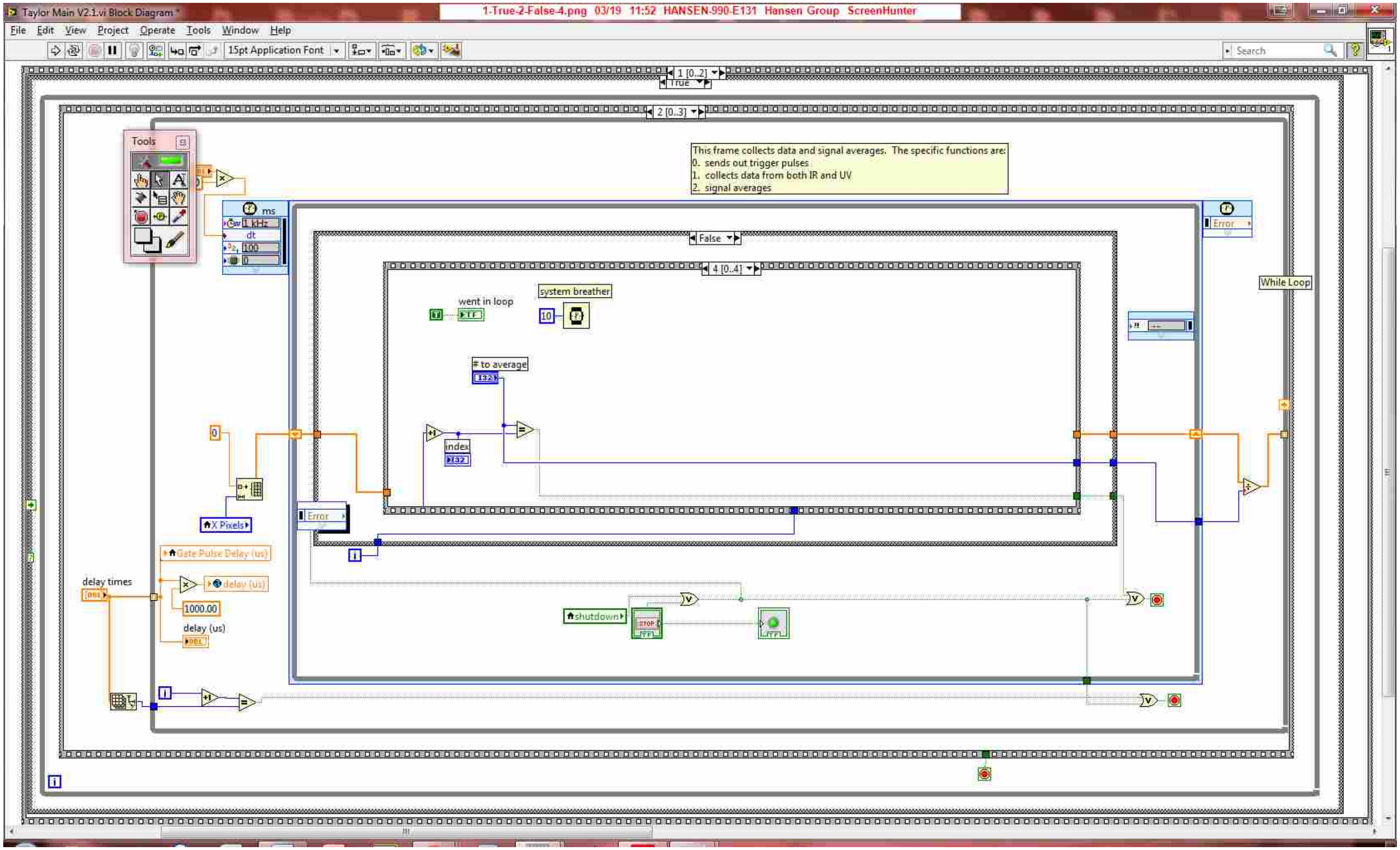

This frame collects data and signal averages. The specific functions are:
0. sends out trigger pulses
1. collects data from both IR and UV
2. signal averages

Collect absorption spectra until the number collected equals the desired averages

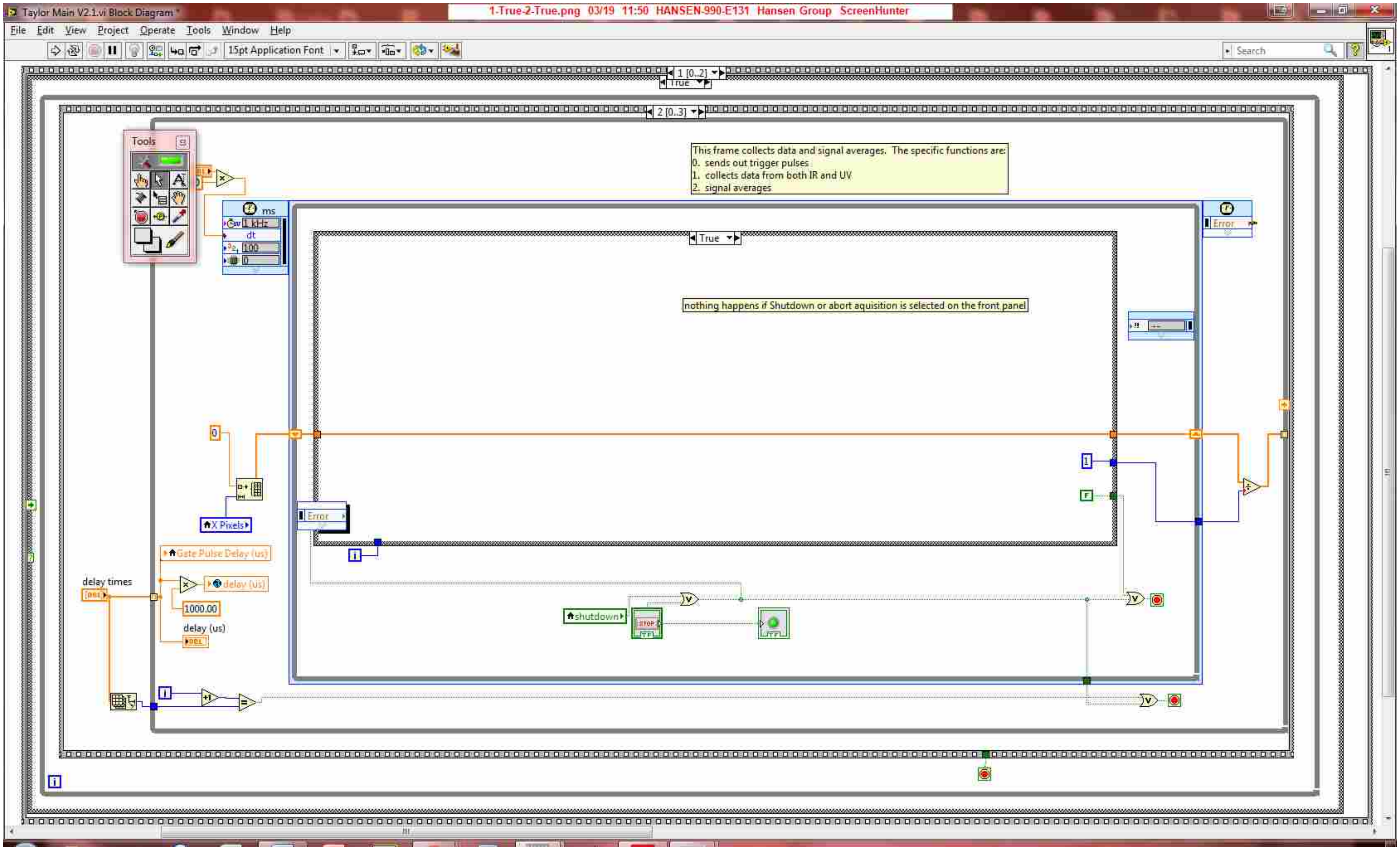

This frame collects data and signal averages. The specific functions are:
0. sends out trigger pulses
1. collects data from both IR and UV
2. signal averages

nothing happens if Shutdown or abort aquisition is selected on the front panel

If the shutdown or abort buttons are pressed it will skip this loop

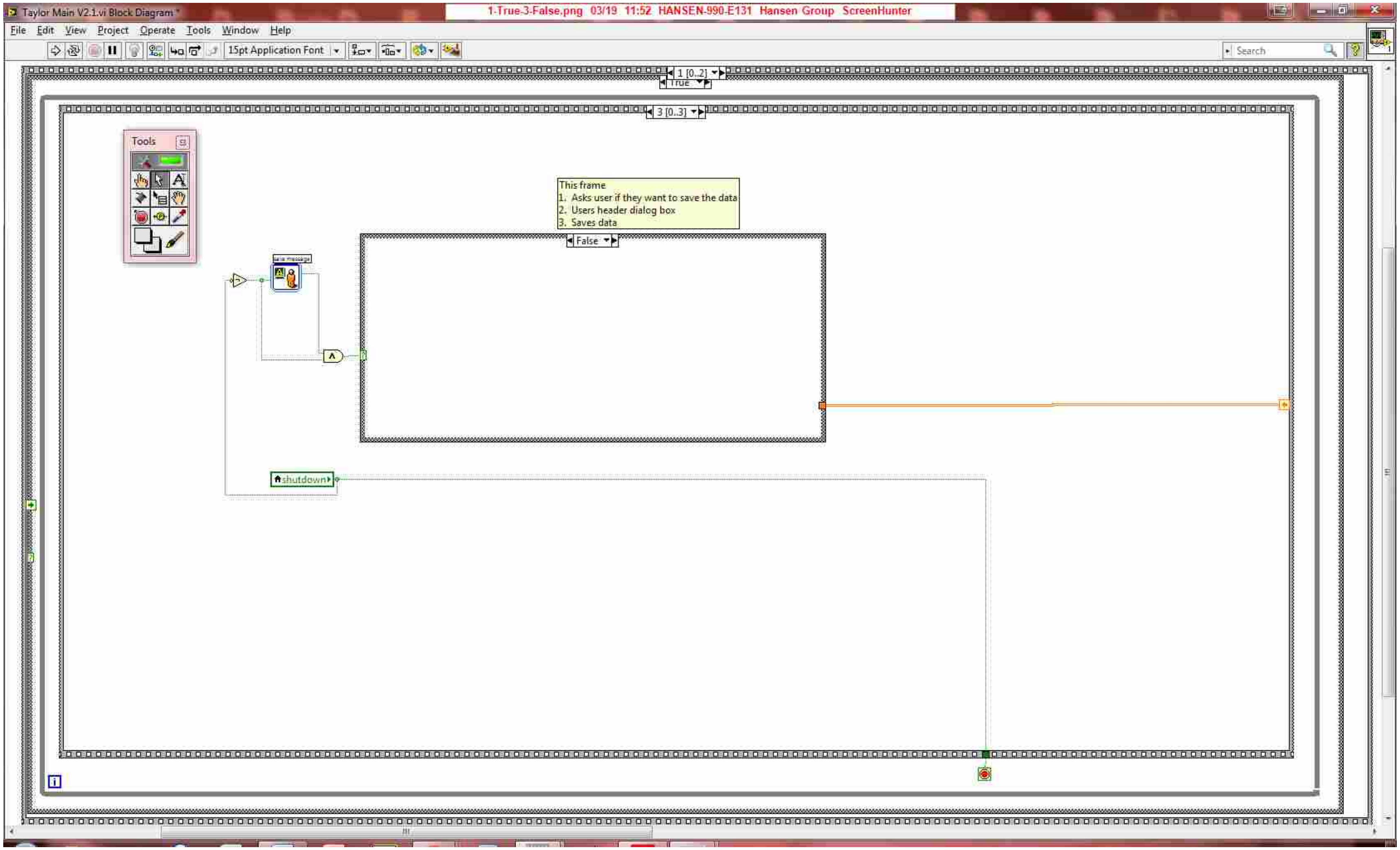

This frame
1. Asks user if they want to save the data
2. Users header dialog box
3. Saves data

Abort the save and it will delete the data.

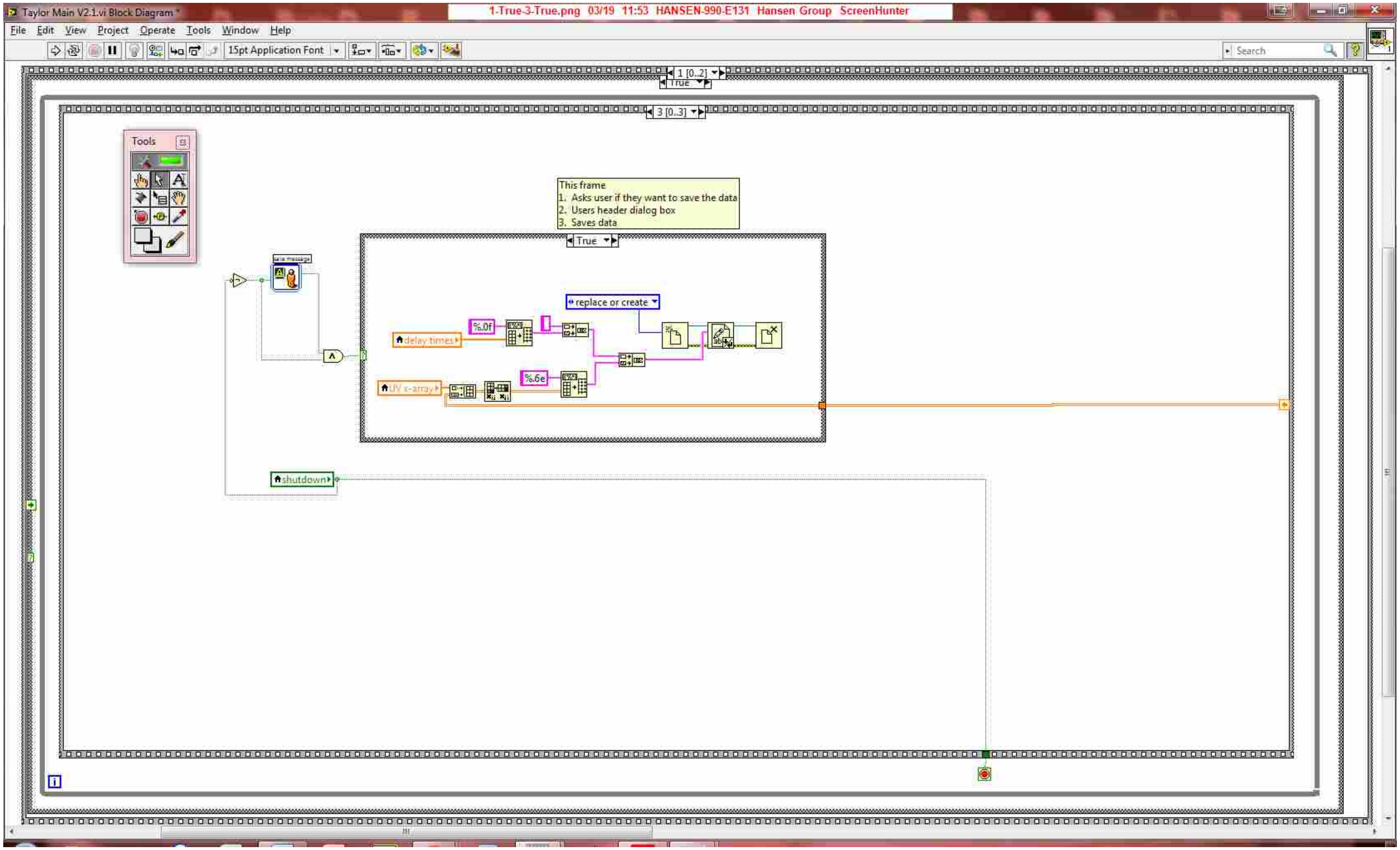

This frame
1. Asks user if they want to save the data
2. Users header dialog box
3. Saves data

If the prompt is accepted to save the data it will save the data with proper headers in a .csv file format

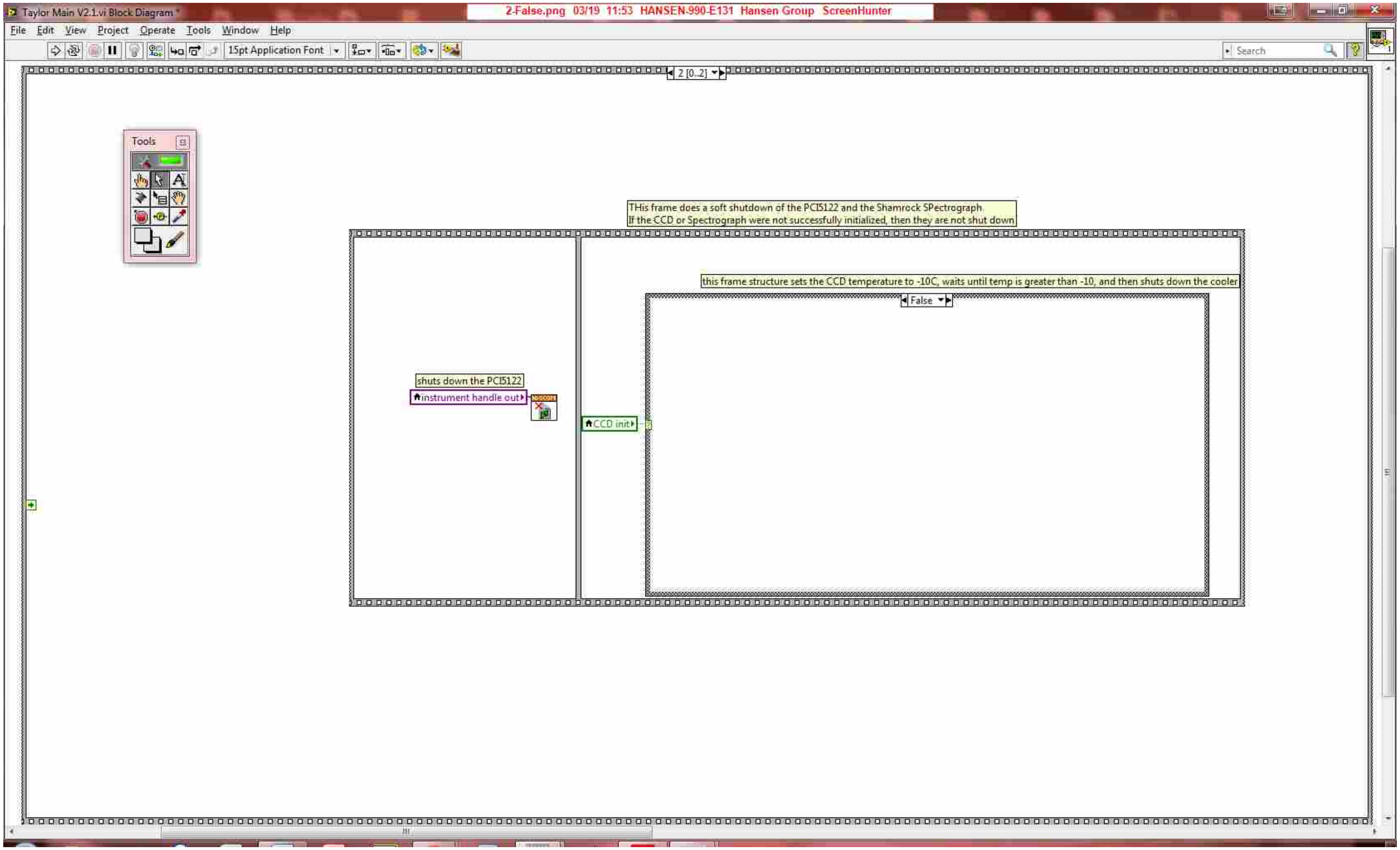

THis frame does a soft shutdown of the PCI5122 and the Shamrock SPectrograph
If the CCD or Spectrograph were not successfully initialized, then they are not shut down

this frame structure sets the CCD temperature to -10C, waits until temp is greater than -10, and then shuts down the cooler

shuts down the PCI5122

instrument handle out

This is the soft shutdown of the CCD temperature control

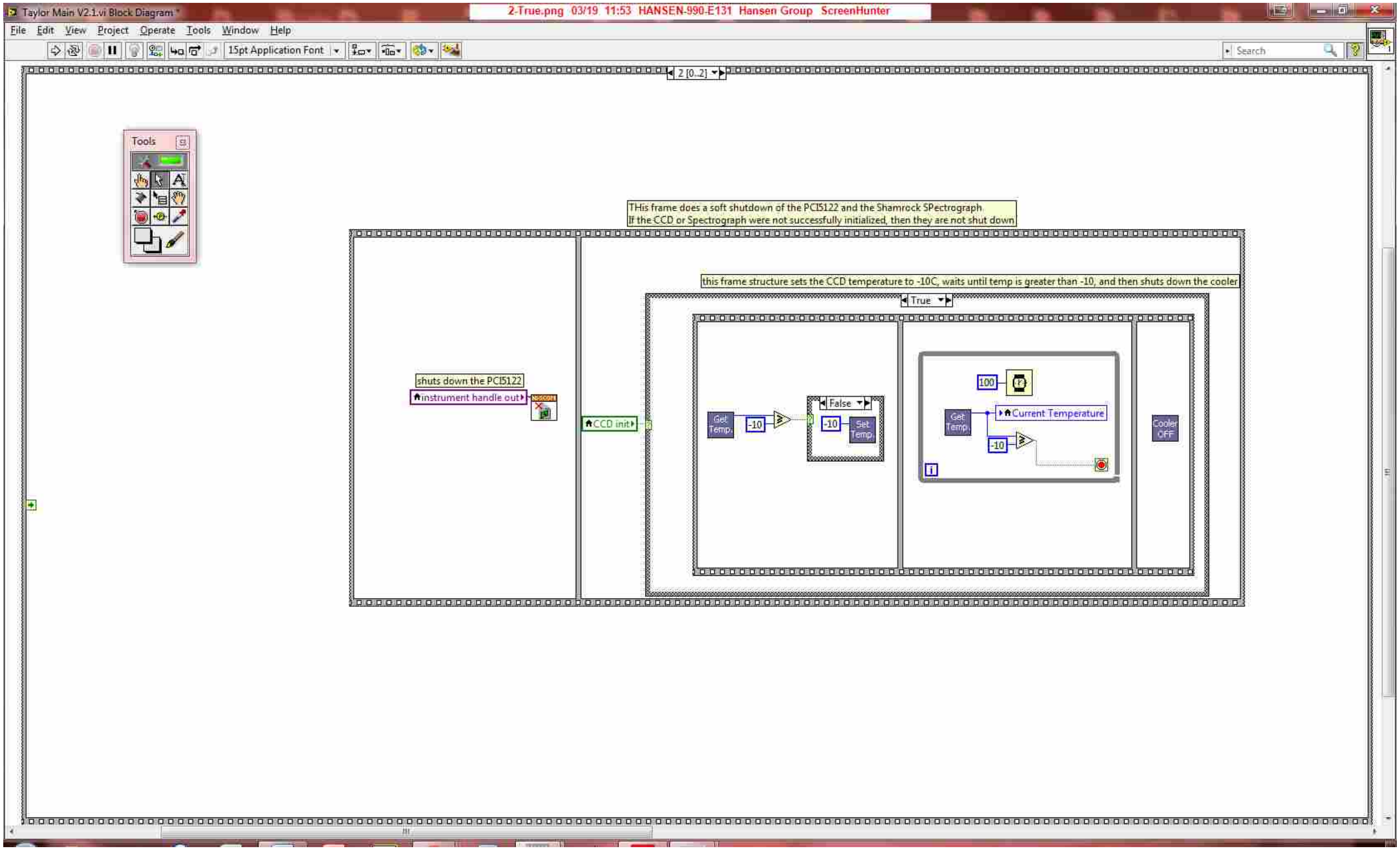

THis frame does a soft shutdown of the PCI5122 and the Shamrock SPectrograph
If the CCD or Spectrograph were not successfully initialized, then they are not shut down

this frame structure sets the CCD temperature to -10C, waits until temp is greater than -10, and then shuts down the cooler

This will raise the temperature of the CCD to -10C before shutting down.

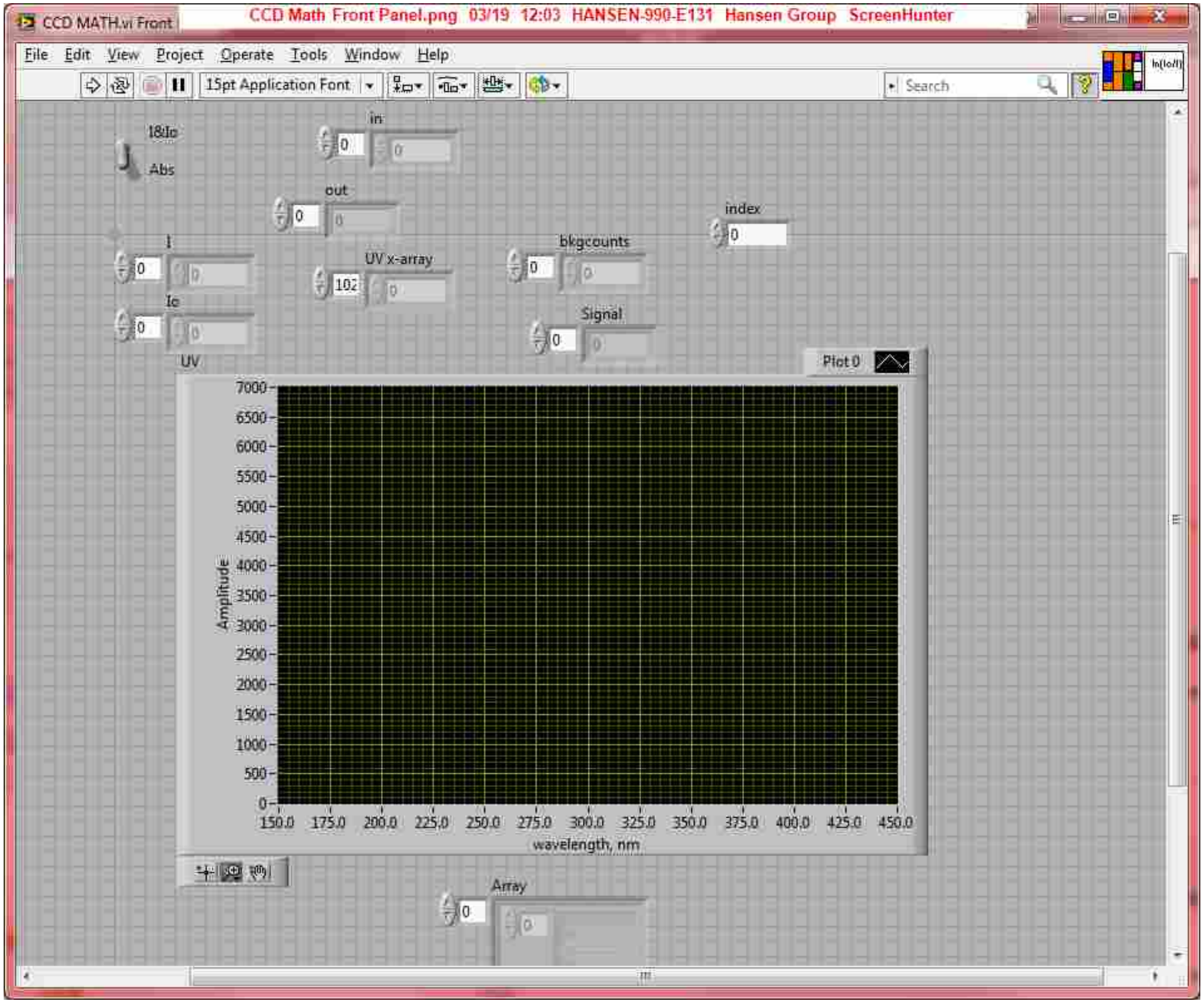

The following Vi's are used just as sub Vi's. The front panels are not very important because the user never sees them.

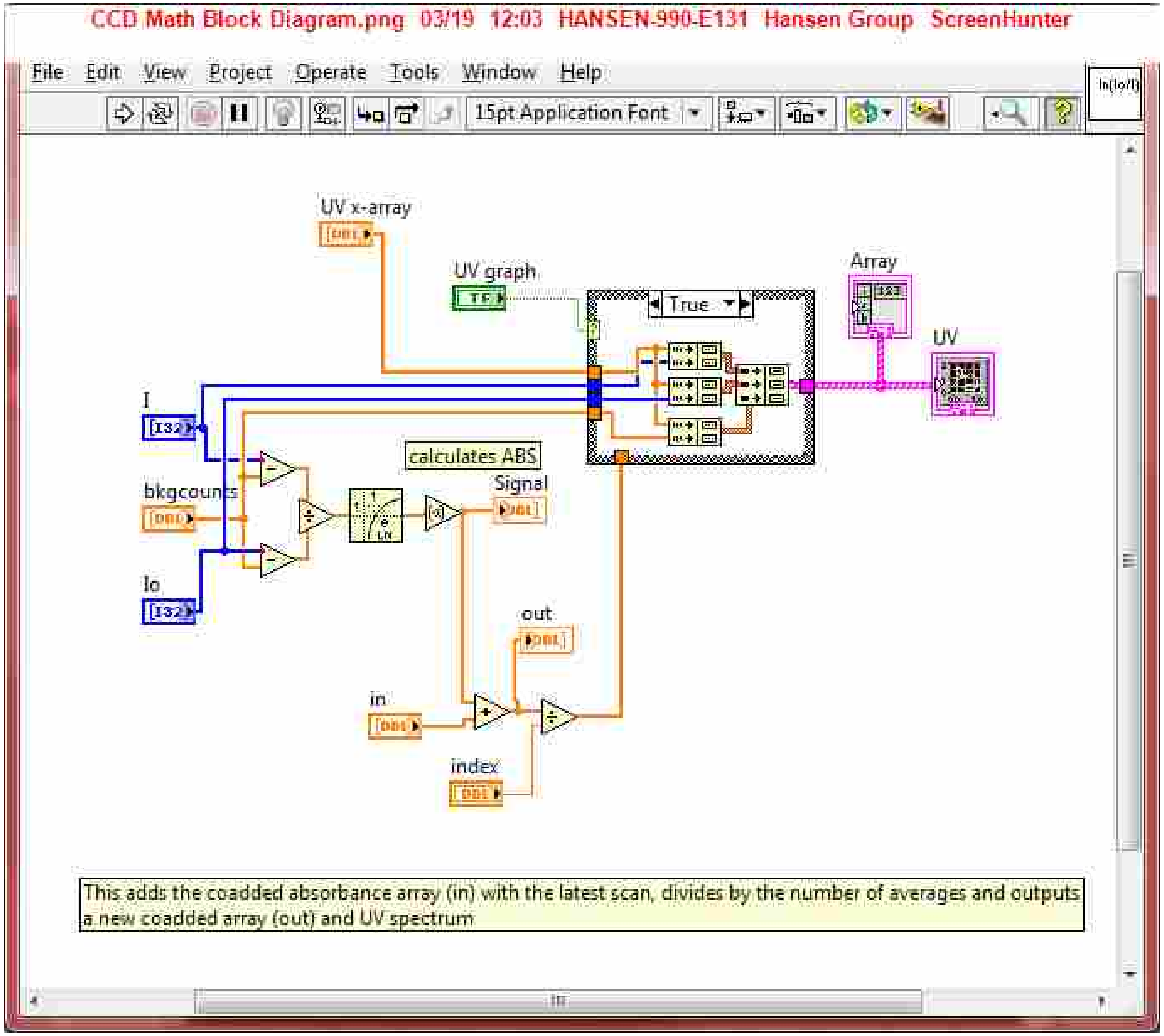

This adds the coadded absorbance array (in) with the latest scan, divides by the number of averages and outputs a new coadded array (out) and UV spectrum

Subtract the background counts from I and Io. Divide the two and take the natural log to convert the spectrum into absorbances. Three build array functions are used to construct the spectra of I, Io , and absorbances so that they may be plotted in the Main.VI

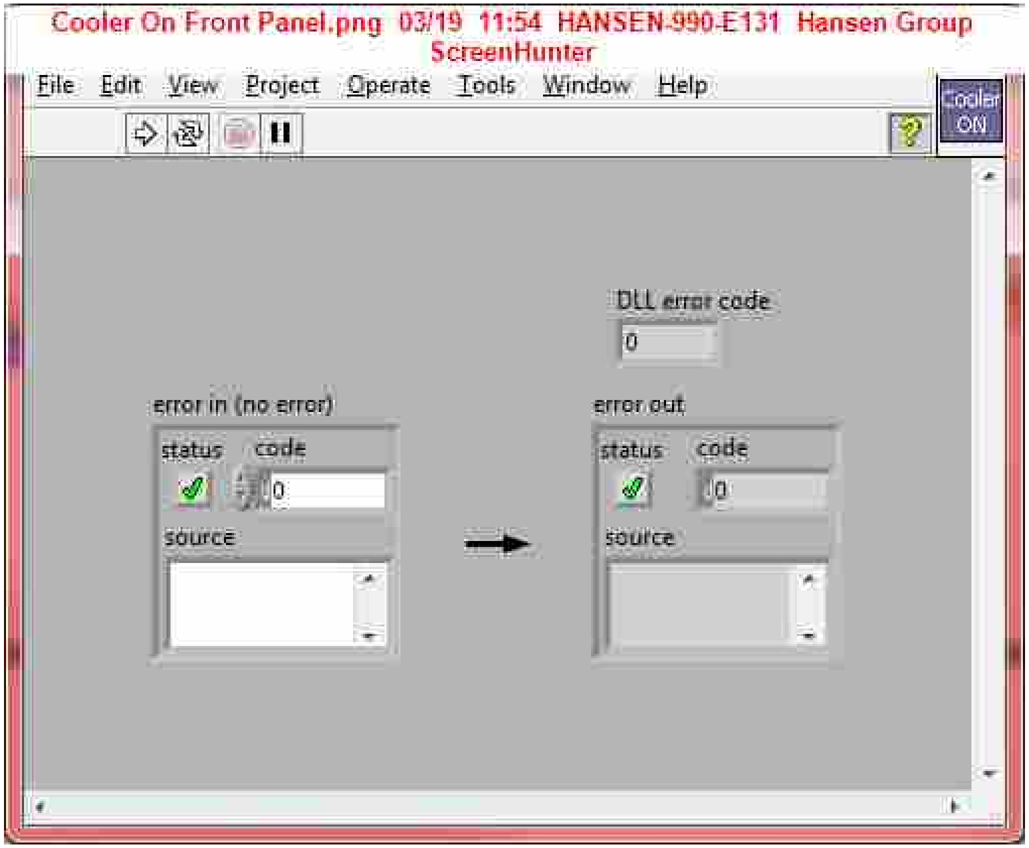

Cooler On Front Panel.png 03/19 11:54 HANSEN-990-E131 Hansen Group ScreenHunter

DLL error code: 0

error in (no error): status ✓ code 0 source

error out: status ✓ code 0 source

Here is an example of an Andor SDK Vi. They are extremely simple as shown here. The only input and output are error reporting. The sub vi's trigger a task that is programmed into the CCD and will return an error if one occurs. Some will have an output like collected data or time cycles or cooler temperature.

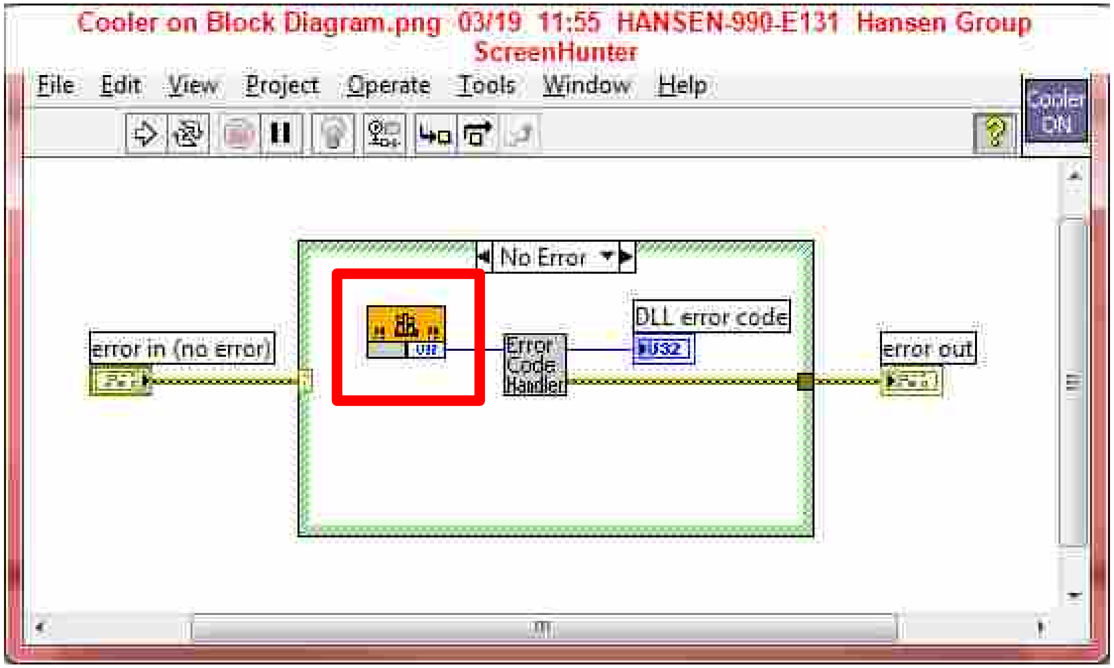

The highlighted area is the “Call Library Function” function. It goes directly into a library, in this case the Andor SDK (atm32cd), and calls a specific function. Some requires inputs and give outputs but this one just turns the cooler on.

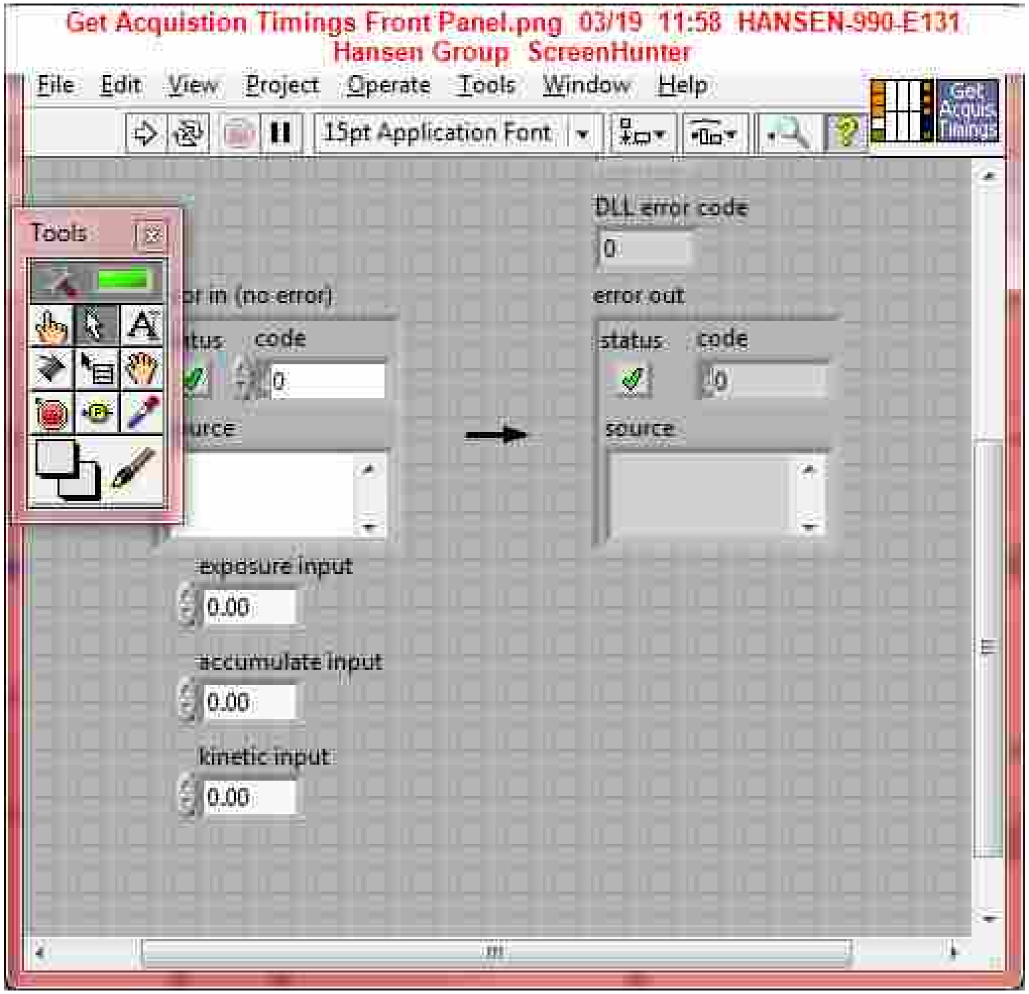

Get Acquistion Timings Front Panel.png 03/19 11:58 HANSEN-990-E131
Hansen Group ScreenHunter

DLL error code: 0

or in (no error)
tus: ✓ code: 0
urce:

error out
status: ✓ code: 0
source:

exposure input: 0.00

accumulate input: 0.00

kinetic input: 0.00

Another example of an Andor SDK Vi but with inputs and outputs

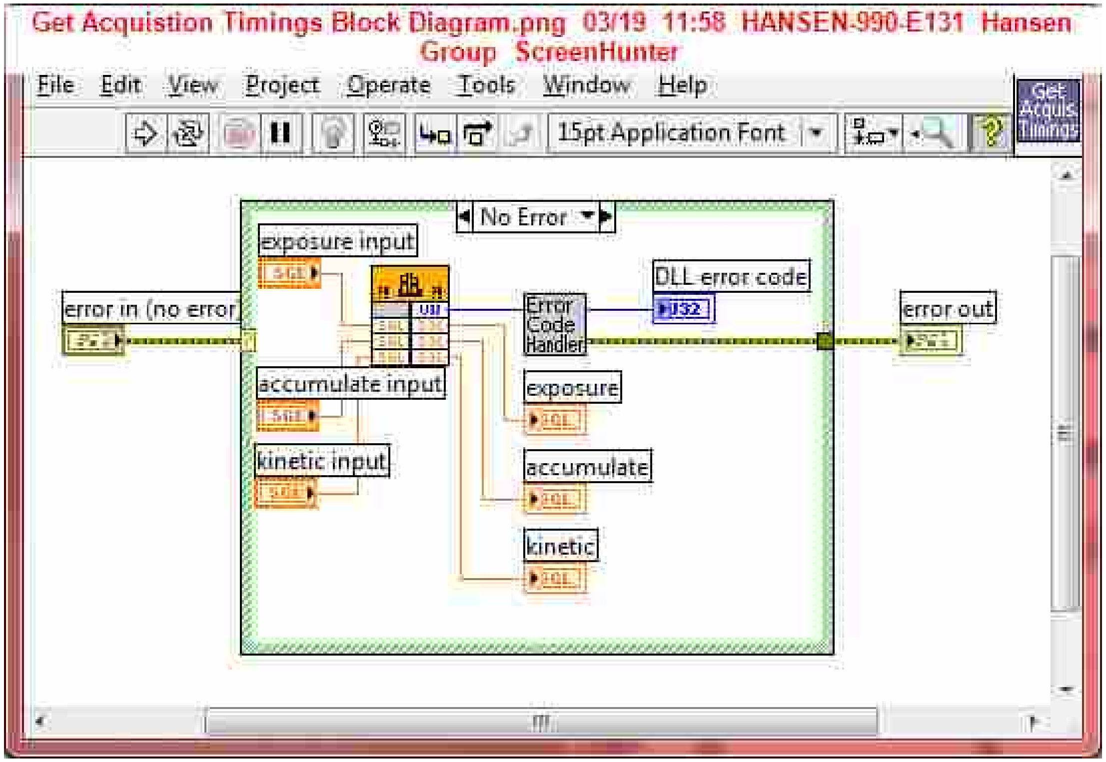

Both inputs and outputs are used like normal subvi's and the inputs and out puts are wired to the icon when used in the main vi

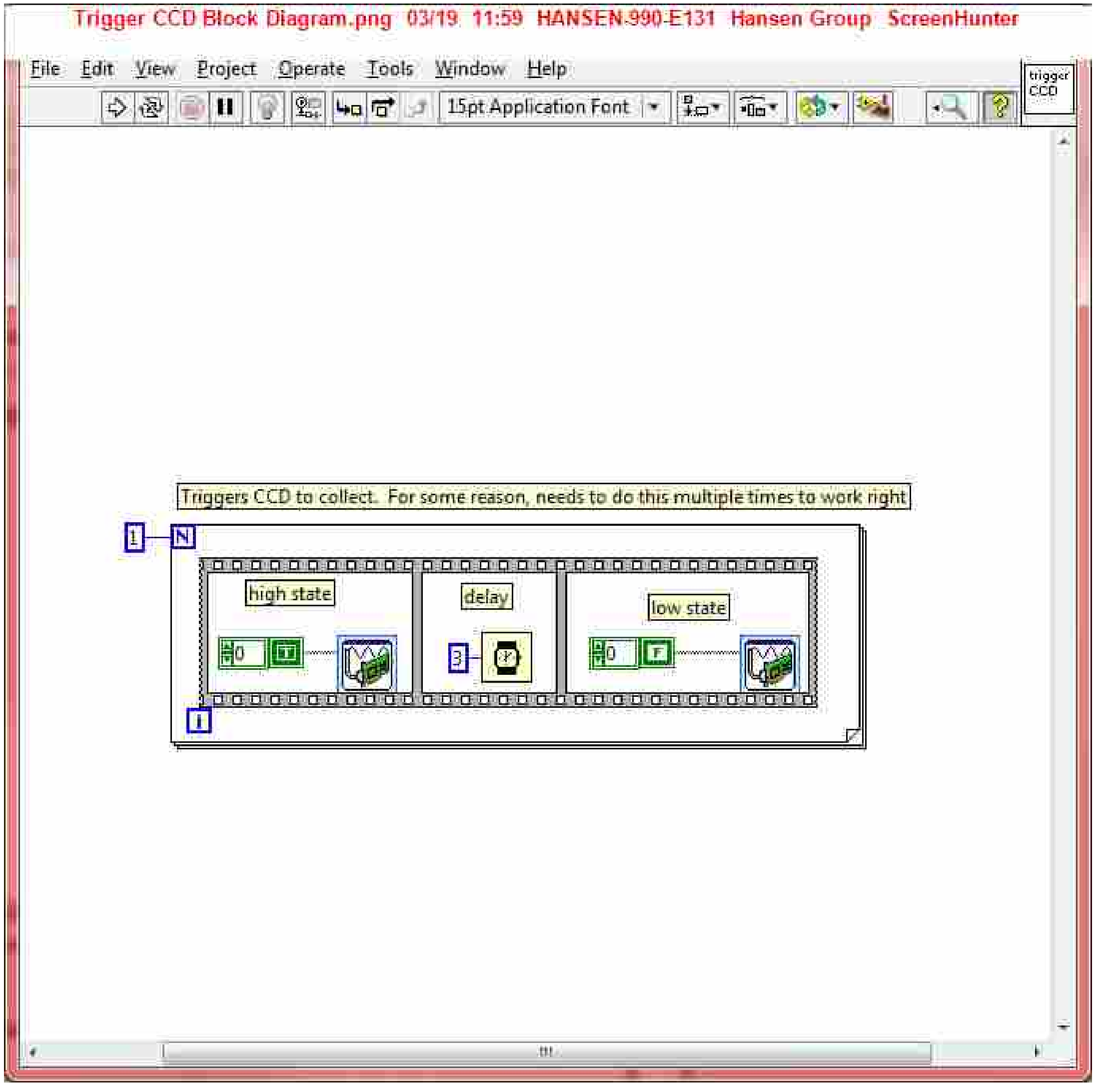

Triggers CCD to collect. For some reason, needs to do this multiple times to work right

Both the CCD trigger and Excimer Trigger functions work by sending a signal output through the DAQ to a DDG. This DDG is explained in the physical wiring section but is used to create the properly conditioned signal for trigger execution. Here we send it twice to trigger it. We never solved why it wanted two signals to respond.

7.5 Physical Wiring

Instructions to setup the external wiring to perform CCD UV absorption experiments using LabVIEW

Physical Wiring

Instructions to setup the external wiring to perform CCD UV absorption experiments using LabVIEW

Laser Controller

“Ext in” is the external trigger input. It requires a +15V signal with 10 to 100 µs pulse duration. The laser triggers on the positive slope.

To operate in external trigger mode first turn on the cooling water and turn the power key on the laser controller. A warm up timer commences and requires 5 minutes before the voltage can be activated. Press **Laser On** and then press **HV On**. The high voltage level should be set at zero from when it was turned off last. Turn the voltage up to 17 or 18 KV and let the laser fire for a minute at 1Hz, then turn the voltage up to a maximum of 25 KV. With the laser firing press the **Ext Trigger**. Now the laser will wait for a trigger pulse. Take caution that the laser in this state may fire at any time. Be aware that leaving the laser in a state with high voltage applied and not firing puts strain on the electronics and hence the HV is the last step before starting an experiment.

GPIB – General Purpose Interface Bus

GPIB is an interface between instruments and computers. Most instruments come with instrument drivers to control them through GPIB. We use GPIB to control the oscilloscope, the New Focus Laser, and the single photon counter. As shown in the picture GPIB cables may be daisy-chained and connect multiple instruments through one GPIB to USB converter.

National Instruments NI-6008 DAQ or Data Acquisition Device

These devices are cheap and work well for collecting data at 10 KSamples/sec. This rate is not great for fast experiments but works well for sending out trigger pulses and collecting signals with little variation. We use it to collect flows, temperature, and pressure into LabVIEW. At times in Windows 7 these USB devices are disconnected automatically when not in use. This doesn’t happen on XP and hasn’t been on windows 8. Simply disconnect the device from the USB and reconnect.

Pulse Generator

This pulse generator takes the 5V signal from the DAQ and converts it into a 15V 50 µs trigger for the excimer laser. As you can see from all the dials there are many different signals that you may produce with this. The DAQ on the other hand can only produce 5 V TTL pulses.

Digital Delay Generator / Pulse Generator

The DDG works similar to the DDG Labview Vi. Here it is used to condition two signals to trigger the CCD. We use a T-BNC so the trigger input can accept signal from the DAQ or the PhotoDiode setup to collect Excimer light. The out put is a 3 V TTL pulse sent directly to the CCD. The signal to the CCD must be less than 5V. At times the signal from the photo diode is not triggering. Readjust the photodiode to make sure sufficient Excimer light is collected on the active area. DO NOT place the photodiode directly in the path of the excimer because it will destroy it.

7.6 Water Detection with FMS

The IR Water 3.0 is used in FMS spectroscopy. This VI can be used for any molecule in the near IR with the New Focus Laser. The Line intensity needs to be obtained from the HITRAN Database

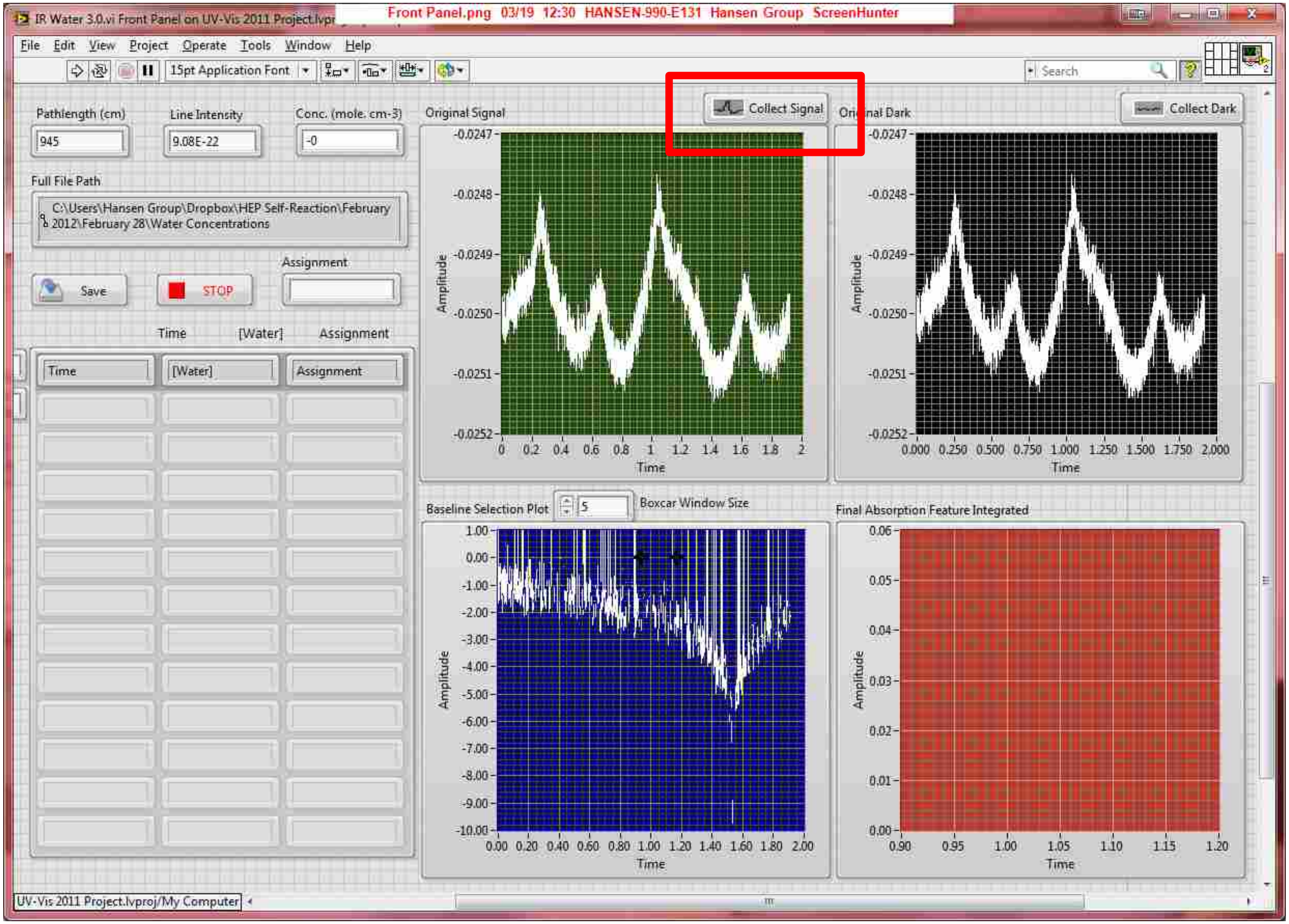

Pathlength (cm): 945

Line Intensity: 9.08E-22

Conc. (mole. cm-3): -0

Full File Path: C:\Users\Hansen Group\Dropbox\HEP Self-Reaction\February 2012\February 28\Water Concentrations

Boxcar Window Size: 5

Time	[Water]	Assignment

The frequency modulation with a 3 volt 100 Hz signal causes a 1 wavenumber deviation in both directions. Make sure the Oscilloscope is collecting the full 2 wavenumbers by looking at the symmetry of the waveform. The modulation will pass over the feature twice. Collect signal button will record the waveform.

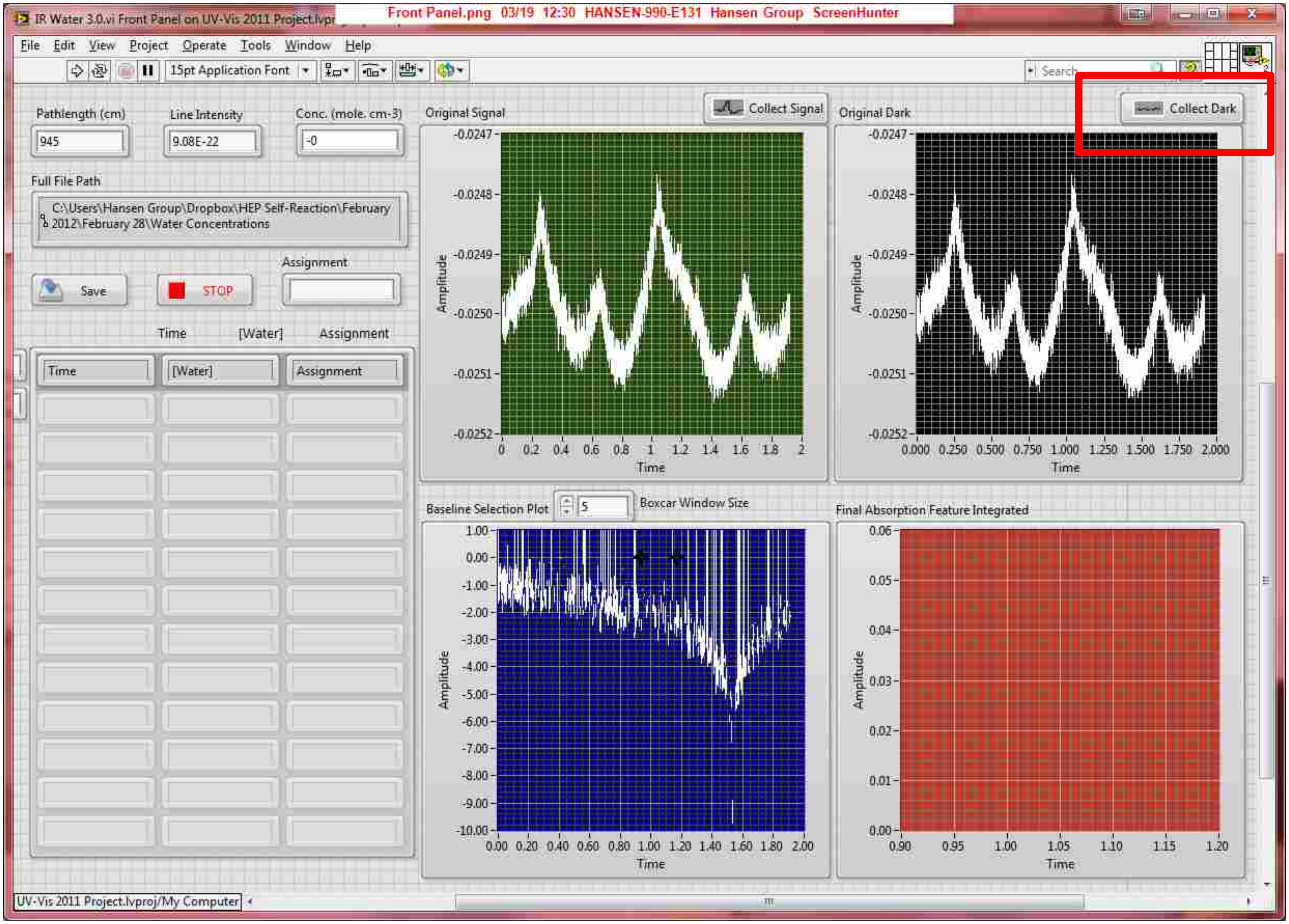

Pathlength (cm): 945

Line Intensity: 9.08E-22

Conc. (mole. cm-3): -0

Full File Path: C:\Users\Hansen Group\Dropbox\HEP Self-Reaction\February 2012\February 28\Water Concentrations

Assignment:

Boxcar Window Size: 5

Place a dark card over the detector and collect the dark signal.

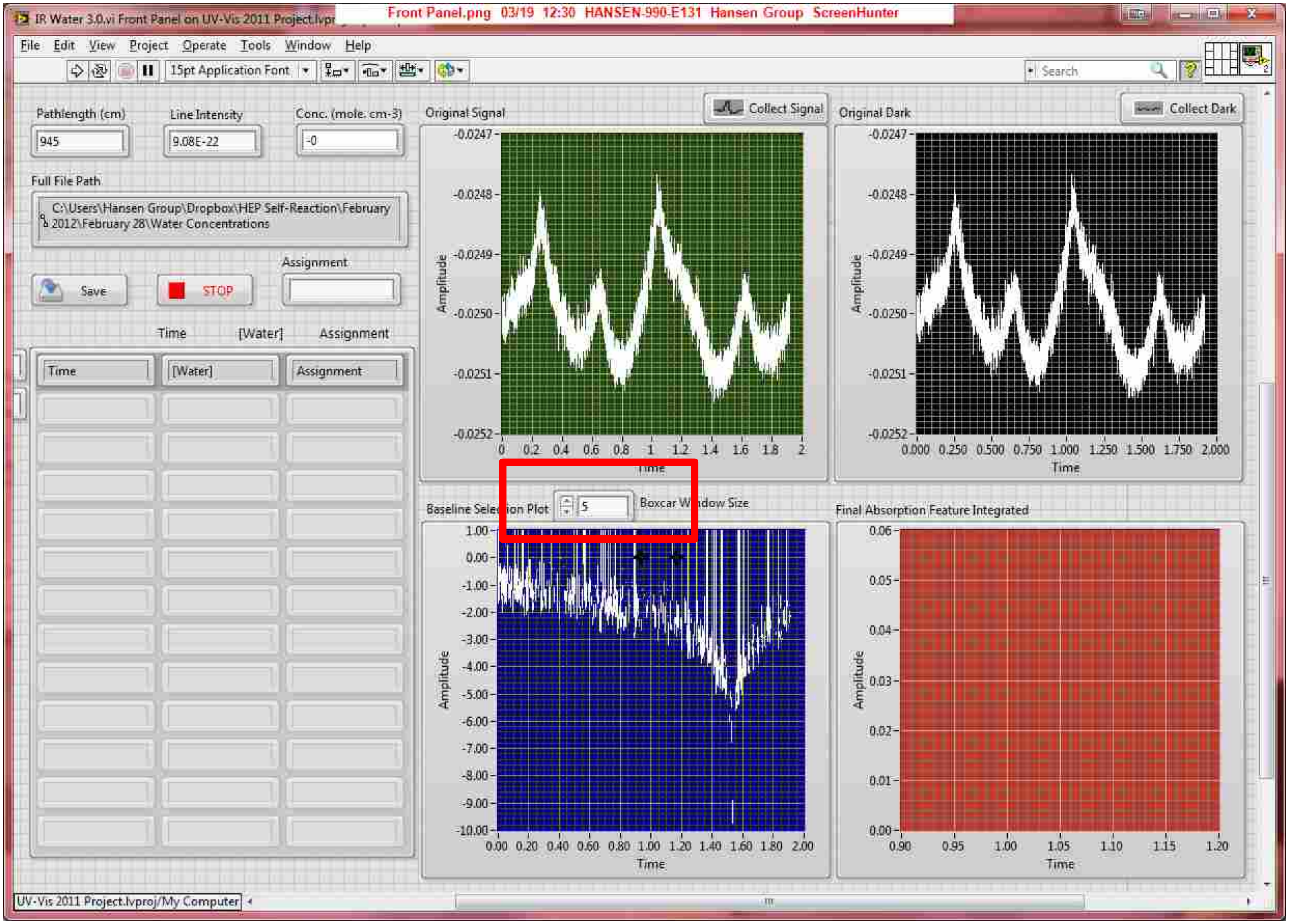

Pathlength (cm): 945

Line Intensity: 9.08E-22

Conc. (mole. cm-3): -0

Full File Path: C:\Users\Hansen Group\Dropbox\HEP Self-Reaction\February 2012\February 28\Water Concentrations

Assignment:

Time	[Water]	Assignment

Boxcar Window Size: 5

As the Boxcar Window Size is adjusted it will update the absorption spectrum. After the spectrum is sufficiently smoothed, use the two cursor cross hairs to eyeball a baseline. Typically a small 100 Hz signal shows in the spectrum and you make your own baseline with the cursors. Each time the cursor is moved the final absorption feature will update and the concentration will be displayed in the Conc box.

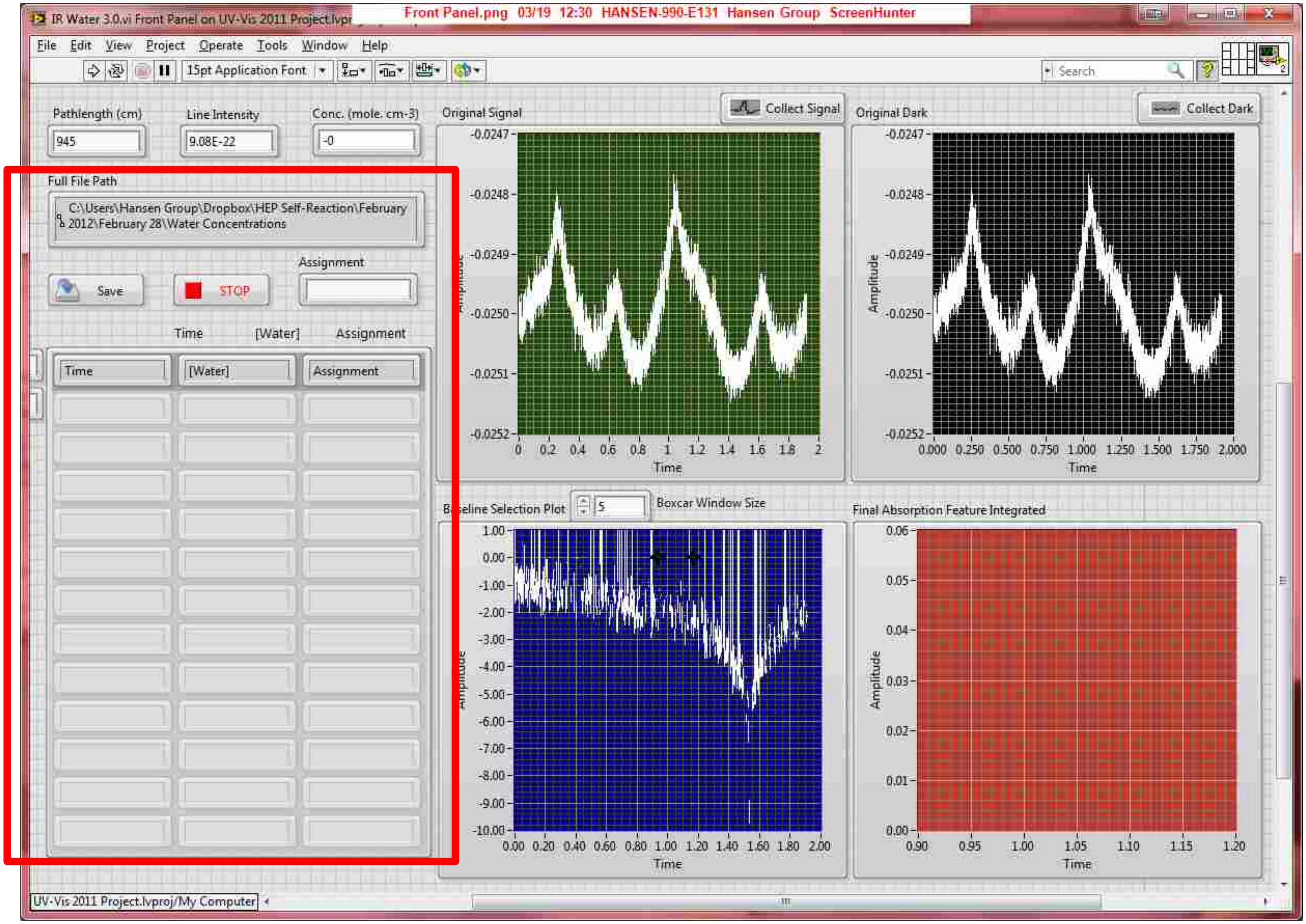

Pathlength (cm): 945

Line Intensity: 9.08E-22

Conc. (mole. cm-3): -0

Full File Path: C:\Users\Hansen Group\Dropbox\HEP Self-Reaction\February 2012\February 28\Water Concentrations

Assignment:

Boxcar Window Size: 5

Time	[Water]	Assignment

This box to the left is a record of all the concentrations measured. When satisfied with a measurement, press "Save" and it will be added to the file for the day. A file does not need to be designated as it is created automatically. Use the assignment box to specify the measurement. Example: Run 1 Prior.

This Vi is too large to show in one picture because of this side box. This box creates a file for the day to continue to save each measurement to the file. The file path can be changed here because it is sent dropbox in the HEP self-reaction folder but access is limited to this folder. Designate a folder with open access. The file is actually named Water Concentrations.

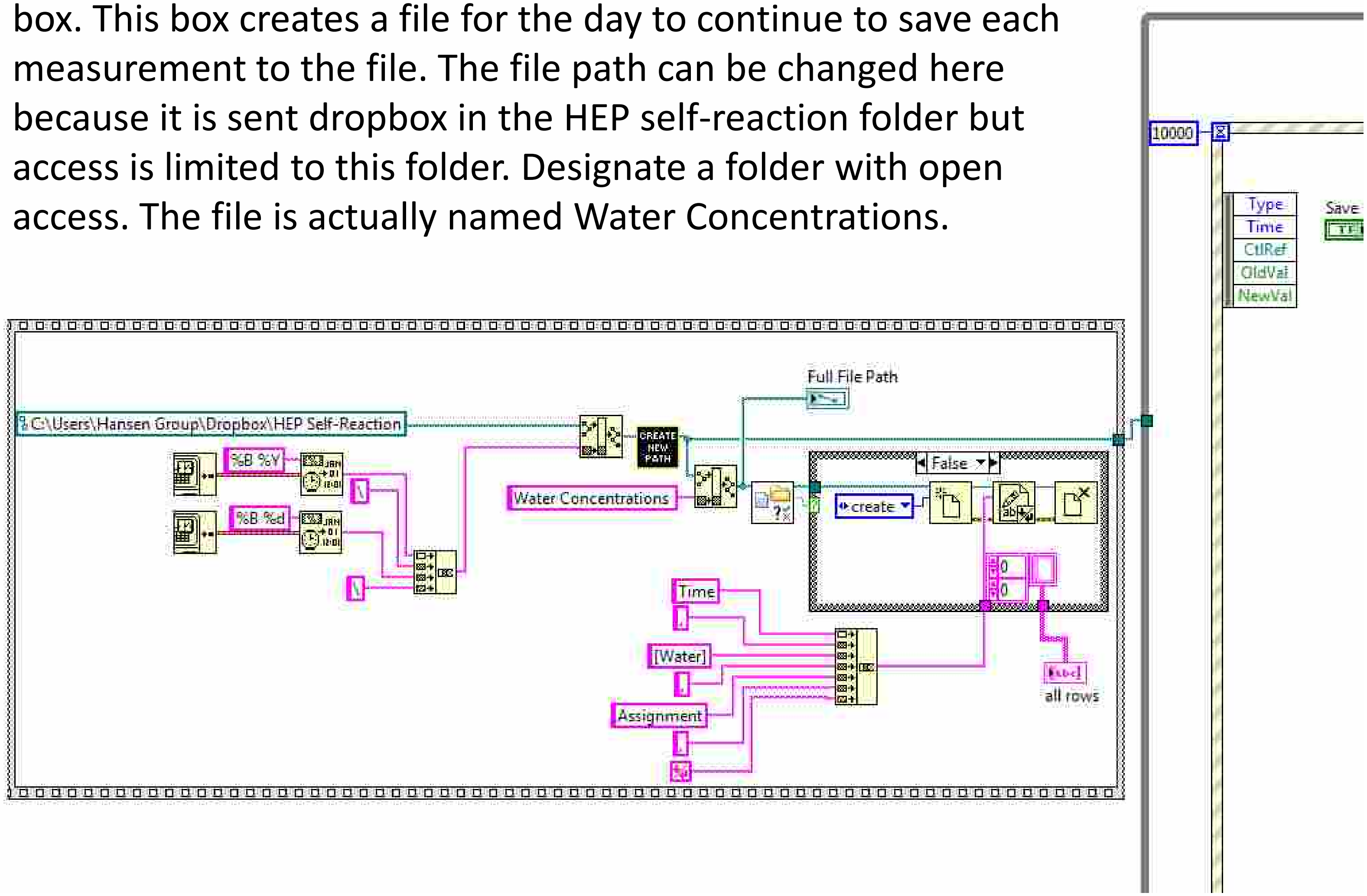

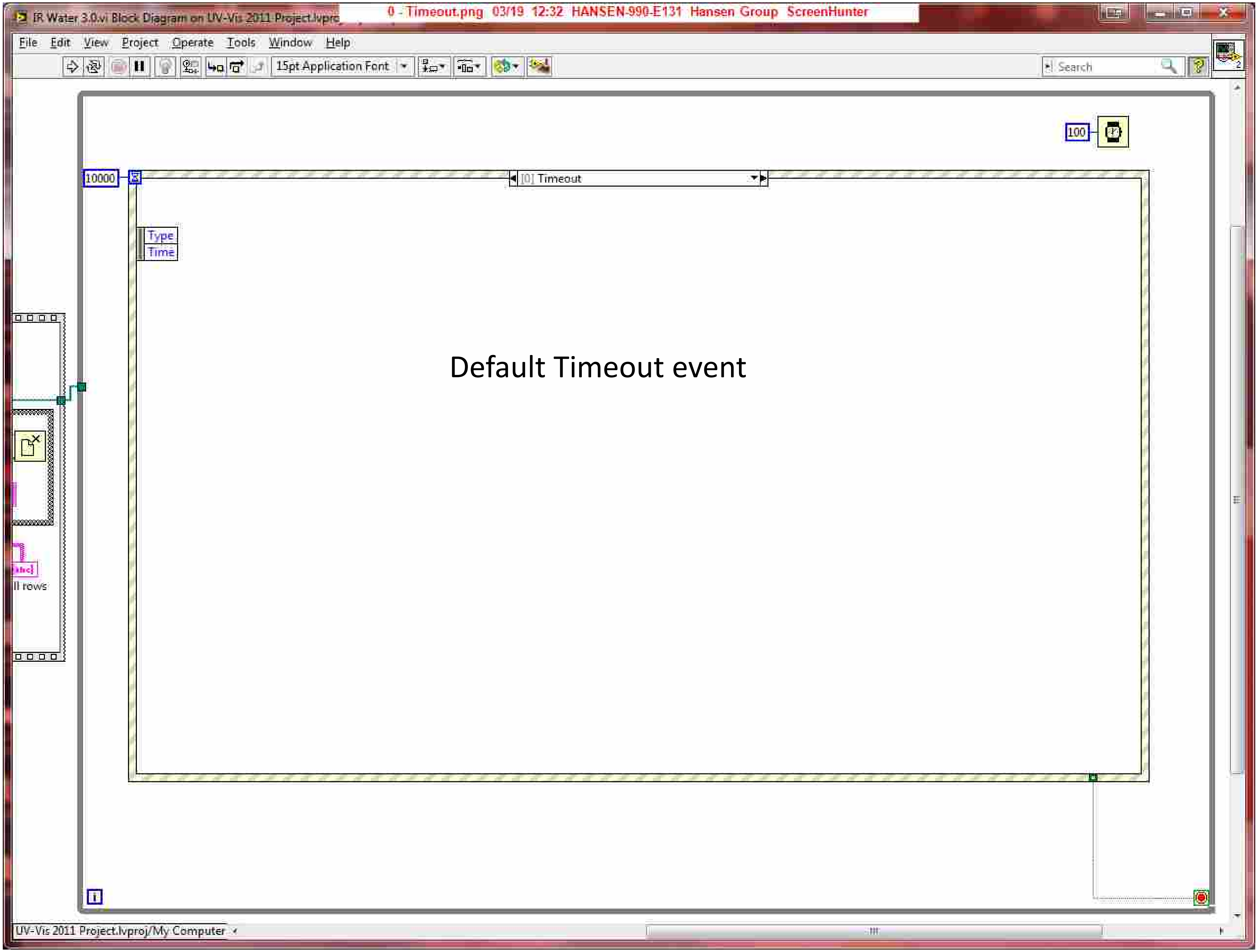

Default Timeout event

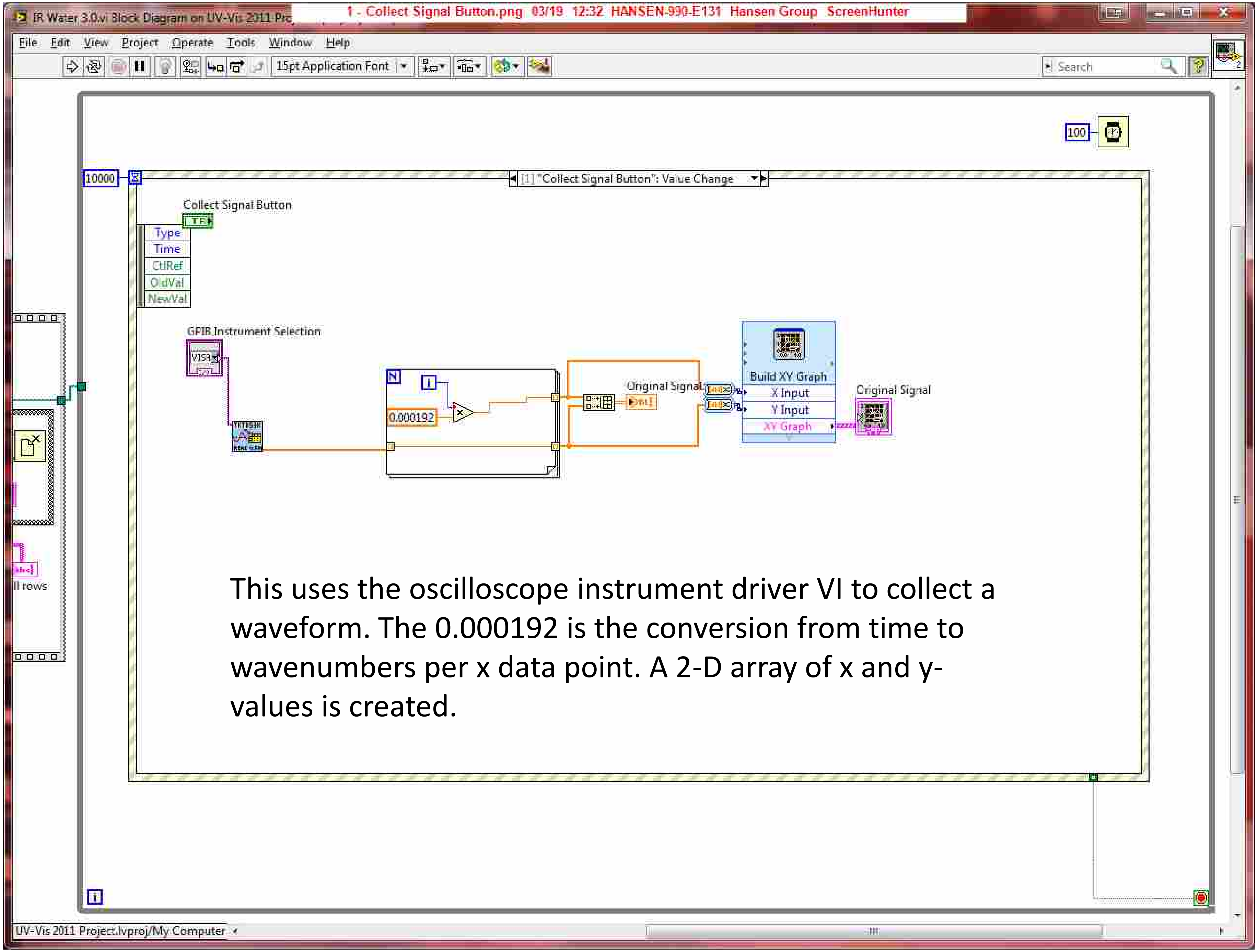

This uses the oscilloscope instrument driver VI to collect a waveform. The 0.000192 is the conversion from time to wavenumbers per x data point. A 2-D array of x and y-values is created.

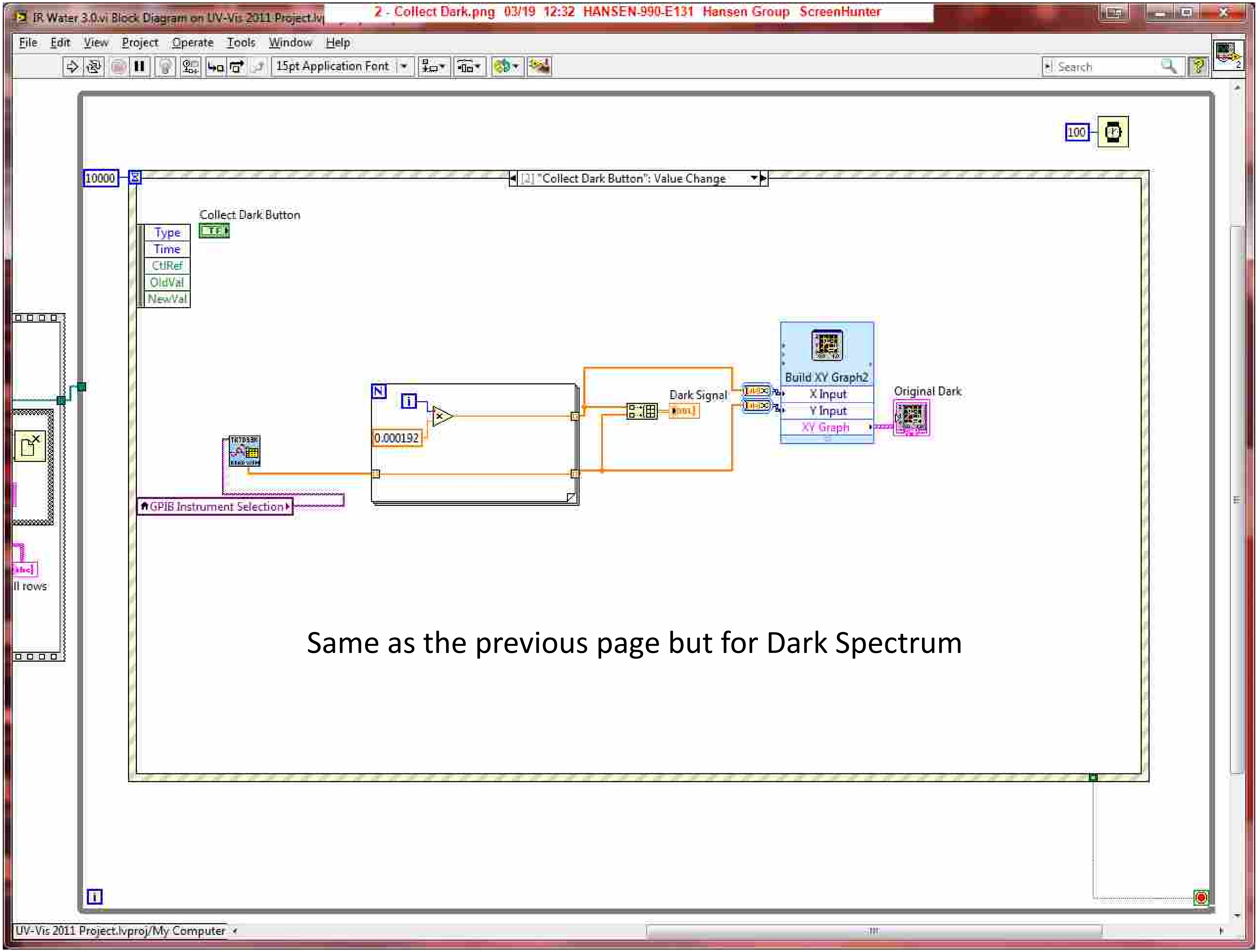

Same as the previous page but for Dark Spectrum

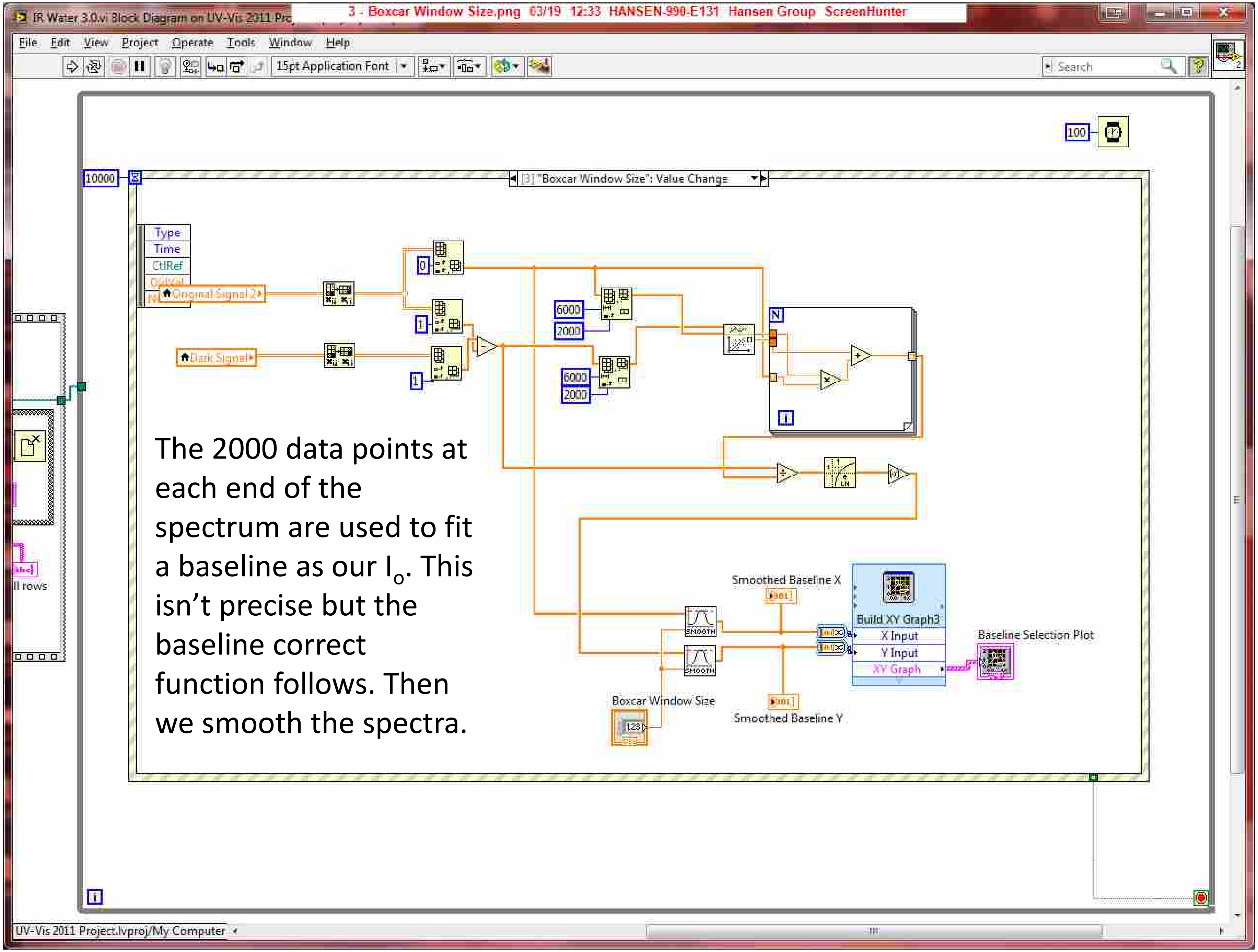

The 2000 data points at each end of the spectrum are used to fit a baseline as our I_o. This isn't precise but the baseline correct function follows. Then we smooth the spectra.

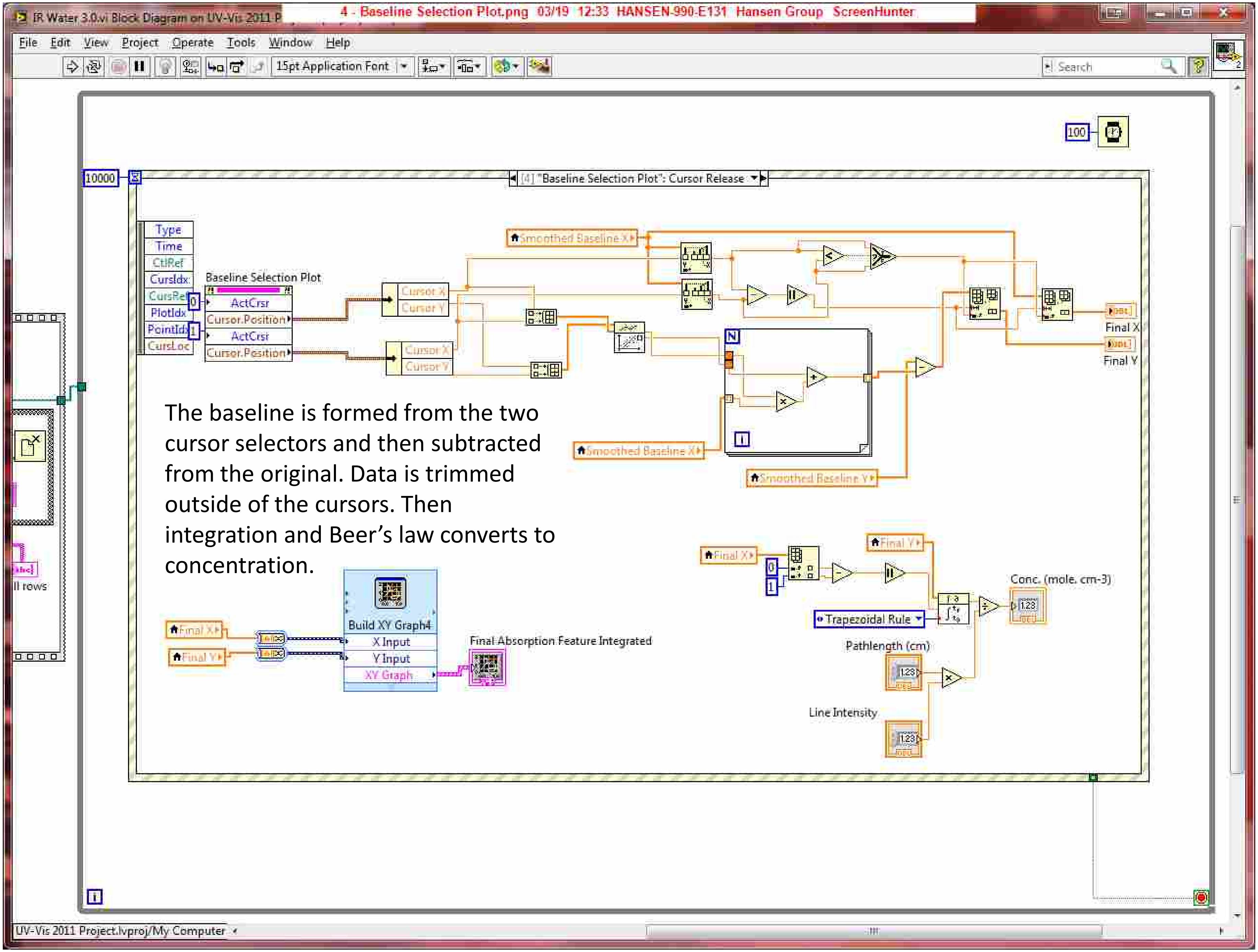

The baseline is formed from the two cursor selectors and then subtracted from the original. Data is trimmed outside of the cursors. Then integration and Beer's law converts to concentration.

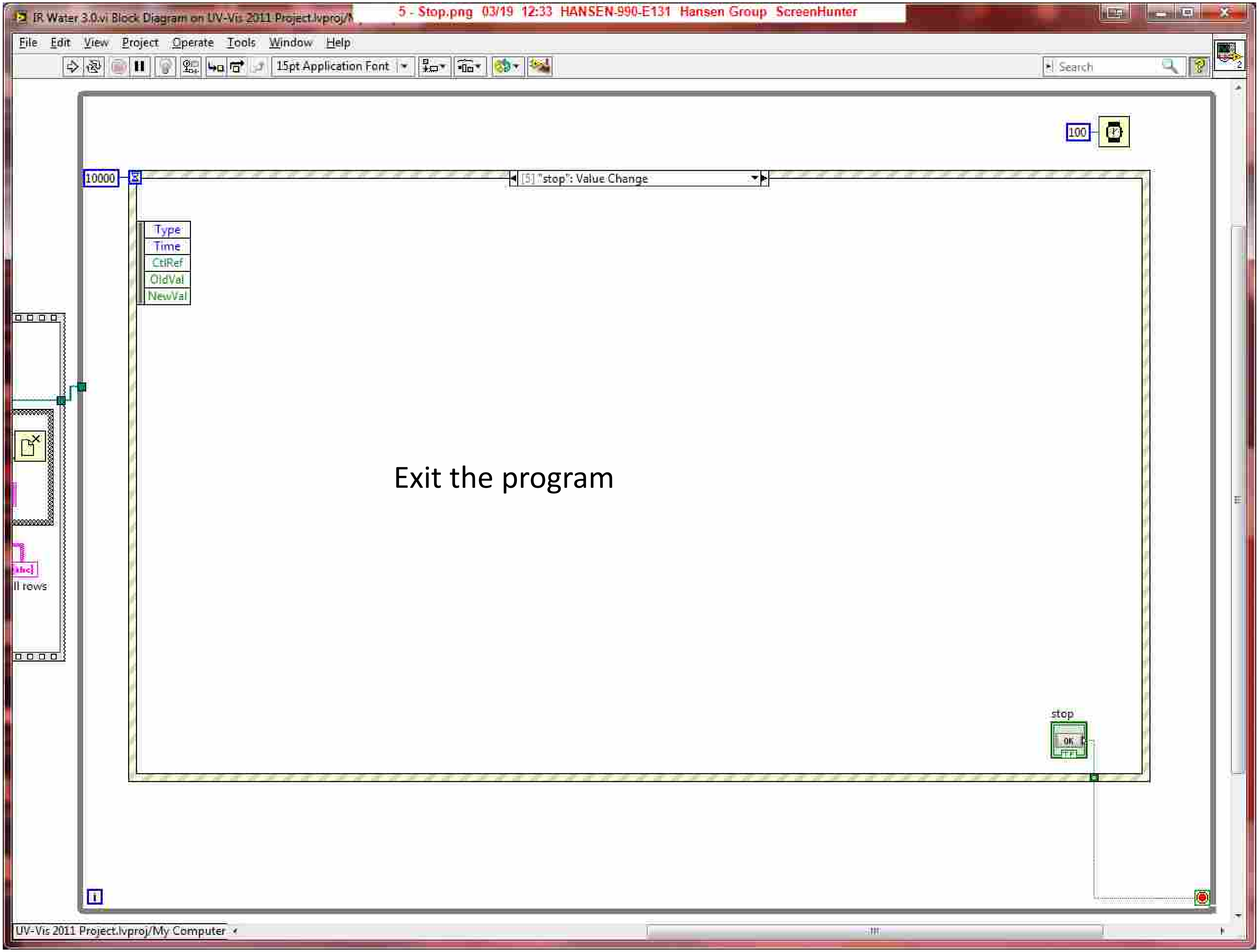

Exit the program

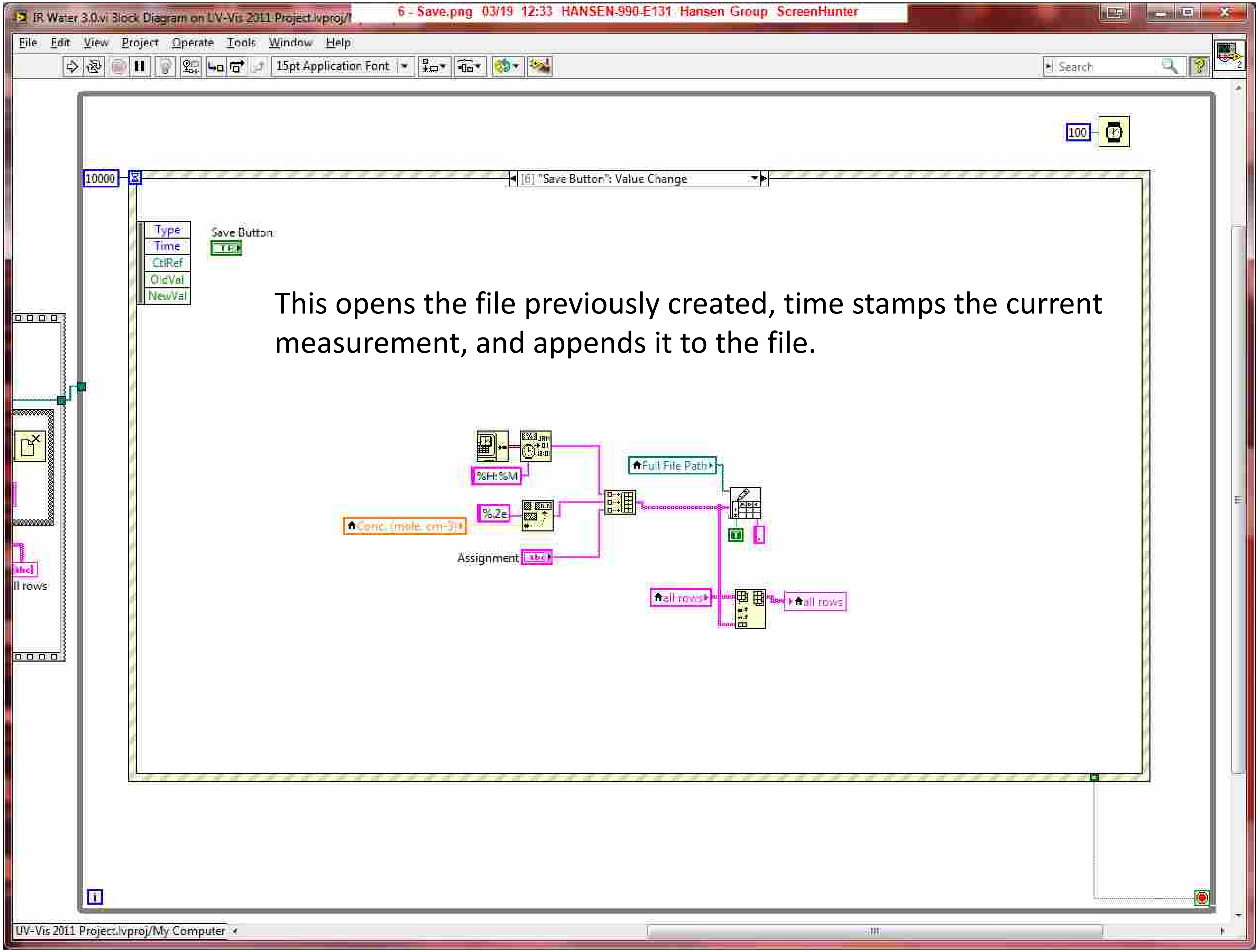

This opens the file previously created, time stamps the current measurement, and appends it to the file.